

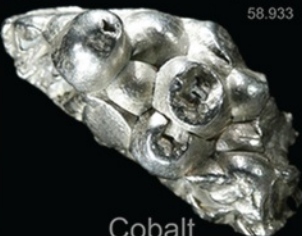






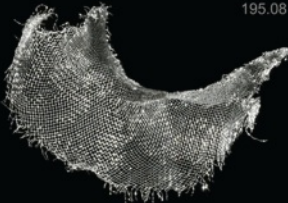

# Конденсированные среды и межфазные границы

РЕЦЕНЗИРУЕМЫЙ НАУЧНЫЙ ЖУРНАЛ

## Condensed Matter and Interphases

PEER-REVIEWED SCIENTIFIC JOURNAL

Том  
Vol. 27, № 3  
2025

<div>Co</div> <div>27</div> <div>58.933</div> <div></div> <div>Cobalt</div>	<div>Ni</div> <div>28</div> <div>58.693</div> <div></div> <div>Nickel</div>	<div>Cu</div> <div>29</div> <div>63.546</div> <div></div> <div>Copper</div>
<div>Rh</div> <div>45</div> <div>102.91</div> <div></div> <div>Rhodium</div>	<div>Pd</div> <div>46</div> <div>106.42</div> <div></div> <div>Palladium</div>	<div>Ag</div> <div>47</div> <div>107.87</div> <div></div> <div>Silver</div>
<div>Ir</div> <div>77</div> <div>192.22</div> <div></div> <div>Iridium</div>	<div>Pt</div> <div>78</div> <div>195.08</div> <div></div> <div>Platinum</div>	<div>Au</div> <div>79</div> <div>196.97</div> <div></div> <div>Gold</div>

# Condensed Matter and Interphases

## Kondensirovannyye sredy i mezhfaznye granitsy

Peer-reviewed scientific journal

Published since January 1999

Periodicity: Quarterly

Volume 27, No. 3, 2025

Full-text version is available in the Russian language on the website: <https://journals.vsu.ru/kcmf>

**Condensed Matter and Interphases** (Kondensirovannyye Sredy i Mezhfaznye Granitsy) publishes articles in Russian and English dedicated to key issues of condensed matter and physicochemical processes at interfaces and in volumes.

**The mission of the journal** is to provide open access to the results of original research (theoretical and experimental) at the intersection of contemporary condensed matter physics and chemistry, material science and nanoindustry, solid state chemistry, inorganic chemistry, and physical chemistry, and to share scientific data in the **following sections**: atomic, electron, and cluster structure of solids, liquids, and interphase boundaries; phase equilibria and defect formation processes; structure and physical and chemical properties of interphases; laser thermochemistry and photostimulated processes on solid surfaces; physics and chemistry of surface, thin films and heterostructures; kinetics and mechanism of formation of film structures; electrophysical processes in interphase boundaries; chemistry of surface phenomena in sorbents; devices and new research methods.

**The journal accepts for publication**: reviews, original articles, short communications by leading Russian scientists, foreign researchers, lecturers, postgraduate and undergraduate students.

### FOUNDER AND PUBLISHER:

Voronezh State University

The journal is registered by the Russian Federal Service for Supervision of Communications, Information Technology and Mass Media, Certificate of Registration ПИ № ФС77-78771 date 20.07.2020

The journal is included in the List of peer reviewed scientific journals published by the Higher Attestation Commission in which major research results from the dissertations of Candidates of Sciences (PhD) and Doctor of Science (DSc) degrees are to be published. Scientific specialties of dissertations and their respective branches of science are as follows: 1.4.1. – Inorganic Chemistry (Chemical sciences); 1.4.4. – Physical Chemistry (Chemical sciences); 1.4.6. – Electrochemistry (Chemical sciences); 1.4.15. – Solid State Chemistry (Chemical sciences); 1.3.8. – Condensed Matter Physics (Physical sciences).

The journal is indexed and archived in: Russian Scientific Index Citations, Scopus, Chemical Abstract, EBSCO, DOAJ, CrossRef

Editorial Board and Publisher Office:  
1 Universitetskaya pl., Voronezh 394018  
Phone: +7 (432) 2208445  
<https://journals.vsu.ru/kcmf>  
E-mail: [kcmf@main.vsu.ru](mailto:kcmf@main.vsu.ru)

When reprinting the materials, a reference to the Condensed Matter and Interphases must be cited

The journal's materials are available under the Creative Commons "Attribution" 4.0 Global License



© Voronezh State University, 2025

### EDITOR-IN-CHIEF:

**Victor N. Semenov**, Dr. Sci. (Chem.), Full Professor, Voronezh State University (Voronezh, Russian Federation)

### VICE EDITORS-IN-CHIEF:

**Evelina P. Domashevskaya**, Dr. Sci. (Phys.–Math.), Full Professor, Voronezh State University (Voronezh, Russian Federation)

**Polina M. Volovitch**, Ph.D. (Chem.), Associate Professor, Institut de Recherche de Chimie (Paris, France)

### EDITORIAL BOARD:

**Nikolay N. Afonin**, Dr. Sci. (Chem.), Voronezh State Pedagogical University (Voronezh, Russian Federation)

**Vera I. Vasil'eva**, Dr. Sci. (Chem.), Full Professor, Voronezh State University (Voronezh, Russian Federation)

**Aleksandr V. Vvedenskii**, Dr. Sci. (Chem.), Full Professor, Voronezh State University (Voronezh, Russian Federation)

**Victor V. Gusarov**, Dr. Sci. (Chem.), Associate Member of the RAS, Ioffe Physical-Technical Institute RAS (St. Petersburg, Russian Federation)

**Vladimir E. Guterman**, Dr. Sci. (Chem.), Full Professor, Southern Federal University (Rostov-on-Don, Russian Federation)

**Boris M. Darinskii**, Dr. Sci. (Phys.–Math.), Full Professor, Voronezh State University (Voronezh, Russian Federation)

**Vladimir P. Zlomanov**, Dr. Sci. (Chem.), Full Professor, Moscow State University (Moscow, Russian Federation)

**Valentin M. Levlev**, Dr. Sci. (Phys.–Math.), Full Member of the RAS, Moscow State University (Moscow, Russian Federation)

**Oleg A. Kozaderov**, Dr. Sci. (Chem.), Associate Professor, Voronezh State University (Voronezh, Russian Federation)

**Andrey I. Marshakov**, Dr. Sci. (Chem.), Full Professor, Frumkin Institute of Physical Chemistry and Electrochemistry RAS (Moscow, Russian Federation)

**Irina Ya. Mittova**, Dr. Sci. (Chem.), Full Professor, Voronezh State University (Voronezh, Russian Federation)

**Victor V. Nikonenko**, Dr. Sci. (Chem.), Full Professor, Kuban State University (Krasnodar, Russian Federation)

**Oleg V. Ovchinnikov**, Dr. Sci. (Phys.–Math.), Full Professor, Voronezh State University (Voronezh, Russian Federation)

**Sergey N. Saltykov**, Dr. Sci. (Chem.), Associate Professor, Novolipetsk Steel (Lipetsk, Russian Federation)

**Vladimir F. Selemenev**, Dr. Sci. (Chem.), Full Professor, Voronezh State University (Voronezh, Russian Federation)

**Pavel V. Seredin**, Dr. Sci. (Phys.–Math.), Associate Professor, Voronezh State University (Voronezh, Russian Federation)

**Evgeny A. Tutov**, Dr. Sci. (Chem.), Associate Professor, Voronezh State Technical University (Voronezh, Russian Federation)

**Vitaly A. Khonik**, Dr. Sci. (Phys.–Math.), Full Professor, Voronezh State Pedagogical University (Voronezh, Russian Federation)

**Andrey B. Yaroslavl'tsev**, Dr. Sci. (Chem.), Full Member of the RAS, Kurnakov Institute of General and Inorganic Chemistry RAS (Moscow, Russian Federation)

### INTERNATIONAL MEMBERS OF THE EDITORIAL BOARD:

**Mahammad Babanly**, Dr. Sci. (Chem.), Associate Member of the ANAS, Institute of Catalysis and Inorganic Chemistry ANAS (Baku, Azerbaijan)

**Tiziano Bellezze**, Dr. Sci. (Chem.), Marche Polytechnic University (Ancona, Italy)

**Mane Rahul Maruti**, Ph.D. (Chem.), Shivaji University (Kolhapur, India)

**Nguyen Anh Tien**, Ph.D. (Chem.), Associate Professor, University of Pedagogy (Ho Chi Minh City, Vietnam)

**Vladimir V. Pankov**, Dr. Sci. (Chem.), Full Professor, Belarusian State University (Minsk, Belarus)

**Fritz Scholz**, Dr. Sci., Professor, Institut für Biochemie Analytische Chemie und Umweltchemie (Greifswald, Germany)

**Mathias S. Wickleder**, Dr. Sci., Professor, University of Cologne (Köln, Germany)

**Vladimir Sivakov**, Dr. rer. nat., Leibniz Institute of Photonic Technology (Jena, Germany)

### EXECUTIVE SECRETARY:

**Vera A. Logacheva**, Cand. Sci. (Chem.), Voronezh State University (Voronezh, Russian Federation)

## CONTENTS

**Original articles***Chandrashekara H. D., Poornima P.*TiO<sub>2</sub> thin-film dielectric properties are impacted by annealing

345

*Shukla S., Kamal M.*

Synthesis and study of graphene oxide obtained from waste transparent polythene bags using modified Hummers method

354

*Darinsky B. M., Efanova N. D., Prizhimov A. S., Surkova A. A.*

Crystallographic classification of special grain boundaries

363

*Ilina E. A., Kozaderov O. A., Sotskaya N. V., Vandyshev D. Yu., Polikarchuk V. A., Shikhaliev Kh. S.*

Kinetics of electrocrystallization of copper from an acid sulfate solution in the presence of N-methylpolyvinylpyridine-methylsulfate

368

*Kovtunets E. V., Spiridonova T. S., Tushinova Yu. L., Bazarova T. T., Logvinova A. V., Bazarov B. G.*Ternary molybdate K<sub>5</sub>Cu<sub>0.5</sub>Hf<sub>1.5</sub>(MoO<sub>4</sub>)<sub>6</sub>: synthesis, structure, thermal expansion, and ionic conductivity

380

*Korotkov L. N., Tolstykh N. A., Popov I. I., Bocharov A. I., Kashirin M. A.*

Dielectric and piezoelectric properties of ceramic material based on modified lead zirconate titanate

391

*Kostyuchenko A. V., Belonogov E. K., Ievlev V. M., Nikonov A. E., Osipov E. A., Osipov P. A.*

Mechanical properties of Li-Nb-O system films

398

*Kruzhilin A. A., Shevtsov D. S., Dmitriev I. A., Potapov M. A., Shikhaliev Kh. S.*

Synthesis of 2-alkyl-5-phenyl-4,5,6,7-tetrahydro-[1,2,4]triazolo[1,5-a]pyrimidin-7-ol derivatives from vegetable oils and their efficiency as inhibitors of hydrochloric acid corrosion of steel

409

*Muratov T. T.*

Refined formula for the calculation of the coefficient of efficiency of an electrochemical generator

417

*Nazarovskaia D. A., Turishchev S. Yu., Titova S. S., Shatov A. A., Tyurin-Kuzmin P. A., Osminkina L. A.*

Photoluminescent properties of porous silicon nanoparticles: synthesis, characterization, and cellular imaging

422

*Nikitina E. V., Kaveev A. K., Fedorov V. V., Pirogov E. V., Nadtochiy A. M., Vasilkova E. I., Kryzhanovskaya N. V., Sobolev M. S.*

Study of photoluminescence kinetics in bulk GaPN and GaPNAs layers on silicon substrates grown by molecular beam epitaxy

433

*Rakitin V. V., Gapanovich M. V., Rabenok E. V., Kalimullina D. R., Lutsenko D. S., Kulemetev I. D., Koltsov E. N., Stanchik A. V., Gremenok V. F.*Research on the influence of the powder stoichiometry of (Ag<sub>x</sub>Cu<sub>1-x</sub>)<sub>0.7</sub>GaSe<sub>2</sub> on the phase composition, structure, and lifetime of photogenerated charge carriers

441

*Sobolev A. N., Kovtunets E. V., Spiridonova T. S., Bogdanov A. B., Subanakov A. K.*Double borate NaScB<sub>2</sub>O<sub>5</sub>: synthesis, thermal stability, ionic conductivity, IR spectroscopy, and electronic structure

454

*Yurchenko O. A., Solonchenko K. V., Pismenskaya N. D.*

Coupled effects of concentration polarization in systems with anion-exchange membranes before and after their participation in electrodialysis of tartrate-containing solutions

464

**Short communication***Sadykov T. T., Mustafin A. G., Kulish E. I., Akhmetkhanov R. M.*The influence of fullerene C<sub>60</sub> on the thermal stability of polyvinyl chloride

478

*Seredin P. V., Goloshchapov D. L., Peshkov Y. A., Buylov N. S., Potapov A. Y., Shikhaliev K. S., Ippolitov Yu. A., Raul O. Freitas, Francisco C. B. Maia*

Infrared synchrotron nanovisualization of a biomimetic layer composed of trimethyl-dihydroquinoline and nanocrystalline hydroxyapatite

483

*Boikov N. I., Chuvenkova O. A., Parinova E. V., Chumakov R. G., Lebedev A. M., Makarova A., Smirnov D., Titova S. S., Fateev K. A., Turishchev S. Yu.*

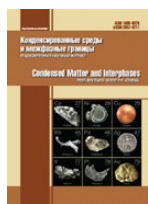
Synchrotron XANES studies of epitaxial tin-silicon solid solutions nanolayers

490

**Chronicle***Domashevskaya E. P.*

90 years of the scientific school of solid state physics at Voronezh State University: from solid state physics to nanophysics (Scientific and historical essay)

497



# Condensed Matter and Interphases

Kondensirovannye Sredy i Mezhfaznye Granitsy  
<https://journals.vsu.ru/kcmf/>

## Original articles

Research article

<https://doi.org/10.17308/kcmf.2025.27/13010>

## TiO<sub>2</sub> thin-film dielectric properties are impacted by annealing

H. D. Chandrashekara<sup>1✉</sup>, P. Poornima<sup>2</sup>

<sup>1</sup>SriHDDGFGC, Department of Physics,  
Paduvalahippe, H. N. Pura 573211, India

<sup>2</sup>Maharanis Science College, Department of Physics,  
Mysore 570005, Karnataka, India,

### Abstract

**Objective:** This study investigates the structural, morphological, and dielectric properties of TiO<sub>2</sub> thin films deposited using the Spray Pyrolysis Deposition (SPD) process and annealed at various temperatures.

**Experimental:** X-ray diffraction (XRD) analysis confirms the absence of an amorphous phase at 300 °C, while the anatase and rutile phases emerge at 400 °C, 500 °C, and 600 °C, with crystallite sizes increasing from 10.62 to 17.35 nm. Scanning electron microscopy (SEM) reveals a consistent grain growth trend, with grain sizes exceeding XRD estimates. Energy-dispersive X-ray (EDAX) spectroscopy confirms a stoichiometric Ti:O ratio and uniform nanoparticle distribution. The dielectric properties of Pt/TiO<sub>2</sub>/Si MOS capacitors were analyzed, demonstrating improved electrical stability with annealing. Conductance studies indicate a reduction in defect states, enhanced crystallinity, and stable dielectric behavior at higher frequencies. The hysteresis loop analysis reveals decreased losses at 600 °C due to minimized trapped charges and broken bonds. Impedance spectroscopy highlights capacitive behavior, with relaxation peaks at 400 °C, 500 °C, and 600 °C, while conductance measurements indicate thermal activation of charge carriers.

**Conclusions:** These findings suggest that TiO<sub>2</sub> thin films exhibit promising dielectric properties for potential applications in Si-based MOS capacitors and VLSI technology.

**Keywords:** Loss tangent, Angular frequency, Conductance, Series resistance, Impedance

**Acknowledgement:** The Indian Nano electronics User's Programme, Centre for Nano Science and Engineering (CeNSE), IISc, Bangalore, is gratefully acknowledged by the authors.

**For citation:** Chandrashekara H. D., Poornima P. TiO<sub>2</sub> thin-film dielectric properties are impacted by annealing. *Condensed Matter and Interphases*. 2025;27(3): 345–353. <https://doi.org/10.17308/kcmf.2025.27/13010>

**Для цитирования:** Чандрасхекхара Х. Д., Пурнима П. Влияние отжига на диэлектрические свойства тонкой пленки TiO<sub>2</sub>. *Конденсированные среды и межфазные границы*. 2025;27(3): 345–353. <https://doi.org/10.17308/kcmf.2025.27/13010>

✉ H. D. Chandrashekara, e-mail: [chandruhdcs@gmail.com](mailto:chandruhdcs@gmail.com)

© Chandrashekara H. D., Poornima P., 2025



The content is available under Creative Commons Attribution 4.0 License.

## 1. Introduction

The heat treatment procedure known as annealing has a substantial effect on the dielectric properties of thin films of titanium dioxide (TiO<sub>2</sub>). The TiO<sub>2</sub> is a material that is frequently used in electronic devices because of its excellent optical transparency, chemical stability, and dielectric constant. These devices include sensors, memory devices, and capacitors. The substantial number of studies published in the literature over the past ten years indicates the interest in TiO<sub>2</sub> [1–9]. TiO<sub>2</sub> thin-film production using atomic layer deposition and its dielectric characteristics [10]. TiO<sub>2</sub> thin films produced by pulsed laser deposition: their structural and dielectric characteristics [11]. Spray pyrolysis is the most used method of film synthesis of all the approaches [12]. Technology-related applications for titanium oxide films include solar cells, thin-film transistors, sensors, and other devices. Numerous techniques, including thermal evaporation of oxide powders, electron beam evaporation, chemical vapor deposition, sputtering, sol–gel, and spray deposition, can be used to generate TiO<sub>2</sub> thin films. However, each technique has pros and cons. Since spray deposition offers low processing temperatures, low cost of manufacturing, and improved control over the deposition settings, it affords an easy solution to include TiO<sub>2</sub> devices into Si technology. In order to improve device performance, future nanoelectronic devices may use metal oxides with high dielectric constants in place of TiO<sub>2</sub> in the gate and high-mobility semiconductors like Si in the active channel [13, 14]. Critical performance parameters of MOS capacitors and transistors for aggressive oxide scaling with equivalent oxide thickness (EOT) are determined by the interface between dielectric materials and Si. The capacitance methods of semiconductor examination, which provide comprehensive information about the properties of localized electronic states (or energy levels), have gained significant recognition [15–17]. After being annealed in an oxygen environment, the TiO<sub>2</sub> thin films' dielectric constant greatly increased. Improvements in the films' crystallinity and decrease in oxygen vacancies are responsible for this increase in the dielectric constant. These films can be used in capacitors, transistor

gate dielectrics, and other electronic devices because of their enhanced dielectric qualities [18]. "Surface states" refers to the localized electronic states that are connected to the surface area. Their existence is caused by the periodic lattice structure breaking at the surface, surface preparation, oxide layer development, and semiconductor impurity concentration. The existence of an interfacial layer between the contact materials and interface states at the oxide layer/semiconductor interface, however, frequently disturbs this idealized scenario. In this study, the dielectric parameters for (Pt/TiO<sub>2</sub>/Si) MOS capacitors in the voltage range of -2V to +2V at different temperatures were examined. The dielectric parameters were obtained from *C*–*V*, *tan*( $\delta$ )–Voltage, *G*/ $\omega$ – $\omega$ , and *Z*–*f* measurements. The capacitors were deposited at 300 °C and then annealed at 400 °C, 500 °C, and 600 °C.

The primary goal of this research involves growing. Depending on the annealing temperature, annealing usually improves the films crystalline structure by converting their amorphous or less crystalline structures into clearly defined crystalline phases like rutile or anatase. Because there are fewer flaws and grain boundaries in the film as a result of this increased crystalline, the dielectric qualities—such as a higher dielectric constant and less dielectric loss—are improved.

## 2. Experimental

Acetyl acetate was used as a complexing agent, absolute ethanol was used as a solvent, and titanium (IV) isopropoxide was used as the source material for the spray pyrolysis deposition (SPD), which produced the TiO<sub>2</sub> thin films under ideal conditions [19]. The silicon wafers were cleaned using RCA-1 and RCA-2 prior to deposition. TiO<sub>2</sub> thin films were deposited using 0.1 mol TiO<sub>2</sub> precursor solution at 300 °C substrate temperature. Following deposition, isochronal annealing experiments were conducted in air at 400 °C, 500 °C, and 600 °C for a continuous duration of 30 minutes.

An EDAX and SEM were used to study the surface morphology under a field emission scanning electron microscope (ULTRA 55, Karl Zeiss). To investigate the dielectric characteristics, 100 platinum dots were deposited to create electrical connections. The microstructure,

surface morphology, and general quality of the TiO<sub>2</sub> thin films are similarly impacted by annealing. It can boost the density of the film and lessen the existence of residual stresses, both of which add to the improved dielectric performance. Because of this, annealed TiO<sub>2</sub> thin films have better electrical insulation and stability, which makes them more appropriate for use in optoelectronic and electronic devices.

### 2.1. Material characterization

The X-ray diffraction (XRD) patterns of TiO<sub>2</sub> films as-deposited at 300 °C and those annealed in air at 400 °C, 500 °C, and 600 °C are displayed in Fig. 1. There are no noticeable peaks in the amorphous structure of the film as it was deposited at 300 °C. The anatase phase of TiO<sub>2</sub> is shown by peaks in the film that was annealed at 400 °C. Along with the anatase phase, the films annealed at 500 °C and 600 °C exhibit the appearance of peaks corresponding to the rutile phase of TiO<sub>2</sub>. Higher annealing temperatures result in more intense rutile peaks, suggesting a larger percentage of the rutile phase at higher temperatures [20].

A distinct pattern of growing crystallite size with increasing annealing temperature is seen in the estimated crystallite sizes of 10.62, 13.73, 16.04, and 17.35 nm derived from X-ray diffraction using the Scherrer formula. Grain sizes derived from SEM pictures are, on average, 13.6, 16.3, 17.5, and 27.3 nm. As expected given that grains seen in SEM may include several

crystallites, the grain sizes derived from SEM are consistently greater than the crystallite sizes ascertained via XRD. This disparity raises the possibility of smaller crystallites coalescing at higher temperatures as well as the presence of contributions from grain boundaries. Smooth surface roughness and a consistent, compact distribution of grains are shown in the SEM picture of the deposited TiO<sub>2</sub> films in Fig. 2a. The histograms reveals that, the *x*-axis represents grain size ranges, and the *y*-axis shows the number of grains in each size range. Temperature affects the distribution of grain sizes. The distribution of grain sizes in TiO<sub>2</sub> films at various temperatures is revealed by the investigation. The histograms demonstrate that the distribution of grain sizes changes with temperature, with smaller grain clusters becoming more pronounced at 500 °C and 600 °C, expanding at 400 °C, and more densely packed at 300 °C.

The energy dispersive analysis X-ray spectrum is displayed in Fig. 2b. As samples are deposited and annealed, the weight fraction of oxygen and Ti changes. The produced TiO<sub>2</sub> thin films' chemical composition analysis shows good stoichiometry. The weight % of Ti and oxygen fluctuates for samples that are annealed and deposited, according to energy dispersive analysis X-ray spectrum analysis. The results obtained are in good agreement with the previously reported works [21, 22].

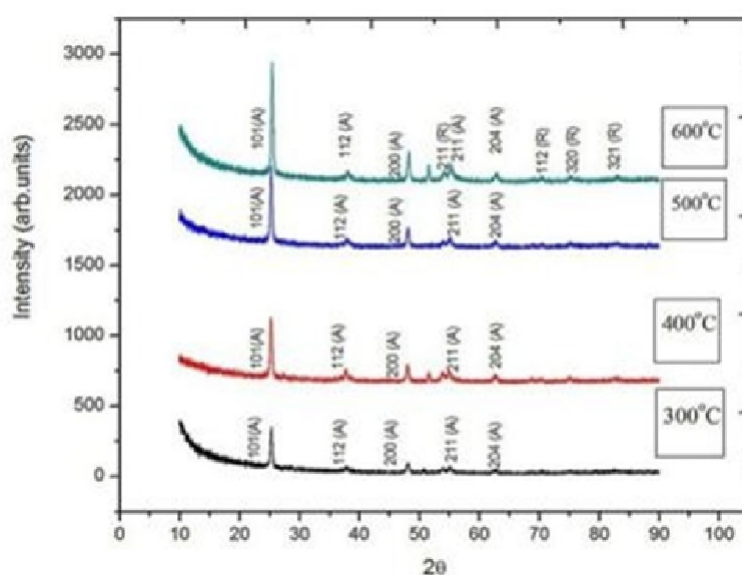


Fig. 1. XRD pattern of air-annealed and as-deposited thin films of TiO<sub>2</sub>

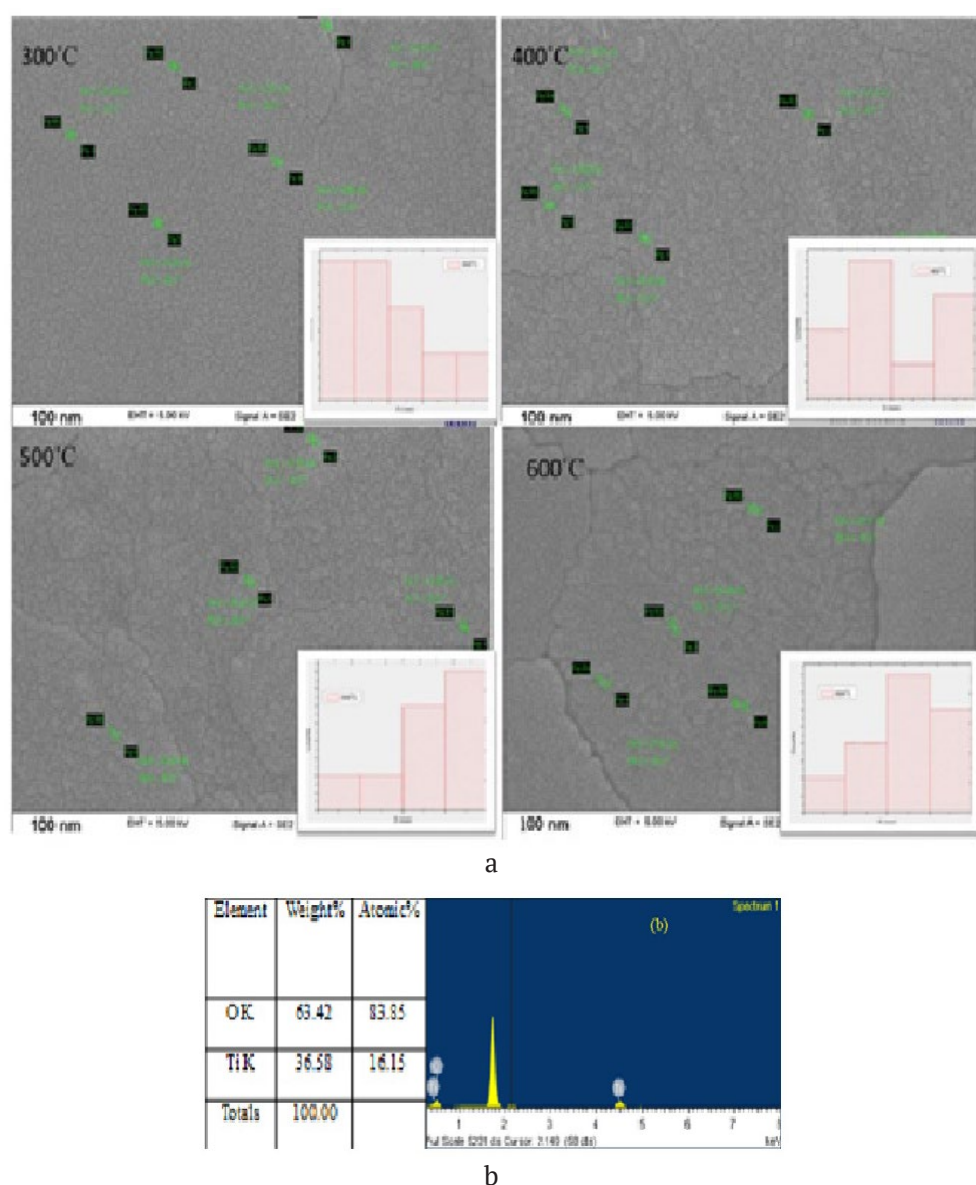
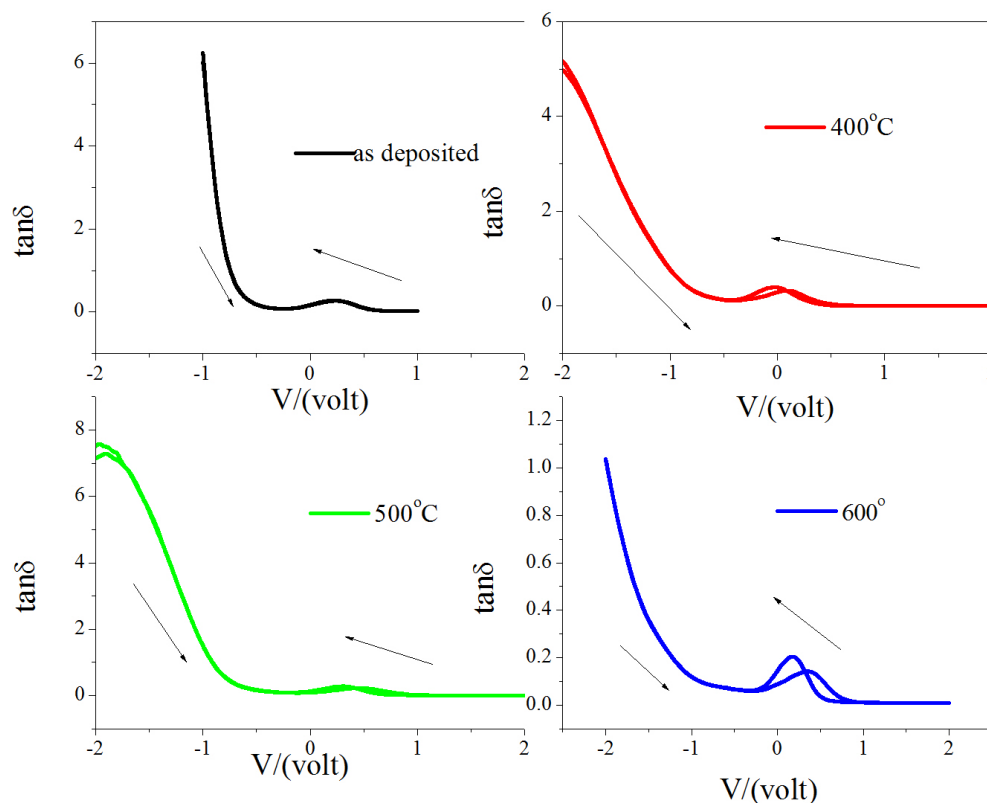


Fig. 2. (a) SEM (inset: Histogram) and (b) EDX spectrum of TiO<sub>2</sub> thin films as deposited

## 2.2. Dielectric features

The  $\tan(\delta)$ –Voltage characteristics for both deposited and annealed films are displayed in Fig. 3 as a function of voltage (+2V to –2V) at a constant frequency of 1MHz. Near zero bias, a tiny peak emerges, which could be the result of the flat band shift making the dielectric losses more noticeable. As heat treatment is applied, it can be seen that the resulting dissipation factor or loss factor decreases, which reduces interface trapped charge and dangling bonds. Low-frequency impedance is controlled by the interface states with the substrate and the dielectric properties of the TiO<sub>2</sub> layer, as shown in Fig. 4. Capacitive reactance decreases with frequency, allowing the

intrinsic characteristics of the dielectric material to have a greater impact on impedance behavior. An injection locking phenomena involving oxide charge density oscillation may be the cause of the lowering impedance values with increasing frequency [23, 24]. The dielectric and conductive characteristics of the films are revealed by conducting conductance versus angular frequency analysis for MOS devices with as-deposited TiO<sub>2</sub> thin films annealed at different temperatures [25]. Interface states with the substrate and the dielectric characteristics of the TiO<sub>2</sub> layer control low-frequency impedance. Because capacitive reactance decreases with frequency, the inherent properties of the dielectric material can have



**Fig. 3.**  $\tan \delta$ -Voltage characteristic of MOS devices for TiO<sub>2</sub> thin films annealed at various temperatures

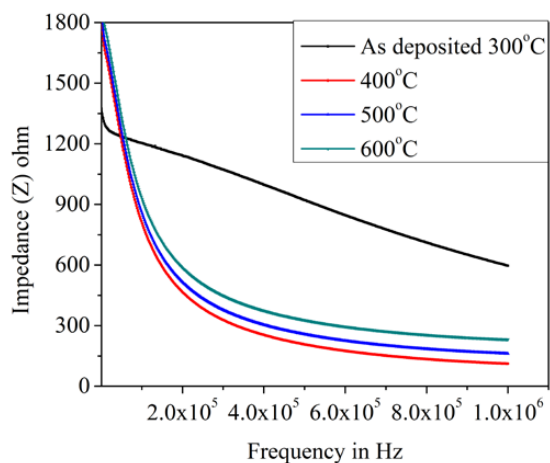


**Fig. 4.** Impedance versus frequency of MOS devices for TiO<sub>2</sub> thin films annealed at various temperatures

a greater impact on impedance behavior. The decreasing impedance values at increasing frequencies could be explained by an injection locking phenomenon involving oxide charge density oscillation.

The intriguing characteristic is that conductance increases with frequency shown in Fig. 5, this may be due to an interface-

trapped charge [26]. An increasing annealing temperature is shown to cause a decrease in conductance, which is ascribed to an increase in leakage current [27]. The variation of dielectric losses with applied voltage is shown by the  $\tan(\delta)$  – Voltage characteristic of MOS devices employing as-deposited TiO<sub>2</sub> thin films. Due to dielectric property changes, this characteristic can be significantly altered when TiO<sub>2</sub> thin films are annealed at different temperatures. The  $\tan(\delta)$  becomes more stable at higher annealing temperatures across a wider voltage range. This stability suggests lower leakage currents and better film quality. The Fig. 6 shows parallel resistance ( $R_p$ ) versus frequency at different temperatures for a MOS device. The steepest decrease is at lower frequencies, while higher frequencies show more gradual decreases. The device's AC response characteristics and temperature dependence suggest thermal activation of charge carriers, and the variation in resistance patterns suggests changes in the material's electronic properties. The MOS device's series resistance ( $R_s$ ) is displayed against frequency in Fig. 7. The main findings are

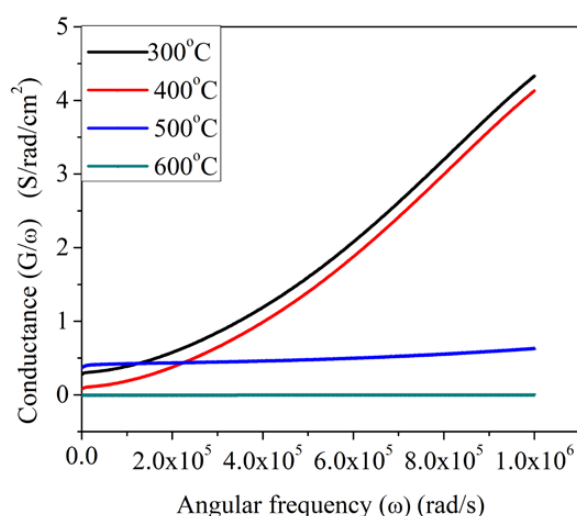


**Fig. 5.**  $(G/\omega-\omega)$  conductance versus angular frequency of MOS devices for TiO<sub>2</sub> thin films annealed at various temperatures

that the series resistance exhibits capacitive behavior, beginning high at low frequencies and gradually decreasing with increasing frequency. In comparison to the as-deposited state, the series resistance dramatically drops at 300, 400, 500, and 600 °C, particularly at higher frequencies. The presence of relaxation processes connected to the microstructure alterations in the MOS stack is suggested by the resistance plots' unique peaks at different frequencies. The MOS device's zeta ( $Z$ ) is shown against frequency in Fig. 8. The authors noted that impedance exhibits normal capacitive behaviour, beginning high at low frequencies and decreasing with increasing frequency. The presence of relaxation processes is indicated by the impedance plots unique peaks at different frequencies at 500 °C. The impedance curve exhibits a further decline in magnitude at 600 °C, suggesting a lessening of the capacitive effects. The impedance curve rapidly decreases at higher frequencies at 400 °C, indicating better conductive qualities.

### 3. Conclusion

At a temperature of 300 °C, the interfacial insulating layers were deposited using the SPD process and subsequently annealed isochronally. The XRD patterns of TiO<sub>2</sub> films observed that, the amorphous structure is absent at 300 °C, while the anatase phase and rutile phase are visible at annealed at 400 °C, 500 °C, and 600 °C. Crystallite

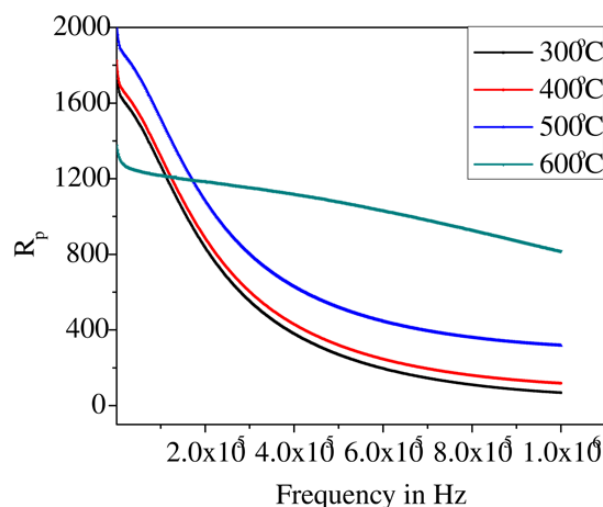


**Fig. 6.** Parallel resistance versus frequency of MOS devices for TiO<sub>2</sub> thin films annealed at various temperatures

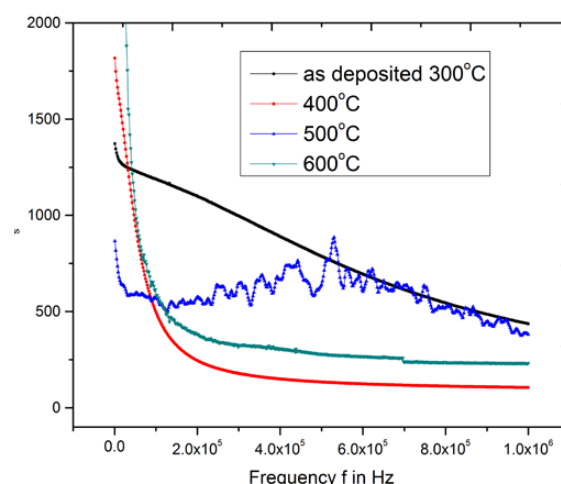


**Fig. 7.** Series resistance versus frequency of MOS devices for TiO<sub>2</sub> thin films annealed at various temperatures

sizes increase with annealing temperature, with estimated sizes of 10.62, 13.73, 16.04, and 17.35 nm. SEM grain sizes are consistently greater than XRD, indicating a growing pattern. The EDAX analysis revealed a stoichiometric Titanium (Ti): Oxygen (O) ratio, with a uniform distribution of TiO<sub>2</sub> nano-particles on the surface.

The dielectric characteristics of MOS devices, including  $\tan(\delta)$ , conductance, and impedance, were investigated. For (Pt/TiO<sub>2</sub>/Si) MOS capacitors, the  $\tan \delta$  – Voltage,  $G/\omega - \omega$ , and  $Z-f$  properties were measured. The influence of annealing on the electrical properties of the films is shown by conductance versus angular frequency study

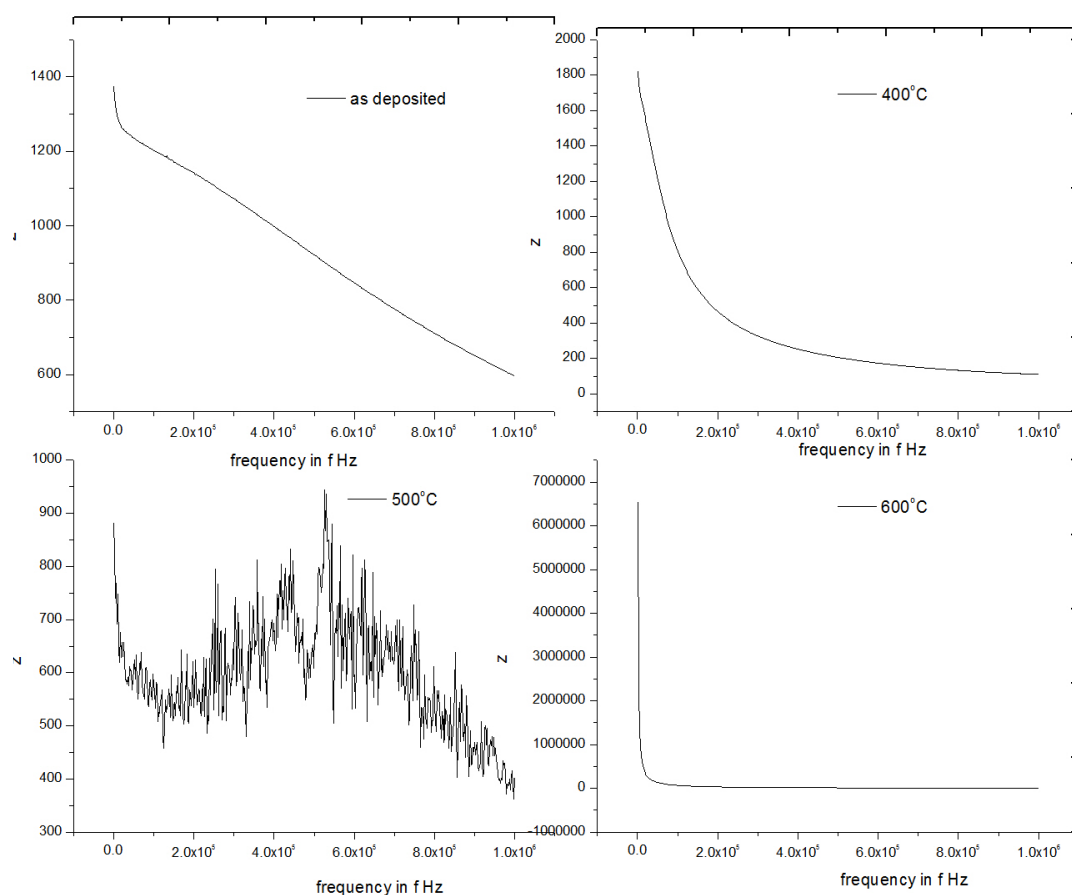


**Fig. 8.** Zeta ( $Z$ ) versus frequency of MOS devices for TiO<sub>2</sub> thin films annealed at various temperatures

for MOS devices with TiO<sub>2</sub> thin films. Lower conductance at low frequencies and more stable dielectric behaviour at higher frequencies are the results of annealing, which efficiently decreases defects and increases crystalline. The hysteresis loop shows decreased losses due to thermal treatment at 600 °C, which they ascribe to fewer broken bonds and trapped charges at the interface. The parallel resistance decreases rapidly at different temperatures, suggesting thermal activation of charge carriers and changes in the material's electronic properties. The MOS device's series resistance, exhibiting capacitive behaviour, decreasing with frequency, particularly at higher frequencies, compared to the as-deposited state. The MOS device's zeta ( $Z$ ) shows normal capacitive behaviour, with relaxation processes indicated by unique peaks at 500 °C, 600 °C, and 400, with a decline in magnitude at 600 °C and better conductive qualities at 400 °C.

### Contribution of the authors

The authors contributed equally to this article.

### Conflict of interests

The authors declare that they have no known competing financial interests or personal relationships that could have influenced the work reported in this paper.

### Reference

1. Zhao L., Wang J., Gai Z., ... Wang X. Annealing effects on the structural and dielectric properties of (Nb + In) co-doped rutile TiO<sub>2</sub> ceramics. *RSC Advances*. 2019;9: 8364-8368. <https://doi.org/10.1039/c9ra00564a>
2. Akgul U. Structural and dielectric properties of TiO<sub>2</sub> thin films grown at different sputtering powers. *The European Physical Journal Plus*. 2019;134: 3. <https://doi.org/10.1140/epjp/i2019-12407-7>
3. Zheng Q., Fang G., Cheng F., Lei H., Qin P., Zhan C. Low-temperature solution-processed graphene oxide derivative hole transport layer for organic solar cells. *Journal of Physics D: Applied Physics*. 2013;46(13): 135101. <https://doi.org/10.1088/0022-3727/46/13/135101>
4. Alaya Y., Souissi R., Toumi M., ... Alaya S. Annealing effect on the physical properties of TiO<sub>2</sub> thin films deposited

by spray pyrolysis. *RSC Advances*. 2023;32(13): 21852–21860. <https://doi.org/10.1039/d3ra02387g>

5. Juma A., Acik I. O., Mere A., Krunk M. Dielectric relaxation and conduction mechanisms in sprayed TiO<sub>2</sub> thin films as a function of the annealing temperature. *Applied Physics A*. 2016;122(4). <https://doi.org/10.1007/s00339-016-9874-4>

6. Sharma R. K., Chan P. C. H., Tang Z., Yan G., Hsing I.-M., Sin J. K. O. Sensitive, selective and stable tin dioxide thin-films for carbon monoxide and hydrogen sensing in integrated gas sensor array applications. *Sensors and Actuators B: Chemical*. 2001;72(2): 160–166. [https://doi.org/10.1016/s0925-4005\(00\)00646-8](https://doi.org/10.1016/s0925-4005(00)00646-8)

7. Brinzari V., Korotcenkov G., Golovanov V. Factors influencing the gas sensing characteristics of tin dioxide films deposited by spray pyrolysis: understanding and possibilities of control. *Thin Solid Films*. 2001;391: 167. [https://doi.org/10.1016/s0040-6090\(01\)00978-6](https://doi.org/10.1016/s0040-6090(01)00978-6)

8. Karadeniz S., Tuğluoğlu N., Serin T. Substrate temperature dependence of series resistance in Al/SnO<sub>2</sub>/p-Si (111) Schottky diodes prepared by spray deposition method. *Applied Surface Science*. 2004;233(1–4): 5–13. <https://doi.org/10.1016/j.apsusc.2004.03.216>

9. Altındal S., Karadeniz S., Tuğluoğlu N., Tataroğlu A. The role of interface states and series resistance on the *I*–*V* and *C*–*V* characteristics in Al/SnO<sub>2</sub>/p-Si Schottky diodes. *Solid-State Electronics*. 2003;47(10), 1847–1854. [https://doi.org/10.1016/s0038-1101\(03\)00182-5](https://doi.org/10.1016/s0038-1101(03)00182-5)

10. Kim T., Jeon J., Ryu S. H. ... Kim S. K. Atomic layer growth of rutile TiO<sub>2</sub> films with ultrahigh dielectric constants via crystal orientation engineering. *ACS Applied Materials & Interfaces*. 2024;16(26): 33877–33884. <https://doi.org/10.1021/acsami.4c08379>

11. Nasir N. A., Shabeeb K. M., Hassan A. K., Mahmood S. M. Structural, optical, and electrical characteristics of titanium dioxide thin films prepared by pulsed laser deposition. *Iraqi Journal of Industrial Research*. 2023;10(3): 1–10. <https://doi.org/10.53523/ijoirvol10i3id349>

12. Chandrashekar H. D., Basavaraj Angadi, Poornima P., Shashidhar R., Murthy L. C. S. Optical properties of (TiO<sub>2</sub>)<sub>1-x</sub>(CuO)<sub>x</sub> pseudo binary oxides thin films prepared by spray pyrolysis technique. *International Journal of Nanotechnology*. 2017;14: 9–10. <https://doi.org/10.1504/ijnt.2017.086771>

13. Chi On Chui, Ramanathan S., Triplett B. B., McIntyre P. C., Saraswat K. C. Germanium MOS capacitors incorporating ultrathin high- $\kappa$ /gate dielectric. *IEEE Electron Device Letters*. 2002;23(8): 473–475. <https://doi.org/10.1109/led.2002.801319>

14. Ritenour A., Khakifirooz D. A., Antoniadis R. Z., Lei W., Tsai A., Dimoulas A. Subnanometer-equivalent-oxide-thickness germanium *p*-metal-oxide-semiconductor field effect transistors fabricated using molecular-beam-deposited high- $\kappa$ /metal gate stack. *Applied Physics Letters*. 2006;88(13): 132107. <https://doi.org/10.1063/1.2189456>

15. Deuling H., Klausmann E., Goetzberger A. Interface states in Si/SiO<sub>2</sub> interfaces. *Solid-State Electronics*. 1972;15(5): 559. [https://doi.org/10.1016/0038-1101\(72\)90157-8](https://doi.org/10.1016/0038-1101(72)90157-8)

16. Nicollian E. H., Brews J. R. Rapid interface parameterization using a single MOS conductance curve. In:

*MOS Physics and Technology*. New York: Wiley, 1982. 906 p. 1982

17. Zhao Y., Tripathi M., Čerņevičs K., ... Kis A. Electrical spectroscopy of defect states and their hybridization in monolayer MoS<sub>2</sub>. *Nature Communications*. 2023;14(1). <https://doi.org/10.1038/s41467-022-35651-1>

18. Kumar A., Manavalan S. G., Gurumurthy V., Jeedigunta S., Weller T. Dielectric and structural properties of pulsed laser deposited and sputtered barium strontium titanate thin films. *Materials Science and Engineering B*. 2007;139: 177–185. <https://doi.org/10.1016/j.mseb.2007.02.005>

19. Chandrashekar H. D., Basavaraj Angadi, Ravikiran Y. T., Poornima P., Shashidhar R., Murthy L. C. S. Nano porous Al<sub>2</sub>O<sub>3</sub>-TiO<sub>2</sub> thin film based humidity sensor prepared by spray pyrolysis technique. *AIP Conference Proceedings*. 2016;1728(1): 020615. <https://doi.org/10.1063/1.4946666>

20. Jurek K., Szczesny R., Trzcinski M., Ciesielski A., Borysiuk J., Skowronski L. The influence of annealing on the optical properties and microstructure recrystallization of the TiO<sub>2</sub> layers produced by means of the e-BEAM technique. *Materials*. 2021;14(19): 5863. <https://doi.org/10.3390/ma14195863>

21. Chandrashekar H. D., Basavaraj Angadi, Shashidhar R., Poornima P., Murthy L. C. S. Isochronal effect of optical studies of TiO<sub>2</sub> thin films deposited by spray pyrolysis technique. *Advanced Science Letters*. 2016;22: 739–744. <https://doi.org/10.1166/asl.2016.6975>

22. Ray S. C., Mishra D. K., Panda A. B., Wang H. T., Bhattacharya (Mitra) S., Pong W. F., Temperature-dependent electronic structure of TiO<sub>2</sub> thin film deposited by the radio frequency reactive magnetron sputtering technique: X-ray absorption near-edge structure and X-ray photoelectron spectroscopy. *The Journal of Physical Chemistry C*. 2022;126(20): 8553–8966. <https://doi.org/10.1021/acs.jpcc.2c02311>

23. Hiraoka T., Arikawa T., Yasuda H., ... Tanaka K. Injection locking and noise reduction of resonant tunneling diode terahertz oscillator. *APL Photonics*. 2021;6(2). <https://doi.org/10.1063/5.0033459>

24. Lee D., Kwak M., Lee J., Woo J., Hwang H. Linear frequency modulation of NbO<sub>2</sub>-based nanoscale oscillator with Li-based electrochemical random access memory for compact coupled oscillatory neural network. *Frontiers in Neuroscience*. 2022;16: 939687. <https://doi.org/10.3389/fnins.2022.939687>

25. Chandrashekar H. D., Poornima P. Temperature influences of the interfacial layer in MOS (Pt/TiO<sub>2</sub>/Si) structures. *Condensed Matter and Interphases*. 2023;25(2): 406–414. <https://doi.org/10.17308/kcmf.2023.25/11266>

26. Ahiboz D., Nasser H., Aygün E., Bek A., Turan R. Electrical response of electron selective atomic layer deposited TiO<sub>2-x</sub> hetero contacts on crystalline silicon substrates. *Semiconductor Science and Technology*. 2018;33(4): 045013. <https://doi.org/10.1088/1361-6641/aab535>

27. Zhang D., Shin P., Wu X., Ren W. Structural and electrical properties of sol-gel-derived Al-doped bismuth ferrite thin films. *Ceramic International*. 2013;39(1): S461–S464. <https://doi.org/10.1016/j.ceramint.2012.10.114>

### Information about the authors

*H. D. Chandrashekara*, MSc, Mphil, PhD, Associate Professor, Department of Physics, SriHDDGFGC (Hassan, Karnataka, India).

<https://orcid.org/0000-0001-9976-3128>  
chandruhdcs@gmail.com

*P. Poornima*, MSc, Mphil, PhD, Associate Professor, Department of Physics, Maharani Science College (Mysore, Karnataka, India).

<https://orcid.org/0000-0001-7685-6778>  
poornimaputtegowda81@gmail.com

*Received November 2, 2024; approved after reviewing March 27, 2025; accepted for publication April 15, 2025; published online September 25, 2025.*



## Original articles

Research article

<https://doi.org/10.17308/kcmf.2025.27/13011>

### Synthesis and study of graphene oxide obtained from waste transparent polythene bags using Modified Hummers method

S. Shukla<sup>1</sup>✉, M. Kamal<sup>2</sup>

<sup>1</sup>Department of Chemistry, Christ Church College,  
Mall Road, Bada Chauraha, Kanpur 208001, India

<sup>2</sup>Department of Chemistry, Christ Church College,  
Mall Road, Bada Chauraha, Kanpur 208001, India

#### Abstract

**Objective:** Plastic industry has seen explosive growth in previous decades over the world. Every sphere of day to day life revolves around plastic products. The used plastic gets accumulated on the Earth's surface and serves as a contaminant causing soil, land and water pollution. Waste plastic needs proper management and elimination from the biotic layer of the ecosystem. Most potent solution is conversion of plastic waste into a functional carbon material. Present work concentrates on upcycling of waste plastic into economically crucial material that is graphene oxide. The waste polythene bags were successfully converted to graphitic carbon which in turn serves as the base for the synthesis of graphene oxide using modified Hummers method.

**Experimental:** The analysis was made by studying the FTIR spectra, SEM images and XRD graphs. The FTIR confirms the presence of hydroxyl and carbonyl groups along with carbon carbon interaction. Surface morphology shows the porous and layered structure with an average particle size of 2.74  $\mu\text{m}$ . X ray diffractogram illustrates the crystal structure of the graphene oxide and interlayer spacing.

**Conclusions:** With the characterisation results, the synthesis of graphene oxide from plastic waste was verified.

**Keywords:** Polythene bags, Carbon material, Graphene oxide, Modified Hummers method, Environment protection

**Acknowledgement:** We are highly grateful for the support provided by the principal of our institution Christ Church College, Kanpur. We would also like to extend our gratitude to IIT Kanpur for providing the analysis facilities.

**For citation:** Shukla S., Kamal M. Synthesis and study of graphene oxide obtained from waste transparent polythene bags using Modified Hummers method. *Condensed Matter and Interphases*. 2025;27(3): 354–362. <https://doi.org/10.17308/kcmf.2025.27/13011>

**Для цитирования:** Шукла С., Камал М. Синтез и исследование оксида графена, полученного из отходов прозрачных полиэтиленовых пакетов с использованием модифицированного метода Хаммерса. *Конденсированные среды и межфазные границы*. 2025;27(3): 354–362. <https://doi.org/10.17308/kcmf.2025.27/13011>

✉ Shireen Shukla, e-mail: [Shireenshukla97@gmail.com](mailto:Shireenshukla97@gmail.com)

© Shukla S., Kamal M., 2025



The content is available under Creative Commons Attribution 4.0 License.

## 1. Introduction

Plastic contamination of ecosphere has become a common issue all around the Globe. Many developing countries are not only finding possible alternatives for plastic products but also researching extensively to reduce the plastic currently present in the environment as pollutant. Plastic products are sizeable components of automotive, construction, healthcare and electronic industries. Packaging industry forms one of the highest plastic consuming industry [1, 2]. Due to its increasing demand the production is increasing exponentially every year. The unique properties of plastic such as flexibility and durability have now become the disadvantage of plastic usage. The persistent plastic waste on Earth surface is the source of air, water and land pollution. Apart from this, polythene bags also cause major clogging of roadside drains in India resulting in stagnant polluted water in human colonies [2]. The dumped plastic somehow finds its way into water bodied, henceforth causing a negative impact on the marine environment. The presence of microscopic pieces of plastic termed as microplastic was reported by Surthy and Ramasamy [3] in the Vembanad Lake, Kerala, India. The results from the 10 samples of sediments collected from various latitudes of the lake reveals a range of microplastic concentration in the water body. The concentration ranges from 96 to 497 microplastics in per metre square of area with an average of  $252.2 \text{ m}^{-2}$ . Out of the all types of plastic, Low Density Polythene was found to be most abundant in the lake water. Marina beach, the longest stretched beach of India under investigation revealed the presence of microplastic of different shapes, colour and category of plastic [4]. These microplastic show detrimental effects in all strata of living organisms and thus an ideal solution is required. The methods of plastic control such as recycling, incineration and landfill were found best previously.

A recent study shows the release of chemicals and toxicants from incineration and landfill of plastic waste. The particulate emission, volatile organic compounds, polycyclic aromatic hydrocarbons are the by products of plastic combustion [5]. The mentioned paths along with Government policies are required for diminishing the plastic pollution. However, the methods fall

short due to lack of awareness and public effort [6, 7]. A scientific step of creating a novel polymer with different sets of properties as of plastic would mark a difference [7].

Another alternative is conversion of plastic waste to fuel and functional carbon material. Pyrolysis and catalytic pyrolysis have been utilised for conversion of waste plastic to oil which further was experimented as transportation fuel [8, 9]. More recent study reveals the accomplished efforts of converting plastic waste into carbon material of various forms. Nanostructures such as spheres, fibres, tubes and sheets can be obtained by varying the synthesis conditions [10, 11]. Scientist have experimented the conversion of various types of plastics into diverse carbon materials. The experimental conditions play an impactful role in determining the characteristics of the material formed [12]. The most crucial allotrope of carbon is Graphene and its derivatives, it has gained great attention in the recent years since its extraction using scotch tape. In a review by Berktaş and team, the importance of graphene is highlighted along with stating varied greener and cost effective raw materials for its production [13]. Graphene has exceptional conducting, mechanical and optical properties owing to which it attracts both physicists and chemists [14]. Graphene oxide has a similar layered structure as that of graphite and can be synthesised by introducing oxygen atoms in between graphitic layers. Graphene oxide can act as a precursor for the synthesis of graphene sheets namely reduced graphene oxide [15, 16].

Graphene oxide having properties similar to graphene is utilised in diverse fields such as an adsorbent for purification, as biosensors and as membranes [16]. Graphene has multiple synthesis procedures including mechanical exfoliation and chemical vapour deposition. However, these methods are restricted to small scale synthesis. For bulk scale chemical methods are preferred, one of them is use of strong oxidising agents under the Modified Hummers method [17, 18]. Graphene is obtained in the form of the graphene oxide using this method, which can further reduced to graphene. Hummer's method although being an efficient and trusted route still has some major defects. The use of  $\text{KClO}_3$  along with  $\text{HNO}_3$  was highly exothermic as well as liberated toxic gases such as  $\text{NO}_2$ ,  $\text{N}_2\text{O}_4$  and  $\text{ClO}_4$  [19, 20]. The

Modified Hummers method employs  $\text{NaNO}_3$ ,  $\text{KMnO}_4$  and  $\text{H}_2\text{SO}_4$  as oxidising agents by the production of  $\text{MnO}_4^-$  ions. Addition of  $\text{H}_2\text{O}_2$  helps in the removal of residual manganate ions and termination of the reaction [20, 21]. The modified method is considerably effective, less toxic and highly applicable [22, 23].

In this study, we convert plastic waste in the form of Polyethylene (PE) into graphitic material which acts as the substrate for Graphene oxide synthesis. The method is environment friendly and highly efficient as well as less laborious.

## 2. Experimental procedure

### 2.1. Collection of waste polythene bags

Waste plastic bags were collected from various garbage dumping areas of our city Kanpur as illustrated in Fig. 1. The bags were washed to remove the unwanted dust, dirt and other degradable waste. The cleaned bags were allowed

to sun dry until extra moisture is lost and then further steps were carried on.

### 2.2. Preparation of cleaned polythene bags

After washing and drying, the cleaned bags underwent a manual separation on the basis of colour, transparent bags were kept separately. The bags were then cut into small sized pieces manually using a paper cutter and scissor as shown in Fig. 2.

### 2.3. Conversion to graphite

The small chips of polythene were weighed and mixed with  $\text{Fe}(\text{NO}_3)_3 \cdot 9\text{H}_2\text{O}$  in 1: 3 ratio. To this 5 ml of ethanol and 45 ml of deionized water were added and stirred. Temperature range was maintained between 35–40 °C and rotation speed around 250 rpm. The mixture was stirred for 2 hours and then kept at rest for 24 hrs. The mixture was then heated inside a muffle furnace with a gradual rise of 10 °C per minute till the temperature reached

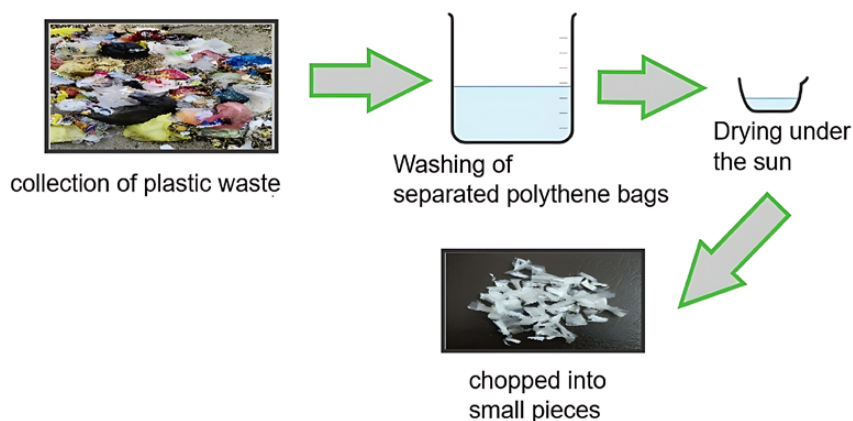


Fig. 1. Graphical Abstract showing the preparation of waste polythene

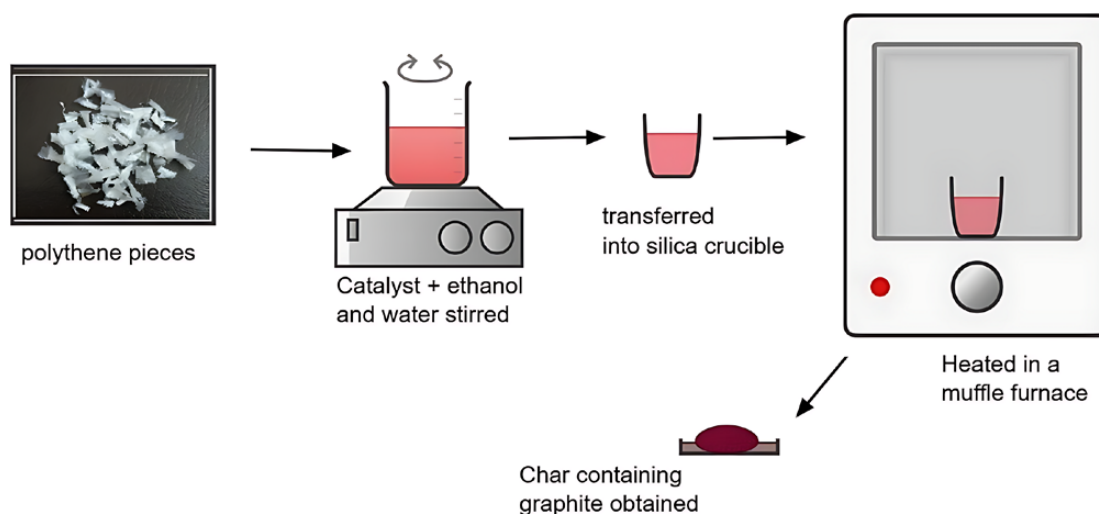


Fig. 2. Graphical Abstract show casing the formation the char

700 °C. The furnace was allowed to cool, then the char was obtained and weighed.

## 2.4. Graphene oxide synthesis

### 2.4.1. Acid wash of char

The 1g of char obtained in the previous step was acid washed to remove the catalyst and other impurities. The char was sonicated for an hour in 0.1 M HCl and kept for 24 hours in 0.1 M NaOH. The obtained graphitic carbon (GC) was used for further conversion to graphene oxide. This step helps in removal of all the excess ions of iron present in it.

### 2.4.2. Conversion to Graphene oxide

The Modified Hummers method employs  $\text{NaNO}_3$  and  $\text{KMnO}_4$  as the agents to introduce oxygen in between the layers of GC. The three components were mixed in a 1:1:5 ratio respectively as GC :  $\text{NaNO}_3$  :  $\text{KMnO}_4$ . The mixture was tardily added to 46.6 ml of  $\text{H}_2\text{SO}_4$  and then stirred for an hour at a speed around 200 rpm as shown in Fig. 3.. After an hour the temperature was raise to 35–40 °C and again stirred for another half an hour. 5.3 ml of  $\text{H}_2\text{O}_2$  and 80 ml of deionized water was added to the mixture continuing the stirring for another 30 minutes. On addition of  $\text{H}_2\text{O}_2$ , occurrence of yellowish brown colour confirms

the formation of graphene oxide. On completion of the two hour process, the mixture was allowed to settle for a few minutes and then 10 ml HCl was added to balance the pH of the mixture. The mixture was centrifuged to obtain the graphene oxide (TGO) in semi liquid state which was allowed to dry at 60 °C in an oven for 24 hours to obtain a brownish and blackish powder. The TGO powder was further utilised for various characterisations.

## 3. Material characterisation

To confirm the formation of Graphene oxide the bonding was analysed by FTIR PerkinElmer Spectrum IR Version 10.6.1 with a range of 4000–400  $\text{cm}^{-1}$ . The surface morphology was studied using FE Scanning Electron Microscopy (FESEM). To further detect the structure of the graphene oxide formed X Ray diffractometer XPERT-PRO with K alpha value of 1.540598 was brought into use.

## 4. Results and discussions

### 4.1. FTIR

The FTIR graph of TGO Fig. 5 are the FTIR graphs obtained for graphite carbon and graphene oxide. Fig. 5 b shows the presence of carbon carbon

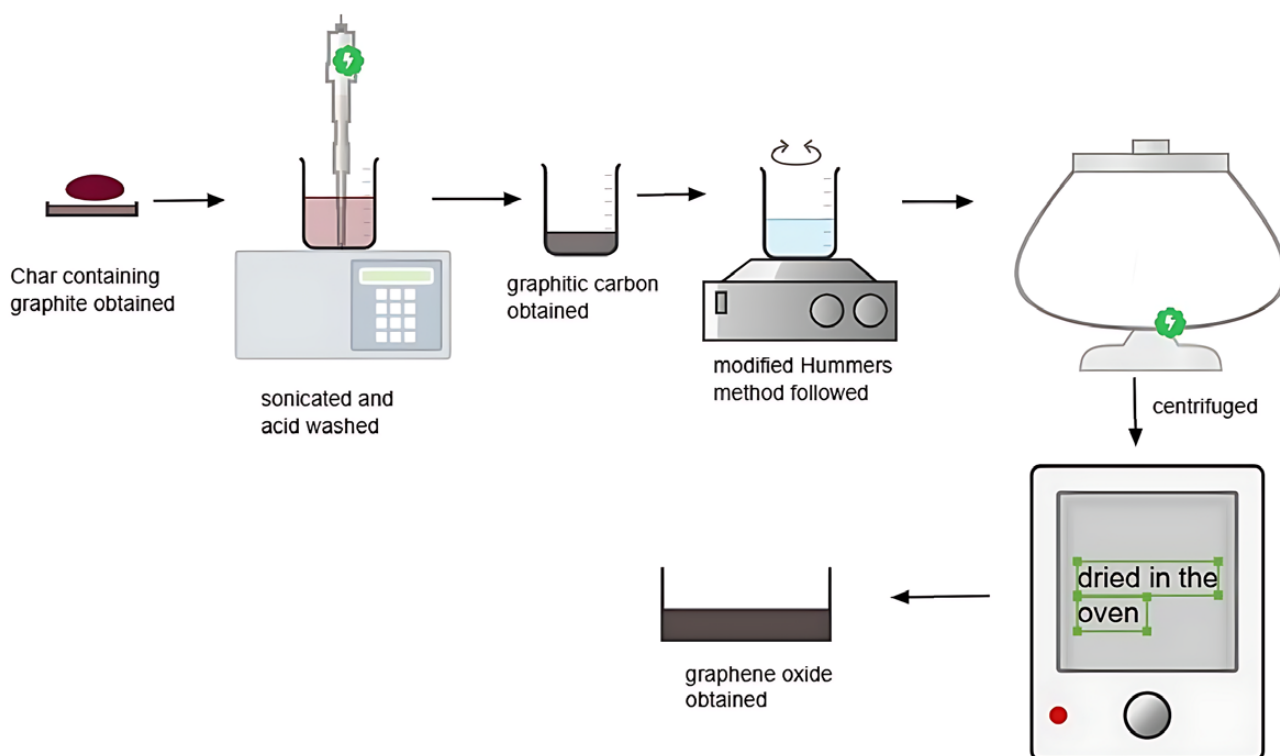
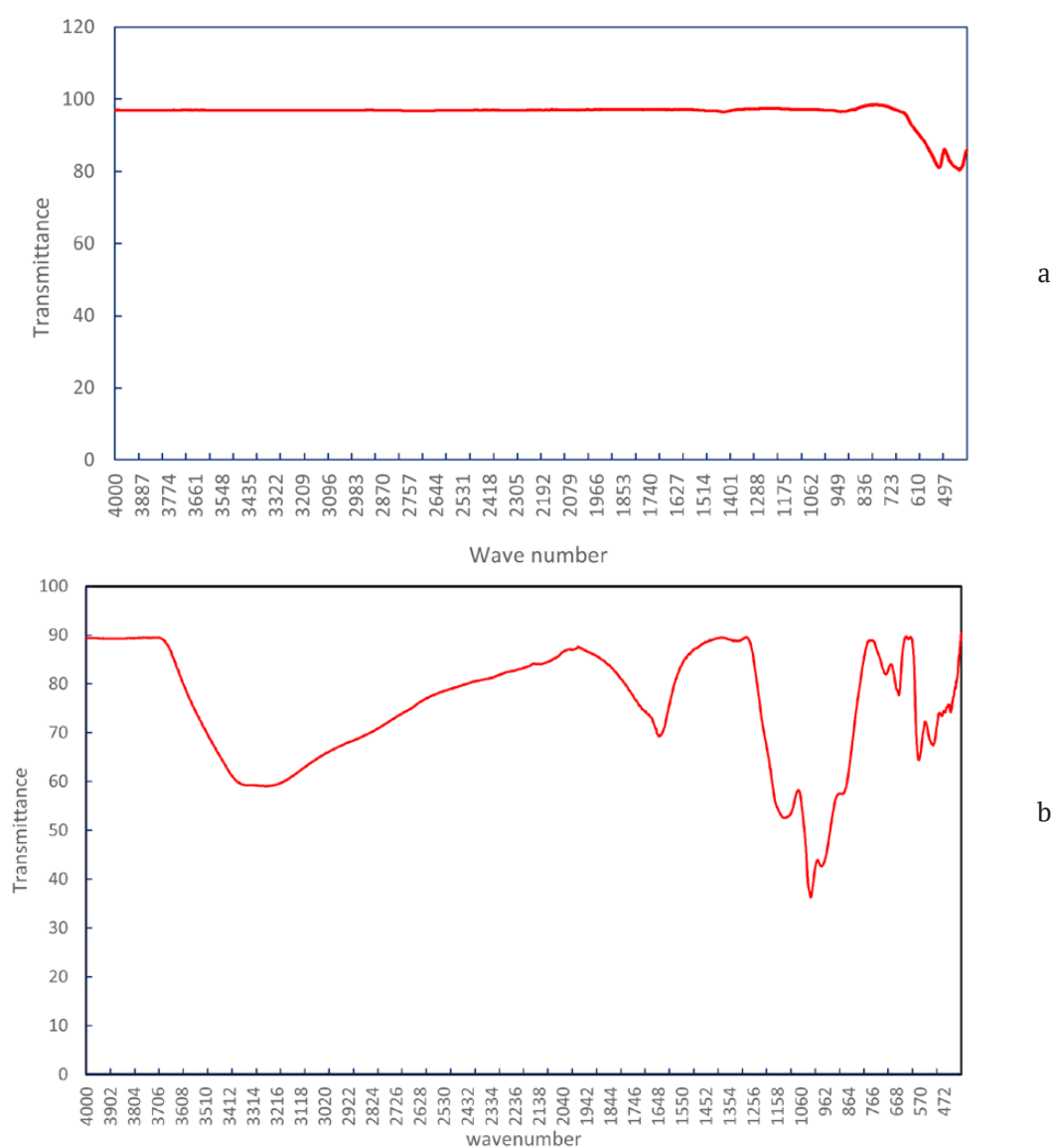


Fig. 3. Graphical Abstract for the preparation of graphene oxide



**Fig. 4.** Graphene oxide obtained from graphitic carbon

bond and carbon oxygen bonds to varying degrees. The spectra illustrates the vibrational group bands that include hydroxyl, carbonyl and aromatic double bond. The band around  $3261.01\text{ cm}^{-1}$  is attributed to hydroxyl and carbonyl groups present in TGO. This confirms the addition of oxygen to the carbon atoms providing it the characteristic properties. The band in the region of  $1644.94\text{ cm}^{-1}$  is due to the aromatic  $sp^2$  carbon present in the form of C=O groups. The band around  $1127.6\text{ cm}^{-1}$  and  $1019.20\text{ cm}^{-1}$  confirms the presence of carbon oxygen stretching and C-O-C epoxy group in the TGO. The band at  $974\text{ cm}^{-1}$  corresponds to the carbon carbon bending stretch. The obtained



**Fig. 5.** The FTIR graph obtained for (a) graphitic carbon (b) graphene oxide synthesised

**Table 1.** Encloses the various peaks obtained from FTIR spectra for TGO and their analysis

S.no	(cm <sup>-1</sup> )	Bonding
	3261.01	-O-H stretching
	1644.94	-C=C-
	1127.6	-C=O- stretching
	1019.20	-C=O- stretching
	974.98	-C=C Bending

major peaks shown in Table 1 are consistent with the results for graphene oxide synthesized by the Hammer method in the previous literature [24, 25]. Thus, the graph is in favour of oxidation

of graphitic carbon using Modified Hummers Method. Fig. 5a shows a linear graph confirming the synthesis of graphitic carbon. A linear FTIR is often attributed to carbon rich compounds. The results as per the study of literature [26] are assuring the carbon carbon linkage.

#### 4.2. Surface studies

The SEM (Fig. 6) images reveal the flaky and layered structure of the synthesised graphene oxide. In the images (a) and (b) under low magnification show the aggregated crystalline forms with pores on the surface. A similar image is obtained in the previous studies along

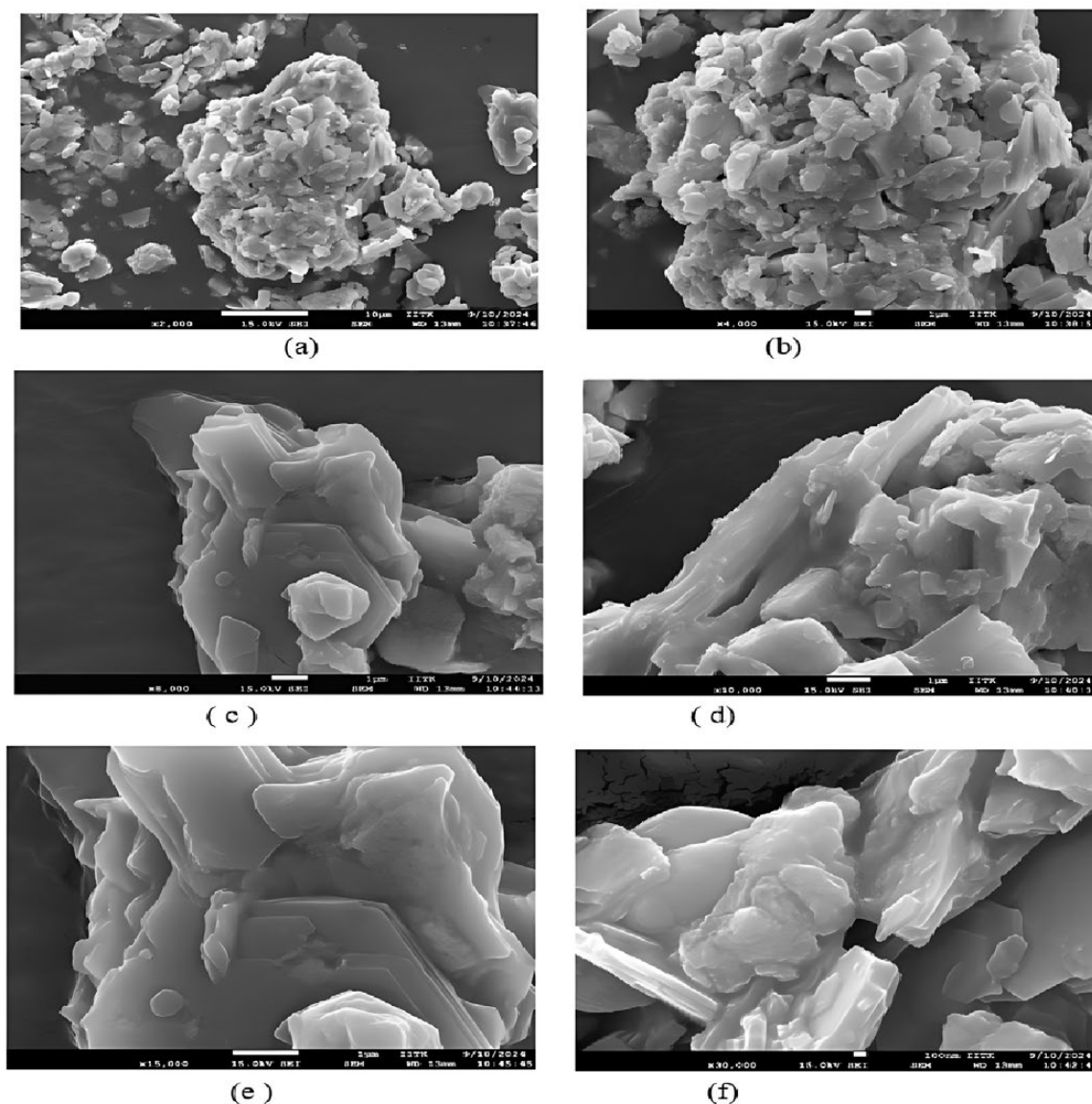


**Fig. 6.** FESEM was analysed under different magnifications (a) the image obtained at 2000× (b) image under 4000× (c) image obtained at 8000× (d) image under 10,000× (e) image obtained under 15,000× (f) image under 30,000×

with a highly compact structure [27]. Image (c) is revealing a symmetrical form with layered arranged sequentially giving it a high degree of orderness. Different magnifications reveal various forms of structures, the images obtained for TGO coincide with previous literature. A layered morphology can be noted in many studies and can thus be regarded as a significant feature of graphene oxide [28, 29]. The higher magnification also show case the presence of benzene ring like structure along with some hollow spaces. In images (e) and (f), the arrangement of layers can be seen vividly. The average particle size  $2.74\ \mu\text{m}$  calculated from the image (b) assures the nanoscale particle formation. Particle size can influence the properties and application of graphene oxide [30]. The aggregation of particles and solubility depend upon the size of the grain.

#### 4.3. X Ray Diffraction spectroscopy

XRD analysis was utilised to determine the crystal structure and inter layer distance of the graphene oxide. The peak observed at around  $13^\circ$  (as shown in Fig. 7(b)) is due the graphene oxide (110) with inter layer spacing calculated to be  $0.337\ \text{nm}$  using the Bragg's Law:

$$n\lambda = 2d \sin \theta.$$

A small peak at around  $13^\circ$  (as shown in Fig. 7(b)) shows the presence of graphitic carbon which was utilised as the substrate for the synthesis of graphene oxide. The interlayer spacing shows us the degree of oxidation that has occurred between the layers of graphite. A minute variation in the values of the diffraction peaks can be attributed to the amount of oxygen molecules that have occupied the inter layer space of graphitic carbon.

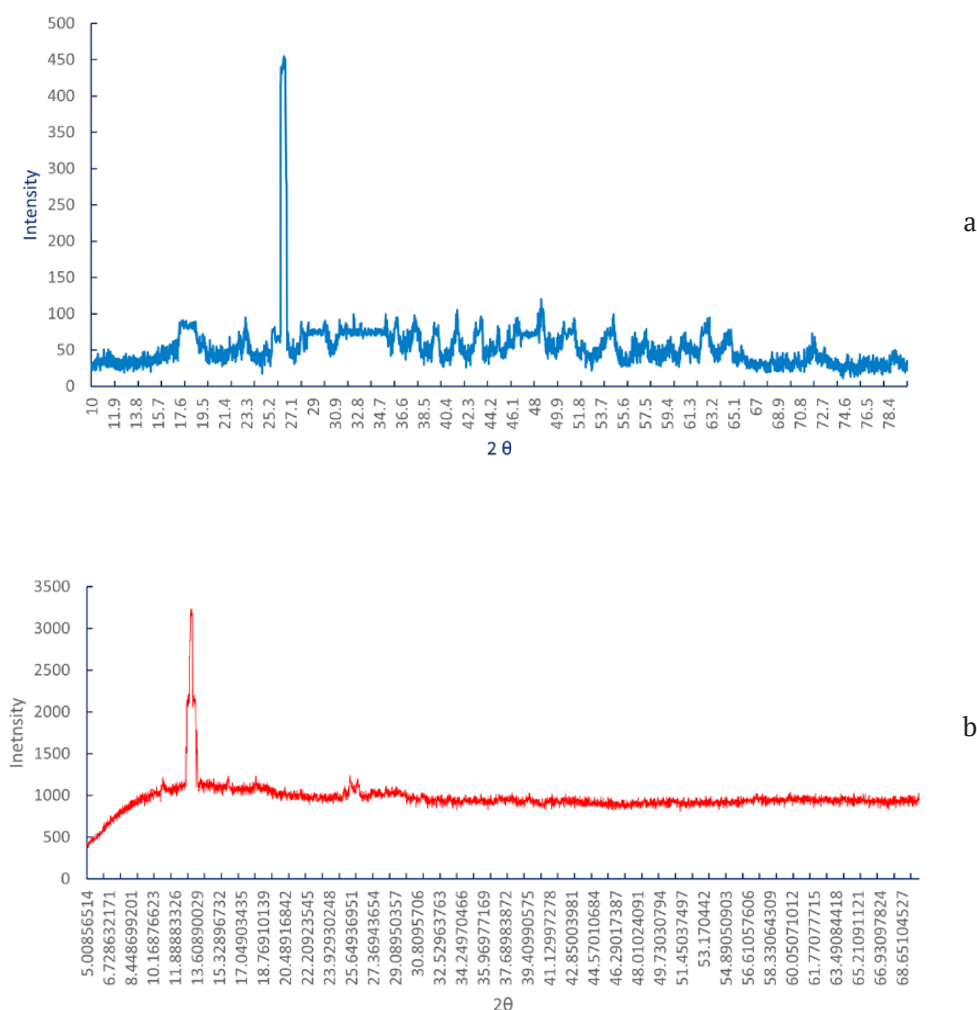


**Fig. 7.** Diffractogram of the (a) Graphitic carbon (b) graphene oxide synthesised using Modified Hummers method

The degree of oxidation can be a determining factor for the peak obtained, different reagents offer different extent of oxidation. As per the study of literature, synthesis conditions provide a set of results [31, 32]. Some studied also show variable results due the difference in nature of oxidising reagent used and peaks are in a scale of  $10^\circ$  to  $12^\circ$  for  $2\theta$  values [33, 34].

## 5. Conclusion

In the present experiment, Graphene oxide was successfully synthesised from the waste plastic that is Polyethylene using the Modified Hummers method. The graphitic carbon obtained from the pyrolysis act as the precursor of the oxidation method. Modified Hummers method applied is less tedious and time consuming along with satisfactory product formation. The characterisation including FTIR, SEM and XRD confirm the synthesised product is graphene oxide. The graphene oxide with particles of nano scale has various application in the fields of medicine and electronics. The research promotes the conversion waste to functional materials. Overall procedures are environment friendly and helps in the field of sustainable development.

## Contributions of the authors

Shireen Shukla – Investigation, Methodology development, writing, Final conclusions; Meet Kamal – Supervision, Research concept, review and editing.

## Conflict of interests

The authors declare that they have no known competing financial interests or personal relationships that could have influenced the work reported in this paper.

## References

1. Bhattacharya R. R., Chandrasekhar K., Roy P., Khan A. *Challenges and opportunities: plastic waste management in India*. Available at: <http://hdl.handle.net/2451/42242>
2. Sandipan D. S. The concept of control and manage plastic pollution of India/world. *The International Journal of Engineering and Science*. 2016;5(6): 1–7. Available at: <https://theijes.com/papers/v5-i6/version-2/A0506020107.pdf>
3. Sruthy S., Ramasamy E. V. Microplastic pollution in Vembanad Lake, Kerala, India: the first report of microplastics in lake and estuarine sediments in India. *Environmental pollution*. 2017;222: 315–322. <https://doi.org/10.1016/j.envpol.2016.12.038>
4. Sunitha T. G., Monisha V., Sivanesan S., ... Darchen A. Micro-plastic pollution along the Bay of Bengal coastal stretch of Tamil Nadu, South India. *Science of the Total Environment*. 2021;756: 144073. <https://doi.org/10.1016/j.scitotenv.2020.144073>
5. Verma R., Vinoda K. S., Papireddy M., Gowda A. N. Toxic pollutants from plastic waste-a review. *Procedia Environmental Sciences*. 2016;35: 701–708. <https://doi.org/10.1016/j.proenv.2016.07.069>
6. Schmaltz E., Melvin E. C., Diana Z., ... Dunphy-Daly M. M. Plastic pollution solutions: emerging technologies to prevent and collect marine plastic pollution. *Environment International*. 2020;144: 106067. <https://doi.org/10.1016/j.envint.2020.106067>
8. Syamsiro M., Saptoadi H., Norsujianto T., ... Yoshikawa K. Fuel oil production from municipal plastic wastes in sequential pyrolysis and catalytic reforming reactors. *Energy Procedia*. 2014;47: 180–188. <https://doi.org/10.1016/j.egypro.2014.01.212>
9. Faussone G. C. Transportation fuel from plastic: Two cases of study. *Waste Management*. 2018;73: 416–423. <https://doi.org/10.1016/j.wasman.2017.11.027>
10. Kumari M., Chaudhary G. R., Chaudhary S., Umar A. Transformation of solid plastic waste to activated carbon fibres for wastewater treatment. *Chemosphere*. 2022;294: 133692. <https://doi.org/10.1016/j.chemosphere.2022.133692>
11. da Silva E. P., Fragal V. H., Fragal E. H., ... Muniz E. C. Sustainable energy and waste management: how to transform plastic waste into carbon nanostructures for electrochemical supercapacitors. *Waste Management*. 2023;171: 71–85. <https://doi.org/10.1016/j.wasman.2023.08.028>
12. Shukla S., Kamal M. Plastic waste to functional carbon nanomaterials/graphene: a review. *Essential Chem*. 2024; 1(1): 1–2. <https://doi.org/10.1080/28378083.2024.2407322>
13. Berktaş I., Hezarkhani M., Haghighi Poudeh L., Saner Okan B. Recent developments in the synthesis of graphene and graphene-like structures from waste sources by recycling and upcycling technologies: a review. *Graphene Technology*. 2020;5: 59–73. <https://doi.org/10.1007/s41127-020-00033-1>
14. Cooper D. R., D'Anjou B., Ghattamaneni N., ... Yu V. Experimental review of graphene. *ISRN Condensed Matter Physics*. 2012: 1–56. <https://doi.org/10.5402/2012/501686>
15. Pei S., Cheng H. M. The reduction of graphene oxide. *Carbon*. 2012;50(9): 3210–3228. <https://doi.org/10.1016/j.carbon.2011.11.010>
16. Tiwari S. K., Mishra R. K., Ha S. K., Huczko A. Evolution of graphene oxide and graphene: from imagination to industrialization. *ChemNanoMat*. 2018;4(7): 598–620. <https://doi.org/10.1002/cnma.201800089>
17. Jiříčková A., Jankovský O., Sofer Z., Sedmidubský D. Synthesis and applications of graphene oxide. *Materials*. 2022;15(3): 920. <https://doi.org/10.3390/ma15030920>
18. Shahriary L., Athawale A. A. Graphene oxide synthesized by using modified hummers approach. *International Journal of Renewable Energy and Environmental Engineering*. 2014;2(01): 58–63.

19. Alam S. N., Sharma N., Kumar L. Synthesis of graphene oxide (GO) by modified hummers method and its thermal reduction to obtain reduced graphene oxide (rGO). *Graphene*. 2017;6(01): 1–18. <https://doi.org/10.4236/graphene.2017.61001>
20. Santamaría-Juárez G., Gómez-Barojas E., Quiroga-González E., Sánchez-Mora E., Quintana-Ruiz M., Santamaría-Juárez J. D. Safer modified Hummers' method for the synthesis of graphene oxide with high quality and high yield. *Materials Research Express*. 2020;6(12): 125631. <https://doi.org/10.1088/2053-1591/ab4cbf>
21. Yoo M. J., Park H. B. Effect of hydrogen peroxide on properties of graphene oxide in Hummers method. *Carbon*. 2019;141: 515–22. <https://doi.org/10.1016/j.carbon.2018.10.009>
22. Sujiono E. H., Zabrian D., Dahlan M. Y., Amin B. D., Agus J. Graphene oxide based coconut shell waste: synthesis by modified Hummers method and characterization. *Heliyon*. 2020;6(8): e04568. <https://doi.org/10.1016/j.heliyon.2020.e04568>
23. Méndez-Lozano N., Pérez-Reynoso F., González-Gutiérrez C. Eco-friendly approach for graphene oxide synthesis by Modified Hummers method. *Materials*. 2022;15(20): 7228. <https://doi.org/10.3390/ma15207228>
24. Cao N., Zhang Y. Study of reduced graphene oxide preparation by Hummers' method and related characterization. *Journal of Nanomaterials*. 2015;2015(1): 168125. <https://doi.org/10.1155/2015/168125>
25. Guerrero-Contreras J., Caballero-Briones F. Graphene oxide powders with different oxidation degree, prepared by synthesis variations of the Hummers method. *Materials Chemistry and Physics*. 2015;153: 209–220. <https://doi.org/10.1016/j.matchemphys.2015.01.005>
26. Alkhouzaam A., Qiblawey H., Khraisheh M., Atieh M., Al-Ghouti M. Synthesis of graphene oxides particle of high oxidation degree using a modified Hummers method. *Ceramics International*. 2020;46(15): 23997–4007. <https://doi.org/10.1016/j.ceramint.2020.06.177>
27. Gul W., Akbar Shah R. S., Khan A., ...Khan R. Synthesis of graphene oxide (GO) and reduced graphene oxide (rGO) and their application as nano-fillers to improve the physical and mechanical properties of medium density fibreboard. *Frontiers in Materials*. 2023;10. <https://doi.org/10.3389/fmats.2023.1206918>
28. Chen X., Qu Z., Liu Z., Ren G. Mechanism of oxidization of graphite to graphene oxide by the Hummers Method. *ACS Omega*. 2022;7(27): 23503–23510. <https://doi.org/10.1021/acsomega.2c01963>
29. Shamailla S., Sajjad A. K. L., Iqbal A. Modifications in development of graphene oxide synthetic routes. *Chemical Engineering Journal*. 2016; 294: 458–477. <https://doi.org/10.1016/j.cej.2016.02.109>
30. Szabo T., Maroni P., Szilagyi I. Size-dependent aggregation of graphene oxide. *Carbon*. 2020;160: 145–55. <https://doi.org/10.1016/j.carbon.2020.01.022>
31. Hou Y., Lv S., Liu L., Liu X. High-quality preparation of graphene oxide via the Hummers' method: understanding the roles of the intercalator, oxidant, and graphite particle size. *Ceramics International*. 2020;46(2): 2392–2402. <https://doi.org/10.1016/j.ceramint.2019.09.231>
32. Marcano D. C., Kosynkin D. V., Berlin J. M., ... Tour J. M. Improved synthesis of graphene oxide. *ACS nano*. 2010;4(8): 4806–4814. <https://doi.org/10.1021/nn1006368>
33. Surekha G., Krishnaiah K. V., Ravi N., Suvana R. P. FTIR, Raman and XRD analysis of graphene oxide films prepared by modified Hummers method. *Journal of Physics: Conference Series*. 2020;1495(1): 012012. <https://doi.org/10.1088/1742-6596/1495/1/012012>
34. Zaaba N. I., Foo K. L., Hashim U., Tan S. J., Liu W. W., Voon C. H. Synthesis of graphene oxide using modified hummers method: solvent influence. *Procedia Engineering*. 2017;184: 469–477. <https://doi.org/10.1016/j.proeng.2017.04.118>

## Information about the authors

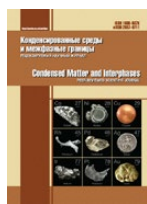
Shireen Shukla, Research scholar, Department of Chemistry, Christ Church College (Kanpur, Uttar Pradesh, India).

<https://orcid.org/0009-0007-8470-4177>  
Shireenshukla97@gmail.com

Meet Kamal, Professor (Chemistry), Department of Chemistry, Christ Church College (Kanpur, Uttar Pradesh, India).

<https://orcid.org/0000-0002-7355-1087>  
Meetkamal46@gmail.com

Received January 15, 2025; approved after reviewing March 24, 2025; accepted for publication April 15, 2025; published online September 25, 2025.



# Condensed Matter and Interphases

Kondensirovannye Sredy i Mezhfaznye Granitsy  
<https://journals.vsu.ru/kcmf/>

## Original articles

Research article

<https://doi.org/10.17308/kcmf.2025.27/13012>

## Crystallographic classification of special grain boundaries

B. M. Darinsky, N. D. Efanova, A. S. Prizhimov✉, A. A. Surkova

Voronezh State University,  
1 Universitetskaya pl., Voronezh 394018, Russian Federation

### Abstract

**Object of research:** Special grain boundaries in centrosymmetric crystals.

**The aim of this work** is to classify special grain boundaries in centrosymmetric crystals of all syngonies based on the symmetric properties of plane lattices that are the crystallographic planes of these crystals.

**Conclusions:** It is shown that the set of geometric parameters identifying special boundaries consists of elements of the symmetry of the plane formed by coinciding atoms that preserve the atomic structure of this plane. Possible misorientations of contacting crystals are found depending on the symmetry of the crystallographic plane for different crystallographic syngonies.

**Keywords:** Lattice of matching nodes, Interfaces, Crystal, Special grain boundaries

**Funding:** The work was carried out with the financial support of the Russian Science Foundation project No. 24-12-20010.

**For citation:** Darinsky B. M., Efanova N. D., Prizhimov A. S., Surkova A. A. Crystallographic classification of special grain boundaries. *Condensed Matter and Interphases*. 2025;27(3): 363–367. <https://doi.org/10.17308/kcmf.2025.27/13012>

**Для цитирования:** Даринский Б. М., Ефанова Н. Д., Прижимов А. С., Суркова А. А. Кристаллографическая классификация специальных межкристаллитных границ. *Конденсированные среды и межфазные границы*. 2025;27(3): 363–367. <https://doi.org/10.17308/kcmf.2025.27/13012>

✉ Andrey S. Prizhimov, e-mail: [rnileme@mail.ru](mailto:rnileme@mail.ru)

© Darinsky B. M., Efanova N. D., Prizhimov A. S., Surkova A. A., 2025



The content is available under Creative Commons Attribution 4.0 License.

## 1. Introduction

Special grain boundaries are flat boundaries exhibiting a biperiodic atomic structure. Unlike general-type grain boundaries that do not have a periodic atomic structure, their energy is relatively low, which leads to their thermodynamic stability with respect to various rearrangements [1–4]. Therefore, despite the discreteness of many geometric parameters of these boundaries, they can occupy a large share in polycrystalline samples [3]. An important property of the boundaries of this class is their relatively simple atomic structure, which simplifies the construction of theoretical models for interpreting various properties and phenomena in polycrystalline samples associated with the presence of grain boundaries in crystals [5–11]. Progress in the field of experimental studies of grain boundaries is largely associated with the development of methods for the purposeful preparation of the grain boundary structures of samples (Grain Boundary Engineering, [12–18]). Studies of grain boundaries in metals were mainly carried out to study their influence on the mechanical characteristics of materials [19]. Similar studies in ionic crystals containing two or more chemical elements were carried out in order to understand the effect of their structure on the domain structure, electronic and ionic electrical conductivity [19], characteristics of the Schottky barrier [20], and solar cells [21]. The study of boundaries and their totality in polycrystalline samples in these aspects is currently relevant.

Methods for calculating possible geometric parameters and atomic structures of special grain boundaries were initially based on representations of lattices of coinciding nodes [22] and were designed for the boundaries of various crystallographic syngonies: cubic [23], tetragonal [24], rhombohedral [25], and hexagonal [26]. In [27, 28], a method for classifying grain boundaries based on the consideration of coordination polyhedra was developed and applied to one-component and ionic crystals of a cubic structure.

In this paper, we propose a single method that allows us to specify possible special boundaries for crystals of any syngony. This method is based on the crystallographic classification of planar periodic structures.

## 2. Results and discussion

Since the atomic structure of a flat special boundary has a periodic structure, its primitive cell has five possible shapes: a parallelogram with sides of different lengths, a rectangle, a rhombus, a rhombus with an angle of  $60^\circ$ , and a square. Further, various rotations will be considered as symmetry operations of the boundary cell; generalization to the case of reflections from possible planes of symmetry is not difficult.

Crystallographic planes that have cells in the form of a parallelogram can be found in crystals of any crystallographic syngony. These planes form an infinite discrete set on the sphere of directions. Let's call these planes general-type planes. Only such planes are present in the crystals of triclinic syngony. The only non-trivial rotation for such a border is a  $180^\circ$  rotation around the normal. Since this rotation is not a symmetry for the entire crystal, by rotating half of the crystal and bringing the resulting halves into contact, we obtain a  $180^\circ$  torsion boundary. Therefore, all boundaries of the general type in all crystallographic syngonies will be  $180^\circ$  torsion boundaries. Note that if we take into account the presence of other symmetry elements of the crystallographic plane, namely, the reflection from the plane coinciding with this plane, and the inversion center located at the intersection of the diagonals of the parallelogram, then in general, other atomic configurations of the atoms of the grain boundary are obtained. In the first case, the specular boundary is obtained, and in the second case, the inverse boundary is obtained. Moreover, if the crystal as a whole is centrosymmetric, then the inversion transformation does not generate a grain boundary. An example of an inverse boundary is any plane in a polarized ferroelectric that is a  $180^\circ$  inter-domain boundary.

Crystallographic planes with rectangular cells are present in all other syngonies. In monoclinic syngony, they form a discrete one-dimensional set of rotations around the *z*-axis. The symmetry group of a rectangle generated by  $180^\circ$  rotations around the normal and edges of a cell in the crystallographic plane consists of three nontrivial operations that are not elements of crystal symmetry. Therefore, they lead to three different atomic configurations of the intergranular boundary. In the rhombic syngony, there are three

one-dimensional families of boundaries with rectangular cells; in the rhombohedral one, there are similar planes passing through the third-order axis and lying perpendicular to this axis.

Crystallographic planes having rhombic cells are present in crystals of rhombohedral syngony, in particular, in the basic planes of the crystal cell and sublattices perpendicular to the third-order axis. The symmetry group includes  $180^\circ$  rotations around the normal to the rhombus plane and around its diagonals. Therefore, in crystals belonging to the orthorhombic syngony, three atomic configurations are possible at the grain boundaries, which have a rhombic lattice structure of matching atoms.

In tetragonal syngony crystals, the crystallographic planes with rectangular cells are defined by the normals lying in two planes passing through the sides of the base square and the fourth-order  $z$  axis. The normals to planes with rhombic cells are located in vertical planes passing through the diagonals of the square. In addition, grain boundaries obtained by rotations at angles other than  $180^\circ$  around the fourth-order axis can be realized in crystals of this syngony. The totality of these rotation angles is obtained by considering square sublattices in the  $(xy)$  plane. Provided that the edge length of the square is taken as one and the origin is located at one of the lattice nodes, the sides of the square sublattices have coordinates  $(m, n, 0)$ , where  $m, n$  are positive and negative coprime integers. In particular cases, when  $m = 0, n = 1$  and  $m = 1, n = 1$ , squares are obtained. In a typical case, they generate a coordination octagon, which can be represented as the sum of squares expanded with respect to each other at an angle  $\varphi$ , determined by the relation:

$$\operatorname{tg}(\varphi/2) = m/n, \quad (1)$$

or an additional angle. Turning the upper part of the crystal by this angle and then bringing it into contact generates the special torsion boundary in the  $z = 0$  plane. A three-dimensional lattice of matching nodes appears in the volume of the bicrystal. Any crystallographic plane in this lattice can serve as a basis for constructing a grain boundary. At the same time, the variants of multiplication of atomic structures of the grain boundary, depending on the cell shape, are preserved.

In some special cases, the coordinate polygon may have more than eight vertices. This requires that the distance between atoms, whose positions are defined by different sets  $(m_1, n_{1,0}), (m_2, n_{2,0})$ , be equal. As an example, we consider a coordination dodecagon defined by the vertices of the  $(3, 4, 0)$  and  $(5, 0, 0)$  types. The two square sublattices defined by these vectors are superposed by a rotation determined by the formula:

$$\cos \varphi = 3/5, \quad (2)$$

or an additional angle.

For crystals of hexagonal syngony, in general, the same regularities are observed as for tetragonal crystals, with the only difference being that instead of a square cell in the base plane, we need to consider a hexagonal one.

In crystals of cubic syngony, a special feature is fulfilled that distinguishes this syngony from the rest, namely, that any crystallographic plane generates a spatial lattice of coinciding atoms, which in general has a monoclinic structure. This conclusion follows from the obvious regularity that the coordinates of the vector product of two vectors with integer coordinates are also integer coordinates. In particular cases, a sieve of matching atoms can have tetragonal and cubic symmetry.

All the regularities for the characteristics of possible grain boundaries arising from the presence of high-order symmetry axes occur in crystals with a cubic syngony. Furthermore, these crystals contain nontrivial planes with square and hexagonal sublattices. As an example, we consider a crystallographic plane with the following basis vectors of the cell:  $(-1, 2, 2)$  and  $(2, -1, 2)$ . The normal to this plane has coordinates  $(2, 2, -1)$ , so the lattice of matching atoms is a simple cubic one. Rotations of the crystal around the normal leave the lattice invariant in the plane, but change the positions of the atoms in the crystal, since these rotations are not elements of the crystal's symmetry. Thus, these rotations give rise to different atomic configurations at the grain boundary. Other atomic configurations are obtained by performing operations of  $180^\circ$  rotation around the edges of the square and one of its diagonals  $(1, 1, 4)$ . The other diagonal  $(-1, 1, 0)$  is the second-order axis of the crystal, so rotating around it will not result in a new atomic configuration of the grain boundary.

An example of a hexagonal sublattice in a plane that does not coincide with the cell faces of a crystal with cubic syngony is given by a set of basis vectors (4, 1, 1), (1, 4, 1), (3, -3, 0). It is not difficult to check that these vectors have the same lengths, lie in the same plane, and the angle between them is 60°. The common normal to these vectors has coordinates (-1, 1, 5). Since this normal is not the axis of symmetry of the crystal, rotations around it while preserving any hexagonal sublattice will lead to new atomic configurations in the region of the torsion boundary. The second-order axes that leave the above-mentioned hexagonal structure invariant are defined by the vectors (4, 1, 1), (1, 4, 1), (7, -2, 1), (5, 5, 2), (-2, 7, 1), (1, -1, 0). Rotations around the first five axes, which are not elements of crystal symmetry, will also lead to other atomic configurations at the intergranular boundary. The last axis (1, -1, 0) is the second-order axis of the crystal and therefore will not lead to a new atomic configuration.

### 3. Conclusion

1. A grain boundary can be constructed on a general-type crystallographic plane in crystals of all syngonies by the 180° rotation of half of the crystal around the normal to this boundary.

2. In crystals with second-order axes, the grain boundaries passing through this axis can have three different atomic configurations.

3. In crystals with high-order symmetry axes, grain boundaries with different misorientation angles and atomic configurations can be present. A lattice of matching nodes appears in the region of contacting crystals.

4. In crystals of cubic syngony, there are crystallographic planes that do not coincide with the basic planes, which contain plane sublattices with high-order symmetry axes. Such planes allow several misorientations of contacting crystals and atomic configurations.

### Contribution of the authors

The authors contributed equally to this article.

### Conflict of interests

The authors declare that they have no known competing financial interests or personal relationships that could have influenced the work reported in this paper.

### References

1. Gleyter G., Chalmers B. *High-angle Grain Boundaries*. Pergamon Press.; 1972. 274 p.
2. Orlov A. N., Perevezentsev V. N., Rybin V. V. *Grain Boundaries in Metals*. Moscow, Metallurgy Publ., 1980, 224 p. (In Russ.)
3. Straumal B. B., Shvindlerman H. P. Thermal stability and regions of existence of special grain boundaries\*. *Physics, Chemistry and Mechanics of Surfaces*. 1986;10: 5 –14. (In Russ.)
4. Wolf D. Structure and energy of grain boundaries. In: *Handbook of Materials Modeling*. Dordrecht: Springer; 2005. p. 1953–1983. [https://doi.org/10.1007/978-1-4020-3286-8\\_102](https://doi.org/10.1007/978-1-4020-3286-8_102)
5. Lindman A., Helgee E. E., Nyman B. J., Wahnström G. Oxygen vacancy segregation in grain boundaries of BaZrO<sub>3</sub> using interatomic potentials. *Solid State Ionics*. 2013;230: 27–31. <https://doi.org/10.1016/j.ssi.2012.07.001>
6. Helgee E. E., Lindman A., Wahnström G. Oxygen vacancy segregation in grain boundaries of BaZrO<sub>3</sub> using interatomic potentials. *Fuel Cells*. 2013;13: 19–28. <https://doi.org/10.1002/fuce.201200071>
7. Polfus J. M., Toyoura K., Oba F., Tanaka I., Haugsrud R. Defect chemistry of a BaZrO<sub>3</sub> Σ3 (111) grain boundary by first principles calculations and space-charge theory. *Physical Chemistry Chemical Physics*. 2012;14: 12339–12346. <https://doi.org/10.1039/c2cp41101f>
8. Fortes M. A. Coincidence site lattices in non-cubic lattices. *Physica Status Solidi (b)*. 1977;82(1): 377–382. <https://doi.org/10.1002/pssb.2220820143>
9. Mishin Y., Asta M., Li J. Atomistic modeling of interfaces and their impact on microstructure and properties. *Acta Materialia*. 2010;58: 1117–1151. <https://doi.org/10.1016/j.actamat.2009.10.049>
10. Bonnet R., Durand F. A general analytical method to find a basis for the DSC lattice. *Scripta Metallurgica*. 1975;9(9): 935–939. [https://doi.org/10.1016/0036-9748\(75\)90548-7](https://doi.org/10.1016/0036-9748(75)90548-7)
11. Watanabe T. Grain boundary engineering: historical perspective and future prospects. *Journal of Materials Science*. 2011;46: 4095–4115. <https://doi.org/10.1007/s10853-011-5393-z>
12. Kobayashia S., Hirataa M., Tsurekawab S., Watanabe T. Grain boundary engineering for control of fatigue crack propagation in austenitic stainless steel. *Procedia Engineering*. 2011;10: 112–117. <https://doi.org/10.1016/j.proeng.2011.04.021>
13. Randle V. ‘Special’ boundaries and grain boundary plane engineering. *Scripta Materialia*. 2006;54: 1011–1015. <https://doi.org/10.1016/j.scriptamat.2005.11.050>
14. Geng X., Vega-Paredes M., Wang Z., ... Gault B. Grain boundary engineering for efficient and durable electrocatalysis. *Nature Communications*. 2024;15(1): 8534. <https://doi.org/10.1038/s41467-024-52919-w>
15. Zelinsky J. A. *An evaluation of grain boundary engineering technology and processing scale- up*. Thesis (M. Eng.), Massachusetts Institute of Technology. 2005. pp. 74. Available at: <http://hdl.handle.net/1721.1/33616>
16. De Souza R. A., Munir Z. A., Kim S., Martin M. Defect chemistry of grain boundaries in proton-conducting solid

oxides. *Solid State Ionics*. 2011;196: 1–8. <https://doi.org/10.1016/j.ssi.2011.07.001>

17. Nyman B. J., Helgee E. E., Wahnström G. Oxygen vacancy segregation and space-charge effects in grain boundaries of dry and hydrated BaZrO<sub>3</sub>. *Applied Physics Letters*. 2012;100: 061903. <https://doi.org/10.1063/1.3681169>

18. Aus M. J., Szpunar B., Erb U. Electrical, magnetic and mechanical properties of nanocrystalline nickel. *MRS Proceedings*. 1993;318: 39–44. <https://doi.org/10.1557/PROC-318-39>

19. Radle V., Coleman M. A study of low-strain and medium-strain grain boundary engineering. *Acta Materialia*. 2009;57: 3410–3421. <https://doi.org/10.1016/j.actamat.2009.04.002>

20. Adams T. B., Sinclair D. C., West A. R. Characterization of grain boundary impedances in fine- and coarse-grained CaCu<sub>3</sub>Ti<sub>4</sub>O<sub>12</sub> ceramics. *Physical Review B*. 2006;73: 094124. <https://doi.org/10.1103/PhysRevB.73.094124>

21. Cao G., Shen J., Ng D., ... Yan C. 2D materials for conducting holes from grain boundaries in perovskite solar cells. *Light: Science and Applications*. 2021;10:1. <https://doi.org/10.1038/s41377-021-00515-8>

22. Bollmann W. Crystal defects and crystalline interfaces. Berlin: Springer; 1970. <https://doi.org/10.1007/978-3-642-49173-3>

23. Grimmer H. A method of determining the coincidence site lattices for cubic crystals. *Acta Crystallographica Section A*. 1974;30(5): 680–680. <https://doi.org/10.1107/S056773947400163X>

24. Singh A., Chandrasekhar N., King A. H. Coincidence orientations of crystals in tetragonal systems with applications to YBa<sub>2</sub>Cu<sub>3</sub>O<sub>7</sub>. *Acta Crystallographica Section B Structural Science*. 1990;46: 117–125. <https://doi.org/10.1107/S0108768189011006>

25. Grimmer H. Coincidence orientations of grains in rhombohedral materials. *Acta Crystallographica Section A*

*Foundations of Crystallography*. 1989;45: 505–523. <https://doi.org/10.1107/S0108767389002291>

26. Grimmer H., Warrington D. H. Fundamentals for the description of hexagonal lattices in general and in coincidence orientation. *Acta Crystallographica Section A Foundations of Crystallography*. 1987;43: 232–243. <https://doi.org/10.1107/s0108767387099513>

27. Darinskiy B. M., Efanova N. D., Prizhimov A. S. Structure of the special intercrystalline boundaries in two component crystals. *Condensed Matter and Interphases*. 2019;21(4): 490–496. <https://doi.org/10.17308/kcmf.2019.21/2361>

28. Darinskiy B. M., Efanova N. D., Saiko D. S. Special grain boundaries in perovskite crystals. *Ferroelectrics*. 2020;567: 13–19. <https://doi.org/10.1080/00150193.2020.1791582>

\*Translated by author of the article

## Information about the authors

Boris M. Darinskiy, Dr. Sci. (Phys.-Math.), Full Professor, Voronezh State University (Voronezh, Russian Federation). <https://orcid.org/0000-0003-0780-9040>

darinskii@mail.ru

Natalia D. Efanova, graduate student of Faculty of Physics, Voronezh State University (Voronezh, Russian Federation).

efanowanatalia@gmail.com

Andrey S. Prizhimov, Cand. Sci. (Phys.-Math.), Senior Researcher, Voronezh State University (Voronezh, Russian Federation).

<https://orcid.org/0000-0003-0052-0826>

rnileme@mail.ru

Anastasiya A. Surkova, student of Faculty of Chemistry, Voronezh State University (Voronezh, Russian Federation). anastasiasurok@gmail.com

Received December 2, 2024; approved after reviewing January 29, 2025; accepted for publication February 14, 2025; published online September 25, 2025.



# Condensed Matter and Interphases

Kondensirovannye Sredy i Mezhfaznye Granitsy  
<https://journals.vsu.ru/kcmf/>

## Original articles

Research article

<https://doi.org/10.17308/kcmf.2025.27/13013>

## Kinetics of electrocrystallization of copper from an acid sulfate solution in the presence of N-methylpolyvinylpyridine-methylsulfate

E. A. Ilina, O. A. Kozaderov<sup>✉</sup>, N. V. Sotskaya, D. Yu. Vandyshev, V. A. Polikarchuk, Kh. S. Shikhaliev

Voronezh State University,  
1 Universitetskaya pl., Voronezh 394018, Russian Federation

### Abstract

**Objective:** In this work, kinetic patterns are established and the main parameters of heterogeneous nucleation and the growth of a new phase during electrocrystallization of copper during cathodic deposition from an acid sulfate solution in the presence of *N*-methyl polyvinylpyridine-methyl sulfate of various molar masses are estimated. The polymers under study are quaternized polyvinylpyridine derivatives and are promising organic additives for use in the technology of electrochemical void-free filling of through holes (through silicon vias) of silicon wafers used in microelectronics in the manufacture of microcircuits.

**Experimental:** Using scanning electron microscopy, it was found that the use of *N*-methyl polyvinylpyridine-methyl sulfate additive leads to a noticeable decrease in the size of crystallites and blurring of grain boundaries, however, it can contribute to the localized formation of globular formations (if the molecular weight of the polymer is relatively small) or the formation of a layered structure (in the case of high-molecular derivatives). The introduction of a quaternized polymer into a copper plating solution significantly inhibits the electrodeposition process, which includes the stages of irreversible charge transfer and diffusion-controlled electrocrystallization.

**Conclusions:** It has been found that the activation process of heterogeneous nucleation sites in the presence of a polymer additive is instantaneous regardless of the molar mass. At the same time, as it increases, the density of active nucleation centers decreases significantly.

**Keywords:** Copper, Electrodeposition, Nucleation, Kinetics, Polyvinylpyridine, Quaternized derivatives

**Funding:** The study received financial support from the Ministry of Science and Higher Education of the Russian Federation within the framework of State Contract with universities regarding scientific research in 2025–2027, project No. FZGU-2025-0001.

**Acknowledgements:** The SEM studies were performed on the equipment of the Center for the Collective Use of Scientific Equipment of Voronezh State University.

**For citation:** Ilina E. A., Kozaderov O. A., Sotskaya N. V., Vandyshev D. Yu., Polikarchuk V. A., Shikhaliev Kh. S. Kinetics of copper electrocrystallization from an acid sulfate solution in the presence of *N*-methyl polyvinylpyridine-methyl sulfate. *Condensed Matter and Interphases*. 2025;27(3): 368–379. <https://doi.org/10.17308/kcmf.2025.27/13013>

**Для цитирования:** Ильина Е. А., Козадеров О. А., Соцкая Н. В., Вандышев Д. Ю., Поликарчук В. А., Шихалиев Х. С. Кинетика электрокристаллизации меди из кислого сульфатного раствора в присутствии *N*-метилполивинилпиридин-метилсульфата. *Конденсированные среды и межфазные границы*. 2025;27(3): 368–379. <https://doi.org/10.17308/kcmf.2025.27/13013>

✉ Oleg A. Kozaderov, e-mail: [ok@chem.vsu.ru](mailto:ok@chem.vsu.ru)

© Ilina E. A., Kozaderov O. A., Sotskaya N. V., Vandyshev D. Yu., Polikarchuk V. A., Shikhaliev Kh. S., 2025



The content is available under Creative Commons Attribution 4.0 License.

## 1. Introduction

The electrochemical deposition of metals is widely used to obtain functional coatings. Particular preference is given to copper, which has high electrical conductivity, solderability, and ductility. In microelectronics, high demands are placed on the quality of the cathode copper coating when implementing TSV (through silicon vias) technology based on electrochemical copper filling of through-holes in a silicon wafer [1, 2]. This technology makes it possible to create vertical electrical connections between different levels of semiconductor devices in a compact package [3, 4]. Given that copper electroplated TSV coatings are characterized by a complex geometric configuration, high requirements for the morphological properties of their surface require careful selection of the composition of the copper electrolyte. Acid sulfate electrolytes containing two main components, copper sulfate and sulfuric acid, are most widely used in copper cathodic deposition, since they are stable and easy to prepare. However, such electrolytes have a low scattering capacity, which negatively affects the quality of the coating, especially if it is necessary to fill holes with an unusual geometric profile and/or characterized by a high aspect ratio. To ensure a high-quality copper coating acceptable for TSV technology, several additional components are introduced into the acid sulfate electrolyte of copper plating: a suppressor, an accelerator, and a leveler, which perform specific functions during deposition [5–7]. When adsorbed on the surface of the cathode, they have a certain effect on the kinetics and mechanism of the electrodeposition process, providing a synergistic effect on the structure, morphology, and other properties of the resulting precipitation. A suppressor (for example, polyethylene glycol in the presence of chloride ions [8, 9]) forms a blocking layer on the copper surface, thereby significantly reducing the rate of copper deposition on the planar sections of the electrode. In turn, the accelerator (most often organic disulfide [10, 11]) is adsorbed mainly in the holes of the silicon wafer and ensures their superconformal filling, reducing the polarization of the cathodic process. Levelers play a special role in TSV technology, which locally affect the rate of copper electrodeposition depending on the curvature of the surface, slowing down the

process on the protrusions and accelerating in the depressions. As a result, the surface roughness of the copper deposit should decrease, however, it should be noted that the leveling effect is observed only in the presence of two other additives, a suppressor and an accelerator, since it is the result of competing adsorption of additives [12, 13]. It is in the combination of a leveler with an accelerator and a suppressor that more favorable conditions are created for copper deposition in the lower part of TSV holes compared to their upper part and side walls, which contributes to superconformal filling with copper without the formation of voids.

The levellers are, as a rule, heterocyclic nitrogen-containing compounds and polymers [14–18]. The electron-donating properties of nitrogen atoms contribute to their strong interaction with copper atoms. The molecular chains of the leveling additives contain tertiary and quaternary amines carrying a positive charge, which further enhances their adsorption on the negatively charged surface of the cathode. The leveler molecule must be large enough not to compete with the accelerator for adsorption sites inside the hole filled with copper and thus not disrupt its superconformal filling, and at the same time not too large so as not to interfere with the suppressor's operation on planar sections of the silicon wafer. In this regard, polymer levelers with variable molar mass seem to be the most promising. It has been shown [19] that compounds with a molar mass of 3500 g/mol are too small to fulfill the above requirement, and the necessary effect is manifested only when exceeding 60,000 g/mol. In addition, a leveler with an even larger molar mass is preferred, since it does not adversely affect the process inside the hole, even at high concentrations.

Polyvinylpyrrolidone of various molecular weights was used as a potential leveler in [20, 21], however, only minor improvements were noted after its addition. A stronger effect can be achieved not only by increasing the molar mass, but also by modifying the polymer molecule, including by quaternization. Indeed, it is quaternary ammonium compounds with cationic functional groups that are considered the most promising levelers due to their low cost, accessibility, and environmental friendliness compared to other

organic additives [12]. Quaternized derivatives, as a rule, are more strongly adsorbed on the protrusions of the electrode surface and locally reduce the rate of copper deposition [13]. This effect has been confirmed by the example of a number of cationic nitrogen-containing polymers. Thus, electrochemical and spectroscopic studies of dodecyltrimethylammonium bromide, benzyldimethylhexadecylammonium chloride, and thonzonium bromide have shown that the deposition of copper electroplating in their presence is characterized by a decrease in the rate of Cu deposition [22]. A significant slowdown in the cathodic deposition of copper in the presence of benzetonium chloride was showed in [12]. Quaternary ammonium salts of 3,3'-bicarbazole also proved to be promising levelers during the electrodeposition of copper in through holes [23]: the leveling effect was observed in the combined presence of an inhibitor and accelerator, and kinetic analysis made it possible to establish an instantaneous nucleation. It was shown [24] that the quaternary ammonium salt based on anthraquinone has an excellent inhibitory effect on copper deposition and a high adsorption capacity. Using cyclic voltammetry, it was found in [25] that when the dodecyltrimethylammonium cation was added to the copper electrolyte, inhibition of the electrochemical reduction of copper due to adsorption was observed, regardless of the electrode material used. Quaternized porphyrin derivatives also exhibit a pronounced inhibitory effect [26].

Until now, the mechanism of action of quaternary ammonium compounds as components of copper electrolytes has not been fully established, and the study of the relationship between their structure, electrochemical process parameters in their presence, and filling efficiency needs further study, as it is of great importance for the targeted selection of highly effective leveling additives.

In this work, *N*-methyl polyvinylpyridine-methyl sulfate (MPVP-MS) is investigated as a potential leveling agent, which satisfies all the characteristics of an organic leveling additive: it is a cationic heterocyclic polymer with quaternized nitrogen and a sufficiently high (variable) molar mass.

To establish the role of MPVP-MS of various

molar masses on the kinetics of copper deposition, it is necessary to investigate the effect of the additive on the patterns and parameters of the process at the stage of electrocrystallization of the galvanic precipitate, that is, at the stages of nucleation and growth of a new copper phase. It should be borne in mind that the process is often complicated by the adsorption of solution components on the electrode surface and the occurrence of a side reaction of hydrogen evolution [27], which requires a preliminary determination of the partial rate of the electrocrystallization stage. Non-stationary electrochemical methods such as chronopotentiometry and voltammetry allow us to identify the general effect of MPVP-MS on the kinetics of copper cathodic deposition. Chronoamperometry plays a special role, as it allows us to determine the effect of the additive on the quantitative characteristics of the electrocrystallization stage, which is responsible for the formation of a galvanic deposit and determines its structure and properties. A feature of the approach we use to identify the role of MPVP-MS in the kinetics of copper electrocrystallization is that in this work the differentiated effect of one additive is studied, which will reveal the behavior of MPVP-MS, unlike most similar works, which consider only the combined (synergistic) effect of several additives (accelerator, suppressor, leveler).

The purpose of the work is to establish the kinetic patterns of the electrocrystallization of copper in an acid sulfate solution in the presence of *N*-methylpolyvinylpyridine-methylsulfate.

The objectives were:

1. To determine the effect of *N*-methylpolyvinylpyridine-methyl sulfate on the morphology of electrodeposition of copper coatings.
2. To identify the role of *N*-methylpolyvinylpyridine-methyl sulfate in the non-stationary electrochemical deposition of copper from a sulfate solution.
3. To establish the nucleation parameters during electrodeposition of copper in the presence of *N*-methyl polyvinylpyridine-methyl sulfate of various molar masses.

## 2. Experimental

The electrodeposition of copper coatings

was carried out from aqueous solutions of the following compositions: (1) – 156 g/L  $\text{CuSO}_4 \cdot 5\text{H}_2\text{O}$  + 10 g/L  $\text{H}_2\text{SO}_4$  + 50 mg/L  $\text{Cl}^-$  (pH 1.3); (2) – 12.5 g/L  $\text{CuSO}_4 \cdot 5\text{H}_2\text{O}$  + 0.8 g/L  $\text{H}_2\text{SO}_4$  + 50 mg/L  $\text{Cl}^-$  (pH 2.1) at room temperature ( $\sim 20^\circ\text{C}$ ) in a three-electrode electrochemical cell with undivided cathode and anode spaces, without mixing, under conditions of natural aeration. Solution (1) was used for galvanostatic deposition and analysis of the morphology of the obtained coatings, solution (2) was used for non-stationary electrochemical measurements and study of the kinetics of electrocrystallization of copper.

A copper electrode reinforced in polymerized epoxy resin was used as a working electrode in non-stationary studies. To determine the morphology of the coating and the current efficiency, deposition was performed on a copper plate. Before electrochemical studies, the working electrode was cleaned using sandpaper with a grain size of P2500, polished on vacuum rubber with  $\text{Al}_2\text{O}_3$  powder with a grain size of F800, washed with distilled water, cleaned using an ultrasonic bath, the surface was degreased with isopropyl alcohol, rinsed again with distilled water and dried with filter paper. The preparation of the copper plate surface for electrochemical deposition included degreasing with isopropyl alcohol, rinsing with distilled water, etching in  $\text{HNO}_3$  for 7 seconds, repeated rinsing with distilled water, and drying with filter paper. The auxiliary electrode was a platinum plate, and a silver chloride electrode (S.C.E.) was used as a reference electrode, connected to the working solution by an electrolytic bridge filled with a saturated solution of potassium nitrate.

The kinetics of cathodic deposition of copper coatings was studied using non-stationary electrochemical methods of voltammetry, chronopotential, and chronoammetry. The measurements were carried out using a computerized P-40X potentiostat-galvanostat. The potentials are given relative to the silver chloride electrode, the potential of which is 205 mV on the scale of a standard hydrogen electrode. The current density  $i$  was calculated per unit of the visible (geometric) area of the electrode, which was  $0.045\text{ cm}^2$ . Chronopotentiograms of copper deposition were recorded at a current density of  $i = -1.5\text{ A/dm}^2$  for 1000 s. Cathodic potentiodynamic

curves were recorded by scanning the electrode potential over time  $t$  from an open-circuit value to  $E = -1000\text{ mV}$  with a preset scan rate  $v = dE/dt$ . The kinetics of electrocrystallization was studied by chronoamperometry, recording  $I$ - $t$  current transients at different  $E_{\text{dep}}$  deposition potentials in the region of the voltammetric maximum ( $-400\text{ mV}$ ,  $-500\text{ mV}$ ). The current efficiency was determined by gravimetric method. The morphology of the coatings was studied by scanning electron microscopy on a JSM-6380LV JEOL installation.

*N*-methyl polyvinylpyridine-methyl sulfate (Fig. 1) with different molar weights (800, 35,000, 300,000, 600,000 g/mol) at a concentration of 0.025 g/l was used as an organic additive, the synthesis of which was carried out as follows [28].

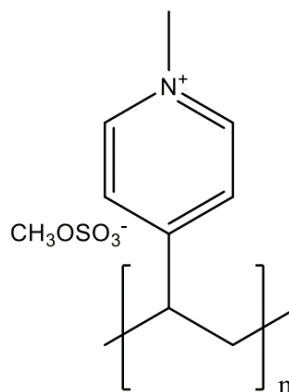


**Fig. 1.** Molecular structure of *N*-methylpolyvinylpyridine-methylsulfate

The monomer 4-vinylpyridine (4-VP) was purified by high-vacuum distillation at a temperature of  $68^\circ\text{C}$  at 18 mmHg. Poly-4-vinylpyridine (P-4-VP) was obtained by radical polymerization by the lacquer method in the presence of azoisobutyronitrile (AIBN), previously purified by recrystallization from ethyl alcohol, in an inert gas atmosphere (nitrogen) with constant stirring under various conditions shown in Table 1.

Given the ability of 4-VP to oxidize in the presence of light when even small amounts of oxygen enter the reaction system (formation of pyridine oxides, cleavage of the cycle to form red-colored products), polymerization was carried out in a darkened chamber. The resulting polymers were reconstituted from isopropyl alcohol (IPA) into petroleum ether, filtered, and washed with hexane to remove the residual monomer, dried

**Table 1.** Synthesis conditions for poly-4-vinylpyridine of different molar weights

M, g/mol	4-VP, g	AIBN, g	IPA, g	$t$ , °C	$\tau$ , hr	Efficiency, %
800	5	0.015	25	80	4	64
35000	5	0.01	25	70	5	57
300000	10	0.01	20	60	7	50
600000	10	0.01	20	50	9	50

at 55 °C (under vacuum) to a constant weight. The average molar mass (MM) of the resulting polymers was calculated using the viscometric method. 0.9 g of the obtained polymer was dissolved in 10 ml of methanol in a conical flask. About 5 ml of methanol was poured into a viscometer installed in a glass thermostat with distilled water, thermostated for 10–15 minutes at 25 °C, and the expiration time  $\tau_0$  was measured. The resulting polymer solution was placed in a viscometer, thermostated for 5 minutes, and the expiration time was measured at least three times. The concentration of the polymer solution was changed directly in a viscometer by successively adding 2, 3, and 5 ml of methanol. After each dilution, the solution was stirred by blowing through a viscometer tube, thermostated, and then the corresponding leakage time was measured. Further calculations were performed using the Kuhn-Mark- Houwink equation [29].

To obtain quaternized derivatives of P-4 VP, a mixture of 2.1 g of the obtained polymer,

50 ml of absolutized methanol and 5 mmol of dimethyl sulfate was mixed for 8–10 hours at a temperature not exceeding 40 °C. At the end of the reaction, the solvent was evaporated on a rotary evaporator in a vacuum of a water jet pump to  $\frac{1}{4}$  volume. The resulting residue was cooled and 30 ml of toluene was added. The resulting suspension was thoroughly stirred and boiled for 5–10 minutes. The mixture was cooled and after ~1 hour, the precipitate was filtered, thoroughly rinsed with ether on a filter, crushed and dried at 70–80 °C. The resulting salts were kept at 60 °C (under vacuum) to a constant mass. The degree of quaternization reached 75% (titrimetrically determined).

### 3. Results and discussion

Analysis of cathodic chronopotentiograms obtained by galvanostatic deposition of copper (Fig. 2) shows that the introduction of *N*-methyl polyvinylpyridine-methyl sulfate into an acid copper sulfate solution leads to a noticeable

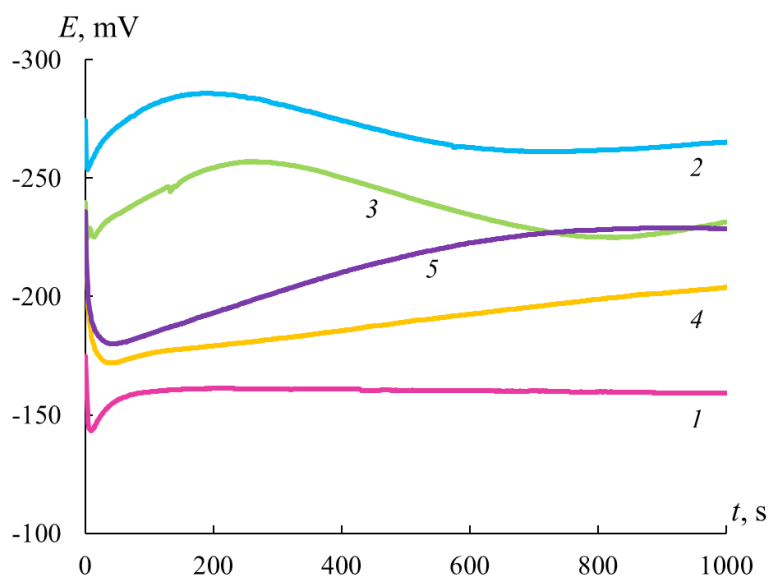


**Fig. 2.** Chronopotentiograms of copper deposition from solution (1) at  $i = -1.5 \text{ A/dm}^2$  in the absence of additives (1) and in the presence of *N*-methyl polyvinylpyridine-methyl sulfate with molecular weight 800 (2), 35000 (3), 300000 (4), 600000 (5) g/mol

shift in the deposition potential of copper towards more negative values compared with a solution containing no additives. This indicates an increase in the electrode polarization of the deposition process, i.e., an inhibition of the cathodic deposition of copper in the presence of MPVP-MS, regardless of its molar mass. In general, the lower the molar mass of the polymer, the more the potential shifts to the negative region, and the more pronounced its inhibitory effect.

The results of cathodic voltammetry of copper electrodeposition are consistent with chronopotentiometry data. Indeed, if, in the absence of MPVP-MS, potentiodynamic polarization leads to a sharp increase in current even at small overvoltages, then when an additive is added to the deposition solution, the current density increases much more slowly, and the maximum  $i_{\max}$  on the polarization curve decreases significantly. In addition, the potential of the  $E_{\max}$  peak is sufficiently shifted to the negative side (Fig. 3).

The observed changes in the voltammetric response indicate an inhibition of the deposition process in the presence of *N*-methyl polyvinylpyridine-methyl sulfate, but only at potentials more positive than the maximum potential. Indeed, at potentials  $E < E_{\max}$ , the potentiodynamic deposition in the presence of

MPVP-MS in this potential range is characterized by higher current values. In an acid sulfate solution without additives, at more negative potentials  $E$  compared to  $E_{\max}$ , a decrease in current is observed, probably due to an increase in diffusion limitations. In solutions with polymer, current fluctuations are observed in the voltammograms in the same potential range and, as a result, several maxima are formed. In other words, at potentials more negative than the maximum potential, *N*-methyl polyvinylpyridine-methyl sulfate increases the copper deposition current. Current fluctuations observed at corresponding sufficiently high overvoltages are probably due to changes in surface roughness, for example, due to the formation of a coating with a morphologically heterogeneous or layered structure.

The dual effect of MPVP-MS on the deposition rate of copper in an acid sulfate solution observed on voltammograms is confirmed by the results of scanning electron microscopy (Fig. 4). The surface of the copper coating obtained from an acid sulfate electrolyte without additives is characterized by a coarse-crystalline structure. The use of the MPVP-MS additive with the lowest molar mass of 800 g/mol generally smooths the coating surface due to a significant decrease in the size of crystallites because of increased overvoltage and blurring of grain boundaries,

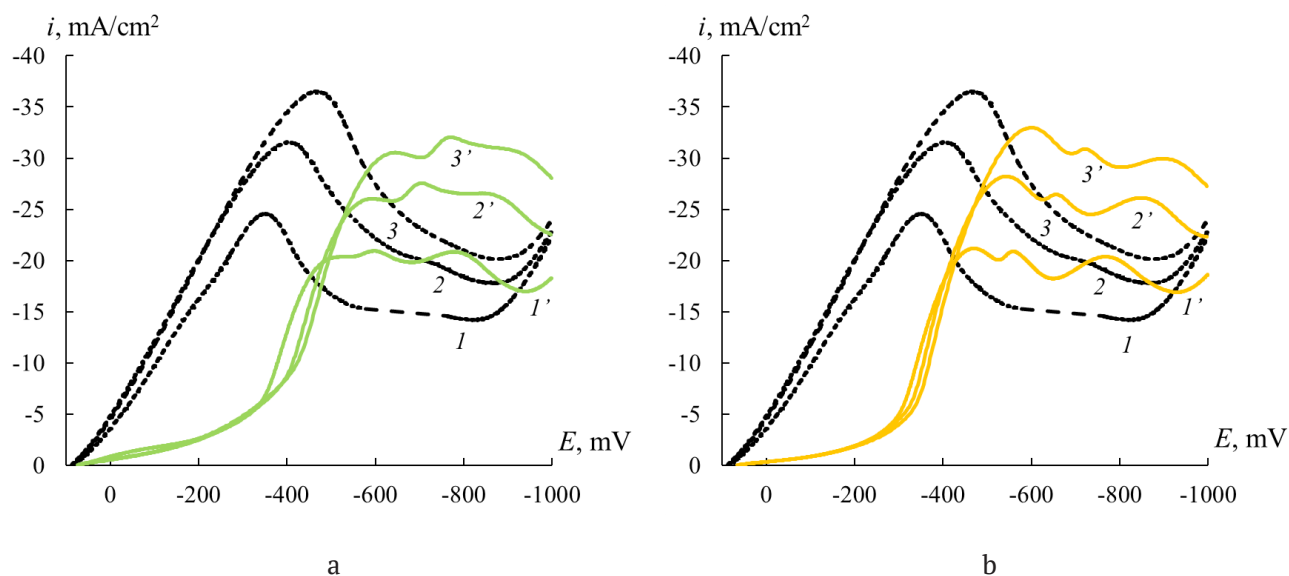


**Fig. 3.** Cathodic voltammograms obtained in solution (2) at  $\nu = 100$  (1, 1'), 200 (2, 2'), 300 (3, 3') mV/s in the absence of additives (1, 2, 3) and with the introduction of *N*-methyl polyvinylpyridine-methyl sulfate (1', 2', 3') with a molar weight of 35000 (a) and 300000 (b) g/mol

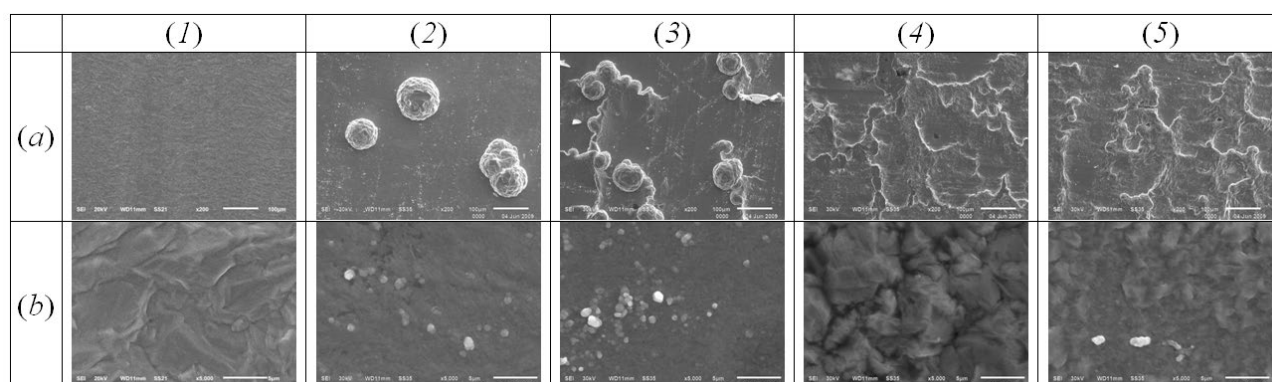


**Fig. 4.** SEM images obtained with magnification  $\times 200$  (a) and  $\times 5000$  (b) of the surface of copper coatings galvanostatically deposited (current density  $i = -1.5 \text{ A/dm}^2$ , deposition time 1000 s) from solution (1) without additives (1) and in the presence of *N*-methyl polyvinylpyridine-methyl sulfate with a molar weight of 800 (2), 35000 (3), 300000 (4) and 600000 (5) g/mol

however, it leads to the localized formation of sufficiently large globular formations up to 100 microns in size. With an increase in the molar mass of the polymer to 35,000 g/mol, the size of both globular formations and crystallites decreases, there is a partial blurring of the grain boundaries and a decrease in the number of globules on the surface of the coating, the structure of which becomes layered. With a subsequent increase in the molar mass of the additive to 300,000 and 600,000 g/mol, the formation of globular formations is no longer observed, and the layered nature of the coating becomes the most pronounced, which is reflected in an increase in surface roughness. The observed morphological changes are most likely due to the pronounced adsorption of the polymer on the surface of the copper coating, which leads to localization of metal deposition and, as a result, uneven globular and/or layered growth. It should be noted that a similar heterogeneity of morphology with differentiated (i.e., in the absence of a suppressor and accelerator) introduction of levelers into an acid sulfate solution of copper plating was also observed in [14], which confirms the manifestation of the greatest leveling effect only in the presence of a complex of additives of all three types.

Obviously, the introduction of a polymer into a copper solution has a strong effect on the kinetics of the deposition process, in order to establish the patterns of which the data of non-stationary electrochemical measurements were analyzed.

The linearity of the dependence of the current density at the maximum of the voltammogram on the root of the potential scan rate confirms the presence of diffusion limitations of the process (Fig. 5a). The curves are not extrapolated to the origin, probably due to a parallel side process (most likely, the hydrogen evolution reaction). Indeed, the current efficiency according to gravimetric measurements is  $85 \pm 4\%$ . At the same time, a significant shift of the maximum potential to the negative side with an increase in the scan rate indicates the irreversibility of the charge transfer stage (Fig. 5b).

The role of the polymer in the kinetics of electrocrystallization was established by determining the parameters of nucleation and growth of a new phase during copper deposition. The kinetics of the process is usually determined within the framework of instantaneous or continuous nucleation [30] within the framework of the 3D nucleation model proposed by Sharifker and Hills [31]. However, a preliminary comparison of the experimental chronoamperograms with the theoretical curves of the Sharifker–Hills model showed their significant discrepancy, which made it impossible to establish the nature of nucleation, much less to quantify the characteristics of the copper electrocrystallization process. The most likely causes of the revealed deviation are the significant contribution of the hydrogen evolution reaction, as well as the presence of substances capable of adsorption in the copper electrolyte. In this regard, for further analysis, we used an extended model of nucleation and growth of a new phase [27],

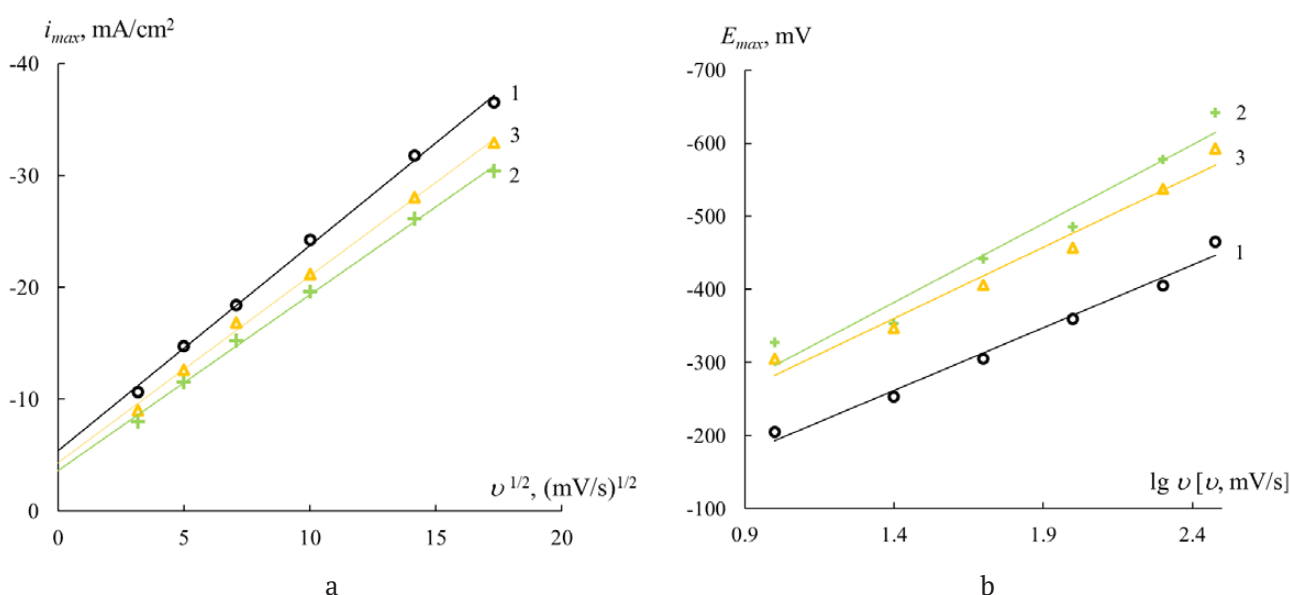


**Fig. 5.** (a) – Current density of the voltammetric maximum vs. root of the potential scan rate, (b) potential of the voltammetric maximum vs. decimal logarithm of the potential scan rate obtained in solution (2) without additives (1) and with the introduction of *N*-methyl polyvinylpyridine-methyl sulfate with a molar weight of 35000 (2) and 300000 (3) g/mol

which takes into account that diffusion-controlled electrodeposition of metal occurs together with hydrogen reduction and adsorption of solution components. The extended model makes it possible to describe the potentiostatic transient current  $i(t)$  obtained during electrodeposition as the sum of three components:

$$i(t) = i_{Cu}(t) + i_H(t) + i_{ads}(t). \quad (1)$$

Here, the current density  $i_H$  determines the rate of the proton reduction reaction [27] and can be described by the ratio:

$$i_H(t) = P_1 S(t), \quad (2)$$

in which the coefficient  $P_1 = z_H F k_H$  includes the charge  $z_H F$  responsible for the reduction of 1 mol of protons ( $z_H = 1$ ,  $F = 96485$  C/mol),  $k_H$  is the rate constant of the proton reduction reaction. The proportion of the surface occupied by electrodeposited copper

$$S(t) = (2c_0 M / \pi \rho)^{1/2} \theta(t) \quad (3)$$

includes  $c_0$  – the initial volume concentration of copper ions (0.05 M),  $M$  – the molar mass of copper (63.5 g/mol),  $\rho$  – the density of the copper (8.96 g/cm<sup>3</sup>), as well as the function

$$\theta(t) = \{1 - \exp[-P_2 t - (1 - \exp(P_3 t)) / P_3]\}. \quad (4)$$

Here, the parameters  $P_2 = N_0 \pi k D$  and  $P_3 = A$  represent, respectively, the density of active nucle-

ation sites on the electrode surface ( $N_0$ ), the diffusion coefficient of copper ions ( $D$ ) in solution, the rate constant of activation of nucleation sites ( $A$ ) and the constant  $k = (8\pi c_0 / \rho)^{1/2}$ .

The current density  $i_{Cu}$ , which determines the rate of the diffusion-controlled copper reduction process, obeys the ratio [27]:

$$i_{Cu}(t) = P_4 t^{-1/2} \theta(t), \quad (5)$$

where  $P_4 = 2FD^{1/2}c_0/\pi^{1/2}$ .

Finally, the third term  $i_{ads}$  is due to the adsorption process described in [27] as an exponential decrease in current:

$$i_{ads}(t) = K_1 \exp(-K_2 t). \quad (6)$$

Thus, the total current density will be described by the following expression:

$$i(t) = \{P_1^* + P_4 t^{-1/2}\} \times \left\{1 - \exp\left\{-P_2 \left[t - \frac{1 - \exp(P_3 t)}{P_3}\right]\right\}\right\} + K_1 \exp(-K_2 t), \quad (7)$$

where  $P_1^* = P_1(2c_0 M / \pi \rho)^{1/2}$ .

To identify the effect of *N*-methyl polyvinylpyridine methyl sulfate on the stage of heterogeneous nucleation during cathodic deposition of copper, the kinetic parameters of the electrocrystallization process were obtained by the nonlinear approximation comparison of equation (7) and experimental

chronoamperograms recorded at potentials in the vicinity of the voltammetric peak. Experimental chronoamperograms have the shape of a curve with a maximum (Fig. 6), which is typical for nucleation processes: a sharp increase in current during the initial period of the electrodeposition process is followed by a decrease in current and a constant value. The maximum current decreases with the introduction of additives, but increases with an increase in the molar mass of the additive. Their comparison with the current transients found in accordance with the extended model of the 3D nucleation process shows that the use of generalized equation (7) made it possible to obtain a complete coincidence of experimental and theoretical chronoamperograms. In addition, partial  $i, t$ -curves were calculated for three parallel non-stationary processes (electrocrystallization, hydrogen evolution, and adsorption). The nucleation current is characterized by the formation of a maximum in the initial period of the process, the height of which depends on the molar mass of the additive in the same way as the height of the maximum of the total current density: an increase in current is observed with an increase in the molar mass of the additive. The nucleation current in the presence of MPVP-MS

with a molecular weight of 300,000 and 600,000 g/mol is higher than in a solution without additives. The adsorption current is predominant at short process times, but it quickly decreases to zero. The adsorption current is higher in a solution without additives than in their presence. In addition, in solutions containing MPVP-MS, there is a smoother decrease in the current associated with the adsorption process. The current caused by the hydrogen release reaction increases and reaches a constant value, which does not significantly depend on the presence and molar mass of the additive. Using the extended electrocrystallization model, it was also possible to determine the values of kinetic parameters of electrodeposition at the stage of nucleation and growth of a new phase, including in the presence of MPVP-MS of various molecular weights (Fig. 7).

The analysis shows that *N*-methyl polyvinylpyridine-methyl sulfate has a noticeable effect on the parameters of copper nucleation, which depends on the electrode potential and the molar mass of the polymer. Regardless of the deposition potential, the density of nucleation sites decreases markedly (Fig. 7a) when MPVP-MS is introduced into the electrolyte solution, which can be explained by the strong adsorption

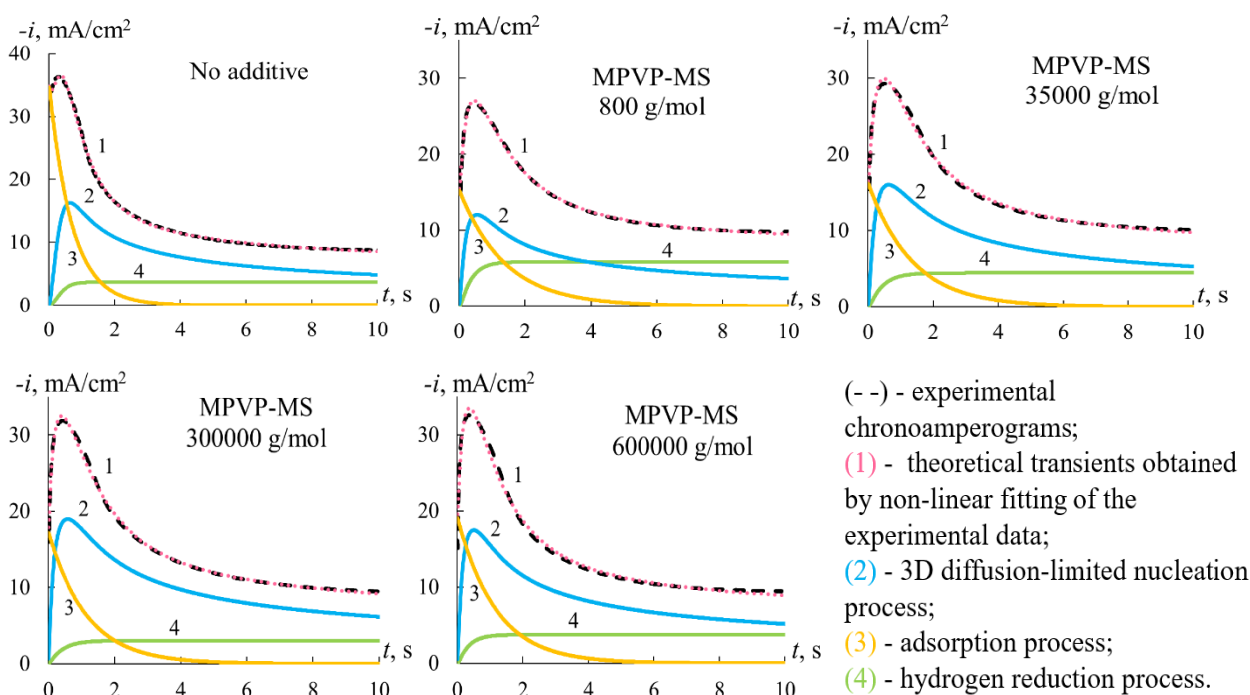


**Fig. 6.** Experimental and theoretically calculated chronoamperograms obtained by electrodeposition of copper at a potential of  $-500$  mV

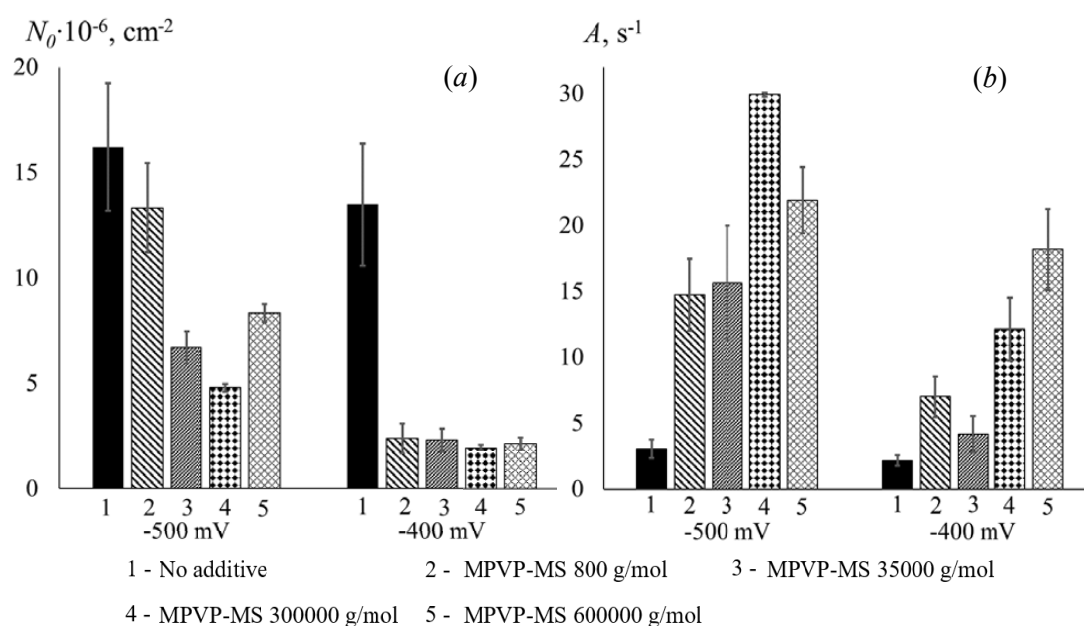


**Fig. 7.** Kinetic parameters of nucleation: (a) – nucleation active sites density ( $N_0$ ), (b) – rate constant of nucleation sites activation ( $A$ )

of quaternized polyvinylpyrrolidone derivatives on the copper surface. Thus, the inhibitory effect of *N*-methylpolyvinylpyrrolidone-methyl sulfate revealed by chronopotential and voltammetry methods is explained by a significant (up to 5-6 times) decrease in the concentration of active sites of copper nucleation in the presence of an organic additive.

In turn, the rate constant of nucleation sites activation ( $A$ ) increases with the introduction of MPVP-MS into the solution (Fig. 7b) and, in general, the higher the molar mass of the additive. It is known that, depending on the value of parameter  $A$ , the process of activation of potential nucleation centers can be classified as instantaneous (at  $At \gg 1$ ) or continuous (at  $At \ll 1$ ) [31]. The estimation of  $At$  by the time the maximum is reached on the partial nucleation curve ( $t \approx 1$  s) results in the case of a solution without an additive to the value of  $At \approx 3$ , which does not allow the process under study to be attributed to one of the limiting cases of instantaneous or continuous nucleation. In the presence of MPVP-MS with a molar mass of 800, 35,000, 300,000, 600,000 g/mol,  $At$  takes the value  $\approx 15$ ,  $\approx 16$ ,  $\approx 30$ ,  $\approx 22$ , respectively. According to the obtained values, the process of activation of nucleation sites in the presence of MPVP-MS in the plating solution is instantaneous. Probably, the introduction of quaternized

polyvinylpyrrolidone derivatives into an acid sulfate copper solution due to its adsorption on the electrode surface contributes to a more uniform potential distribution along the surface and the transition of nucleation sites activation to an instantaneous mode.

Thus, an analysis of the kinetic parameters of nucleation/growth of the new copper phase shows that the effect of *N*-methyl polyvinylpyrrolidone-methyl sulfate is complex, depending on the potential and molar mass of the polymer. By varying the values of these parameters, it is possible to adjust the morphological state and surface roughness of the copper coating, as well as its structure. This is especially important when choosing the electrolyte composition for microelectronics, in which the additive under study could perform the universal role of a suppressor and leveler: the research of such electrolytes is an urgent task of TSV technology [32].

#### 4. Conclusion

The introduction of *N*-methyl polyvinylpyrrolidone-methyl sulfate into an acid sulfate solution of copper plating has a noticeable inhibitory effect on the process of copper electrodeposition at relatively low overvoltages, and this effect is higher the lower the molar mass of the polymer. The potentiodynamic deposition in the presence of the polymer additive

under study at high cathodic overvoltages is characterized by higher current values compared to the electrolyte without the additive. As a result, *N*-methylpolyvinylpyridine-methylsulfate, depending on the molecular weight, makes it possible to obtain copper coatings of varying morphology. Electrodeposition of copper in the presence of *N*-methyl polyvinylpyridine-methyl sulfate is a diffusion-controlled process and involves a step of irreversible charge transfer. Within the framework of an expanded model of heterogeneous nucleation and growth of a new phase complicated by hydrogen reduction and adsorption of solution components, it was found that the activation of nucleation sites in the presence of *N*-methyl polyvinylpyridine-methyl sulfate is instantaneous, and the introduction of a polymer into a copper electrolyte significantly reduces the density of nucleation sites, which explains its inhibitory effect on copper electrodeposition.

### Contribution of the authors

Ilina E. A. – conducting electrochemical research, text writing. Kozaderov O. A. – scientific guidance, research concept, methodology development, text editing, final conclusions. Sotskaya N. V. – conducting research, editing text. Vandyshov D. Y. – conducting organic synthesis, writing text. Polikarchuk V. P. – conducting organic synthesis. Shikhaliev Kh. S. – organic synthesis concept.

### Conflict of interests

The authors declare that they have no known competing financial interests or personal relationships that could have influenced the work reported in this paper.

### References

1. Wang F., Zeng P., Wang Y., Ren X., Xiao H., Zhu, W. High-speed and high-quality TSV filling with the direct ultrasonic agitation for copper electrodeposition. *Microelectronic Engineering*. 2017;180: 30–34. <https://doi.org/10.1016/j.mee.2017.05.052>
2. Beica R., Siblerud P., Erickson D. Advanced TSV copper electrodeposition for 3D interconnect applications. *IMAPSource Proceedings 2010(DPC)*: 774–802. <https://doi.org/10.4071/2010DPC-tp13>
3. Chen X., Chen Z., Xiao L., ... Zhang Z. Fabrication and electrical characterization of high aspect ratio through-silicon vias with polyimide liner for 3D integration. *Micromachines*. 2022;13(7): 1147. <https://doi.org/10.3390/mi13071147>
4. Shen W.-W., Chen K.-N. Three-dimensional integrated circuit (3D IC) key technology: through-silicon via (TSV). *Nanoscale Research Letters*. 2017;12(1): 56. <https://doi.org/10.1186/s11671-017-1831-4>
5. Kondo K., Matsumoto T., Watanabe K. Role of additives for copper damascene electrodeposition: experimental study on inhibition and acceleration effects. *Journal of The Electrochemical Society*. 2004;151: C250. <http://dx.doi.org/10.1149/1.1649235>
6. Xiao H., He H., Ren X., Zeng P., Wang F. Numerical modeling and experimental verification of copper electrodeposition for through silicon via (TSV) with additives. *Microelectronic Engineering*. 2016;170: 54–58. <https://doi.org/10.1016/j.mee.2016.12.030>
7. Tsai T.-H., Huang J.-H. Electrochemical investigations for copper electrodeposition of through-silicon via. *Microelectronic Engineering*. 2011;88: 195–199. <https://doi.org/10.1016/j.mee.2010.10.018>
8. Jin Y., Sun M., Mu D., Ren X., Wang Q., Wen L. Investigation of PEG adsorption on copper in Cu<sup>2+</sup>-free solution by SERS and AFM. *Electrochimica Acta*. 2012;78: 459–465. <https://doi.org/10.1016/j.electacta.2012.06.039>
9. Kelly J., West A. Copper deposition in the presence of polyethylene glycol I. Quartz crystal microbalance study. *Journal of The Electrochemical Society*. 1998;145: 3472–3476. <https://doi.org/10.1149/1.1838829>
10. Dow W.-P., Chiu Y.-D., Yen M.-Y. Microvia filling by Cu electroplating over a Au seed layer modified by a disulfide. *Journal of The Electrochemical Society*. 2009;156: D155. <https://doi.org/10.1149/1.3078407>
11. Sun Q., Cao H., Ling H., Li M. Analysis of accelerator consumption in TSV copper electroplating. *Proceedings - 2013 14th International Conference on Electronic Packaging Technology*. 2013: 818–821. <https://doi.org/10.1109/ICEPT.2013.6756589>
12. Meng Y., Zhou M., Huang W., Min Y., Shen X., Xu Q. Benzyl-containing quaternary ammonium salt as a new leveler for microvia copper electroplating. *Electrochimica Acta*. 2022;429: 141013. <https://doi.org/10.1016/j.electacta.2022.141013>
13. Moffat T., Wheeler D., Kim S.-K., Josell D. Curvature enhanced adsorbate coverage mechanism for bottom-up superfilling and bump control in damascene processing. *Electrochimica Acta*. 2007;53: 145–154. <https://doi.org/10.1016/j.electacta.2007.03.025>
14. Jung M.-W., Kim K.-T., Koo Y.-S., Lee J.-H. The effects of levelers on electrodeposition of copper in TSV filling. *Journal of the Microelectronics and Packaging Society*. 2012;19. <https://doi.org/10.6117/kmeps.2012.19.2.055>
15. Kelly J., Tian Chunyan, West A. Leveling and microstructural effects of additives for copper electrodeposition. *Journal of The Electrochemical Society*. 1999;146: 2540–2545. <https://doi.org/10.1149/1.1391968>
16. Wang C., Zhang J., Yang P., An M. Electrochemical behaviors of Janus Green B in through-hole copper electroplating: An insight by experiment and density functional theory calculation using Safranin T as a comparison. *Electrochimica Acta*. 2013;92: 356–364. <https://doi.org/10.1016/j.electacta.2013.01.064>
17. Li J., Xu J., Wang X., Wei X., Lv J., Wang L. Novel 2,5-bis(6-(trimethylammonium)hexyl)-3,6-diaryl-1,4-diketo-pyrrolo[3,4-c] pyrrole pigments as levelers for efficient

electroplating applications. *Dyes and Pigments*, 2020;186: 109064. <https://doi.org/10.1016/j.dyepig.2020.109064>

18. Yaqiang L., Ren P., Zhang Yu., ... An M. Investigation of novel leveler Rhodamine B on copper superconformal electrodeposition of microvias by theoretical and experimental studies. *Applied Surface Science*. 2022;615: 156266. <https://doi.org/10.1016/j.apsusc.2022.156266>

19. Willey M. J., West A. C. SPS adsorption and desorption during copper electrodeposition and its impact on PEG adsorption. *Journal of The Electrochemical Society*. 2007;154(3): D156–D162. <https://doi.org/10.1149/1.2431320>

20. Zhou J., Reid J. D. Impact of leveler molecular weight and concentration on Damascene copper electroplating. *ECS Transactions*. 2007;2(6): 77–92. <https://doi.org/10.1149/1.2408866>

21. Jin S. H., Yoon Y., Jo Y., ... Lee M. H.. The effects of polyvinylpyrrolidone molecular weight on defect-free filling of through-glass vias (TGVs). *Journal of Industrial and Engineering Chemistry*. 2021;96: 376–381. <https://doi.org/10.1016/j.jiec.2021.01.046>

22. Hatch J. J., Willey M. J., Gewirth A. A. Influence of aromatic functionality on quaternary ammonium levelers for Cu plating. *Journal of The Electrochemical Society*. 2011;158(6): D323–D329. <https://doi.org/10.1149/1.3575636>

23. Yuan B., Chen X., Zhao Y., Zhou W., Li X., Wang L. Unveiling the potential and mechanisms of 3,3'-bicarbazole-based quaternary ammonium salts as levelers. *Electrochimica Acta*. 2023;471: 143345. <https://doi.org/10.1016/j.electacta.2023.143345>

24. Li X., Yin X., Li J., ... Wang L. Synthesis of coplanar quaternary ammonium salts with excellent electrochemical properties based on an anthraquinone skeleton and their application in copper plating. *Electrochimica Acta*. 2022;437: 141541. <https://doi.org/10.1016/j.electacta.2022.141541>

25. Jo Y. E., Yu D. Y., Cho S. K. Revealing the inhibition effect of quaternary ammonium cations on Cu electrodeposition. *Journal of Applied Electrochemistry*. 2020;50: 245–253. <https://doi.org/10.1007/s10800-019-01381-4>

26. Zou P., Li X., Chen X., Zhou W., Du K., Wang L. Synthesis and mechanism of quaternary ammonium salts based on porphyrin as high-performance copper levelers. *Tetrahedron*. 2024;159: 134011. <https://doi.org/10.1016/j.tet.2024.134011>

27. Garfias Garcia E., Romero-Romo M., María T., Ramírez-Silva, Palomar-Pardavé M. Overpotential nucleation and growth of copper onto polycrystalline and single crystal gold electrodes. *International Journal of Electrochemical Science*. 2012;7(4): 3102–3114. [https://doi.org/10.1016/S1452-3981\(23\)13938-1](https://doi.org/10.1016/S1452-3981(23)13938-1)

28. Sainsbury F. *Stirling engine arrangement*. Pat. US 3 682 939 A. Оpubл. 08.08.1972.

29. Lyapkov A. V. Physicochemical methods for studying polymers: textbook\* [Electronic resource] 2022. 152 p. Available at: <https://www.researchgate.net/profile/Alex-Lyapkov/publication/360862354Fiziko-himiceskiemetodyisledovaniapolimerov/links/628f641055273755ebb77b52/Fiziko-himiceskie-metody-issledovania-polimerov.pdf>

30. Zhang Q., Yu X., Hua Y., Xue W. The effect of quaternary ammonium-based ionic liquids on copper electrodeposition from acidic sulfate electrolyte. *Journal of Applied Electrochemistry*. 2015;45: 79–86. <https://doi.org/10.1007/s10800-014-0774-z>

31. Scharifker B., Hills G. Theoretical and experimental studies of multiple nucleation. *Electrochimica Acta*. 1983;28(7): 879–889. [https://doi.org/10.1016/0013-4686\(83\)85163-9](https://doi.org/10.1016/0013-4686(83)85163-9)

32. Wang F., Tian Y., Zhou K., ... Yao W. Using a triblock copolymer as a single additive in high aspect ratio through silicon via (TSV) copper filling. *Microelectronic Engineering*. 2021;244–246: 111554. <https://doi.org/10.1016/j.mee.2021.111554>

\* Translated by author of the article

## Information about the authors

Evgenia A. Ilina, Junior Researcher, Laboratory of organic additives for the processes of chemical and electrochemical deposition of metals and alloys used in the electronics industry, Voronezh State University (Voronezh, Russian Federation).

<https://orcid.org/0009-0004-4825-5894>

[zhenya.ali@yandex.ru](mailto:zhenya.ali@yandex.ru)

Oleg A. Kozaderov, Dr. Sci. (Chem.), Leading Researcher, Laboratory of organic additives for the processes of chemical and electrochemical deposition of metals and alloys used in the electronics industry, Voronezh State University (Voronezh, Russian Federation).

<https://orcid.org/0000-0002-0249-9517>

[ok@chem.vsu.ru](mailto:ok@chem.vsu.ru)

Nadezhda V. Sotskaya, Cand. Sci. (Chem.), Associate Professor at the Department of Physical Chemistry, Voronezh State University (Voronezh, Russian Federation).

<https://orcid.org/0000-0003-4088-1546>

[nvs@chem.vsu.ru](mailto:nvs@chem.vsu.ru)

Dmitriy Yu. Vandyshev, Cand. Sci. (Chem.), Associate Professor at the Department of Organic Chemistry, Voronezh State University (Voronezh, Russian Federation).

<https://orcid.org/0000-0001-8606-458X>

[francy\\_2007@mail.ru](mailto:francy_2007@mail.ru)

Vladimir A. Polikarchuk, Cand. Sci. (Chem.), Junior Researcher, Laboratory of organic additives for the processes of chemical and electrochemical deposition of metals and alloys used in the electronics industry, Voronezh State University (Voronezh, Russian Federation).

<https://orcid.org/0009-0001-7339-5803>

[polikarchyk@mail.ru](mailto:polikarchyk@mail.ru)

Khidmet S. Shikhaliev, Doctor of Chemical Sciences, Chief Scientific Officer, Laboratory of organic additives for the processes of chemical and electrochemical deposition of metals and alloys used in the electronics industry, Voronezh State University (Voronezh, Russian Federation).

<https://orcid.org/0000-0002-6576-0305>

[shikh1961@yandex.ru](mailto:shikh1961@yandex.ru)

Received May 14, 2025; approved after reviewing June 16, 2025; accepted for publication July 16, 2025; published online September 25, 2025.



# Condensed Matter and Interphases

Kondensirovannye Sredy i Mezhfaznye Granitsy  
<https://journals.vsu.ru/kcmf/>

## Original articles

Research article

<https://doi.org/10.17308/kcmf.2025.27/13014>

## Ternary molybdate $K_5Cu_{0.5}Hf_{1.5}(MoO_4)_6$ : synthesis, structure, thermal expansion, and ionic conductivity

E. V. Kovtunets<sup>✉</sup>, T. S. Spiridonova, Yu. L. Tushinova, T. T. Bazarova, A. V. Logvinova, B. G. Bazarov

Baikal Institute of Nature Management, Siberian Branch of the Russian Academy of Sciences,  
6, Sakhyanova st., 670047 Ulan-Ude, Republic of Buryatia, Russian Federation

### Abstract

**Objective:** A novel ternary molybdate,  $K_5Cu_{0.5}Hf_{1.5}(MoO_4)_6$ , was synthesized using a solid-state ceramic method. The sequence of chemical transformations involved in its formation was determined, revealing that the compound undergoes incongruent melting at 634 °C.

**Experimental:** The crystal structure was refined using the Rietveld method, revealing a trigonal structure (space group  $R\bar{3}c$ ) with unit cell parameters  $a = 10.5617(2)$  Å;  $c = 37.5017(7)$  Å;  $V = 3622.9(1)$  Å<sup>3</sup>,  $R_{wp} = 3.78$ . Attenuated total reflection Fourier-transform infrared (ATR-FTIR) spectroscopy confirmed the presence of isolated  $MoO_4$  tetrahedra. The electrical conductivity of the title compound reached  $7.5 \cdot 10^{-4}$  S/cm at 550 °C, with an activation energy of  $E_a = 0.9$  eV. Thermal deformations were investigated by high temperature powder X-ray diffraction (HT-XRD) over the temperature range of 30–500 °C.

**Results:**  $K_5Cu_{0.5}Hf_{1.5}(MoO_4)_6$  was classified as a high thermal expansion material ( $\alpha_v = 45 \cdot 10^{-6}$  °C<sup>-1</sup> at 500 °C), and exhibited low anisotropy. Combined results from electrochemical impedance spectroscopy (EIS) and HT-XRD indicated that the endothermic peak observed at 479 °C in the differential scanning calorimetry (DSC) curve corresponded to a first-order phase transition.

**Keywords:** Potassium; copper; Hafnium; Ternary molybdate; Synthesis; Crystal structure; Thermal expansion; Ionic conductivity

**Funding:** This research was conducted within the framework of the state assignment to Baikal Institute of Nature Management SB RAS (No. 0273-2021-0008) and was supported by the Russian Science Foundation (project No. 23-29-00327).

**Acknowledgments:** The studies involving XRD, thermal analysis, ATR-FTIR, HT-XRD, and conductivity measurements were performed using the resources of the Research Equipment Sharing Center of BINM SB RAS.

**For citation:** Kovtunets E. V., Spiridonova T. S., Tushinova Yu. L., Bazarova Ts. T., Logvinova A. V., Bazarov B. G. Ternary molybdate  $K_5Cu_{0.5}Hf_{1.5}(MoO_4)_6$ : synthesis, structure, thermal expansion and ionic conductivity. *Condensed Matter and Interphases*. 2025;27(3): 380–390. <https://doi.org/10.17308/kcmf.2025.27/13014>

**Для цитирования:** Ковтунец Е. В., Спиридонова Т. С., Тушинова Ю. Л., Базарова Ц. Т., Логвинова А. В., Базаров Б. Г.  $K_5Cu_{0.5}Hf_{1.5}(MoO_4)_6$ : синтез, структура, термические деформации и ионная проводимость. *Конденсированные среды и межфазные границы*. 2025;27(3): 380–390. <https://doi.org/10.17308/kcmf.2025.27/13014>

✉ Evgeniy V. Kovtunets, e-mail: [kovtunets@binm.ru](mailto:kovtunets@binm.ru)

© Kovtunets E. V., Spiridonova T. S., Tushinova Yu. L., Bazarova Ts. T., Logvinova A. V., Bazarov B. G., 2025



The content is available under Creative Commons Attribution 4.0 License.

## 1. Introduction

Progress in modern materials science is closely linked to advances in the synthesis and characterization of complex inorganic oxides. Ternary molybdates and tungstates are particularly promising due to their structural versatility, tunable cation compositions, and a wide range of functional properties, including ferroelectricity [1], piezoelectricity [2], luminescence [3, 4], laser activity [5,6], photocatalysis [7], magnetism [8], antiferromagnetism [9], and ionic conductivity [10–14]. The crystal structures of this class of compounds typically form three-dimensional frameworks containing numerous cavities and interconnected channels, constructed from metal polyhedra and  $EO_4$  tetrahedra ( $E = Mo, W$ ). Among them are representatives of well-known structural types such as NASICON [15], scheelite [16], alluaudite [17], glaserite [18], lyonsite [19], and others [20].

In the present study, the family of ternary molybdates with the general formula  $M_5^{I}M_{0.5}^{II}M_{1.5}^{IV}(MoO_4)_6$  [21–29] is extended through the synthesis of  $K_5Cu_{0.5}Hf_{1.5}(MoO_4)_6$ . A preliminary characterization of this compound was performed, including crystal structure refinement by the Rietveld method based on XRD data, along with investigations of its thermal expansion and ionic conductivity properties.

## 2. Experimental

The following reagents were used for the solid-state synthesis of  $K_5Cu_{0.5}Hf_{1.5}(MoO_4)_6$ :  $K_2CO_3$  – analytical grade;  $CuO$  and  $HfO_2$  – high purity;  $MoO_3$  and  $K_2MoO_4$  – chemically pure.  $CuMoO_4$  was synthesized by annealing a stoichiometric mixture of  $CuO$  and  $MoO_3$  at 350–500 °C for 50 hours. Hafnium molybdate was obtained via the reaction:

$$HfO_2 + 2 MoO_3 = Hf(MoO_4)_2 \text{ (500–750 °C, 50 hours)}$$

The phase purity of the synthesized compounds was confirmed by XRD, and phase identification was performed by comparison with the ICDD PDF-2 [30].

XRD analysis was conducted using a D8 ADVANCE automated powder diffractometer (Bruker) equipped with a VANTEC detector,  $CuK\alpha$  radiation ( $\lambda = 1.5418 \text{ \AA}$ ), reflection geometry, a secondary monochromator, and a scanning step size of  $0.02076^\circ$ . HT-XRD measurements were

performed on the same instrument using an Anton Paar HTK16 high-temperature chamber over the 30–500 °C range, with 50 °C intervals. Structural refinement and unit cell parameter determination for  $K_5Cu_{0.5}Hf_{1.5}(MoO_4)_6$  were carried out using the Topas 4.2 software package [31]. Thermal expansion tensor parameters were calculated and visualized using the TTT software suite [32]. The temperature dependence of the unit cell parameters was modeled using first and second degree polynomial approximations. Based on these data, the principal values of the thermal expansion tensor were determined, and cross-sectional plots of the thermal expansion coefficient surface were constructed.

ATR-FTIR spectra were recorded using a SIMEX FT-801 FT-IR spectrometer equipped with an attenuated total reflectance (ATR) accessory featuring a diamond crystal. Measurements were performed at room temperature over the 500–1100  $cm^{-1}$  range with a resolution of 1  $cm^{-1}$ .

Thermal analysis was carried out on an STA 449 F1 Jupiter thermoanalyzer (NETZSCH) using a platinum crucible, with a heating rate of 10 °C/min under an argon atmosphere over the temperature range of 30–800 °C.

EIS profiles of  $K_5Cu_{0.5}Hf_{1.5}(MoO_4)_6$  were registered using a Z-1500J impedance analyzer (Elins, LLC) with an AC signal amplitude of 200 mV. Measurements were taken over a frequency range of 1 Hz to 1 MHz and a resistance range of 20 mΩ to 20 MΩ, within a temperature interval of 200–550 °C. For electrical characterization, the sample was fabricated as a pressed disk-shaped pellet (9 mm in diameter, 1.9 mm in height), sintered at 570 °C, and coated with platinum electrodes on the flat surfaces.

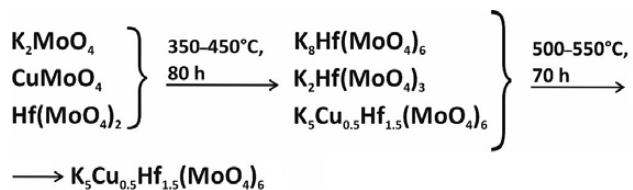
## 3. Results and discussion

### 3.1. Solid-state synthesis of $K_5Cu_{0.5}Hf_{1.5}(MoO_4)_6$

The single-phase polycrystalline form of the ternary molybdate  $K_5Cu_{0.5}Hf_{1.5}(MoO_4)_6$  was synthesized by annealing stoichiometric mixtures of  $K_2MoO_4$ ,  $CuMoO_4$ , and  $Hf(MoO_4)_2$  at 350–550 °C for 150 hours.

According to XRD data, the formation of  $K_5Cu_{0.5}Hf_{1.5}(MoO_4)_6$  from a stoichiometric mixture of simple molybdates proceeded through a sequential transformation pathway, with

the formation of potassium–hafnium binary molybdates as an intermediate stage:



When simple oxides and potassium carbonate were used as starting materials, the reaction pathway become more complex. In this case, the intermediate phase  $K_2Mo_3O_{10}$  persisted in the annealed products at temperatures up to 500 °C.

### 3.2. Rietveld refinement of $K_5Cu_{0.5}Hf_{1.5}(MoO_4)_6$

The crystal structure of  $K_5Cu_{0.5}Hf_{1.5}(MoO_4)_6$  was refined using the Rietveld method, employing the atomic positional parameters of  $Rb_5Co_{0.5}Hf_{1.5}(MoO_4)_6$  [27] as the initial structural model. Peak profiles were modeled using the Pearson VII function. The refinement was performed iteratively, with progressive addition of variables and simultaneous graphical background modeling. To reduce the number of refined parameters, the isotropic displacement factors ( $B_{iso}$ ) for oxygen atoms were constrained to be equal.

The refinement process was stable and yielded low residual R-factors, which indicated good agreement between the experimental and calculated patterns. Final refinement results are presented in Table 1, selected interatomic distances in Table 2, and atomic coordinates along with isotropic displacement parameters in Table 3. The experimental, calculated, and

**Table 1.** Crystallographic parameters and structure refinement details for  $K_5Cu_{0.5}Hf_{1.5}(MoO_4)_6$

Compound	$K_5Cu_{0.5}Hf_{1.5}(MoO_4)_6$
Space group	Trigonal, $R\bar{3}c$
$a$ , Å	10.5617(2)
$c$ , Å	37.5017(7)
$V$ , Å <sup>3</sup>	3622.9(1)
$Z$	6
$2\theta$ -interval, °	10–100
$R_{wp}$ , %	3.78
$R_p$ , %	3.01
$R_{exp}$ , %	2.67
$\chi^2$	1.42
$R_B$ , %	1.35

**Table 2.** Selected interatomic distances (Å) in the crystal structure of  $K_5Cu_{0.5}Hf_{1.5}(MoO_4)_6$

Tetrahedron $MoO_4$		Polyhedron $K1O_9$	
Mo–O1	1.854(16)	K1–O2	3.189(13) × 3
Mo–O2	1.852(11)	K1–O3	2.739(18) × 3
Mo–O3	1.727(17)	K1–O4	2.865(14) × 3
Mo–O4	1.670(12)	Polyhedron $K2O_{12}$	
⟨Mo(1)–O⟩	1.776	K2–O1	3.368(12) × 2
Octahedron $(Cu1/Hf1)O_6$		K2–O1'	3.481(13) × 2
(Cu1/Hf1)–O1	2.017(16) × 6	K2–O2	2.928(16) × 2
Octahedron $(Cu2/Hf2)O_6$		K2–O3	3.071(16) × 2
(Cu2/Hf2)–O2	2.087(13) × 6	K2–O3'	3.328(12) × 2
		K2–O4	2.866(12) × 2

**Table 3.** Atomic fractional coordinates and displacement parameters (Å<sup>2</sup>) for  $K_5Cu_{0.5}Hf_{1.5}(MoO_4)_6$

Atom	$x$	$y$	$z$	$B_{iso}$	Occ.
Cu1/Hf1	0	0	0	0.6(1)	$Cu_{0.15(1)}Hf_{0.85(1)}$
Cu2/Hf2	0	0	1/4	0.2(2)	$Cu_{0.35(1)}Hf_{0.65(1)}$
Mo	0.3504(3)	0.0565(2)	0.03253(5)	1.2(1)	
K1	0	0	0.3531(2)	4.5(3)	
K2	0.3801(7)	0	1/4	3.1(2)	
O1	0.163(1)	0.030(1)	0.0331(3)	1.3(2)	
O2	0.479(2)	0.238(1)	0.0518(3)	1.3(2)	
O3	0.353(2)	0.909(2)	0.0517(3)	1.3(2)	
O4	0.405(1)	0.058(1)	0.9907(3)	1.3(2)	

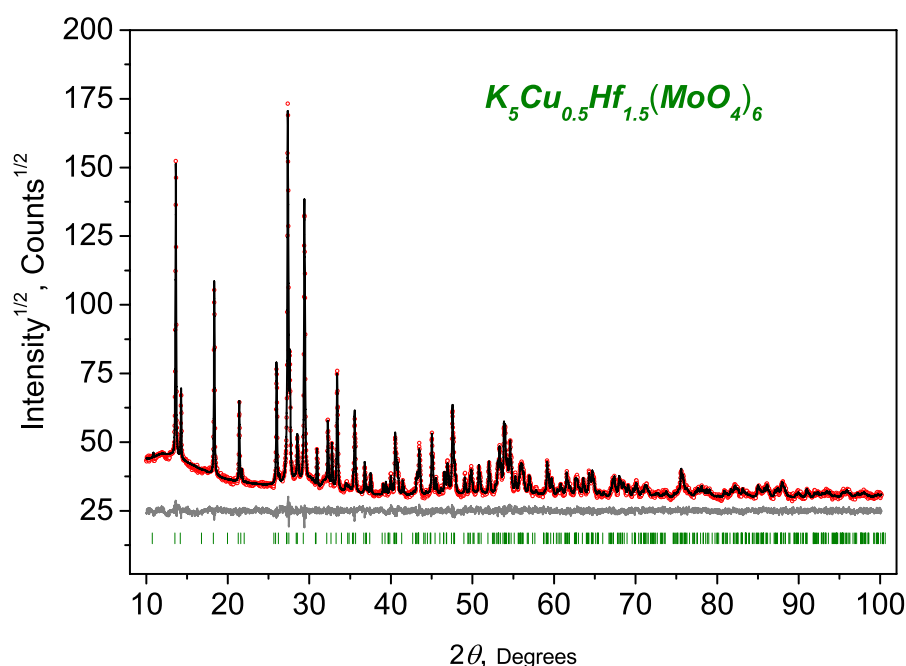


**Fig. 1.** Experimental (circles), calculated (solid line), difference, and dashed XRD patterns for  $K_5Cu_{0.5}Hf_{1.5}(MoO_4)_6$

difference XRD patterns are shown in Figure 1.

Crystallographic data for  $K_5Cu_{0.5}Hf_{1.5}(MoO_4)_6$  have been deposited with the Cambridge Crystallographic Data Centre under deposition number CSD 2386835 and are accessible at ([www.ccdc.cam.ac.uk/data\\_request/cif](http://www.ccdc.cam.ac.uk/data_request/cif)).

The crystal structure of  $K_5Cu_{0.5}Hf_{1.5}(MoO_4)_6$  consists of a three-dimensional framework formed by alternating, slightly distorted  $MoO_4$  tetrahedra and two types of (Cu/Hf) octahedra, interconnected via shared oxygen vertices. Two distinct potassium cation sites are located within the spacious cavities of this framework (Figure 2).

Copper and hafnium atoms are statistically distributed over two special crystallographic sites: (Cu1/Hf1) and (Cu2/Hf2) with point symmetries 3 and  $\bar{3}2$ , respectively. The (Cu1/Hf1) site is occupied by  $0.85(1)Hf + 0.15(1)Cu$ , with an average (Cu1/Hf1)–O bond length of 2.017(16) Å. The (Cu2/Hf2) site contains  $0.65(1)Hf + 0.35(1)Cu$ , with a corresponding (Cu2/Hf2)–O bond length of 2.087(16) Å. These Cu/Hf–O distances are comparable to the Hf–O bond lengths in the binary molybdate  $K_8Hf(MoO_4)_6$ , where  $Hf1-O1 = 2.0288$  Å and  $Hf1-O12 = 2.0806$  Å [33].

Molybdenum cations are coordinated by four oxygen atoms, forming  $MoO_4$  tetrahedra with an average Mo–O bond length of 1.776 Å. The distortion of these tetrahedra is attributed to the

differing local environments of the coordinating oxygen atoms. The longest Mo–O bonds are observed for O(2) and O(1), which also participate in the octahedral coordination of Cu and Hf cations. In contrast, the shortest Mo–O bonds

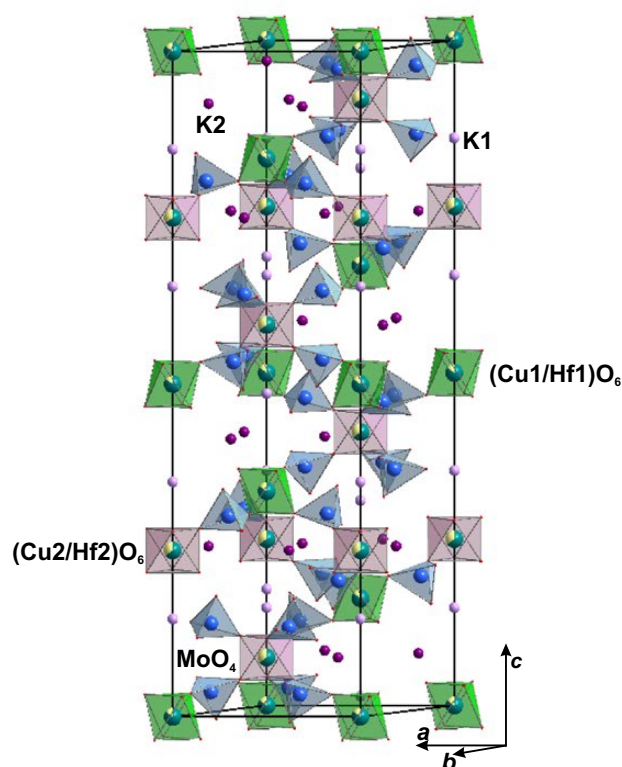


**Fig. 2.** Unit cell of  $K_5Cu_{0.5}Hf_{1.5}(MoO_4)_6$

involve O(3) and O(4), which additionally bond to potassium cations located within the framework cavities. The potassium cations exhibit two distinct coordination environments: a  $K1O_9$  nine-vertex polyhedron with  $\langle K1-O \rangle$  bond lengths ranging from 2.739(18) to 3.189(13) Å, and a  $K2O_{12}$  twelve-vertex polyhedron with bond lengths spanning 2.866(12) to 3.481(13) Å.

### 3.3. ATR-FTIR spectra

To elucidate the coordination environment of molybdenum atoms, ATR-FTIR absorption spectrum of  $K_5Cu_{0.5}Hf_{1.5}(MoO_4)_6$  was recorded and is shown in Figure 3. In the vibrational spectra of molybdates, intense  $MoO_4$  absorption bands typically appeared in the 700–980  $cm^{-1}$  region, corresponding to symmetric and asymmetric stretching vibrations of Mo–O bonds within the  $MoO_4$  tetrahedra. Additional bands in the 300–410  $cm^{-1}$  range were attributed to O–Mo–O bending (deformation) modes [34].

Generally, the infrared spectra of molybdates are dominated by stretching vibrations of the  $MoO_4$  tetrahedra. In the case of  $K_5Cu_{0.5}Hf_{1.5}(MoO_4)_6$ , ten distinct absorption bands were observed in the 500–1000  $cm^{-1}$  range, all of which were assigned to internal vibrations of the  $MoO_4$  tetrahedra (Table 4).

### 3.4. Thermal behavior

The thermal behavior of  $K_5Cu_{0.5}Hf_{1.5}(MoO_4)_6$  was investigated using HT-XRD, DSC, and thermogravimetric analysis (TGA).

The DSC curve (Figure 4) displayed two endothermic events: a weak effect with a peak at 479 °C, and a more pronounced peak at 634 °C, corresponding to the melting of the compound. The TGA curve showed no mass loss over the studied temperature range. However, XRD analysis of the solidified melt revealed the presence of  $CuMoO_4$ ,  $HfO_2$ , and  $K_2Mo_4O_{13}$ .

To clarify the origin of the endothermic effect at 479 °C, the sample was subjected to cyclic heating and cooling within the 200–600 °C range, remaining below the melting point. The endothermic peak was consistently reproduced on the heating curves in the range of 474–483 °C with high precision, while no thermal effects were observed on the corresponding cooling curves.

**Table 4.** Vibrational frequencies ( $cm^{-1}$ ) observed in the ATR-FTIR spectrum of  $K_5Cu_{0.5}Hf_{1.5}(MoO_4)_6$

Attribution	Vibration frequencies in the IR-spectr $K_5Cu_{0.5}Hf_{1.5}(MoO_4)_6$ , $cm^{-1}$
$\nu_1(MoO_4)$	946, 926, 912
$\nu_2(MoO_4)$	898, 878, 848, 832, 806, 734, 714

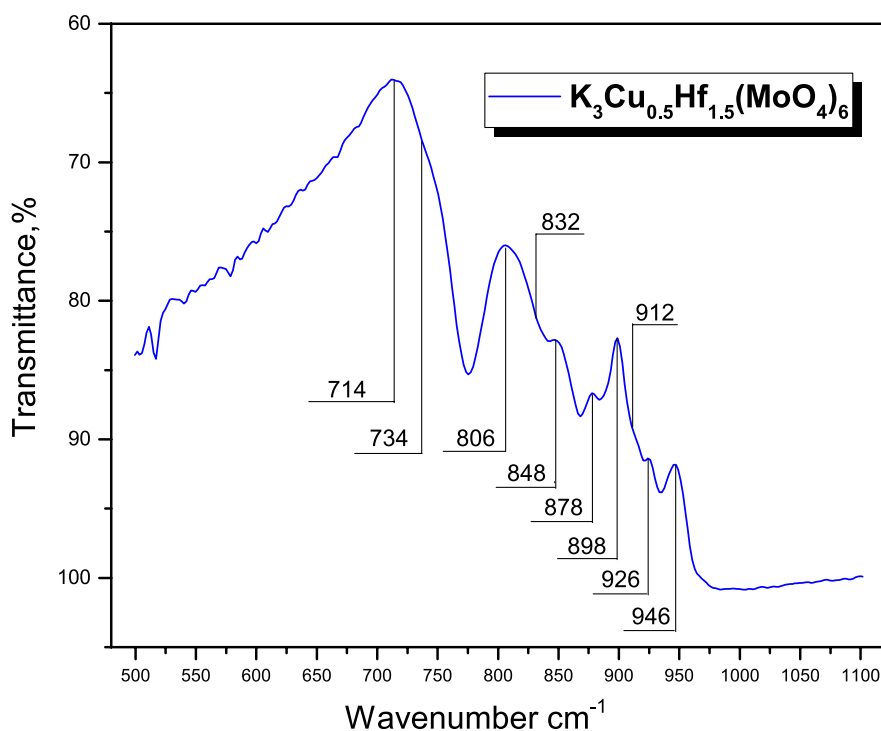


**Fig. 3.** ATR-FTIR absorption spectrum of  $K_5Cu_{0.5}Hf_{1.5}(MoO_4)_6$

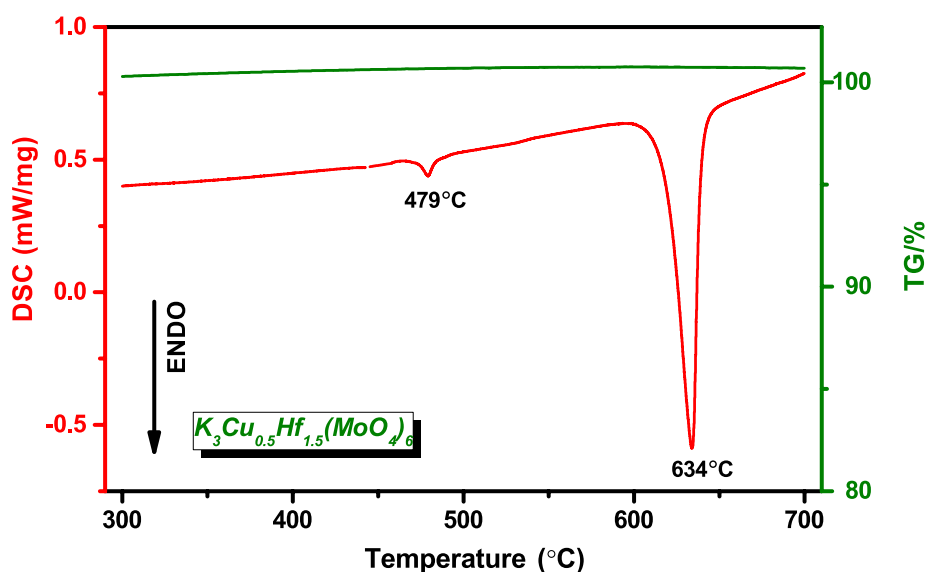


Fig. 4. TGA and DSC curves of  $K_5Cu_{0.5}Hf_{1.5}(MoO_4)_6$

The temperature dependence of the unit cell parameters of  $K_5Cu_{0.5}Hf_{1.5}(MoO_4)_6$ , as determined by HT-XRD, is presented in Figure 7 and summarized in Table 5. Both lattice parameters,  $a$  and  $c$ , increased over the entire temperature range studied. The coefficients of thermal expansion (CTE), listed in Table 6, were calculated from polynomial approximations of the temperature-dependent trends in the lattice parameters and unit cell volume (Table 7). The  $a$  parameter and the unit

cell volume were adequately described by linear fits. However, the  $c$  parameter displayed a distinct inflection between 400 and 500 °C, which coincided with the endothermic peak at 479 °C observed in the DSC curve, thereby requiring a second-degree polynomial approximation. A cross-sectional view of the thermal expansion tensor was compared with the  $bc$ -plane structural projection in Figure 8.

The coefficient  $\alpha_a$  remained constant at  $9.8 \cdot 10^{-6} \text{ } ^\circ\text{C}^{-1}$  throughout the investigated

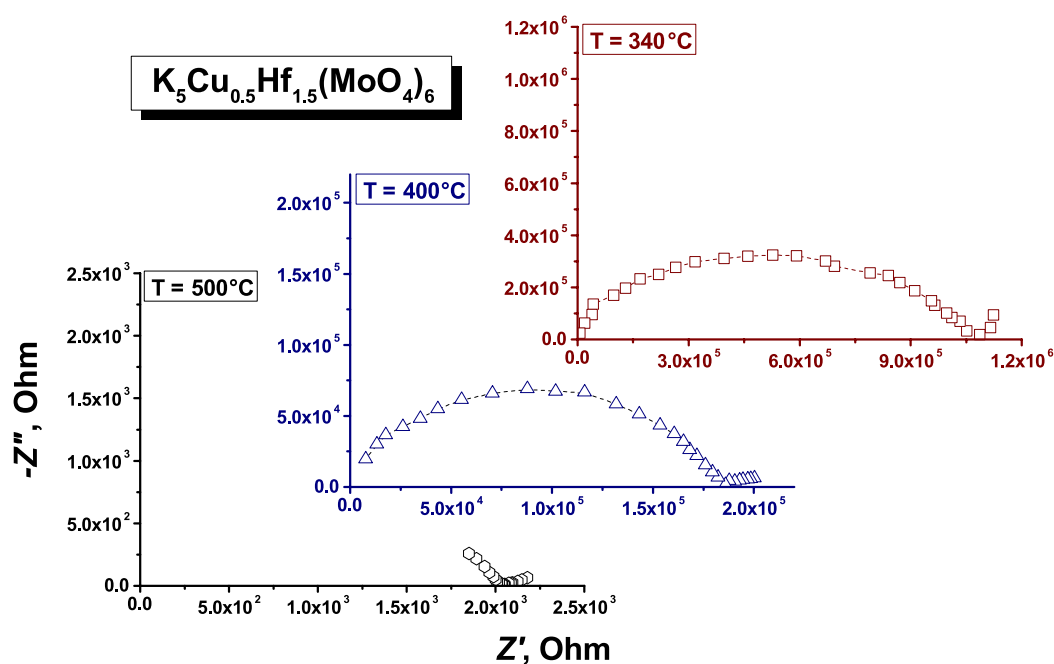


Fig. 5. EIS profiles of  $K_5Cu_{0.5}Hf_{1.5}(MoO_4)_6$

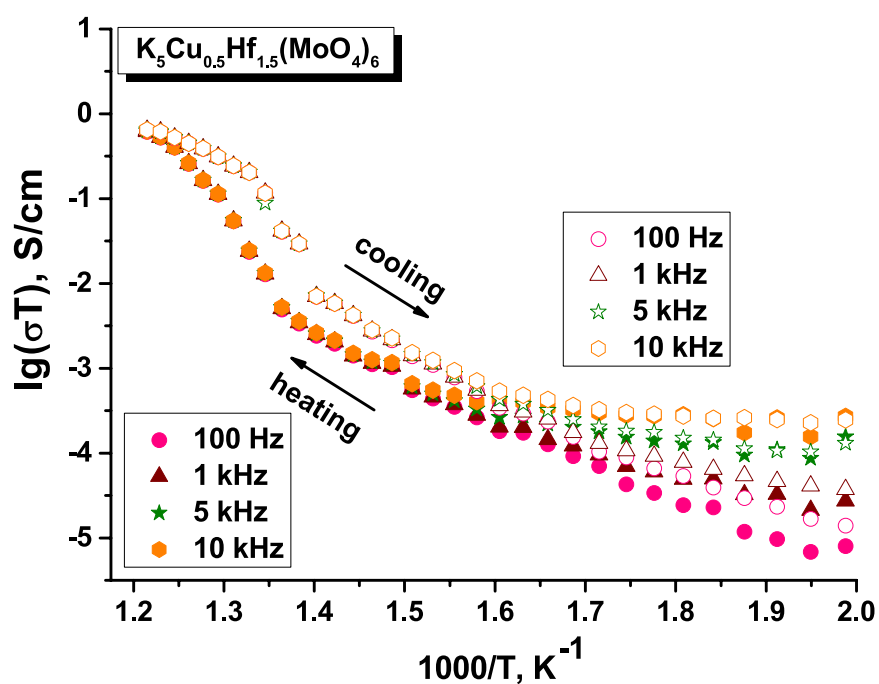


Fig. 6. Temperature dependence of the electrical conductivity of  $K_5Cu_{0.5}Hf_{1.5}(MoO_4)_6$

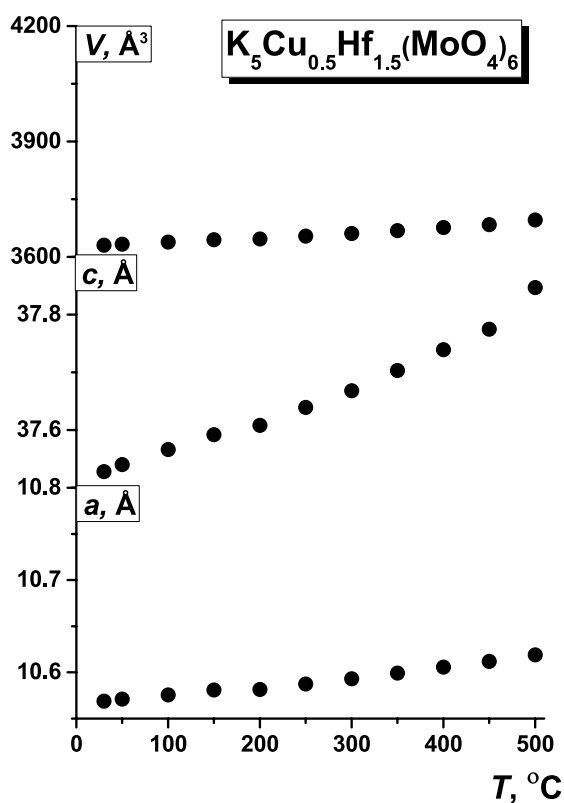


Fig. 7. Temperature dependence of lattice parameters for  $K_5Cu_{0.5}Hf_{1.5}(MoO_4)_6$

Table 5. Unit cell parameters of  $K_5Cu_{0.5}Hf_{1.5}(MoO_4)_6$  measured at various temperatures

$T, ^\circ C$	$a, \text{\AA}$	$c, \text{\AA}$	$V, \text{\AA}^3$
30	10.5689(4)	37.528(2)	3630.3(4)
50	10.5710(3)	37.540(2)	3632.9(3)
100	10.5756(3)	37.566(1)	3638.6(2)
150	10.5810(4)	37.592(2)	3644.9(3)
200	10.5815(7)	37.608(3)	3646.8(5)
250	10.5874(4)	37.639(2)	3653.8(3)
300	10.5932(4)	37.668(2)	3660.6(3)
350	10.5994(5)	37.703(2)	3668.3(4)
400	10.6058(4)	37.739(2)	3676.3(3)
450	10.6119(4)	37.775(3)	3684.0(4)
500	10.6190(3)	37.847(2)	3696.0(3)

Table 6. Thermal expansion coefficients ( $\times 10^{-6} \text{ } ^\circ C^{-1}$ ) for  $K_5Cu_{0.5}Hf_{1.5}(MoO_4)_6$

$T, ^\circ C$	$\alpha_a$	$\alpha_c$	$\alpha_v$
30	9.8(3)	8(2)	28(2)
50	9.8(3)	9(1)	28(2)
100	9.8(3)	11(1)	30(2)
150	9.8(3)	12.5(8)	32(2)
200	9.8(3)	14.4(5)	34(2)
250	9.8(3)	16.3(4)	36(2)
300	9.8(3)	18.2(5)	38(2)
350	9.8(3)	20.0(8)	40(2)
400	9.8(3)	22(1)	42(2)
450	9.8(3)	25(1)	43(2)
500	9.8(3)	26(2)	45(2)

**Table 7.** Temperature dependence of unit cell parameters approximated by linear and quadratic polynomial functions  $a_0 + a_1 \times 10^{-3}t + a_2 \times 10^{-6}t^2$  in the range 30–500 °C

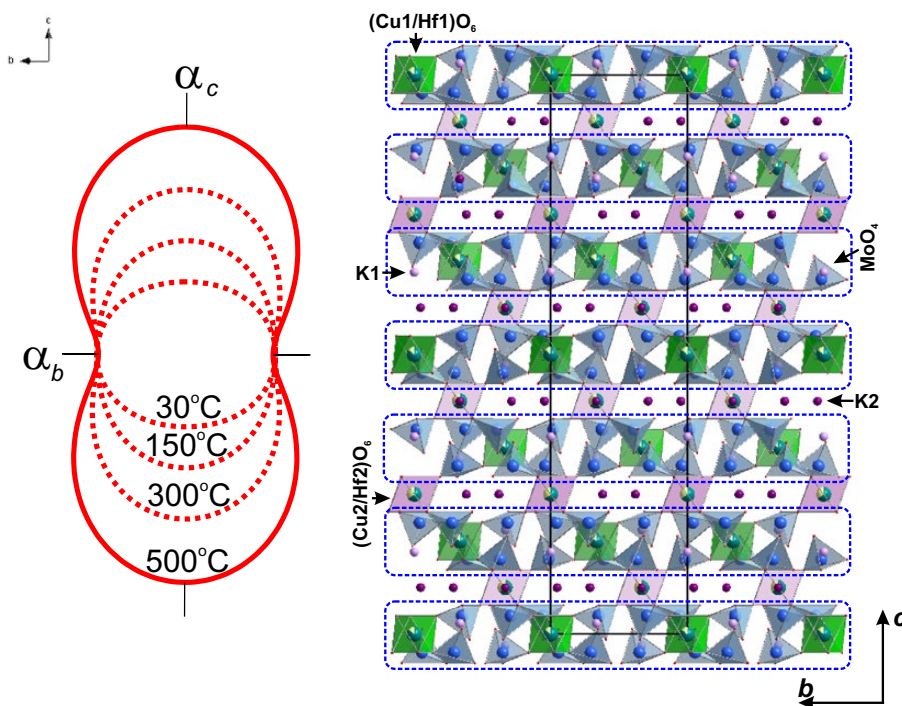
Cell	$a_0$	$a_1$	$a_2$	$R^2$
<i>a</i>	10.565(1)	0.104(4)		1.00000
<i>c</i>	37.530(6)	0.26(7)	0.7(1)	0.99434
<i>V</i>	3625(2)	132(6)		1.00000

temperature range, indicating uniform expansion in the *ab*-plane. In contrast,  $\alpha_c$  increased with temperature, ranging from  $8 \cdot 10^{-6} \text{ }^\circ\text{C}^{-1}$  to  $26 \cdot 10^{-6} \text{ }^\circ\text{C}^{-1}$ . The title compound exhibited relatively weak thermal expansion anisotropy, with the  $\alpha_{\max}/\alpha_{\min}$  ratio varying from 1.2 to 2.7 depending on temperature (Table 8).

As with its isostructural analogs,  $K_5Mn_{0.5}Zr_{1.5}(MoO_4)_6$  (space group  $R\bar{3}c$ ) [28] and  $K_5Pb_{0.5}Zr_{1.5}(MoO_4)_6$  (space group  $R\bar{3}c$ ) [29], the crystal structure of  $K_5Cu_{0.5}Hf_{1.5}(MoO_4)_6$  can be described as a sequence of quasi-two-dimensional layers composed of  $(Cu1/Hf1)O_6$  octahedra and  $MoO_4$  tetrahedra. These layers are interconnected by  $(Cu2/Hf2)O_6$  octahedra and twelve-vertex  $K_{12}$  polyhedra (Figure 8). Thermal deformation in such framework

materials is commonly interpreted using the concept of rigid unit modes (RUMs). These modes represent collective vibrational patterns responsible for the correlated rotation of rigid bodies within the framework, where the connectivity between “rigid” polyhedra is facilitated by relatively flexible bridging oxygen atoms [35]. Within this framework, thermal expansion in the *ab*-plane is primarily governed by interactions between rigid  $Hf1O_6$  octahedra and  $MoO_4$  tetrahedra and the more flexible  $Cu1O_6$  octahedra. The expansion is driven by increasing deformation of  $Cu1-O$  bonds with temperature. The relatively weak anisotropy observed along the *c*-axis can be attributed to the presence of a greater number of deformable  $Cu2-O$  bonds in the interlayer space and the absence of rigid  $Mo-O$  linkages in this direction.

As shown in Table 8, the volumetric thermal expansion coefficient  $\alpha_v$  of  $K_5Cu_{0.5}Hf_{1.5}(MoO_4)_6$  reached  $45 \cdot 10^{-6} \text{ }^\circ\text{C}^{-1}$  at 500 °C, a value comparable to that of the isostructural zirconium analog  $K_5Mn_{0.5}Zr_{1.5}(MoO_4)_6$  and approximately 30% lower than that of  $K_5Pb_{0.5}Zr_{1.5}(MoO_4)_6$ . This magnitude of  $\alpha_v$  categorizes  $K_5Cu_{0.5}Hf_{1.5}(MoO_4)_6$  as a material exhibiting high thermal expansion [36].

**Fig. 8.** Projection of the  $K_5Cu_{0.5}Hf_{1.5}(MoO_4)_6$  crystal structure onto the *bc*-plane compared with cross sections of the thermal expansion tensor at 30, 150, 300, and 500 °C. Quasi-two-dimensional layers are highlighted by blue dashed lines

**Table 8.** Crystallographic parameters and thermal expansion coefficients of selected ternary molybdates with composition  $K_5A_{0.5}E_{1.5}(MoO_4)_6$  ( $A$  = divalent,  $E$  = tetravalent element) [28, 29]

Compound	$K_5Cu_{0.5}Hf_{1.5}(MoO_4)_6$	$K_5Mn_{0.5}Zr_{1.5}(MoO_4)_6$	$K_5Pb_{0.5}Zr_{1.5}(MoO_4)_6$
Space group	$R\bar{3}c$	$R\bar{3}c$	$R\bar{3}$
$a, \text{\AA}$	10.5617(2)	10.6026(1)	10.6604 (2)
$c, \text{\AA}$	37.5017(7)	37.6253(5)	37.9769 (9)
$V, \text{\AA}^3$	3622.9(1)	3663.0(1)	3737.6 (2)
$\alpha_a, \times 10^{-6} \text{ } ^\circ\text{C}^{-1}$ at 500 °C	9.8(3)	10.9(2)	11.3(1)
$\alpha_c, \times 10^{-6} \text{ } ^\circ\text{C}^{-1}$ at 500 °C	26(2)	22(2)	37(2)
$\alpha_v, \times 10^{-6} \text{ } ^\circ\text{C}^{-1}$ at 500 °C	45(2)	43.7(1)	59.8(1)
$\alpha_{\max}/\alpha_{\min}$ at 500 °C	2.7	2	3.3

Based on the results from HT-XRD and EIS (Section 3.5), the endothermic peak observed at 479 °C in the DSC curve is indicative of a first-order phase transition (Type I).

### 3.5. Electrical conductivity

The EIS profiles of  $K_5Cu_{0.5}Hf_{1.5}(MoO_4)_6$ , shown in Figure 5, displayed a single, high-frequency semicircle (or its segment at elevated temperatures, such as 500 °C, Figure 5). It represents the combined contribution of bulk and grain boundary conductivity. At lower frequencies, the plots exhibited a linear spike, indicative of ionic conduction and characteristic of the use of blocking electrodes.

The temperature dependence of the electrical conductivity of  $K_5Cu_{0.5}Hf_{1.5}(MoO_4)_6$  is presented in Figure 6. A sharp increase in conductivity was observed at 473 °C, coinciding with the endothermic peak at 479 °C on the DSC curve (Figure 4), and corresponding to a polymorphic phase transition. The cooling curve revealed a pronounced thermal hysteresis, consistent with a first-order phase transition.

Below the transition temperature, the activation energy  $E_a = 0.8$  eV, and the conductivity reaches  $2.4 \cdot 10^{-7}$  S/cm at 300 °C. Above the transition, the activation energy increased slightly to 0.9 eV, with the conductivity reaching  $7.5 \cdot 10^{-4}$  S/cm at 550 °C.

## 4. Conclusion

A novel ternary molybdate  $K_5Cu_{0.5}Hf_{1.5}(MoO_4)_6$  was successfully synthesized via solid-state reaction, expanding the family of isostructural compounds with the general formula  $M_5^I M_{0.5}^{II} M_{1.5}^{IV}(MoO_4)_6$ . The sequence of chemical

transformations leading to the formation of the potassium–copper–hafnium molybdate from a stoichiometric mixture of simple molybdates was elucidated. The compound's thermal stability was evaluated, and its crystal structure was refined using the Rietveld method within the trigonal space group  $R\bar{3}c$ . The coordination environment of molybdenum atoms was confirmed by ATR-FTIR spectroscopy, which revealed characteristic vibrational bands of  $MoO_4$  tetrahedra. HT-XRD analysis demonstrated that  $K_5Cu_{0.5}Hf_{1.5}(MoO_4)_6$  exhibited pronounced thermal expansion, categorizing it as a high thermal expansion material. The compound's ion-conducting properties were also investigated, with conductivity reaching  $7.5 \cdot 10^{-4}$  S/cm at 550 °C with an activation energy of  $E_a = 0.9$  eV. Combined evidence from HTXRD and EIS indicated that the endothermic effect observed at 479 °C in the DSC curve corresponded to a first-order phase transition.

## Contribution of the authors

The authors contributed equally to this article.

## Conflict of interests

The authors declare that they have no known competing financial interests or personal relationships that could have influenced the work reported in this paper.

## References

1. Ben N. W., Ben R. A. Ferroelectric properties and alternative current conduction mechanisms of lithium rubidium molybdate. *Ionics*. 2019;25: 4003–4012. <https://doi.org/10.1007/s11581-019-02921-w>
2. Tsyrenova G. D., Pavlova E. T., Solodovnikov S. F., ... Lazoryak B. I. New ferroelastic  $K_2Sr(MoO_4)_2$ : synthesis, phase transitions, crystal and domain structures, ionic conductivity.

- ity. *Journal of Solid State Chemistry*. 2016;237: 64–71. <https://doi.org/10.1016/j.jssc.2016.01.011>
3. Spassky D., Vasil'ev A., Jamal M. U., ... Nagirnyi V. Temperature dependent energy transfer to  $Eu^{3+}$  emission centres in  $K_3Eu(MoO_4)_4$  crystals. *CrystEngComm*. 2024;26(8): 1106–1116. <https://doi.org/10.1039/d3ce01201h>
  4. Wang J., Luo L., Huang B., ... Wang J. The preparation and optical properties of novel  $LiLa(MoO_4)_2:Sm^{3+}, Eu^{3+}$  red phosphor. *Materials*. 2018;11(2): 297. <https://doi.org/10.3390/ma11020297>
  5. Loiko P., Pavlyuk A., Slimi S., ... Mateos X. Growth, spectroscopy and laser operation of monoclinic  $Nd:CsGd(MoO_4)_2$  crystal with a layered structure. *Journal of Luminescence*. 2021;231: 117793. <https://doi.org/10.1016/j.jlumin.2020.117793>
  6. Binish B., Durairaj M., Girisun Sabari T. C., Mani Rahulan K. Engineering the nonlinear optical properties of barium molybdate by doping  $Sn^{4+}$  ions for optical limiting device applications. *Ceramics International*. 2023;49(11): 17629–17638. <https://doi.org/10.1016/j.ceramint.2023.02.129>
  7. Nasri R., Larbi T., Amlouk M., Zid M. F. Investigation of the physical properties of  $K_2Co_2(MoO_4)_3$  for photocatalytic application. *Journal of Materials Science: Materials in Electronics*. 2018;29: 18372–18379. <https://doi.org/10.1007/s10854-018-9951-x>
  8. Chimitova O. D., Bazarov B. G., Bazarova J. G., ... Ehrenberg H. The crystal growth and properties of novel magnetic double molybdate  $RbFe_5(MoO_4)_7$  with mixed  $Fe^{3+}/Fe^{2+}$  states and 1D negative thermal expansion. *CrystEngComm*. 2021;23: 3297–3307. <https://doi.org/10.1039/D1CE00118C>
  9. Liu M., Zhang Y., Zou T., Garlea V. O., ... Liu J.-M. Antiferromagnetism of double molybdate  $LiFe(MoO_4)_2$ . *Inorganic Chemistry*. 2020;59: 8127–8133. <https://doi.org/10.1021/acs.inorgchem.0c00432>
  10. Grossman V. G., Molokeev M. S., Bazarov B. G., Bazarova J. G. Potassium and thallium conductors with a trigonal structure in the  $M_2MoO_4-Cr_2(MoO_4)_3-Hf(MoO_4)_2$  ( $M = K, Tl$ ) systems: synthesis, structure, and ionic conductivity. *Journal of Alloys and Compounds*. 2021;873: 159828. <https://doi.org/10.1016/j.jallcom.2021.159828>
  11. Savina A. A., Morozov V. A., Buzlukov A. L., ... Khaikina E. G. New solid electrolyte  $Na_9Al(MoO_4)_6$ : structure and  $Na^+$  ion conductivity. *Chemistry of Materials*. 2017;29: 8901–8913. <https://doi.org/10.1021/acs.chemmater.7b03989>
  12. Spiridonova T. S., Solodovnikov S. F., Molokeev M. S., ... Khaikina E. G. Synthesis, crystal structures, and properties of new acentric glaserite-related compounds  $Rb_7Ag_{5-3x}Sc_{2+x}(XO_4)_9$  ( $X = Mo, W$ ). *Journal of Solid State Chemistry*. 2022;305: 122638. <https://doi.org/10.1016/j.jssc.2021.122638>
  13. Solodovnikov S. F., Solodovnikova Z. A., Zolotova E. S., ... Kuchumov B. M. Nonstoichiometry in the systems  $Na_2MoO_4-MMoO_4$  ( $M = Co, Cd$ ), crystal structures of  $Na_{3.36}Co_{1.32}(MoO_4)_3$ ,  $Na_{3.13}Mn_{1.43}(MoO_4)_3$  and  $Na_{3.72}Cd_{1.14}(MoO_4)_3$ , crystal chemistry, compositions and ionic conductivity of alluaudite-type double molybdates and tungstates. *Journal of Solid State Chemistry*. 2017;253: 121–128. <https://doi.org/10.1016/j.jssc.2017.05.031>
  14. Kotova I. Y., Belov D. A., Stefanovich S. Y.  $Ag_{1-x}Mg_{1-x}R_{1+x}(MoO_4)_3$   $Ag^+$ -conducting nasicon-like phases, where  $R = Al$  or  $Sc$  and  $0 \leq x \leq 0.5$ . *Russian Journal of Inorganic Chemistry*. 2011;56: 1189–1193. <https://doi.org/10.1134/S0036023611080122>
  15. Buzlukov A. L., Fedorov D. S., Serdtsev A. V., ... Medvedeva N. I. Ion mobility in triple sodium molybdates and tungstates with a NASICON structure. *Journal of Experimental and Theoretical Physics*. 2022;134: 42–50. <https://doi.org/10.1134/S1063776122010071>
  16. Xu D., Zhang H., Pang L., ... Zhou D. Novel B-site scheelite structure ceramic  $Bi(Ge_{0.5}Mo_{0.5})O_4$  and its dielectric properties. *Journal of the American Ceramic Society*. 2023;106(11): 6675–6683. <https://doi.org/10.1111/jace.19282>
  17. Solodovnikov S. F., Gulyaeva O. A., Savina A. A., ... Denisova T. A. Molybdates and tungstates of the alluaudite family: crystal chemistry, composition, and ionic mobility. *Journal of Structural Chemistry*. 2022;63: 1101–1133. <https://doi.org/10.1134/S0022476622070071>
  18. Spiridonova T. S., Solodovnikov S. F., Molokeev M. S., ... Khaikina E. G. Synthesis, crystal structures, and properties of new acentric glaserite-related compounds  $Rb_7Ag_{(5-3x)}Sc_{(2+x)}(XO_4)_9$  ( $X = Mo, W$ ). *Journal of Solid State Chemistry*. 2022;305: 122638. <https://doi.org/10.1016/j.jssc.2021.122638>
  19. Bugaris D. E., Loe H.-C.  $Li_3Al(MoO_4)_3$ , a lyonsite molybdate. *Acta Crystallographica Section C Crystal Structure Communications*. 2012;C68: i34–i36. <https://doi.org/10.1107/S0108270112020513>
  20. Grossman V. G., Molokeev M. S., Bazarov B. G., Bazarova J. G. Synthesis and characterization of a new magnesium molybdates  $Tl_{1.85}M_{0.15}Mg_2(MoO_4)_3$  ( $M = K, Rb$ ) with a langbeinite type structure. *Solid State Sciences*. 2023;142: 107249. <https://doi.org/10.1016/j.solidstatesciences.2023.107249>
  21. Klevtsova R. F., Bazarova Zh. G., Glinskaya L. A., ... Fedorov K. N. Synthesis of ternary potassium, magnesium, and zirconium molybdates. The crystal structure of  $K_5(Mg_{0.5}Zr_{1.5})(MoO_4)_6$ . *Journal of Structural Chemistry*. 1994;35: 286–290. <https://doi.org/10.1007/BF02578278>
  22. Klevtsova R. F., Bazarova Zh. G., Glinskaya L. A., Bazarov B. G., Fedorov K. N., Klevtsov P. V. Crystal structure investigation of ternary molybdate  $K_5(Mn_{0.5}Zr_{1.5})(MoO_4)_6$ . *J Struct Chem*. 1995;36: 813–817. <https://doi.org/10.1007/BF02579674>
  23. Klevtsova R. F., Bazarov B. G., Glinskaya L. A., ... Bazarova Zh. G. Synthesis and X-ray study of single crystals of  $K_5(Cd_{0.5}Zr_{1.5})(MoO_4)_6$  triple molybdate. *J Struct Chem*. 2002;43: 939–943. <https://doi.org/10.1023/A:1023686325616>
  24. Grossman V. G., Molokeev M. S., Bazarova J. G., Bazarov B. G. High ionic conductivity of  $K_{5-x}Tl_x(Mg_{0.5}Hf_{1.5})(MoO_4)_6$  ( $0 \leq x \leq 5$ ) solid solutions. *Solid State Sciences*. 2022;134: 107027. <https://doi.org/10.1016/j.solidstatesciences.2022.107027>
  25. Bazarov B. G., Klevtsova R. F., Sarapulova A. E., Fedorov K. N., Glinskaya L. A., Bazarova Zh. G. Synthesis and crystal structure of ternary molybdate compound  $K_5Pb_{0.5}Hf_{1.5}(MoO_4)_6$ . *Journal of Structural Chemistry*. 2005;46: 756–760. <https://doi.org/10.1007/s10947-006-0197-8>
  26. Bazarov B. G., Sarapulova A. E., Klevtsova R. F., Glinskaya L. A., Fedorov K. N., Bazarova Zh. G. Synthesis, structure and vibration spectra of the triple molybdates  $Tl_5A_{0.5}Hf_{1.5}(MoO_4)_6$ ,  $A = Ca, Sr, Ba, Pb$ . *Journal of Alloys and Compounds*. 2008;448 (1–2): 325–330. <https://doi.org/10.1016/j.jallcom.2006.11.086>

27. Aksenov S. M., Pavlova E. T., Popova N. N., Tsyrenova G. D., Lazoryak B. I. Stoichiometry and topological features of triple molybdates  $A_xB_yC_z(MoO_4)_n$  with the heteropolyhedral open MT-frameworks: synthesis, crystal structure of  $Rb_5\{Hf_{1.5}Co_{0.5}(MoO_4)_6\}$ , and comparative crystal chemistry. *Solid State Sciences*. 2024;151: 107525. <https://doi.org/10.1016/j.solidstatesciences.2024.107525>

28. Kovtunets E. V., Tushinova Yu. L., Logvinova A. V., Bazarova Ts. T., Bazarov B. G. Thermal expansion of ternary molybdate  $K_5[Mn_{0.5}Zr_{1.5}](MoO_4)_6$ . *ESSUTM Bulletin*. 2024;3(94): 90–97. [https://doi.org/10.53980/24131997\\_2024\\_3\\_90](https://doi.org/10.53980/24131997_2024_3_90)

29. Kovtunets E. V., Spiridonova T. S., Tushinova Yu. L., Logvinova A. V., Bazarova Ts. T., Bazarov B. G. Thermal expansion and ionic conductivity of  $K_5Pb_{0.5}Zr_{1.5}(MoO_4)_6$ . *Proceedings of Universities. Applied Chemistry and Biotechnology*. 2024;14(4): 444–452. <https://doi.org/10.21285/achb.939> (In Russ.)

30. ICDD PDF-2 Database, Cards № 01-072-0735, 01-073-0488, 01-077-0699, 01-083-2240.

31. Coelho A. A. TOPAS and TOPAS-Academic: an optimization program integrating computer algebra and crystallographic objects written in C++. *Journal of Applied Crystallography*. 2018;51: 210–218. <https://doi.org/10.1107/S1600576718000183>

32. Bubnova R. S., Firsova V. A., Filatov S. K. Software for determining the thermal expansion tensor and the graphic representation of its characteristic surface (theta to tensor-TTT). *Glass Physics and Chemistry*. 2013;39: 347–350. <https://doi.org/10.1134/S108765961303005X>

33. Klevtsova R. F., Glinskaya L. A., Pasechnyuk N. P. Crystal structure of the binary molybdates  $K_8Zr(MoO_4)_6$  and  $K_8Hf(MoO_4)_6$ . *Kristallografiya*. 1977;22: 1191–1195. (In Russ.)

34. Fomichev V. V., Poloznikova M. E., Kondratov O. I. Structural features and spectroscopic and energy characteristics of alkali metal molybdates and tungstates. *Russian Chemical Reviews* 1992;61(9): 877–888. <https://doi.org/10.1070/RC1992v061n09ABEH001004>

35. Petrushina M. Y., Korenev S. V., Dedova E. S., Gubanov A. I. Materials  $AM_2O_8$  (A = Zr, Hf; M = W, Mo) with negative thermal expansion. *J. Struct. Chem*. 2020;61: 1655–1680. <https://doi.org/10.1134/S0022476620110013>

36. Pet'kov V. I., Shipilov A. S., Sukhanov M. V. Thermal expansion of  $MZr_2(AsO_4)_3$  and  $MZr_2(TO_4)_x(PO_4)_{3-x}$  (M = Li, Na, K, Rb, Cs; T = As, V). *Inorganic Materials*. 2015;51(11): 1079–1085. <https://doi.org/10.1134/S002016851510012X>

## Information about the authors

*Evgeniy V. Kovtunets*, Cand. Sci. (Phys.–Math.), Researcher, Laboratory of Oxide Systems, Baikal Institute of Nature Management, Siberian Branch of the Russian Academy of Sciences (Ulan-Ude, Russian Federation).

<https://orcid.org/0000-0003-1301-1983>

[kovtunets@binm.ru](mailto:kovtunets@binm.ru)

*Tatiana S. Spiridonova*, Cand. Sci. (Chem.), Senior Researcher, Laboratory of Oxide Systems, Baikal Institute of Nature Management, Siberian Branch of the Russian Academy of Sciences (Ulan-Ude, Russian Federation).

<https://orcid.org/0000-0001-7498-5103>

[spiridonova@binm.ru](mailto:spiridonova@binm.ru)

*Yunna L. Tushinova*, Cand. Sci. (Chem.), Researcher, Laboratory of Oxide Systems, Baikal Institute of Nature Management, Siberian Branch of the Russian Academy of Sciences (Ulan-Ude, Russian Federation).

<https://orcid.org/0000-0003-1032-8854>

[tushinova@binm.ru](mailto:tushinova@binm.ru)

*Tsyrendyzhit T. Bazarova*, Cand. Sci. (Chem.), Lead Engineer, Laboratory of Oxide Systems, Baikal Institute of Nature Management, Siberian Branch of the Russian Academy of Sciences (Ulan-Ude, Russian Federation).

<https://orcid.org/0000-0001-9697-6320>

[basst@list.ru](mailto:basst@list.ru)

*Alexandra V. Logvinova*, Engineer, Laboratory of Oxide Systems, Baikal Institute of Nature Management, Siberian Branch of the Russian Academy of Sciences (Ulan-Ude, Russian Federation).

<https://orcid.org/0000-0001-9850-2719>

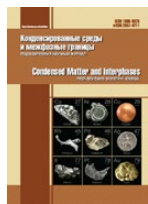
[logvinova\\_alexandra@bk.ru](mailto:logvinova_alexandra@bk.ru)

*Bair G. Bazarov*, Dr. Sci. (Phys.–Math.), Leading Researcher, Laboratory of Oxide Systems, Baikal Institute of Nature Management, Siberian Branch of the Russian Academy of Sciences (Ulan-Ude, Russian Federation).

<https://orcid.org/0000-0003-1712-6964>

[bazbg@rambler.ru](mailto:bazbg@rambler.ru)

*Received October 23, 2024; approved after reviewing November 11, 2024; accepted for publication November 15, 2024; published online September 25, 2025.*



## Original articles

Research article

<https://doi.org/10.17308/kcmf.2025.27/13015>

## Dielectric and piezoelectric properties of ceramic material based on modified lead zirconate titanate

L. N. Korotkov, N. A. Tolstykh, I. I. Popov✉, A. I. Bocharov, M. A. Kashirin

Voronezh State Technical University,  
20 let Oktyabrya st., 84, Voronezh 394006, Russian Federation

### Abstract

**Objective:** A new high-entropy ferroelectric material  $0.9\text{Pb}_{0.95}\text{Sr}_{0.05}(\text{Zr}_{0.52}\text{Ti}_{0.48})\text{O}_3-0.05\text{Pb}(\text{Zn}_{1/3}\text{Nb}_{2/3})\text{O}_3-0.05\text{Pb}(\text{Mn}_{1/3}\text{Sb}_{2/3})\text{O}_3$  was synthesized. At room temperature, it has a tetragonal perovskite-like crystal lattice and is characterized by a high electromechanical quality factor.

**Experimental:** The dielectric properties were studied in the temperature range of 20–500 °C at frequencies of 0.5–500 kHz. A noticeable decrease in the temperature of the ferroelectric phase transition ( $T_m$ ) in comparison with the base composition  $\text{Pb}_{0.95}\text{Sr}_{0.05}(\text{Zr}_{0.52}\text{Ti}_{0.48})\text{O}_3$  and its diffusion were revealed.

**Conclusions:** Analysis of experimental data suggests that the material under study is an “intermediate link” between conventional and relaxor ferroelectrics.

**Keywords:** High-entropy ferroelectrics, Electromechanical quality factor, Permittivity, Diffuse phase transition, Dielectric relaxation

**Funding:** This work was funded by Russian Science Foundation according to the research project No. 24-22-20054.

**For citation:** Korotkov L. N., Tolstykh N. A., Popov I. I., Bocharov A. I., Kashirin M. A. Dielectric and piezoelectric properties of ceramic material based on modified lead zirconate titanate. *Condensed Matter and Interphases*. 2024;25(1): 000-000. *Condensed Matter and Interphases*. 2025;27(3): 391–397. <https://doi.org/10.17308/kcmf.2025.27/13015>

**Для цитирования:** Коротков Л. Н., Толстых Н. А., Попов И. И., Бочаров А. И., Каширин М. А. Диэлектрические и пьезоэлектрические свойства керамического материала на основе модифицированного цирконата-титаната свинца. *Конденсированные среды и межфазные границы*. 2024;26(1): 391–397. <https://doi.org/10.17308/kcmf.2025.27/13015>

✉ Ivan I. Popov, e-mail: [popovich\\_vano@mail.ru](mailto:popovich_vano@mail.ru)

© Korotkov L. N., Tolstykh N. A., Popov I. I., Bocharov A. I., Kashirin M. A., 2025



The content is available under Creative Commons Attribution 4.0 License.

## 1. Introduction

To create some electronic devices (piezoelectric resonators, filters), materials with a high electromechanical quality factor are required. They are produced on the basis of hard ferroelectric ceramics with a homogeneous fine-grained structure and small dissipation of elastic and electric energy over a wide frequency range. Despite the fairly wide range of piezoelectric materials with a high quality factor at present, research aimed at improving their technical characteristics continues.

In recent years, the interest of researchers in the so-called high-entropy materials and, in particular, in high-entropy ferroelectrics has noticeably increased [1]. These materials are distinguished by the fact that in their crystal lattice a certain position can be randomly occupied by various ions with different ionic radii and charge states. For example, in the  $0.9\text{Pb}_{0.95}\text{Sr}_{0.05}(\text{Zr}_{0.52}\text{Ti}_{0.48})\text{O}_3 - 0.05\text{Pb}(\text{Zn}_{1/3}\text{Nb}_{2/3})\text{O}_3 - 0.05\text{Pb}(\text{Mn}_{1/3}\text{Sb}_{2/3})\text{O}_3$  perovskite solid solution studied in this work, the “A” sublattice is randomly occupied by  $\text{Pb}^{2+}$  and  $\text{Sr}^{2+}$  cations, and the “B” sublattice is randomly occupied by  $\text{Zr}^{4+}$ ,  $\text{Ti}^{4+}$ ,  $\text{Zn}^{2+}$ ,  $\text{Nb}^{5+}$ ,  $\text{Mn}^{2+}$ ,  $\text{Sb}^{5+}$  cations. High configurational entropy can lead to the following effects [1]: stabilization of new materials, causing significant lattice distortions, preventing grain coarsening, etc. High-entropy ferroelectric materials are widely used in energy storage devices [2, 3], electronic memory devices [1], and piezoelectric transducers [4–7] due to their unique physical properties.

It was shown [7] that the introduction of several cations with different valences and ionic radii can lower the local crystallographic symmetry and, thus, increase the misorientation of the polarization vector relative to the crystal axes. A high-entropy crystal structure can exhibit the so-called flexible polarization, when the crystallographic symmetry restrictions are violated and some rotation of the polarization relative to the “allowed” directions under an electric field becomes possible. Despite the fact that a fairly wide range of high-entropy piezoelectric ceramics currently exists [4–7], including ceramics with a high electromechanical quality factor, a detailed analysis of the dielectric properties in the vicinity of the ferroelectric phase transition has not been carried out.

In this regard, the aim of this work was to synthesize and to investigate the dielectric response of a new high-entropy ferroelectric ceramic material in the vicinity of the ferroelectric phase transition and to study its piezoelectric properties.

## 2. Experimental

High-entropy ferroelectric ceramics PMZN–PZT [4], PZTM [5], and PZT–PMS–PZN [6] with high electromechanical quality factors were chosen as prototypes of the material synthesized in this work. The synthesized compound has the general formula  $0.9\text{Pb}_{0.95}\text{Sr}_{0.05}(\text{Zr}_{0.52}\text{Ti}_{0.48})\text{O}_3 - 0.05\text{Pb}(\text{Zn}_{1/3}\text{Nb}_{2/3})\text{O}_3 - 0.05\text{Pb}(\text{Mn}_{1/3}\text{Sb}_{2/3})\text{O}_3 + 0.1 \text{ mol. \% CeO}_2$  (PSZT–PZN–PMS). It is evident from the general formula that the main component of the studied ceramics is a lead zirconate – titanate solid solution, and its composition corresponds to the morphotropic phase boundary. Cerium dioxide localized predominantly at grain boundaries [8] was added to prevent grain growth.

The studied samples were obtained using standard two-stage ceramic technology. Powders of  $\text{PbO}$ ,  $\text{ZrO}_2$ ,  $\text{TiO}_2$ ,  $\text{MnO}_2$ ,  $\text{MgO}$ ,  $\text{Nb}_2\text{O}_5$ ,  $\text{ZnO}$ ,  $\text{Sb}_2\text{O}_3$ , and  $\text{SrCO}_3$  taken in a given stoichiometric ratio were used as initial components in the synthesis. The material was synthesized at a temperature of 850 °C. The powder of the synthesized material was ground in a solution of polyvinyl alcohol in a mortar until the alcohol solution was completely dry. The samples were sintered in an air atmosphere at a temperature of 1100 °C.

X-ray phase analysis (Fig. 1) performed on a Bruker D2 Phaser X-ray diffractometer with  $\text{CuK}\alpha$  radiation showed that the obtained samples have a slightly distorted tetragonal lattice of perovskite  $P4mm$  with parameters  $a \approx 4.068 \text{ \AA}$  and  $c \approx 4.086 \text{ \AA}$ . Another phase with an undefined structure is present in an insignificant volume along with the tetragonal phase.

The samples for studying the dielectric and piezoelectric properties had the shape of a disk with a diameter of 11 mm and a thickness of 1 mm. Silver conductive paste was applied to the flat surfaces of the samples, then dried and fired at a temperature of 770 °C. Dielectric measurements were carried out on an E7-20 immittance meter at frequencies of 500 Hz – 500 kHz in the temperature range of 20–500 °C.

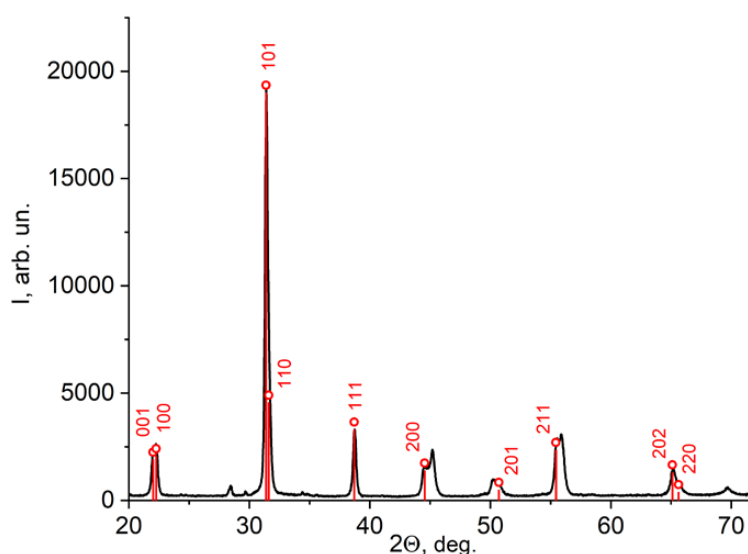


Fig. 1. X-ray diffraction pattern of the studied material

during slow heating (cooling) of the sample at a rate of about 2 °C/min. The temperature was controlled by an alumel – chromel thermocouple with an error of no more than  $\pm 0.5$  °C.

The samples for measuring the piezoelectric response were polarized at 120 °C in a DC electric field of 3 kV/mm for 30 minutes. The piezoelectric modulus  $d_{31}$ , the electromechanical coupling coefficient  $K_p$ , and the mechanical quality factor  $Q_m$  were measured at room temperature using the resonance-antiresonance method described in [9].

The microstructure of the samples was examined using a Tescan MIRA 3 scanning electron microscope. The fracture morphology of the sample is shown in Fig. 2. It can be seen that the material has a uniform microstructure with grain sizes of about 2  $\mu\text{m}$ .

### 3. Results and discussion

Studies of the piezoelectric properties of the material showed that at  $T \approx 23$  °C it had a relatively high mechanical quality factor of  $Q_m \approx 1095$ . The electromechanical coupling coefficient  $K_p \approx 0.29$  and the piezoelectric modulus  $d_{31} \approx 55$  pC/N had relatively low values, which is typical for ferroelectric ceramics with an increased electromechanical quality factor [9].

Let us discuss the dielectric properties of the synthesized material, which largely determine its piezoelectric activity. The temperature dependences of the permittivity ( $\epsilon'$ ) obtained by

heating the unpolarized sample passed through an almost symmetrical maximum in the vicinity of the temperature  $T_{mh} \approx 260$  °C (Fig. 3). This temperature is noticeably lower than in the base composition  $\text{Pb}_{0.95}\text{Sr}_{0.05}(\text{Zr}_{0.52}\text{Ti}_{0.48})\text{O}_3$ , where it is about 320 °C [9].

On the cooling curve, the maximum  $\epsilon'$  was observed at a temperature of  $T_{mc} \approx 257$  °C (insert on the right in Fig. 3). The existence of a

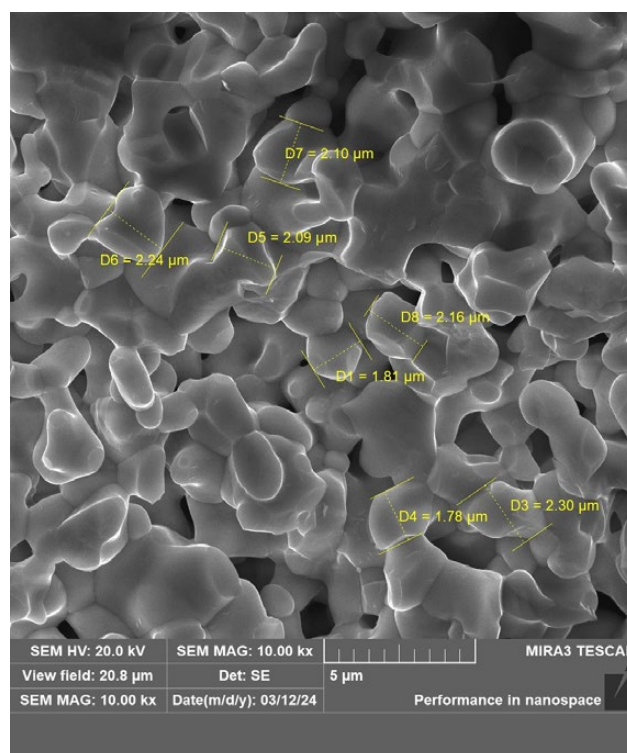
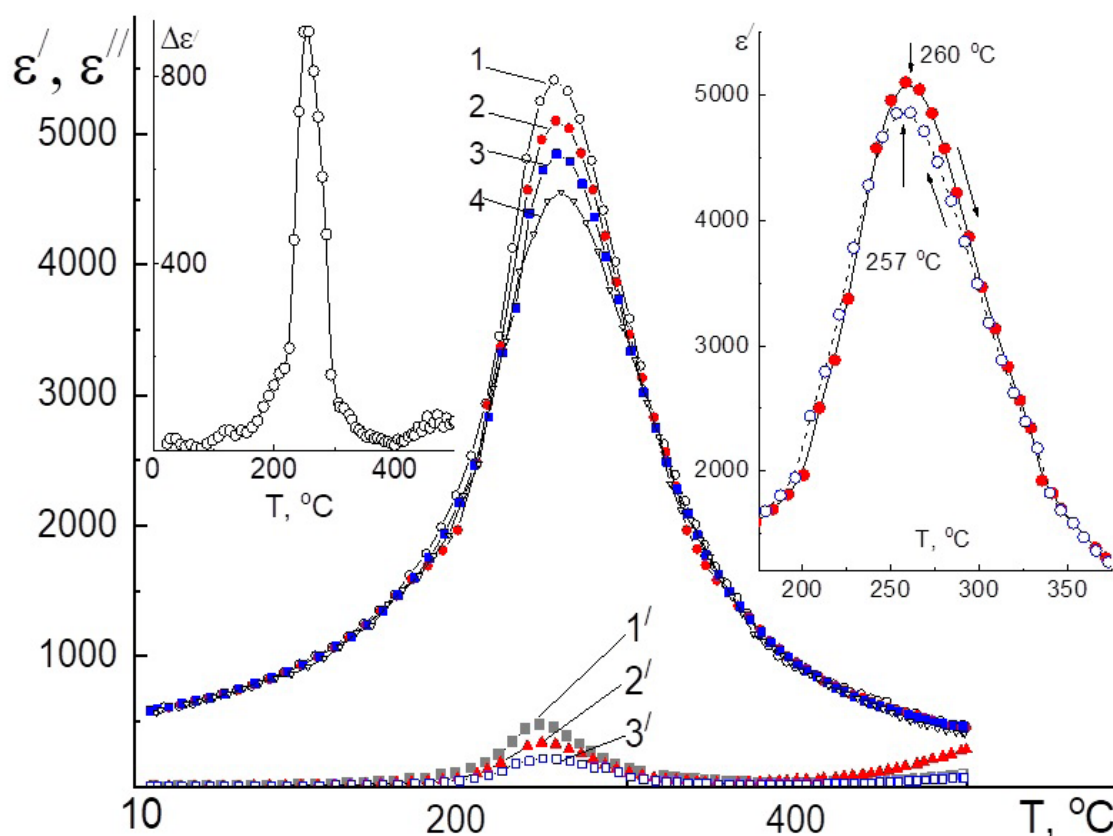


Fig. 2. SEM image of sintered ceramics



**Fig. 3.** Temperature dependences of real (1 – 4) and imaginary (1'–3') parts of dielectric permittivity obtained at frequencies 0.5 (1 and 1'), 2 (2 and 2'), 10 (3 and 3') and 500 (4) kHz during sample heating. The inset on the left shows the  $\Delta\epsilon'(T)$  dependence. The inset on the right shows the  $\epsilon'(T)$  dependences obtained during heating and cooling at a frequency of 2 kHz

temperature hysteresis of the permittivity in the material under study indicates that it underwent a first-order phase transition.

Note, however, that the detected temperature hysteresis  $\epsilon'$  differed from the characteristic hysteresis of permittivity observed for canonical ferroelectrics, such as  $\text{BaTiO}_3$ ,  $\text{KNbO}_3$ , and others, in which hysteresis phenomena are localized in the region of the phase transition and in the polar phase [9, 10]. In this case,  $\epsilon'(T_{\text{mh}}) < \epsilon'(T_{\text{mc}})$ . In the case under consideration, the hysteresis  $\epsilon'$  extended by more than 50 °C into the paraelectric phase. In this case,  $\epsilon'(T_{\text{mh}}) > \epsilon'(T_{\text{mc}})$ .

Further analysis of the experimental data showed that the  $\epsilon'(T)$  dependences follow the Curie–Weiss law in the vicinity of the phase transition [10]:

$$\epsilon'(T) = \epsilon_{\infty} + \frac{C_1}{T - \theta_1}, \text{ at } T > T_m \quad (1a)$$

and

$$\epsilon'(T) = \epsilon_{\infty} + \frac{C_2}{\theta_2 - T}, \text{ at } T < T_m. \quad (1b)$$

Here  $\epsilon_{\infty}$  is the temperature-independent component of the permittivity,  $C_i$  is the Curie–Weiss constant,  $\theta_i$  is the Curie–Weiss temperature.

The linear dependencies  $1/\epsilon'(T)$  shown in Fig. 4a confirm the applicability of relations (1a) and (1b) to describe the temperature dependences of permittivity in both ferroelectric and paraelectric phases. The best approximation of the experimental results by the Curie–Weiss law was achieved with following parameter values:  $C_1 \approx 86555 \text{ K}$ ,  $\theta_1 \approx 310 \text{ °C}$ ,  $C_2 \approx 146263 \text{ K}$ ,  $\theta_2 \approx 260 \text{ °C}$ . The values of the constants  $C_1$  and  $C_2$  are of the order of  $\sim 10^5 \text{ K}$ , which is typical for a ferroelectric phase transition of the displacement type.

Note that the temperature  $\theta_1 \approx 310 \text{ °C}$  is higher than  $T_{\text{mh}} \approx 260 \text{ °C}$  and the ratio of constants  $C_1/C_2 \approx 0.59$  in the studied material. This contradicts the phenomenological theory of first-order

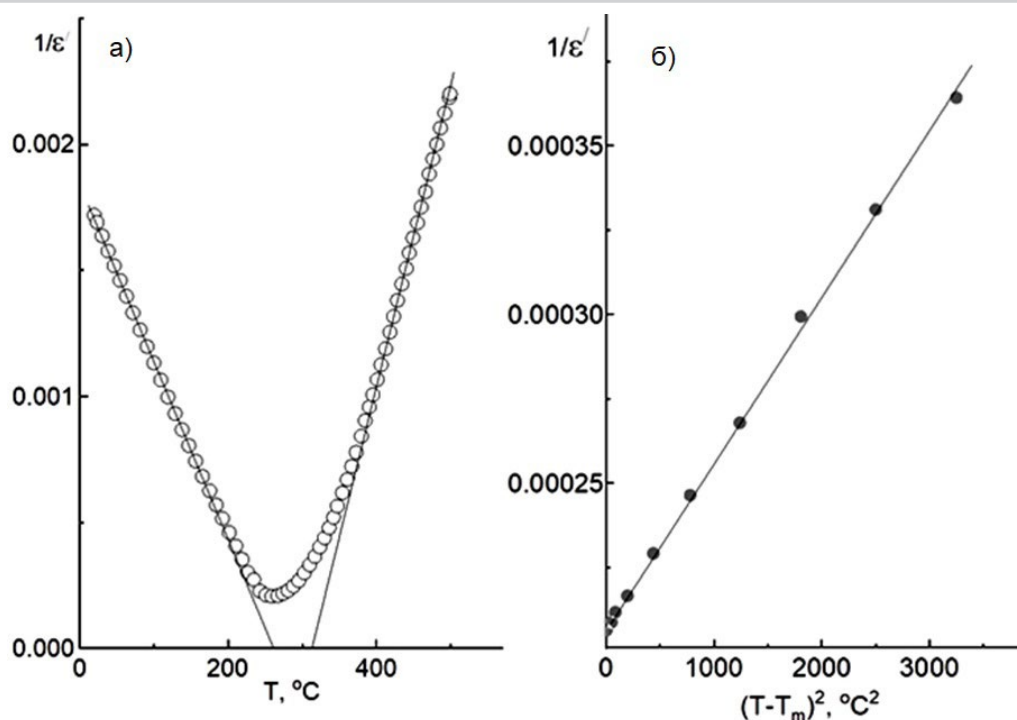


**Fig. 4.** Temperature dependences of the permittivity, plotted at the coordinates  $1/\epsilon'(T)$  (a) and at the coordinates  $1/\epsilon'(T-T_m)^2$  (b)

ferroelectric phase transitions [10], according to which  $C_1/C_2 \approx 4$  and  $\theta_1 < T_m$ . This is probably due to the high degree of phase transition diffusion. Indeed, ferroelectrics with a diffuse phase transition are characterized by a bell-shaped maximum of the permittivity [10] and the fulfillment of the inequality  $\theta_1 \geq T_m$ . It is interesting to note that in the case under consideration  $\theta_1$  differs slightly from the Curie temperature of the base composition  $\text{Pb}_{0.95}\text{Sr}_{0.05}(\text{Zr}_{0.52}\text{Ti}_{0.48})\text{O}_3$ .

The study of the causes of phase transition diffusion is one of the main areas in the research of disordered ferroelectrics. Currently, a number of models explain this phenomenon [10–14]. The most obvious is the model proposed by V. A. Isupov and G. A. Smolensky, where the ferroelectric phase transition diffusion is associated with composition fluctuations [10]. The phase transformation in different microregions of the crystal occurs at different temperatures due to the microscopic inhomogeneity of the material and is accompanied by a broadening of the maximum  $\epsilon'$ . According to the fluctuation model, the temperature dependence of the permittivity near  $T_m$  is determined by the expression [10]:

$$\frac{1}{\epsilon'} = \frac{1}{\epsilon'_m} + \frac{(T_m - T)^2}{2\epsilon'_m \sigma^2}, \quad (2)$$

where  $\epsilon'_m$  is the dielectric permittivity value at temperature  $T_m$ ,  $\sigma$  is the transition diffusion parameter meaning the standard deviation of the local Curie temperature. The dependence  $1/\epsilon'(T-T_m)^2$  should be linear according to expression (2), which is indeed observed in the temperature range  $T_m \leq T \leq T_d$  (Fig. 4b). Here  $T_d$  is the Burns temperature, where the dependence  $\epsilon'(T)$  begins to deviate from the Curie-Weiss law upon cooling from the paraelectric phase. The estimate of the dependence  $\epsilon'(T)$  made according to expression (2) yielded  $\sigma \approx 64^\circ\text{C}$  and  $T_d \approx 400^\circ\text{C}$ .

A characteristic feature of ferroelectrics with a diffuse phase transition is a strong dispersion of the permittivity in the vicinity of  $T_m$  and the dependence of the temperature  $T_m$  on the frequency of the measuring field. Studies of the dielectric response at different frequencies revealed a strong dispersion of  $\epsilon'$  (Fig. 3), the depth of which was determined as  $\Delta\epsilon' \approx \epsilon'(500\text{ Hz}) - \epsilon'(500\text{ kHz})$ . It was found that the maximum of  $\Delta\epsilon'$  is observed in the region of the diffuse ferroelectric phase transition at a temperature of approximately  $7^\circ\text{C}$  below

$T_m$ . The width of the  $\Delta\epsilon'(T)$  dependence at half height is about 55 °C and is close in value to the diffusion parameter  $\sigma \approx 64$  °C. This suggests that the experimentally observed  $\epsilon'$  dispersion may be due to the dynamics of polar microregions in accordance with the approaches proposed for relaxor ferroelectrics [10, 11, 13, 14].

Above  $T_m$ , the value of  $\Delta\epsilon'$  decreases rapidly as the Burns temperature  $T_d \approx 400$  °C is approached, where it reaches a minimum. The growth of  $\Delta\epsilon$  observed at  $T > T_d$  is apparently associated with an increase in electrical conductivity. The small depth of the permittivity dispersion at temperatures significantly below  $T_m$  indicates a low mobility of ferroelectric domain boundaries.

The temperature dependence of the imaginary part of the dielectric permittivity  $\Delta\epsilon''$  slightly below  $T_m$  passes through a maximum (Fig. 3), which shifts toward higher temperatures with increasing measurement frequency, as in the case of relaxor ferroelectrics. However, unlike the latter, the maximum of  $\epsilon''$  noticeably decreases with increasing frequency of the measurement field  $f$ .

The temperature dependence of the characteristic time of dielectric relaxation near  $T_m$ , determined from the frequency shift of the maximum  $\epsilon''$ , was approximated by both the Arrhenius equation and the empirical Vogel–Fulcher–Tammann equation [15], but in both cases the obtained values of the parameters (pre-exponential factor and activation energy) go beyond the physically reasonable values.

Thus, the observed dielectric relaxation requires further study. However, it is assumed that the experimentally observed dispersion of the dielectric response near  $T_m$  is due to several dielectric relaxation mechanisms, as in the case considered in [16].

#### 4. Conclusions

A hard ferroelectric high-entropy ceramic  $0.9\text{Pb}_{0.95}\text{Sr}_{0.05}(\text{Zr}_{0.52}\text{Ti}_{0.48})\text{O}_3 - 0.05\text{Pb}(\text{Zn}_{1/3}\text{Nb}_{2/3})\text{O}_3 - 0.05\text{Pb}(\text{Mn}_{1/3}\text{Sb}_{2/3})\text{O}_3 + 0.1 \text{ mol. \% CeO}_2$  with a comparatively high electromechanical quality factor  $Q_m \approx 1095$  was synthesized. It was found that the introduction of complex additives,  $\text{Pb}(\text{Zn}_{1/3}\text{Nb}_{2/3})\text{O}_3$  and  $\text{Pb}(\text{Mn}_{1/3}\text{Sb}_{2/3})\text{O}_3$ , into a solid solution based on the base composition,  $\text{Pb}_{0.95}\text{Sr}_{0.05}(\text{Zr}_{0.52}\text{Ti}_{0.48})\text{O}_3$ , leads to a noticeable

decrease in the ferroelectric phase transition temperature ( $T_m$ ) and its diffusion. With cyclic temperature changes in the vicinity of  $T_m$ , an anomalously wide temperature hysteresis of the permittivity was observed, which extended into both the ferroelectric and paraelectric phases.

Near  $T_m$ , the  $\epsilon'(T)$  dependences are satisfactorily described by the so-called quadratic Curie–Weiss law with a phase transition diffusion parameter of  $\sigma \approx 64$  °C. Analysis of the dispersion of the dielectric response showed that the dispersion depth  $\Delta\epsilon'$  reaches its greatest values near the permittivity maximum in the temperature range of the s order. The nature of the  $\epsilon'$  and  $\epsilon''$  dispersion near  $T_m$  differs qualitatively from that observed for relaxor ferroelectrics and is apparently due to the action of several mechanisms.

Based on the totality of the results obtained, it can be stated that the studied material is an “intermediate link” between conventional and relaxor ferroelectrics. Its composition can be considered as a base for the development of piezoceramics with increased electromechanical quality factor.

#### Contribution of the authors

The authors contributed equally to this article.

#### Conflict of interests

The authors declare that they have no known competing financial interests or personal relationships that could have influenced the work reported in this paper.

#### References

1. Yang B., Liu Y., Lan S., ... Lin Y. H. High-entropy design for dielectric materials: status, challenges, and beyond. *Journal of Applied Physics*. 2023;133(11): 110904. <https://doi.org/10.1063/5.0138877>
2. Palneedi H., Peddigari M., Hwang G. T., Jeong D. Y., Ryu J. High-performance dielectric ceramic films for energy storage capacitors: progress and outlook. *Advanced Functional Materials*. 2018;28(42): 1803665. <https://doi.org/10.1002/adfm.201803665>
3. Zhou S., Pu Y., Zhang X., ... Wang D. High energy density, temperature stable lead-free ceramics by introducing high entropy perovskite oxide. *Chemical Engineering Journal*. 2022;427(1): 131684. <https://doi.org/10.1016/j.cej.2021.131684>
4. Hou Y. D., Zhu M. K., Tian C. S., Yan H. Structure and electrical properties of PMZN–PZT quaternary. *Sensors and Actuators A: Physical*. 2004;116(3): 455–460. <https://doi.org/10.1016/j.sna.2004.05.012>

5. He L. X., Li, C. E. Effects of addition of MnO on piezoelectric properties of lead zirconate titanate. *Journal of Materials Science*. 2000;35(1): 2477–2480. <https://doi.org/10.1023/A:1004717702149>
6. Li H., Yang Z., Wei L., Chang Y. Effect of ZnO addition on the sintering and electrical properties of (Mn,W)-doped PZT–PMS–PZN ceramics. *Materials Research Bulletin*. 2009;44(3): 638–643. <https://doi.org/10.1016/j.materres-bull.2008.06.024>
7. Liu Y., Yang J., Deng S.,... Chen J. Flexible polarization configuration in high-entropy piezoelectrics with high performance. *Acta Materialia*. 2022;236(1): 118115. <https://doi.org/10.1016/j.actamat.2022.118115>
8. Tu L. L., Jin Y. Y., Han M. Z. Piezoelectric ceramic transformer. *Ferroelectrics*. 1980;28(1): 403–406. <https://doi.org/10.1080/00150198008227120>
9. Jaffe B., Cook W. R., Jaffe H. *Piezoelectric ceramics*. Academic Press, London and New York, 1971. 317 p.
10. Smolensky G. A., Bokov V. A., Isupov V. A., Krainik N. N., Pasynkov R. E., Shur M. S. *Ferroelectrics and antiferroelectrics*\*. Leningrad: Nauka Publ., 1971. 476 p. (In Russ.)
11. Bokov A. A. Recent advanced in diffuse ferroelectric phase transitions. *Ferroelectrics*. 1992;131(1): 49–55. <https://doi.org/10.1080/00150199208223391>
12. Cross L. E. Relaxor ferroelectrics: an overview. *Ferroelectrics*. 1994;151(1): 305–320. <https://doi.org/10.1080/00150199408244755>
13. Glinchuk M. D., Farhi R. A random field theory-based model for ferroelectric relaxors. *Journal of Physics: Condensed Matter*. 1996;8(37): 6985–6996. <https://doi.org/10.1088/0953-8984/8/37/019>
14. Pirc R., Blinc R. Spherical random-bond–random-field model of relaxor ferroelectrics. *Physical Review B*. 1999;60(19): 13470–13478. <https://doi.org/10.1103/PhysRevB.60.13470>
15. Feltz A. *Amorphe und glasartige anorganische festkörper*. Berlin: Akademie – Verlag; 1983. 480 p. <https://doi.org/10.1515/9783112611463> (In German)
16. Korotkov L. N., Rogova S. P., Pavlova N. G. Dielectric properties of  $(1-x)[0.7\text{PbZrO}_3 - 0.3\text{K}_{0.5}\text{Bi}_{0.5}\text{TiO}_3] - x\text{SrTiO}_3$  solid solutions in the vicinity of phase transitions, *Tech. Phys.* 1999;44(3): 295–298. <https://doi.org/10.1134/1.1259240>

\* Translated by author of the article

#### Information about the authors

**Leonid N. Korotkov**, Dr. Sci. (Phys.–Math), Professor at the Department of Solid-State Electronics, Voronezh State Technical University (Voronezh, Russian Federation). <https://orcid.org/0000-0002-5350-5841>  
l\_korotkov@mail.ru

**Nikita A. Tolstykh**, Cand. Sci. (Phys.–Math.), Head of the Scientific and Educational Laboratory «Functional Materials», Voronezh State Technical University (Voronezh, Russian Federation). <https://orcid.org/0000-0001-5994-9331>  
mad\_nik@bk.ru

**Ivan I. Popov**, Cand. Sci. (Phys.–Math.), Senior Lecturer at the Department of Solid-State Electronics, Voronezh State Technical University (Voronezh, Russian Federation). <https://orcid.org/0000-0002-1183-0662>  
popovich\_vano@mail.ru

**Alexey I. Bocharov**, Leading Engineer of the BREС «Thermoelectric Phenomena», Voronezh State Technical University (Voronezh, Russian Federation). <https://orcid.org/0000-0003-4812-9586>  
lekha.bocharoff@yandex.ru

**Maxim A. Kashirin**, Engineer of the Scientific and Educational Laboratory «Functional Materials, Voronezh State Technical University (Voronezh, Russian Federation). <https://orcid.org/0000-0003-0150-0317>  
mnitro@yandex.ru

Received September 10, 2024; approved after reviewing October 7, 2024; accepted for publication October 15, 2024; published online September 25, 2025.



# Condensed Matter and Interphases

Kondensirovannye Sredy i Mezhfaznye Granitsy  
<https://journals.vsu.ru/kcmf/>

## Original articles

Research article

<https://doi.org/10.17308/kcmf.2025.27/13016>

## Mechanical properties of Li-Nb-O system films

A. V. Kostyuchenko<sup>1✉</sup>, E. K. Belonogov<sup>1,2</sup>, V. M. Ievlev<sup>1,2,3</sup>, A. E. Nikonov<sup>1</sup>, E. A. Osipov<sup>1</sup>,  
P. A. Osipov<sup>1</sup>

<sup>1</sup>Voronezh State Technical University,  
20 let Oktyabrya st., 84, Voronezh 394006, Russian Federation

<sup>2</sup>Voronezh State University,  
1, University pl., Voronezh 394018, Russian Federation

<sup>3</sup>Moscow State University,  
1, Leninskie Gory, Moscow 119991, Russian Federation

### Abstract

**Objective:** To quantitatively assess the hardness, elasticity, and plasticity of Li-Nb-O system films and to determine the influence of the structure and substructure on these parameters in them.

**Experimental:** Li-Nb-O system films with a thickness of ~0.8 μm were grown on non-heated substrates (oxidized single-crystal silicon wafers (SiO<sub>2</sub> layer ~0.4 μm), single-crystal lithium niobate with (0001) orientation) by ion beam sputtering of a lithium niobate target. Thermal annealing of Li-Nb-O films on substrates was performed in air for 10 min (until complete crystallization) at temperatures of 550, 650, 700, 750, 800, and 850 °C. The heterostructures (film/substrate) were cooled with a furnace. The phase composition of the films was investigated by X-ray diffraction (XRD) and selected area electron diffraction (SAED). The substructure was studied by transmission electron microscopy (TEM) and high-resolution TEM (HRTEM, Tecnai G2 30ST) of cross-sectional specimens prepared by ion milling using a Quanta 3D setup. The surface morphology was investigated by scanning electron microscopy (SEM, Teskan Mira) in the topological contrast mode and atomic force microscopy (AFM, Solver47). The mechanical properties, hardness (H) and Young's modulus (E), were determined from nanoindentation (NI, NanoHardness Tester CSM Instruments) measurements using a Berkovich diamond indenter under the following conditions: maximum load 10 mN, loading rate 10 mN/min, and unloading rate 15 mN/min.

**Results:** It was found that thermal annealing in an oxygen-containing atmosphere at 750°C induces the crystallization of quasi-amorphous Li-Nb-O films and the synthesis of single-phase LN films with lattice parameters closest to those of stoichiometric single-crystal LN. The most probable mechanisms of irreversible deformation in LN films are: brittle fractures, plastic deformation of crystallites, and grain boundary sliding. LN films synthesized at 650-750°C are most susceptible to brittle fracture. Brittle fractures occur due to the buildup of macrostresses in the films, resulting from different coefficients of thermal expansion (CTE) of the film and the substrate. The fracture toughness of the films increases significantly when using a substrate with a CTE close to that of the film. The hardness of nano- and microcrystalline LN films is always higher than the hardness of quasi-amorphous Li-Nb-O system films. The decrease in the hardness of films synthesized at high annealing temperatures is due to a decrease in the concentration of point defects and an increase in the size of the crystallites.

**Keywords:** Thin film, Lithium niobate, Thermal annealing, Crystallization, Structure, Surface morphology, Nanoindentation, Hardness, Cracking

**Funding:** The study was financially supported by the Russian Science Foundation as part of scientific project No. 24-22-20046.

**Acknowledgments:** Scanning electron microscopy studies were performed using equipment at the Basic Scientific and Educational Center "Physics and Technology of Thermoelectric Phenomena" of Voronezh State Technical University.

**For citation:** Kostyuchenko A. V., Belonogov E. K., Ievlev V. M., Nikonov A. E., Osipov E. A., Osipov P. A. Mechanical properties of Li-Nb-O films. *Condensed Matter and Interphases*. 2025;27(3): 398–408. <https://doi.org/10.17308/kcmf.2025.27/13016>

✉ Alexander V. Kostyuchenko, e-mail: [av-kostuchenko@mail.ru](mailto:av-kostuchenko@mail.ru)

© Kostyuchenko A. V., Belonogov E. K., Ievlev V. M., Nikonov A. E., Osipov E. A., Osipov P. A., 2025



The content is available under Creative Commons Attribution 4.0 License.

**Для цитирования:** Костюченко А. В., Белоногов Е. К., Иевлев В. М., Никонов А. Е., Осипов Е. А., Осипов П. А. Механические свойства пленок системы Li-Nb-O. *Конденсированные среды и межфазные границы*. 2025;27(3): 398–408. <https://doi.org/10.17308/kcmf.2025.27/13016>

## 1. Introduction

To realize the potential of lithium niobate (LN,  $\text{LiNbO}_3$ ) thin films as a functional material in optoelectronic [1], acoustoelectronic [2], and memory devices [3], it is necessary to develop an understanding of the deformation mechanism, mechanical properties, and prospects for bringing the functional parameters of thin films closer to those of single-crystal LN. Elastic properties, hardness, plasticity, surface morphology, and macro- and microstresses in the near-surface layer of LN films significantly affect electrical conductivity, sound velocity, acoustic wave attenuation [4, 5], electromechanical conversion efficiency, and optical transmittance [6, 7]. A large number of studies have been devoted to the regularities of LN film growth on substrates, as well as structural and substructural transformations in LN films as a result of various influences, in particular, thermal processing [8, 9, 10]. There are several works devoted to the study of the mechanical properties of LN single crystals. For example, in [11], nanoindentation results established that the hardness (H) and Young's modulus (E) of single-crystal LN wafers are ~12 and 194 GPa, respectively, for the X-cut, and 13 and 211 GPa for the Z-cut. In [12, 13], transmission electron microscopy (TEM) was used to observe dislocations in LN single crystals deformed at high temperatures, showing the dislocation mechanism of plastic deformation of LN. There are isolated works concerning the influence of thermal stresses on the structure and substructure of LN films. In particular, the dislocation mechanism of macrostress relaxation in epitaxial heterostructures with large mismatch in composition, structure, and thermal stresses arising from different coefficients of thermal expansion was established by the authors of [14] and [15]. In [16], the change in the lattice parameters of epitaxial LN films on sapphire as a result of thermal stresses is considered. At the same time, there is practically no data on the dependence of mechanical properties (hardness, Young's modulus, contribution of elastic and plastic components to deformation) of Li-Nb-O

system films on structure, phase composition, and substructure; there is no systematic data necessary to identify the mechanism of stress relaxation in Li-Nb-O system films arising during synthesis and subsequent thermal processing.

The purpose of this work is to quantitatively assess the hardness, elasticity, and plasticity, and to determine the influence of structure and substructure on these parameters in Li-Nb-O system films.

## 2. Experimental

Li-Nb-O system films with a thickness of ~0.8  $\mu\text{m}$  were grown on non-heated substrates (oxidized single-crystal silicon wafers ( $\text{SiO}_2$  layer ~0.4  $\mu\text{m}$ ) and single-crystal lithium niobate with (0001) orientation) by ion beam sputtering of a lithium niobate target. Sputtering conditions: working gas – argon; ion beam current 90 mA; ion source electrode voltage 2.2 kV; a compensator system eliminates the shielding potential on the substrate. The distance from the target to the substrate during deposition was 10 cm.

Thermal annealing (TA) of Li-Nb-O/ $\text{SiO}_2$ /Si heterostructures was performed in air in a coaxial furnace for 10 min (until complete crystallization) at temperatures of 550, 650, 700, 750, 800, and 850 °C. Samples were loaded into the heated furnace. The heterostructures were left to cool in the furnace at a cooling rate of 300 °C/h.

The phase composition of the films was investigated by X-ray diffraction (XRD) using a Bruker D2 Phaser diffractometer (copper tube radiation) and selected area electron diffraction (SAED) using an EG-100M electron diffraction camera. The substructure was studied by transmission electron microscopy (TEM) and high-resolution TEM (HRTEM, Tecnai G2 30ST) of cross-sectional specimens prepared by ion milling using a Quanta 3D setup. The surface morphology was investigated by scanning electron microscopy (SEM, Teskan Mira) in topological contrast mode and atomic force microscopy (AFM, Solver47). The mechanical properties, hardness (H) and Young's modulus (E), were determined from nanoindentation (NI, NanoHardness Tester CSM

Instruments) measurements using a Berkovich diamond indenter under the following conditions: maximum load 10 mN, loading rate 10 mN/min, and unloading rate 15 mN/min.

### 3. Results and discussion

**Phase Composition.** According to XRD data (Fig. 1, diffractogram 1), the Li-Nb-O system films after deposition were X-ray amorphous or quasi-amorphous, in accordance with the terminology previously adopted in [17]. After isochronal annealing (Fig. 1, diffractograms 2–4), single-phase LN films crystallized (Fig. 1, curves 2, 3, 4). The single-phase composition of LN films was maintained throughout the used range of

crystallization annealing temperatures. Profile analysis (Rietveld method) of XRD diffraction peaks showed an increase in the LN lattice parameters  $a$  and  $c$  with increasing annealing temperature (Table 1). The relative increase in the parameters was  $\sim 0.5\%$ , which corresponds to a relative change in the volume of the unit cell of the crystal lattice by 1.1% with a method error of less than 0.1%. The significant increase in the lattice parameters was the result of oxygen diffusion into the LN lattice and a decrease in the concentration of oxygen vacancies. It follows from Table 1 that after thermal annealing at 750 °C and above, the volume of the crystal lattice was closest to the lattice volume of single-crystal

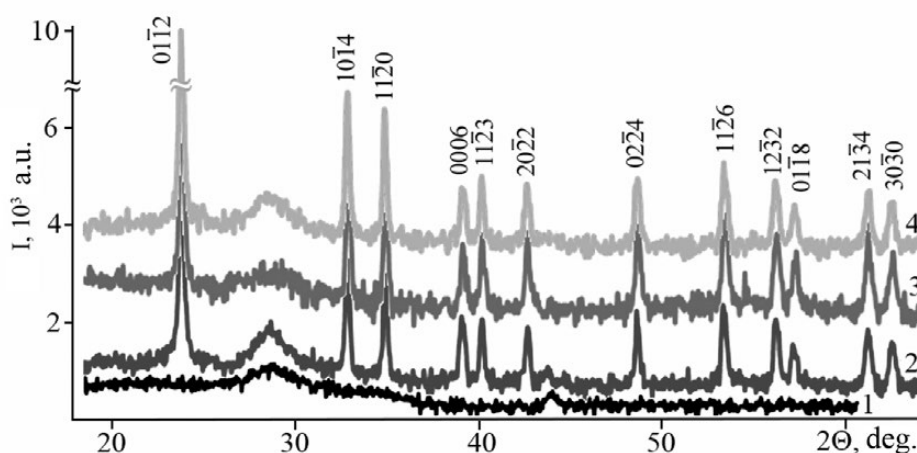


**Fig. 1.** X-ray diffraction of the Li-Nb-O/SiO<sub>2</sub> heterostructure before (1) and after annealing at temperatures of 550 (2), 750 (3), and 850 °C (4)

**Table 1.** Lattice parameters of lithium niobate for single crystal and polycrystalline films on the surface of oxidized silicon and single crystal LN orientation (0001) after TA at different temperatures (°C) of annealing

Substrate	TA, °C	$a$ , Å	$c$ , Å	$(V-V_0)/V_0$ , %
(001) Si/SiO <sub>2</sub>	550	5.132	13.775	–1.3
	650	5.142	13.805	–0.7
	700	5.144	13.819	–0.5
	750	5.151	13.835	–0.1
	800	5.159	13.842	0.2
	850	5.156	13.843	0.1
(0001) LN	550	5.1316	13.785	–1.2
	650	5.1314	13.795	–1.2
	750	5.1328	13.798	–1.1
	800	5.1362	13.798	–1.0
	850	5.1395	13.799	–0.8

$V$  – available lattice volume

$V_0$  – lattice volume of single-crystal LN [18]

Lattice parameters of single-crystal LN:  $a = 5.149$  Å,  $c = 13.862$  Å [18]

LN [18], which indicates a chemical composition closest to stoichiometric LN. An estimate of the average size of LN crystallites on the surface of oxidized silicon by the Scherrer method showed their growth from 25 to 75 nm throughout the entire range of annealing temperatures (Table 2). The most significant increase in crystallite size was observed during annealing at 850 °C (from 25 to 75 nm). The highest rate of crystallite growth (i.e., the change in size per degree) was observed in the temperature range from 550 to 650 °C. With a fixed annealing time, the observed evolution of the film structure with increasing temperature is probably associated with the sequential activation of various grain growth mechanisms. Thus, the rapid growth of crystallites in the range up to 650 °C may be due to collective recrystallization, while the additional increase in their size at 800 and 850 °C is likely associated with secondary recrystallization.

To assess the change in lattice parameters under conditions of minimal macrostresses, the crystal lattice of lithium niobate films obtained on a single-crystal LN was investigated. Fig. 2 shows XRD patterns of films obtained on the surface of (0001) LN single crystal. The diffractogram shows a complete set of maxima corresponding to the LN lattice. The observed increased intensity of the 0006 reflection indicates the formation of an axial texture  $\langle 0001 \rangle$  LN. In films after TA at 750 °C, the intensity of the 0006 reflection was maximal. A further increase in TA temperature

**Table 2.** Average grain size of LN after TA

Temperature TA, °C	550	650	700	750	800	850
Average grain size, nm	24	47	51	54	64	73

led to a decrease in the reflection intensity. The increase in the degree of texturing of the films was probably due to the influence of the substrate on the selective growth of grains oriented along the [0001] axis during the coalescence recrystallization stage. During the stage of secondary recrystallization, the relative proportion of oriented grains decreased. According to the profile analysis of diffraction peaks, the  $a$  and  $c$  lattice parameters of LN increased by 0.2% with increasing TA temperature from 550 to 850 °C. As in the case of films on the surface of oxidized silicon, the increase in lattice parameters was the result of oxygen diffusion into the LN lattice during TA. The smaller change in parameters compared to films on oxidized silicon can be explained by the absence of macrostresses associated with the difference in the coefficients of thermal expansion of the film and the substrate.

Fig. 3 shows TEM images and an SAED pattern of an ultrathin cross-section of an Li-Nb-O system film before annealing. There is no contrast on the TEM image (Fig. 3a) characteristic of regions of coherent scattering. On the HRTEM image (Fig. 3b), the contrast has a stochastic character. On the electron diffraction patterns obtained by the SAED method from various regions of the

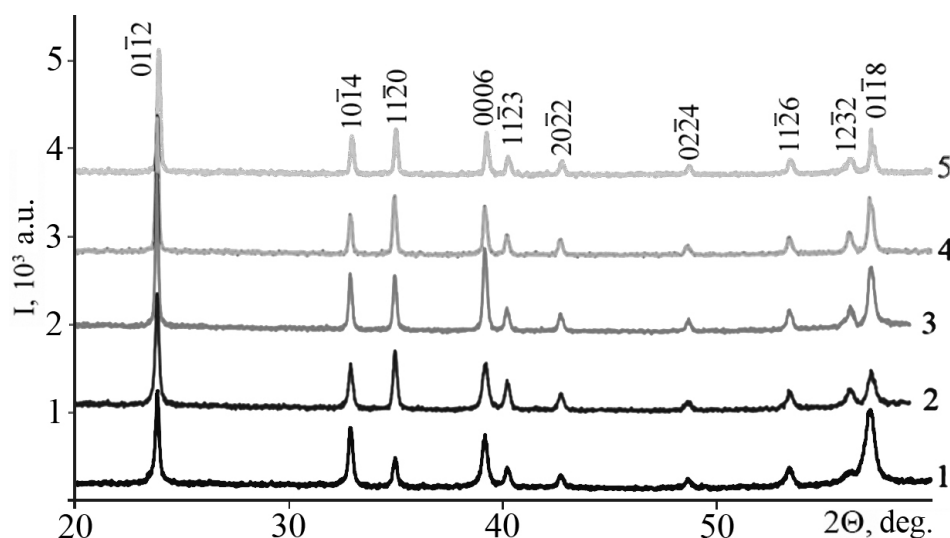


**Fig. 2.** X-ray diffraction of the Li-Nb-O/(0001)LN heterostructure after annealing at temperatures of 550 (1), 650 (2), 750 (3), 800 (4), and 850 °C (5)

film, there is always a characteristic halo (see inset in Fig. 3), indicating a quasi-amorphous structure of the initial Li-Nb-O system films. Figure 4 shows TEM images and an SAED pattern of an ultrathin cross-section of an Li-Nb-O system film after annealing at 550 °C. Regions of coherent scattering are clearly visible on the TEM image (Fig. 4a); the film has a nanocrystalline structure, with an average crystallite size of 40 nm. The HRTEM image (Fig. 4b) is dominated by a characteristic banded contrast with a period of 0.37 nm, corresponding to the period of the atomic planes (10 4) of the LN crystal lattice. Analysis of the electron diffraction pattern (inset in Fig. 4) also revealed a set of interplanar spacings characteristic of the LN lattice.

*Surface Morphology.* According to SEM data, an increase in the size of morphological inhomogeneities on the surface of the films as

a result of increasing TA temperature correlates with a change in the size of the crystallites, as established by TEM and XRD results (Fig. 6). Cracks were observed in all films on SiO<sub>2</sub>/Si substrates after annealing. Their formation is caused by macrostresses – a consequence of different coefficients of thermal expansion (CTE) of the film and the substrate: for silicon, the CTE is 5.1, and for LN it ranges from 5 to 15·10<sup>-6</sup> °C<sup>-1</sup> in the [10 0] and [0001] directions, respectively. Figures 5a and b show AFM images of the surface of LN films on the surface of oxidized silicon after TA at 550 and 800 °C. Table 3 contains parameters obtained by AFM hardware, characterizing the surface relief of quasi-amorphous (Li-Nb-O) and crystalline LN films on the surface of SiO<sub>2</sub>/Si. In films after annealing at 550 °C (Fig. 5a), the lateral dimensions of the relief inhomogeneities were 100 nm or more, and their height did not

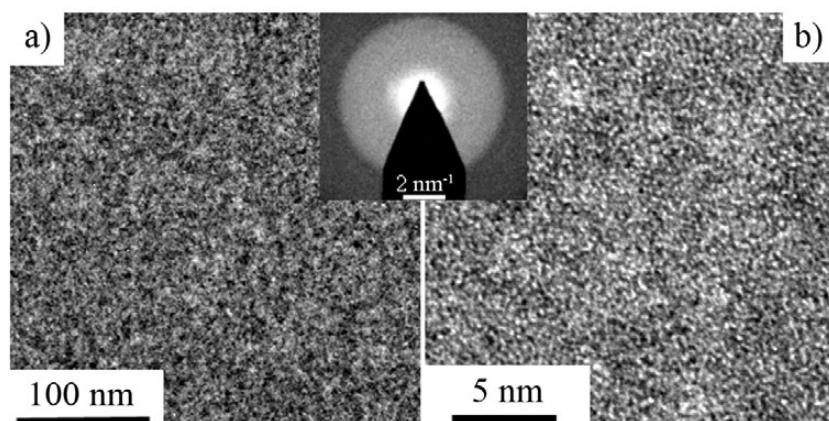


**Fig. 3.** TEM (a) and HRTEM (b) cross-section images of the Li-Nb-O film after deposition; inset shows a fragment of HEED

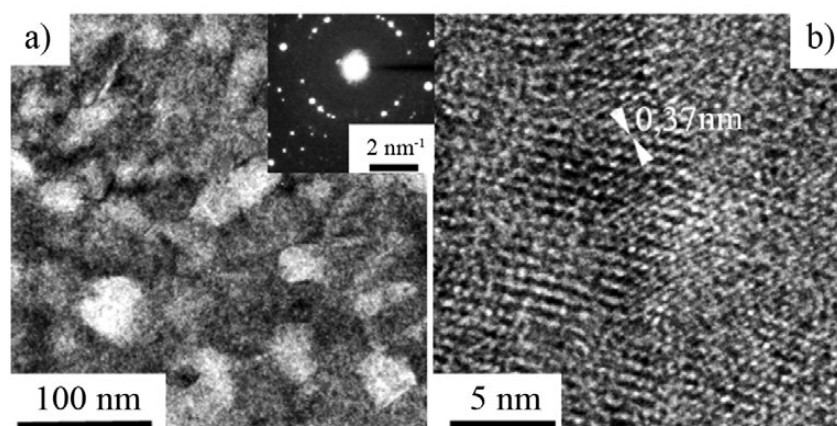


**Fig. 4.** TEM (a) and HRTEM (b) images of a cross-section of a Li-Nb-O film after annealing at 550 °C and a fragment of a HEED microelectron diffraction pattern

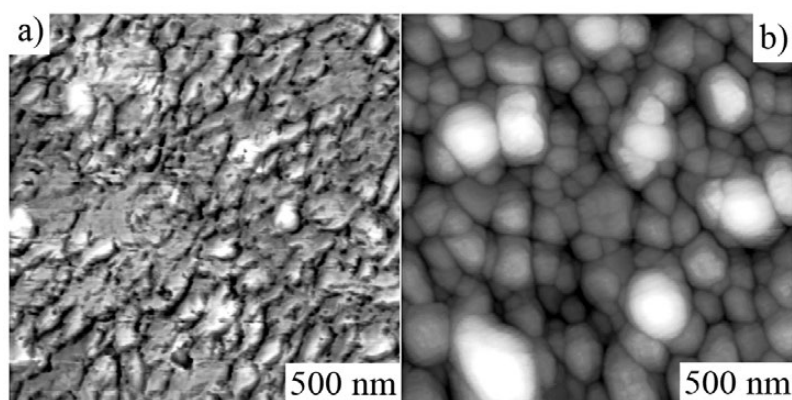


**Fig. 5.** AFM images of the surface of films annealed at 550 (a) and 800 °C (b) on the surface of SiO<sub>2</sub>/Si substrates

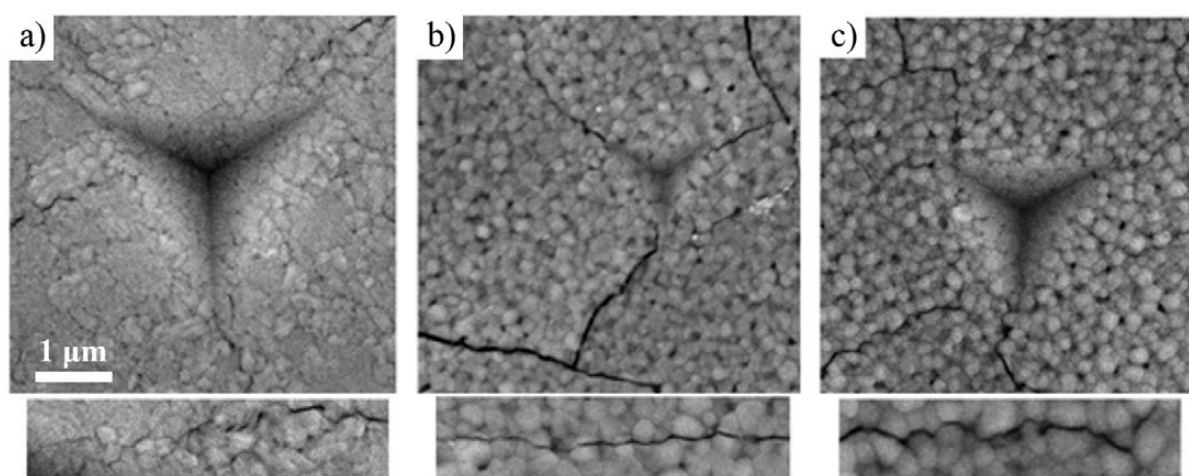


**Fig. 6.** SEM images of indenter imprints on the surface of films grown on SiO<sub>2</sub>/Si and annealed at 550 (a), 750 (b), and 800 °C (c) with an indenter load of 10, 1, and 10 mN, respectively

**Table 3.** Relief parameters of lithium niobate films on the surface of oxidized silicon before and after thermal annealing

Relief parameters	without annealing	550 °C	750 °C	800 °C
Height difference, nm	20	55	110	120
Average roughness, nm	4	15	20	20

exceed 50 nm, i.e., the film relief was markedly flat. After annealing at 800 °C (see Fig. 5b), the most probable lateral dimensions of the inhomogeneities were ~ 150 nm, their height was ~170 nm, and the roughness was 20 nm; therefore, the film relief reflects the dispersity of the crystallites. The most significant changes in the relief were observed with increasing crystallization temperature. The development of

the relief occurred due to an increase in protrusions (presumably, crystallites). After crystallization of quasi-amorphous films, their roughness increased sharply. The roughness of films crystallized at 650–850 °C was practically unchanged (~ 20 nm), and the relief height difference was invariably higher in films crystallized at higher temperatures. That is, the development of the relief occurred due to the selective growth of individual crystallites, but their volume fraction in the film is small. Morphological inhomogeneities after thermal annealing at 550 and 800 °C indicated, respectively, the nano- and microcrystalline structure of Li-Nb-O films.

Fig. 6 shows SEM images of indenter imprints that appeared on the surface of the film on SiO<sub>2</sub>/Si substrates as a result of the applied loads. The sizes of morphological inhomogeneities of the surface relief of the films after thermal

annealing correlate with the results of the study using AFM. In addition to cracks that occurred immediately after thermal annealing, additional cracks appear near the imprints after NI (Fig. 6). The minimum load on the indenter that can cause additional cracking of films annealed at 750 °C was 1 mN (Fig. 6b). The cracking of films annealed at other temperatures was observed only at higher loads on the indenter ( $> 1$  mN). If the load on the indenter was  $> 10$  mN, then the NI process initiated cracking of the film regardless of the annealing temperature (Fig. 6a, c). The nature of crack propagation in the films was different: 1) in films after annealing at 550 °C, as a rule, the cracks propagated along the grain boundaries; 2) after annealing at 750 °C they mainly propagated through the volume of grains; 3) after 800 °C they mainly propagated along the grain boundaries (insets in Fig. 6).

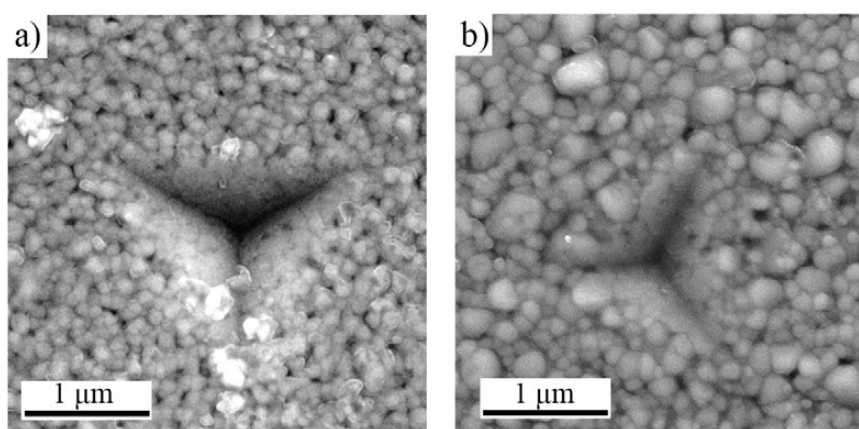
Fig. 7 shows SEM images of indenter imprints on films on the surface of (0001) LN single crystal after TA at 750 and 800 °C. Cracks in the films were not observed. Comparing the obtained result with the result for films on oxidized silicon, it can be argued that the nature of crack formation in lithium niobate films is primarily associated with macrostresses caused by the difference in CTEs of the film and the substrate.

**Elastic Modulus and Hardness.** The mechanical properties of the films after thermal annealing at different temperatures were studied by NI. Table 4 presents the results of measuring the hardness ( $H$ ), Young's modulus ( $E$ ), and the proportion of elastic deformation in the indentation work ( $\eta$ )

of films and single-crystal lithium niobate at a load on the indenter up to 1 mN. Fig. 8 shows P-h diagrams for annealed films and the surface of (0001) LN single crystal obtained by NI when the load on the indenter increased to 10 mN. The P-h diagrams of all samples, including the single crystal, have steps (highlighted in Fig. 8). Moreover, with increasing film annealing temperature, the minimum load for their appearance decreased.

According to [11], the hardness and Young's modulus of bulk single-crystal LN for the X-cut are 11.8 and 194 GPa, respectively. The experimental values of hardness and elastic moduli of Z-cuts of single crystals after technological machining are slightly lower (Table 4).

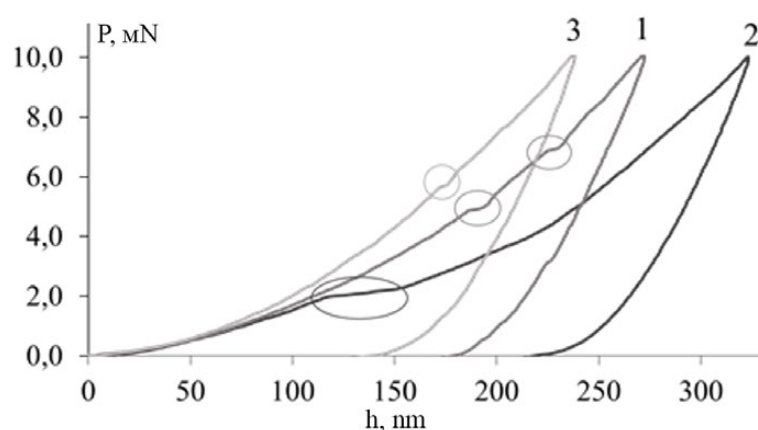
The hardness of quasi-amorphous Li-Nb-O films is lower than the hardness of nano- and microcrystalline LN films. Considering the low probability of implementing a dislocation mechanism of plastic deformation in such films and the absence of cracks in them, the most probable mechanism of plastic deformation is the movement of elementary structural clusters according to the mechanism described in [19] for hydroxyapatite ceramics and films. The hardness and elasticity of crystalline LN films on the  $\text{SiO}_2/\text{Si}$  surface also did not reach the values characteristic of a single crystal. A notable feature for the films is the decrease in the hardness of films annealed at temperatures of 650 and 750 °C compared to films annealed at 550 °C. Considering the minimum crack resistance of such films in a stressed state and the transcrystalline nature



**Fig. 7.** SEM images of indenter imprints on the surface of films grown on a (0001) LN single crystal, annealed at 750 (a) and 800 °C (b), with an indenter load of 10 mN

**Table 4.** Mechanical properties of lithium niobate

Substrate: Si/SiO <sub>2</sub>						
Temperature TA, °C	–	550	650	750	800	850
<i>H</i> , hPa	4.6	7.4	6.0	6.7	8.1	5.0
<i>E</i> , hPa	80.8	118.2	119.5	124.0	129.4	112.7
$\eta$ , %	31	38	34	35	36	30
Substrate: surface (0001) of LN single crystal						
Temperature TA, °C	–	550	650	750	800	850
<i>H</i> , hPa	6.2	10.3	9.3	7.9	7.7	6.9
<i>E</i> , hPa	115.5	144.5	155.0	154.1	128.3	134.7
$\eta$ , %	30	48	36	37	42	38
Single crystal LN (0001)						
<i>H</i> , hPa	8,5					
<i>E</i> , hPa	157					
$\eta$ , %	43					

**Fig. 8.** *P-h* diagrams obtained from the results of indentation of the Li-Nb-O/SiO<sub>2</sub>/Si heterostructure after annealing at 550 (1) and 850 °C (2) and of the surface (0001) LN single crystal (3); indenter load 10 mN

of their cracking, it is possible to assume a relationship between their strength properties and a structural feature: the greatest correspondence of the lattice parameters to single-crystal stoichiometric LN. This correspondence is probably due to the minimum content of point defects (primarily oxygen vacancies) inside the crystallites among the obtained films. This feature of the substructure leads to increased dislocation mobility and intragranular plasticity, which, combined with a minimum amount of impurities at the grain boundaries, contributes to the transcrystalline nature of crack propagation. In [20], it was shown that the scratching depth at which no crack formation was observed in a lithium niobate single crystal was 40 nm. The

indentation depth of the same order for our films corresponded to a load on the indenter of 1 mN. That is, in films annealed at 750 °C, the conditions for crack formation are similar to those for a single crystal. A further increase in the TA temperature leads to saturation of the boundaries with excess oxygen, weakening the intergranular bonds and promoting crack propagation mainly along the boundaries.

The Young's modulus (*E*) of LN films on the surface of (0001) LN single crystal after TA at 550–750 °C (with the greatest correspondence of lattice parameters to the single crystal) was closest to the value of *E* for the single crystal. The hardness of crystalline films on the surface of LN single crystal was maximal in the case

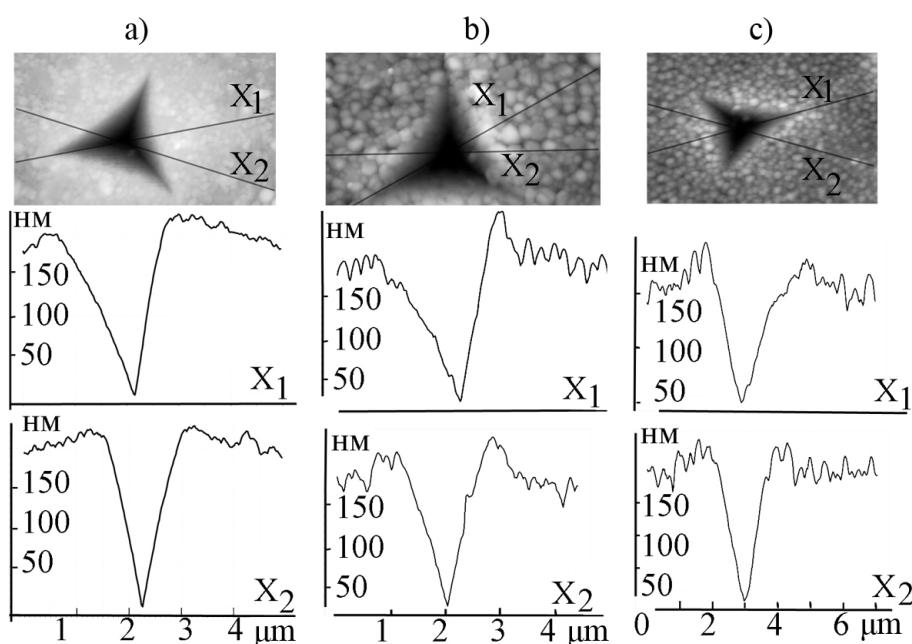
of a fine-grained structure, exceeding the hardness of the single crystal, and decreased with increasing temperature. The observed dependence of hardness, considering the absence of macrostresses in the films, was characteristic of materials with a dislocation mechanism of plastic deformation and corresponds to the Hall-Petch relationship [21].

Fig. 9 shows AFM images of indenter imprints on the surface of films grown on SiO<sub>2</sub>/Si, and profilograms in directions corresponding to the height (X1) and the center line (X2) of the triangular indenter imprint in the film plane. The indenter penetration depth is up to 200 nm, which is an order of magnitude greater than the roughness and four times less than the thickness of the tested film. The angle between the face and the opposite edge in the used indenter is 142°. Consequently, the aperture angle of the profilogram in the X1 direction will be 142° under the condition of absolute plasticity of the material. Considering elastic recovery, this angle will be slightly larger. Based on the geometry of the indenter, the left and right parts of the imprint profile in the X2 direction are absolutely symmetrical. It was found that the profiles of imprints in the X1 direction had an aperture angle of 154°, 152°, and 146° in films after annealing at

550, 750, and 800 °C, respectively (see Table 5). As can be seen from Table 5, in films after annealing at 550 °C, elastic recovery occurred equally in all directions. In contrast, in the film after annealing at 750 and 800 °C, the most significant elastic recovery occurred where the deforming effect was exerted by the indenter face, and not by the edge. This indicates a lower elasticity of the films annealed at higher temperatures, as well as the initiation of brittle fracture of the film by the indenter edges. The profiles of the imprints in the X2 direction do not differ, since the NI process does not cause brittle fractures of the film in this direction. As a result of indentation, heaping is formed at the edges of the imprints (Fig. 9). The surface of the heaping retains relief elements corresponding to the initial surface of the sample. According to SEM data, the relief elements inside the imprint also correspond to the initial surface (Figs. 6, 7). The observed relief indicates that plastic deformation was partially caused by the mechanism of intergranular sliding [19, 22]. In the most dispersed films, this mechanism is obviously dominant.

#### 4. Conclusion

Thus, thermal annealing in an oxygen-containing atmosphere at a temperature of



**Fig. 9.** AFM images of indenter imprints on the surface of films annealed at 550 (a), 750 (b), and 800 °C (c) and the corresponding profilograms in the X1 and X2 directions; indenter load 10 mN

**Table 5.** Geometry of the indenter imprint according to AFM data

Temperature TA, °C	550		750		800		Indenter angles	
Profile direction	X <sub>1</sub>	X <sub>2</sub>	X <sub>1</sub>	X <sub>2</sub>	X <sub>1</sub>	X <sub>2</sub>	X <sub>1</sub>	X <sub>2</sub>
Print Profile Angles, °	7	16	8	17	14	16	14	20
	<b>154</b>	148	<b>152</b>	146	<b>146</b>	148	<b>142</b>	135
	19	16	20	17	20	16	26	20

550–850 °C induces the crystallization of quasi-amorphous Li-Nb-O layers and the synthesis of single-phase LN films with a LN lattice. The lattice parameters of the films approach the parameters of single-crystal LN of a stoichiometric composition with increasing temperature. During the deformation of Li-Nb-O films, the most probable mechanisms are: brittle fractures, plastic deformation of crystallites, and grain boundary sliding. LN films synthesized at a temperature of 650–750 °C are most prone to brittle fractures. Brittle fractures occur due to the buildup of macrostresses in the films, resulting from different coefficients of thermal expansion of the film and the substrate. The crack resistance of the films increases significantly when using a substrate with a CTE close to that of the film. The hardness of nano- and microcrystalline LN films is always higher than the hardness of quasi-amorphous Li-Nb-O composition films. The decrease in the hardness of films synthesized at a high annealing temperature is due to a decrease in the concentration of point defects and an increase in the size of the crystallites.

### Contribution of the authors

The authors contributed equally to this article.

### Conflict of interests

The authors declare that they have no known competing financial interests or personal relationships that could have influenced the work reported in this paper.

### References

- Huang C. H. J., Rabson T. A. Low-loss thin-film LiNbO<sub>3</sub> optical waveguide sputtered onto a SiO<sub>2</sub>/Si substrate. *Optics Letters*. 1993;18(10): 811–813. <https://doi.org/10.1364/OL.18.000811>
- Xu H., Dong S., Xuan W., ... Luo J. Flexible surface acoustic wave strain sensor based on single crystalline LiNbO<sub>3</sub> thin film. *Applied Physics Letters*. 2018;112: 093502. <https://doi.org/10.1063/1.5021663>
- Jiang H., Dai C., Shen B., Jun J. High-performance LiNbO<sub>3</sub> domain wall memory devices with enhanced selectivity via optimized metal–semiconductor contact. *Nanomaterials*. 2024;14(12): 1031. <https://doi.org/10.3390/nano14121031>
- He J., Ye Z. Highly C-axis oriented LiNbO<sub>3</sub> thin film on amorphous SiO<sub>2</sub> buffer layer and its growth mechanism *Chinese Science Bulletin*. 2003;48: 2290–2294. <https://doi.org/10.1360/03ww0053>
- Maurel A., Mercier J.-F., Lund F. Lund scattering of an elastic wave by a single dislocation. *The Journal of the Acoustical Society of America*. 2004;115(6): 2773–2780. <https://doi.org/10.1121/1.1687735>
- Hewig G. M., Jain K., Sequeda F. O., Tom R., Wang P.-W. Sputtering of LiNbO<sub>3</sub>. *Thin Films Thin Solid Films*. 1982;88: 67–74. [https://doi.org/10.1016/0040-6090\(82\)90351-0](https://doi.org/10.1016/0040-6090(82)90351-0)
- Paldi R. L., Qi Z., Misra S., ... Wang H. Nanocomposite-seeded epitaxial growth of single-domain lithium niobate thin films for surface acoustic wave devices. *Advanced Photonics Research*. 2021;2: 2000149. <https://doi.org/10.1002/adpr.202000149>
- Ievlev, V. M., Belonogov E. K., Dybov V. A., ... Sumets M. P. Synthesis of lithium niobate during crystallization of amorphous Li–Nb–O film. *Inorganic Materials*. 2019;55(12): 1237–1241. <https://doi.org/10.1134/S0020168519120069>
- Shandilya S., Tomar M., Gupta V. Deposition of stress free c-axis oriented LiNbO<sub>3</sub> thin film grown on (002) ZnO coated Si substrate. *Journal of Applied Physics*. 2012;111: 10–16. <https://doi.org/10.1063/1.4714664>
- Fakhri M. A., Salim E. T., Hashim U., Abdulwahhab A. W., Salim Z. T. Annealing temperature effect on structural and morphological properties of nano photonic LiNbO<sub>3</sub>. *Journal of Materials Science: Materials in Electronics*. 2017;28: 16728–16735. <https://doi.org/10.1007/s10854-017-7586-y>
- Zhu N., Chen J., Zhou P., Zhu Y. Effect of the anisotropy mechanical properties on LN crystals fixed-abrasive lapping *Materials*. 2020;13(19): 4455. <https://doi.org/10.3390/ma13194455>
- Fries E., Péter A. Plastic deformation of LiNbO<sub>3</sub> single crystals *Revue de Physique Appliquée*. 1987;22(11): 1353–1359. <https://doi.org/10.1051/rphys-ap:0198700220110135300>
- Péter Á., Fries E., Rivière J. P. TEM observation of plastically induced dislocations in lithium niobate LiNbO<sub>3</sub> single crystals. *Physica Status Solidi (a)*. 1991;128(1): 45–53. <https://doi.org/10.1002/pssa.2211280106>
- Xie H., Lu Y.-C., Raj R. Transmission electron microscopy study of microstructure and misfit dislocations in epitaxial LiTaO<sub>3</sub> thin films grown on sapphire by a metalorganic chemical vapor deposition process *Journal of Applied Physics*. 1996;79(7): 3675–3680. <https://doi.org/10.1063/1.361197>

15. Veignant F., Gandais M., Aubert P., Guy G. Epitaxial growth of  $\text{LiNbO}_3$  on  $\alpha\text{Al}_2\text{O}_3$  (0001). *Thin Solid Films*. 1998;336:(1-2): 163–167. [https://doi.org/10.1016/S0040-6090\(98\)01222-X](https://doi.org/10.1016/S0040-6090(98)01222-X)

16. Bartasyte A., Plausinaitiene V., Abrutis A., ... Saltyte Z. Residual stresses and clamped thermal expansion in  $\text{LiNbO}_3$  and  $\text{LiTaO}_3$  thin films. *Applied Physics Letters*. 2012;101: 122902. <https://doi.org/10.1063/1.4752448>

17. Иевлев В. М., Канькин С. В., Костюченко А. В., Белогов Е. К., Путляев В. И. Об информативности рентгеновских дифрактограмм в виде гало. *Неорганические Материалы*. 2020;56(8): 906–913. <https://doi.org/10.31857/s0002337x20080059>

18. Shiozaki Y., Mitsui T. Powder neutron diffraction study of  $\text{LiNbO}_3$ . *Journal of Physics and Chemistry of Solids*. 1963;24: 1057–1061. [https://doi.org/10.1016/0022-3697\(63\)90012-x](https://doi.org/10.1016/0022-3697(63)90012-x)

19. Ievlev V. M., Kostyuchenko A. V., Darinskii B. M., Barinov S. M. Hardness and microplasticity of nanocrystalline and amorphous calcium phosphate coatings. *Physics of the Solid State*. 2014;56(2): 321–329. <https://doi.org/10.1134/s1063783414020127>

20. Nakamura M., Fujiyama H., Sumomogi T. Effects of material properties on ductile mode machining in ultra-precision grinding of lithium niobate. *Hiroshima International University Research Report*. 2012;45: 11–20. Available at: <https://xueshu.baidu.com/usercenter/paper/show?paperid=a25d14fe8a5e8d01a7d1aad2ec1c522e>

21. Hall E. O. Variation of hardness of metals with grain size. *Nature*. 1954;173: 948–949. <https://doi.org/10.1038/173948b0>

22. Kim B.-N., Hiraga K., Sakka Y., Ahn B.-W. A grain-boundary diffusion model of dynamic grain growth during superplastic deformation. *Acta Materialia*. 1999;47(12): 3433–3439. [https://doi.org/10.1016/s1359-6454\(99\)00201-3](https://doi.org/10.1016/s1359-6454(99)00201-3)

## Information about the authors

*Aleksandr V. Kostyuchenko*, Cand. Sci. (Phys.–Math.), Associate Professor, Department of Solid State Electronics, Voronezh State Technical University (Voronezh, Russian Federation).

<http://orcid.org/0000-0002-0049-3664>

[av-kostuchenko@mail.ru](mailto:av-kostuchenko@mail.ru)

*Evgeny K. Belonogov*, Dr. Sci. (Phys.–Math.), Professor, Department of Physics, Voronezh State Technical University (Voronezh, Russian Federation).

<http://orcid.org/0000-0002-0216-0986>

[ekbelonogov@mail.ru](mailto:ekbelonogov@mail.ru)

*Valentin M. Ievlev*, Full Member of the Russian Academy of Sciences, Dr. Sci. (Phys.–Math.), Professor, Head of the Department of Interdisciplinary Materials Science, Lomonosov Moscow State University (Moscow, Russian Federation).

<http://orcid.org/0000-0002-3205-2580>

[rnilme@mail.ru](mailto:rnilme@mail.ru)

*Alexander E. Nikonov*, Cand. Sci. (Phys.–Math.), Researcher of the Functional Materials Laboratory, Voronezh State Technical University (Voronezh, Russian Federation).

<http://orcid.org/0009-0000-0852-2303>

[nikonov.sasha1994@gmail.com](mailto:nikonov.sasha1994@gmail.com)

*Evgeny A. Osipov*, student, Department of Solid State Electronics, Voronezh State Technical University (Voronezh, Russian Federation).

<http://orcid.org/0009-0002-1209-3833>

[sanr1ze1@mail.ru](mailto:sanr1ze1@mail.ru)

*Pavel A. Osipov*, student, Department of Solid State Electronics, Voronezh State Technical University (Voronezh, Russian Federation).

<http://orcid.org/0009-0003-3891-2646>

[rejmefun@mail.ru](mailto:rejmefun@mail.ru)

Received December 11, 2024; approved after reviewing June 18, 2025; accepted for publication July 15, 2025; published online September 25, 2025.



# Condensed Matter and Interphases

Kondensirovannye Sredy i Mezhfaznye Granitsy  
<https://journals.vsu.ru/kcmf/>

## Original articles

Research article

<https://doi.org/10.17308/kcmf.2025.27/13017>

## Synthesis of 2-alkyl-5-phenyl-4,5,6,7-tetrahydro-[1,2,4]triazolo[1,5-a]pyrimidin-7-ol derivatives from vegetable oils and their efficiency as inhibitors of hydrochloric acid corrosion of steel

A. A. Kruzhilin✉, D. S. Shevtsov, I. A. Dmitriev, M. A. Potapov, Kh. S. Shikhaliev

Voronezh State University

1 Universitetskaya pl., Voronezh, 394018, Russian Federation

### Abstract

**Objective:** The study suggests a new method of synthesis of 2-alkyl-5-phenyl-4,5,6,7-tetrahydro-[1,2,4]triazolo[1,5-a]pyrimidin-7-ol derivatives from vegetable oils (sunflower, palm, and coconut oil).

**Experimental:** The novelty of the method is based on the use of renewable raw materials, i.e. vegetable oils. It is also a *one-pot* synthesis method, which involves oil hydrolysis, interaction of the resulting *in situ* fatty acids with aminoguanidine bicarbonate and the subsequent alkaline cyclization to a mixture of 3-alkyl-5-amino-1H-1,2,4-triazoles whose composition is further identified by means of HPLC/MS. During the second stage of the synthesis, the obtained triazole mixtures undergo a two-stage condensation with cinnamaldehyde in the presence of an amphoteric surfactant, resulting in the desired 2-alkyl-5-phenyl-4,5,6,7-tetrahydro-[1,2,4]triazolo[1,5-a]pyrimidin-7-ols of sunflower, palm, and coconut oils. The anti-corrosion properties of the synthesized triazolopyrimidinols were studied with regard to ST-3 steel in 24% HCl using direct (GOST 9.905-82, GOST 9.907-83) and electrochemical (potentiodynamic polarization, Mansfeld method) methods. All derivatives exhibited high anticorrosive activity at concentrations of 1–2 g/l. The most effective were coconut oil derivatives: the protection degree (Z) reached 92.6% (1 g/l) and 98.0% (2 g/l) according to mass loss measurements, and 97.2–97.4% according to polarization measurements ( $i_{\text{cor}}$  decreased to 0.026–0.028 mA/cm<sup>2</sup> as compared to 6.8 mA/cm<sup>2</sup> in the control experiment).

**Conclusions:** The study demonstrated that the high efficiency of coconut oil derivative mixture is associated with the high content of medium-chain fatty acid derivatives (C10–C14, of which ~50% are lauric acid residues) in its composition. The obtained compounds are promising environmentally friendly inhibitors of acid corrosion that can be used in the oil industry.

**Keywords:** Corrosion of metals, steel, Hydrochloric acid, Corrosion inhibitors, Heterocyclic compounds, Vegetable oils, Aminotriazoles, Tetrahydrotriazolopyrimidinols, Physicochemical research methods

**Funding:** The study was supported by Russian Science Foundation (project No. 24-23-00457, <https://rscf.ru/project/24-23-00457/>).

**For citation:** Kruzhilin A. A., Shevtsov D. S., Dmitriev I. A., Potapov M. A., Shikhaliev Kh. S. Synthesis of 2-alkyl-5-phenyl-4,5,6,7-tetrahydro-[1,2,4]triazolo[1,5-a]pyrimidin-7-ol derivatives from vegetable oils and their efficiency as inhibitors of hydrochloric acid corrosion of steel. *Kondensirovannye sredy i mezhfaznye granitsy = Condensed Matter and Interphases*. 2025;27(3): 000-000. <https://doi.org/10.17308/kcmf.2025.27/13017>

**For citation:** Kruzhilin A. A., Shevtsov D. S., Dmitriev I. A., Potapov M. A., Shikhaliev Kh. S. Synthesis of 2-alkyl-5-phenyl-4,5,6,7-tetrahydro-[1,2,4]triazolo[1,5-a]pyrimidin-7-ol derivatives from vegetable oils and their efficiency as inhibitors of hydrochloric acid corrosion of steel. *Kondensirovannye sredy i mezhfaznye granitsy = Condensed Matter and Interphases*. 2025;27(3): 409–416. <https://doi.org/10.17308/kcmf.2025.27/13017>

**Для цитирования:** Кружилин А. А., Шевцов Д. С., Дмитриев И. А., Потапов М. А., Шихалиев Х. С. Синтез производных 2-алкил-5-фенил-4,5,6,7-тетрагидро-[1,2,4]триазоло[1,5-а]пиримидин-7-олов из растительных масел и их эффективность как ингибиторов солянокислотной коррозии стали. *Конденсированные среды и межфазные границы*. 2025;27(3): 409–416. <https://doi.org/10.17308/kcmf.2025.27/13017>

✉ Alexey A. Kruzhilin, e-mail: [kruzhilin.alexey@gmail.com](mailto:kruzhilin.alexey@gmail.com)

© Kruzhilin A. A., Shevtsov D. S., Dmitriev I. A., Potapov M. V., Shikhaliev Kh. S., 2025



The content is available under Creative Commons Attribution 4.0 License.

## 1. Introduction

The intensification of production in oil fields is currently one of the top priorities for the development of the oil industry. Especially promising in terms of the use of new technologies that can intensify production are carbonate reservoirs, where production and oil recovery are relatively low. Hydrochloric acid technologies are most commonly used for the treatment of near-wellbore zones in carbonate reservoirs. These technologies play a vital role in intensifying oil production [1–2]. However, the use of hydrochloric acid can cause the corrosion of metals and stress cracking of pipelines. In order to prevent this, corrosion inhibitors are added to hydrochloric acid solutions. Recent years have seen the intensification of studies focusing on the search for and synthesis of environmentally friendly and harmless natural compounds that can be used as anticorrosion agents. Both organic and inorganic compounds are used as additives [3].

Vegetable oils (castor, palm, coconut, sunflower, soya-bean oils, etc.) are used as raw materials for the extraction of fatty acids (oleic, stearic, linoleic acids, etc.), which are then modified to produce effective inhibitors. The chemical modification of fatty acids allows obtaining various types of corrosion inhibitors, including esters (for HCl and oil-water media), ethoxylates, oxadiazoles/triazole amides, and amidoamines, as well as ammonium salts of triethanolamine as inhibitors for acidic environments (HCl and H<sub>2</sub>SO<sub>4</sub>) and imidazolines for NaCl solutions. According to previous studies, besides their high anticorrosive activity, these inhibitors have some other advantages: they are biodegradable, non-toxic (as compared to other known inhibitors), and cost-efficient due to the use of inexpensive renewable raw materials [4].

In our previous study [5], we discovered an unexpected inhibition effect in the reaction products of 3-alkyl-5-amino-1*H*-1,2,4-triazole with cinnamaldehyde. A detailed analysis demonstrated that active components of the mixture were derivatives of 4,5,6,7-tetrahydro-[1,2,4]triazolo[1,5-a]pyrimidin-7-ol, which form a new class of hydrochloric acid corrosion inhibitors. Their high efficiency can be explained by the presence of triazolopyrimidine matrix in their structure, since neither initial triazoles,

nor pure cinnamaldehyde have compatible protective properties. Of crucial importance is the hydrogenated state of the pyrimidine cycle, which is demonstrated by a low activity of aromatic (non-hydrogenated) triazolopyrimidines also analyzed earlier [6]. Therefore, the purpose of the study was to synthesize 2-alkyl-5-phenyl-4,5,6,7-tetrahydro-[1,2,4]triazolo[1,5-a]pyrimidin-7-ol derivatives using vegetable oils and assess their efficiency as inhibitors of acid corrosion on steel in HCl.

## 2. Experimental

### *Spectral analysis method*

Chromatographic analysis of the purity of the obtained compounds was performed using an Agilent 1260 Infinity chromatograph with UV and mass detection (Agilent 6230 TOF LC/MS detector, electrospray ionization). Chromatographic conditions were as follows: column Gemini C18 (4.6×50 mm); sorbent particle diameter 5 μm; linear gradient elution; mobile phase: eluent A – MeCN–H<sub>2</sub>O, 2.5 : 97.5, 0.1 % CF<sub>3</sub>COOH, eluent B – MeCN, 0.1 % CF<sub>3</sub>COOH, mobile phase flow rate 3.75 ml/min; column oven temperature 40 °C; injection volume 1.5 μl.

### *General procedure for the synthesis of 3-substituted 5-amino-1*H*-1,2,4-triazoles (1a-c)*

1 ml of sulfuric acid was gradually added, while stirring, to a mixture of ~ 0.1 mol of oil with 100 ml of butanol. After a glycerol precipitate appeared, 0.1 mol (13.6 g) of aminoguanidine bicarbonate was added portionwise to the mixture. The mixture was then heated to 90–95 °C (accompanied by the evolution of carbon dioxide) and boiled using a Dean-Stark apparatus and a reflux condenser with a calcium chloride tube for ~20 hours. After that, 2 g of sodium hydroxide was added, and the reaction mass was boiled for another 5 hours in order to ensure the cyclization of the formed intermediate **1a-c**\*. The end of the reaction was determined based on the amount of water collected in the Dean-Stark trap (~ 3.5 cm<sup>3</sup>). The mixture was cooled down and the obtained triazoles were washed with water and extracted in the butanol-water system, thrice removing the water fraction. The organic fraction was dried over sodium sulphate and evaporated using a rotary evaporator.

*General procedure for the synthesis of 2-alkyl-5-phenyl-4,5,6,7-tetrahydro-[1,2,4]triazolo[1,5-a]pyrimidin-7-ol derivatives (2a-c)*

A mixture of 0.1 mol of cinnamaldehyde and ~ 0.1 mol of aminotriazole mixture **1a-c** in the presence of an amphoteric surfactant (40 wt.% of the total reagent weight) was kept at 80-85 °C for 15 minutes. The mixture was then cooled down and analyzed without extraction or further treatment.

*Electrochemical studies*

The obtained 2-alkyl-5-phenyl-4,5,6,7-tetrahydro-[1,2,4]triazolo[1,5-a]pyrimidin-7-ol derivatives were analyzed with regard to their anticorrosive activity towards acid corrosion on ST-3 steel in a 24% HC solution using gravimetric direct corrosion tests and potentiodynamic polarization method.

Gravimetric direct corrosion tests were performed according to GOST 9.907-83 "Methods for the removal of corrosion products after corrosion tests".

Corrosion tests were carried out on steel plates (20×40 mm, thickness 1.2 mm). Each sample was preliminarily polished with K1000 fine-grained sandpaper, after which it was washed with distilled water, ethanol, and dried with filter paper. The experiments were carried out in a 24% HCl solution (for 7 days) under natural aeration without stirring for three samples in parallel (for each inhibitor concentration). After testing, the plates were washed with distilled water and treated with compositions in accordance with GOST 9.907-83.

The corrosion rate was determined according to the mass loss of the samples and was calculated using the formula:

$$k_{\text{inh}} = \frac{\Delta m}{S \times t},$$

where  $\Delta m = m_0 - m$  ( $m_0$  is the mass of the sample before the start of the experiment,  $m$  – is the mass of the sample after the test, g),  $S$  – is the total surface area of the plate,  $\text{m}^2$ .

For each solution, the corrosion rate  $k_0$  without an inhibitor additive was determined ( $k_0(\text{avg}) \approx 16.9 \text{ g/m}^2\cdot\text{day}$ ). The inhibitory effect of aminotriazine derivatives was evaluated according to the value of the inhibition coefficient:

$$\gamma = k_0 / k_{\text{inh}}$$

and the degree of protection:

$$Z = \left[ \frac{k_0 - k_{\text{inh}}}{k_0} \right] \times 100 \%,$$

where  $k_0$  and  $k_{\text{inh}}$  are the corrosion rates in the blank solution and in the solution with the inhibitor, respectively.

Calculation of the corrosion rate using the polarization resistance method

Polarization curves were obtained on an electrode made of ST-3 steel (with an area of  $1.0 \text{ cm}^2$ ) in an electrochemical cell with undivided electrode chambers using an IPC-PRO potentiostat. The working electrode was preliminarily cleaned with K2000 sandpaper and degreased with ethyl alcohol. Electrode potentials ( $E$ ) were measured relative to the silver chloride electrode, connecting the space of the electrochemical cell and the reference electrode through an electrolytic bridge based on agar-agar and sodium nitrate, and recalculated to the scale of a standard hydrogen electrode (potential was +202 mV relative to SHE). The auxiliary electrode was a platinum mesh.

The test substances were introduced into the acid until the required concentration was obtained. The electrodes were placed in the prepared solution and kept until the onset of a stationary state for 30 min. After the corrosion potential ( $E_{\text{cor}}$ ) was established, polarization curves with a potential scan rate of  $0.2 \text{ mV/s}$  in the anode and cathode directions were obtained. Polarization curves were recorded until the current density ( $i$ ) reached  $0.1 \text{ A cm}^{-2}$ .

The rate of corrosion in current units was determined by the polarization resistance technique as summarized by Mansfeld [7].

The studies were carried out using a three-electrode cell with undivided cathode and anode spaces without stirring under natural aeration conditions. The reference electrode was silver chloride (potential +202 mV relative to SHE), and the auxiliary electrode was a platinum mesh. The reference electrode was separated from the cell by an electrolytic bridge based on agar-agar and  $\text{NaNO}_3$ .

The working electrode was preliminarily cleaned with P2000 sandpaper, degreased with ethyl alcohol (96%), and washed with distilled

water. The electrodes were placed in the prepared solution and kept until the onset of a stationary state for 30 min. When the stationary state was reached, the electrode was polarized in the range of  $\pm 30$  mV from the  $E_{\text{cor}}$  value in potentiodynamic mode with a scanning rate of 0.2 mV/s.

Polarization resistance  $R_p$  was determined as the slope of the polarization curve at the point  $E_{\text{cor}}$  in the coordinates  $\Delta E - I$ , where  $\Delta E$  is the difference between the current electrode potential and the corrosion potential ( $E - E_{\text{cor}}$ ), and  $I$  is the electric current in the measuring circuit. Next, the dependence was replotted with the coordinates  $2.3R_p I - \Delta E$ . Coefficients  $b_a$  and  $b_c$  (anodic and cathodic Tafel slopes of the polarization curve) were determined using the TableCurve 2D software as the approximation parameters of the equation:

$$2.3R_p I = \frac{b_a \times b_c}{b_a + b_c} \left[ \exp\left(\frac{E - E_{\text{cor}}}{b_a}\right) - \exp\left(-\frac{E - E_{\text{cor}}}{b_c}\right) \right].$$

The corrosion current was calculated taking into account the obtained coefficients according to the equation:

$$I_{\text{cor}} = \frac{B}{R_p},$$

where  $B$  is the Stern-Geary coefficient calculated using the formula:

$$B = \frac{b_a \times b_c}{2.3(b_a + b_c)}.$$

For the comparison of the data obtained in various studies, the values of the corrosion current density ( $i_{\text{cor}}$ ) calculated using the expression will be presented further:

$$i_{\text{cor}} = \frac{I_{\text{cor}}}{S},$$

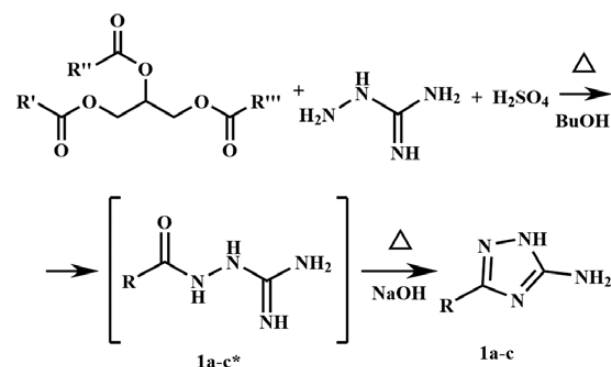
where  $S$  is the geometric area of the electrode. For the convenience of further comparison of the obtained data, the ratio of the corrosion current density of each test sample to the current density of the control experiment was calculated ( $i_{\text{cor}}^0 \approx 6.8$  mA/cm<sup>2</sup>):

$$Z_i = \frac{i_{\text{cor}}}{i_{\text{cor}}^0} \times 100\%.$$

Measurements for each concentration of the substance were made at least 5 times until reproducible data was obtained with subsequent statistical processing of the measurement results.

### 3. Results and discussion

The mixture of 1,2,4-aminotriazoles based on vegetable oil was for the first time obtained through the reaction of the corresponding oil with aminoguanidine bicarbonate. For this purpose the oil underwent hydrolysis in the presence of sulfuric acid. Thus, the obtained *in situ* fatty acids interacted with aminoguanidine. As a result, during the first stage 2-alkylhydrazine-1-carboximidamides **1a-c\*** were formed, which then underwent cyclization in an alkaline medium resulting in the desired 1,2,4-aminotriazoles **1a-c**.



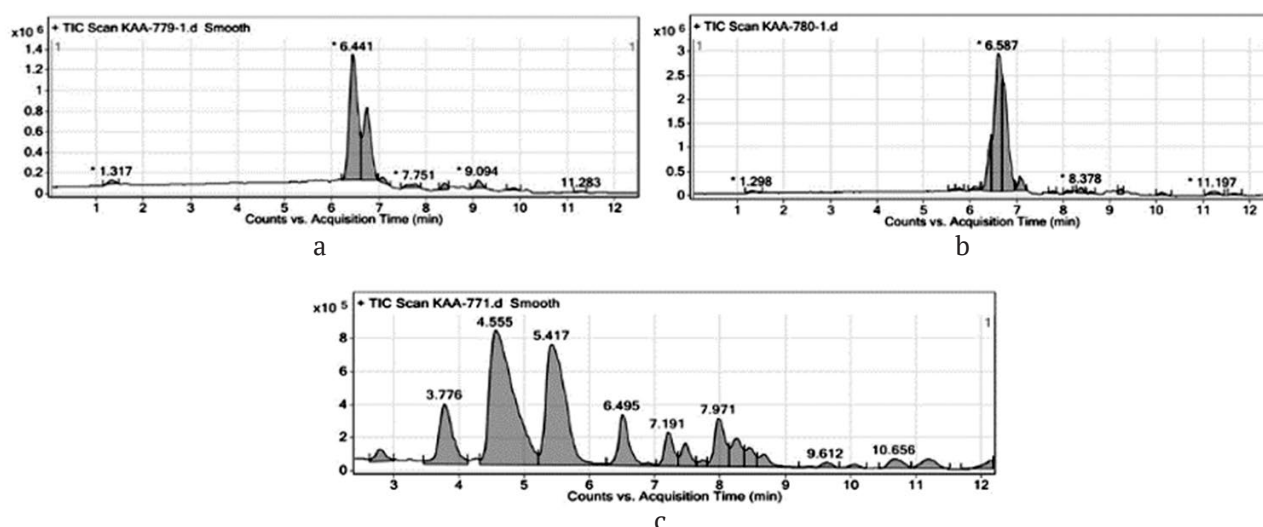
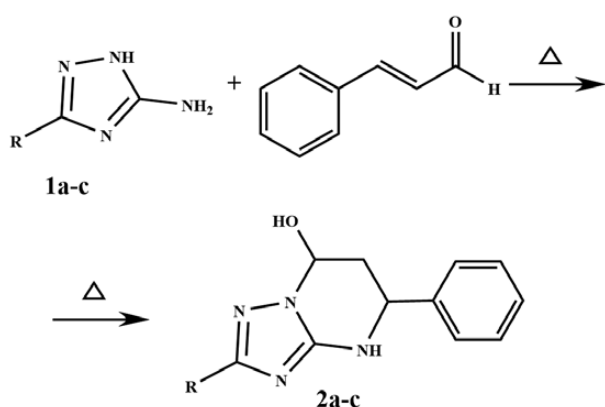
R', R'', R''' : fatty acid residues of sunflower (a), palm (b), coconut (c) oil

The composition of aminotriazole mixtures **1a-c** was determined using the HPLC-MS (/MS) method and is presented in Table 1 and Fig.1. The yield ratio was > 95%.

Thus obtained mixtures of 1,2,4-aminotriazoles were then subjected to further transformations with cinnamaldehyde using the methodology described in [5]. A mixture of 0.1 mol of cinnamaldehyde and ~ 0.1 mol of aminotriazole mixture **1a-c** in the presence of an amphoteric surfactant was kept at 80–85 °C for 15 minutes. During the interaction, 1,2,4-triazoles underwent the following transformations: during the first stage, an exocyclic amino group was added to the multiple bond according to the Michael reaction; during the second stage, intramolecular cyclisation took place with nucleophilic addition to the carbonyl group. This resulted in the formation of 2-alkyl-5-phenyl-4,5,6,7-tetrahydro-[1,2,4]triazolo[1,5-a]pyrimidin-7-ol derivatives (**2a-c**)

**Table 1.** Composition of aminotriazole mixtures **1a-c** according to GC/MS and HPLC/MS

Fatty acids	1a, %	1b, %	1c, %
C6	1.71	–	–
C8	–	–	6.21
C10	–	–	3.19
C12	–	–	44.1
C14	–	2.17	10.21
C16	–	49.92	3.41
C18:0	1.81	3.70	6.2
C18:1	29.91	27.52	14.9
C18:2	57.88	11.22	9.09
C20	5.03	3.31	2.29
other	3.76	2.16	0.40

**Fig. 1.** Total ion current chromatograms of 1,2,4-aminotriazole mixtures **1a-c**

**R:** fatty acid residues of sunflower (a), palm (b), coconut (c) oil

Direct corrosion tests of **2a-c** derivatives demonstrated their strong protective effect (Table 2). At a concentration of 2 g/l, all the studied derivatives exhibited a protection degree of > 95%. At a concentration of 1 g/l, the mixture

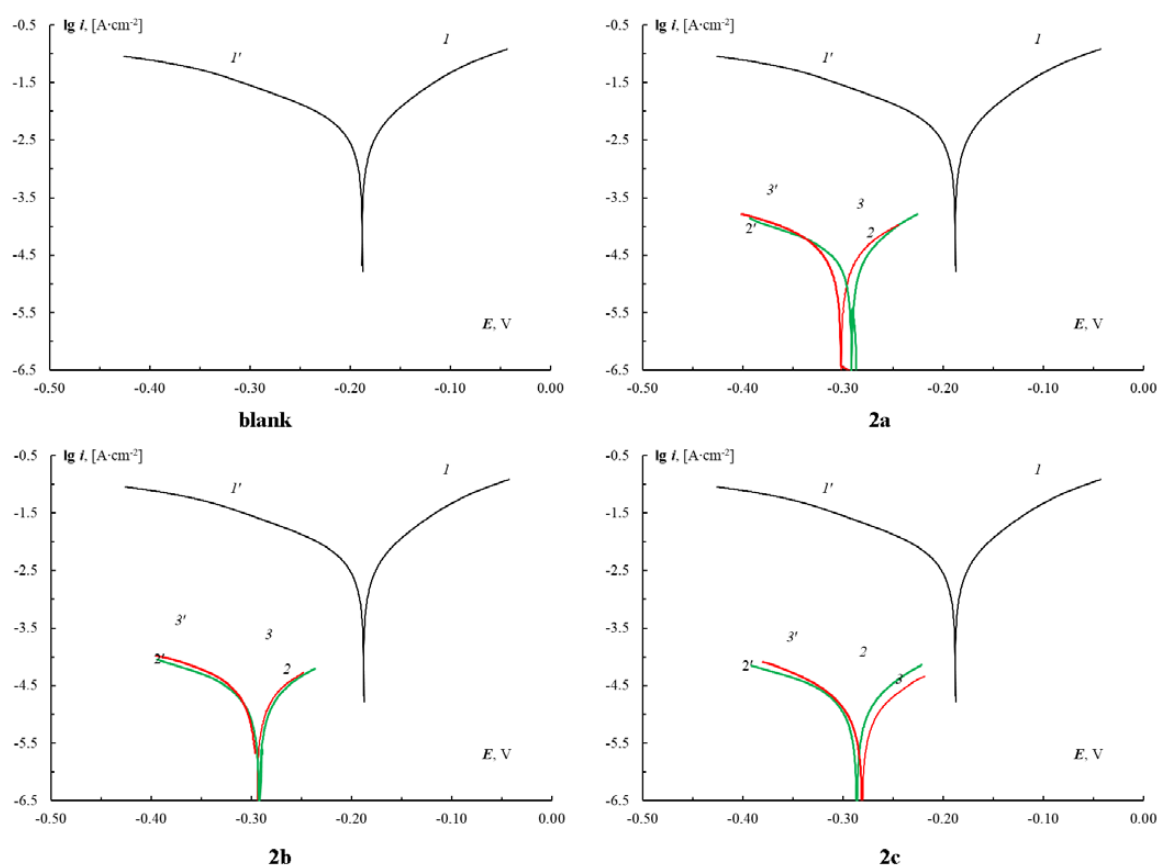
of tetrahydrotriazolopyrimidinols obtained from coconut oil was the most effective (protection degree of 92.6%). The protection degree of palm oil derivatives at a concentration of 1 g/l was only 80 %. This can be explained by a high content of palmitic acid residues.

Polarization studies of derivatives **2a-c** provided us with a set of anodic and cathodic polarization curves (Fig. 2).

$E_{\text{cor}}$  during all the tests ranged from –300 to –280 mV with a 80–100 mV shift to the cathodic region as compared to the control experiment. The polarization resistance grew in the series sunflower – palm – coconut oil. The same was true for  $i_{\text{cor}}$  and  $Z_i$ : the corrosion current density decreased – the protection degree increased. The mixture of coconut oil derivatives demonstrated the greatest anticorrosive activity towards acid

**Table 2.** Anticorrosive activity according to direct corrosion tests in 24% HCl

Inhibitor	$C_{inh}$ , $g \cdot dm^{-3}$	Corrosion rate, $k_{inh}$ , $g/(m^2 \cdot h)$	Inhibition coefficient, $\gamma$ , %	Protection degree, $Z$ , %
Blank	–	16.90	–	–
2a	1	2.65	6.66	85.0
	2	0.75	23.55	98.0
2b	1	3.13	4.89	79.6
	2	0.31	49.39	95.8
2c	1	1.11	13.55	92.6
	2	0.31	49.39	98.0

**Fig. 2.** Anodic (1--3) and cathodic (1'--3') polarization curves of ST-3 steel electrodes in a 24% HCl solution without inhibitor additives (blank), with additives **2a** (2a), with additives **2b** (2b), with additives **2c** (2c) at concentrations of 1 g/l (2--2') and 2 g/l (3--3')

corrosion. The corrosion current density was 0.028 and 0.026  $mA \cdot cm^{-2}$  at concentrations of 1 and 2 g/l respectively. We should note that when the concentration of inhibitors **2a** and **2b** was increased from 1 to 2 g/l, the degree of protection slightly decreased. This can be explained by the measurement error, which is proved by the calculated values of the confidence interval for the corrosion current density.

Thus, based on the conducted polarization measurements, we can assume that all the studied derivatives at all the studied concentrations have high inhibitory activity, which does not change significantly at increased  $C_{inh}$ . Comparing the results of direct and electrochemical tests we can see that 2-alkyl-5-phenyl-4,5,6,7-tetrahydro-[1,2,4]triazolo[1,5-a]pyrimidin-7-ol derivatives based on coconut oil **2c**, which contain

**Table 3.** Results of the electrochemical test of 2-alkyl-5-phenyl-4,5,6,7-tetrahydro-[1,2,4]triazolo[1,5-a]pyrimidin-7-ol mixtures (2a-c)

Inhibitor	$C_{inh}$ , g·dm <sup>-3</sup>	$E_{cor}$ , mV	$R_p$ , kΩ·cm <sup>2</sup>	$i_{cor}$ , mA·cm <sup>-2</sup>	$Z_i$ , %
Blank	–	–188	4.2±0.5	6.8±0.3	–
2a	1.0	–291	969±51	0.047±0.011	95.3
	2.0	–302	584±18	0.057±0.002	94.3
2b	1.0	–292	982±9	0.043±0.004	95.6
	2.0	–295	835±13	0.051±0.006	94.9
2c	1.0	–287	1138±58	0.028±0.006	97.2
	2.0	–281	1529±46	0.026±0.007	97.4

residues of medium-chain fatty acids (C10-C14), are the most effective inhibitors of hydrochloric acid corrosion on ST-3 steel.

#### 4. Conclusions

In our study, we synthesized several mixtures of 2-alkyl-5-phenyl-4,5,6,7-tetrahydro-[1,2,4]triazolo[1,5-a]pyrimidin-7-ols of fatty acids obtained directly from vegetable oils (sunflower, palm, and coconut oil) and confirmed their structure using the HPLC/MS method. The anticorrosive effect of mixtures of 2-alkyl-5-phenyl-4,5,6,7-tetrahydro-[1,2,4]triazolo[1,5-a]pyrimidin-7-ols of fatty acids from vegetable oils towards acid corrosion of ST-3 steel in 24% HCl was analyzed. The mixture based on coconut oil proved to be the most effective (the protection degree of 97.2-97.4% according to polarization tests and 92.6-98.0% according to direct corrosion tests). The obtained results demonstrate that tetrahydrotriazolopyrimidinols containing aliphatic residues of medium-chain fatty acids (C10-C14) are the optimal mixtures for steel passivation against acid corrosion.

#### Author contributions

All authors made an equivalent contribution to the preparation of the publication.

#### Conflict of interests

The authors declare that they have no known competing financial interests or personal relationships that could have influenced the work reported in this paper.

#### References

1. Fredd C. N., Fogler H. S. Alternative stimulation fluids and their impact on carbonate acidizing. *SPE Journal*. 1998;3(1): 34–41. <https://doi.org/10.2118/31074-PA>

2. Iqbal M. I., Kudapa V. K. Oil well production mechanism: training manual on well production operations for non-production engineers (oil and gas production operations). *CRC Press*. 2025. <https://doi.org/10.1201/9781003605706>

3. Avdeev Y. G., Kuznetsov Y. I. Physicochemical aspects of inhibition of acid corrosion of metals by unsaturated organic compounds. *Russian Chemical Reviews*. 2012;81(12): 1133–1145. Available at: <https://elibrary.ru/item.asp?id=18226908>

4. Swathi P. N., Rasheeda K., Samshuddin S., Alva V. D. Fatty acids and its derivatives as corrosion inhibitors for mild steel-an overview. *Journal of Asian Scientific Research*. 2017;7(8): 301–308. <https://doi.org/10.18488/journal.2.2017.78.301.308>

5. Kruzhilin A. A., Shevtsov D. S., Potapov A. Yu., ... Kasatkin V. E. Novel inhibitory compositions based on 4,5,6,7-tetrahydro-[1,2,4]triazolo[1,5-a]pyrimidin-7-ol derivatives for steel acid corrosion protection. *International Journal of Corrosion and Scale Inhibition*. 2022;11(2): 774–795. <https://doi.org/10.17675/2305-6894-2022-11-2-22>

6. Kruzhilin A. A., Lyapun D. V., Shevtsov D. S., ... Shikhaliev Kh. S. New [1, 2, 4] triazolo [1, 5-a] pyrimidine-7-one corrosion inhibitors for copper in chloride environments. *International Journal of Corrosion and Scale Inhibition*. 2021;10(4): 1474–1492. <https://doi.org/10.17675/2305-6894-2021-10-4-7>

7. Mansfeld F. Tafel slopes and corrosion rates obtained in the pre-Tafel region of polarization curves. *Corrosion Science*. 2005;47(12): 3178–3186. <https://doi.org/10.1016/j.corsci.2005.04.012>

#### Information about the authors

Alexey A. Kruzhilin, Cand. Sci. (Chem.), Head of Laboratory of Organic Additives for the Chemical and Electrochemical Deposition of Metals and Alloys Used in the Electronics Industry, Voronezh State University (Voronezh, Russian Federation).

<https://orcid.org/0000-0003-2262-0131>  
kruzhilin.alexey@gmail.com

Dmitry S. Shevtsov, Cand. Sci. (Chem.), researcher at the Laboratory of Organic Additives for the Chemical and Electrochemical Deposition of Metals and Alloys Used in the Electronics Industry, Voronezh State University (Voronezh, Russian Federation).

<https://orcid.org/0000-0003-4480-787X>  
shevtsov@chem.vsu.ru

*Ivan A. Dmitriev*, student at the Department of Organic Chemistry, Voronezh State University (Voronezh, Russian Federation).

*Mikhail A. Potapov*, Cand. Sci. (Chem.), Lead Engineer at the Department of Biochemistry and Cell Physiology of the Faculty of Biomedical Sciences, Voronezh State University (Voronezh, Russian Federation).

<https://orcid.org/0000-0002-1795-7605>  
amidines@mail.ru

*Khidmet S. Shikhaliev*, Dr. Sci. (Chem.), Professor, Head of the Department of Organic Chemistry, Voronezh State University (Voronezh, Russian Federation).

<https://orcid.org/0000-0002-6576-0305>  
chocd261@chem.vsu.ru

*Received February 28, 2025; approved after reviewing March 26, 2025; accepted for publication April 15, 2025; published online September 25, 2025.*



## Original articles

Research article

<https://doi.org/10.17308/kcmf.2025.27/13018>

## Refined formula for the calculation of the coefficient of efficiency of an electrochemical generator

T. T. Muratov✉

National pedagogical university of Uzbekistan named after Nizami  
27 Bunyodkor street, Tashkent 100185, Uzbekistan

### Abstract

**Objective:** Analytical calculations and preliminary assessment of the efficiency of electrochemical generators (chemicurrent generators) are important for the analysis of the mechanisms of conversion of chemical energy into electrical energy. This process is based on the transformation of the energy of a heterogeneous chemical reaction of hydrogen molecule formation into the electronic excitation energy on the surface of a semiconductor catalyst. When calculating the probability of excitation of hot electrons (high-energy electrons in the conduction band of the semiconductor), earlier studies did not take into account the phonon channel of chemical energy accommodation. This is acceptable, if we neglect the interaction between the excited electron and the lattice. However, the scattering of the chemical reaction energy causes an inevitable shift in the equilibrium positions of oscillators, resulting in the emission and absorption of phonons. Therefore, the calculation method should take into account both electron and phonon accommodation channels. The purpose of the study was to derive a theoretical formula for the efficiency coefficient of an electrochemical generator taking into account thermally stimulated excitation of electrons to the conduction band and analyze particular cases of its application.

**Theoretical analysis:** We performed a theoretical analysis of the effect of local thermal vibrations initiated by the chemical reaction energy of formation of a hydrogen molecule on the catalyst surface on the rate of generation of high-energy electrons. The derived formulas for the calculation of the efficiency coefficient of electrochemical generators specify the corresponding formulas suggested in earlier studies. The study demonstrated a significant impact of thermally stimulated excitation of electrons to the conduction band of the semiconductor at room temperatures.

**Conclusions:** The obtained results can be used for qualitative analysis of chemical energy accommodation with regard to the conversion of chemical energy into electrical one.

**Keywords:** Catalyst surface, Accommodation, Phonon channel, Franck-Condon energy, Schottky barrier, Efficiency coefficient of electrochemical generators

**For citation:** Muratov T. T. Refined formula for the calculation of the coefficient of efficiency of an electrochemical generator. *Condensed Matter and Interphases*. 2025;27(3): 417–421. <https://doi.org/10.17308/kcmf.2025.27/13018>

**Для цитирования:** Муратов Т. Т. Уточнение расчета коэффициента полезного действия химического генератора. *Конденсированные среды и межфазные границы*. 2025;27(3): 417–421. <https://doi.org/10.17308/kcmf.2025.27/13018>

✉ Temur T. Muratov, e-mail: [temurmuratov1977@gmail.com](mailto:temurmuratov1977@gmail.com)

© Muratov T. T., 2025



The content is available under Creative Commons Attribution 4.0 License.

## 1. Introduction

Direct conversion of chemical energy into electrical energy can be performed by means of electrochemical generators [1], which are semiconductor heterostructures with various electronic parameters. Semiconductors with pronounced catalytic properties are considered promising materials [2]. Catalytic properties of semiconductors are largely accounted for by surface defects (shallow and deep impurities), which serve as traps for atoms and molecules of gaseous media [3–8]. The surface functions as a catalyst (K) for the formation (decay) of hydrogen molecules and helps to reduce the energy barrier (activation energy) as compared to the gaseous medium. Energy from the heterogeneous exothermic reaction  $H + K \rightarrow HK$ ,  $HK + H \rightarrow H_2 + K$  is used to excite (form) high-energy electrons, which, affected by the electrical double layer, easily overcome the potential barrier at the heterointerface [1, 9]. Chemical energy accommodation can proceed along two channels: electron and phonon. In the first case, the energy of the exothermic reaction is transferred by impulse directly to the bound electron generating a high-energy electron. In the second case, the excessive energy is used for the excitation of high-energy phonons, which actively interact with valence electrons causing them to oscillate in accordance with the vibrations of the crystal lattice [10–13]. The adsorbed  $H_2$  molecules oscillate at frequencies significantly higher than the Debye frequency. Therefore, the decay of local vibrations of hydrogen molecules is hindered, and the electron channel can become dominant over the phonon channel [14]. However, at high temperatures close to critical values, for instance the melting point, thermal fluctuations increase dramatically [15], and there is a possibility of thermally stimulated excitation of the valence electron to the conduction band. In this case, the phonon channel can be compatible with the electron channel. Thermally stimulated excitation of the valence electron to the conduction band is also possible at lower temperatures as a result of electron-phonon interaction [16]. For semiconductors with strong electron-phonon couplings, both accommodation channels should be taken into account. In this case, the

probability of an elementary relaxation act [1] can be described as:

$$P(E_g, T) = \int_{E_g}^{\infty} w(E, T) f(E) dE, \quad (1)$$

$E_g$  is the bandgap of the semiconductor,  $w(E, T)$  is the probability of thermally stimulated excitation of the valence electron to the conduction band,  $f(E) = (1 / \Theta_{\text{char}}) \exp(-E / \Theta_{\text{char}})$  is the experimentally established probability of generation of high-energy electrons [1, 2],  $\Theta_{\text{char}}$  is the characteristic energy of the exothermic reaction forming the  $H_2$  molecule (about 0.2 eV) on the catalyst surface, which generates an electron-hole ( $e^- - p^+$ ) pair [2].

Hot electrons in the conduction band are nonequilibrium charge carriers. Therefore, the function  $f(E)$  characterizes the probability of the formation of a ( $e^- - p^+$ ) pair in the tail of the Maxwellian distribution function in the vicinity of energy  $\Theta_{\text{char}}$  [1] does not take into account the phonon channel of energy accommodation  $w(E, T)$ . This is acceptable in the case of direct electron transitions in direct bandgap semiconductors. However, in the case of indirect-gap semiconductors it is necessary to take into account intermediate phonon states to preserve the quasi momentum of the hot electron. The existing formulas for calculating the efficiency coefficient of electrochemical generators [1, 14, 17] are probably a specific (limited) case of a more general (in terms of theory) formula.

The results presented in [1, 14, 17] do not take into account the shift of the adiabatic term during the transition of the hydrogen molecule back to the ground state:  $H_2^* \rightarrow H_2 + Q$ . The released energy  $Q$  can cause vibrations of the hydrogen molecule. When its own vibrations  $\omega \propto 1/\sqrt{m_{H_2}}$  are within the band gap of the matrix, the  $H_2$  molecule demonstrates local vibrations. The results presented in [1, 14, 17] correspond to the situation, when the natural frequency  $\omega \propto 1/\sqrt{m_{H_2}}$  is within the band gap of the matrix. Besides, the position of the minimum of the configuration coordinate of the term  $^1\Sigma_g^+$  shifts, which also requires energy, since the Franck–Condon principle is only partially met. It is obvious that the energy released by a locally vibrating center (in the case of resonance)

initiates thermally stimulated excitation of the electron to the conduction band of the semiconductor. Therefore, when generating the chemicurrent, both accommodation channels should be taken into account.

The purpose of the study was to derive a theoretical formula for the efficiency coefficient of an electrochemical generator taking into account thermally stimulated excitation of electrons to the conduction band and analyze particular cases of its application [1, 14, 17]. The deriving of the formula was based on the assumption that the generation of hot electrons requires the outer (peripheral) electron to be excited by high-energy phonons in order to break the bonds with neighboring atoms, since each outer electron forms electron-pair bonds between the atoms. In this case, contrary to [1], for  $\Theta_{\text{char}}$ , some of the thermal energy  $Q$  of reaction  $\text{H} + \text{H} \rightarrow \text{H}_2 + Q \uparrow$  is used for the excitation of the electron and the other for the direct (impact) excitation of the outer electron.

## 2. Calculation of the efficiency coefficient and discussion

According to the classical description of multi-phonon transitions valid for  $k_B T \gg \hbar \omega_0$  ( $\hbar \omega_0$  is the energy of the quantum of matrix vibrations) [16]:

$$w(E, T) = \exp\left(-\frac{\mu(E)}{k_B T}\right), \quad \mu(E) = \frac{(E_{\text{opt}} - E)^2}{4 E_{FC}}, \quad (2)$$

where  $E_{\text{opt}}$  is the optical transition energy associated with the thermal energy of excitation:  $E_{\text{opt}} = E_T + E_{FC}$ ,  $E_{FC}$  is the Franck-Condon energy characterizing the  $e$ - $ph$  interaction force. Substitution of (2) in (1) taking into account  $f(E) = (1/\Theta_{\text{char}}) \exp(-E/\Theta_{\text{char}})$  gives the following result:

$$P(E \geq E_g) = \frac{1}{\Theta_{\text{char}}} \int_{E_g}^{\infty} \exp\left(-\frac{E}{\Theta_{\text{char}}}\right) \exp\left[-\frac{(E_{\text{opt}} - E)^2}{4 E_{FC} k_B T}\right] dE. \quad (3)$$

$$\text{A Gauss-type function } \exp\left[-\frac{(E_{\text{opt}} - E)^2}{4 E_{FC} k_B T}\right]$$

characterizes local vibrations of the adiabatic

term with the electron near the point of energy release of the chemical reaction (Fig. 1). These vibrations are loosely coupled with natural vibrations of the crystal lattice. The valence electron of the matrix near the heat release center  $Q$  (of the  $\text{H}_2$  molecule) is associated with the  $DX$  center on the catalyst surface. Calculating the integral (3) we obtain the following expression:

$$P(E \geq E_g) = \frac{\sqrt{\pi}}{2} \exp\left(\frac{E_{FC} k_B T - \Theta_{\text{char}} E_{\text{opt}}}{\Theta_{\text{char}}^2}\right) \times \left[1 - \Phi\left(\frac{E_g - E_{\text{opt}}}{2\sqrt{E_{FC} k_B T}} + \frac{\sqrt{E_{FC} k_B T}}{\Theta_{\text{char}}}\right)\right]. \quad (4)$$

$\Phi(x)$  – is the error function; the electric current occurrence condition  $E_{\text{opt}} \geq E_g + \varphi$  ( $\varphi$  is the potential barrier) (Fig. 1):

$$P(E \geq E_g) = \frac{\sqrt{\pi}}{2} \exp\left(\frac{E_{FC} k_B T}{\Theta_{\text{char}}^2} - \frac{E_g + \varphi}{\Theta_{\text{char}}}\right) \times \left[1 - \Phi\left(\frac{\sqrt{E_{FC} k_B T}}{\Theta_{\text{char}}} - \frac{\varphi}{2\sqrt{E_{FC} k_B T}}\right)\right]. \quad (5)$$

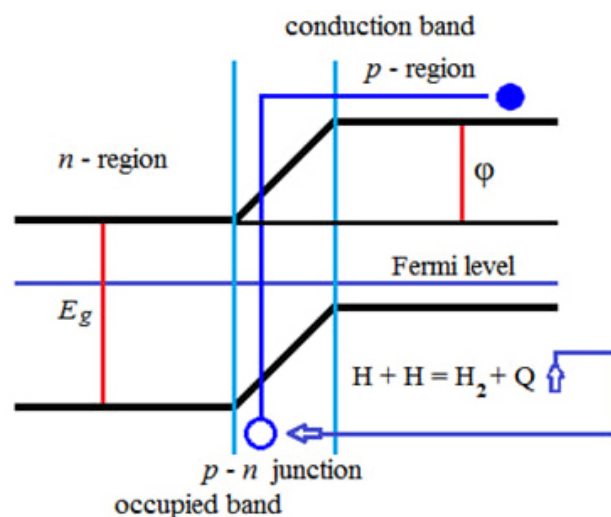


**Fig. 1.** Generation of mobile carriers under effect of chemical reaction energy. In the electric field of the depletion layer high-excited electrons accelerates and throws into conduction band  $p$ -type semiconductor, forming the external current. Semiconductor-catalyst  $p$ -type sufficiently thin so that the condition  $\exp(-d/l) \approx 1$  was complied, where  $d$  – its thickness,  $l$  – diffusion length path of high-energy electron into width of catalyst, which, for example, in high-quality monocrystalline silicon can be constitute of hundreds and thousands of micrometers

Provided that  $2E_{FC}k_B T \equiv \varphi\Theta_{\text{char}}$  (which demonstrates that the spread of the electron transition energy near  $E = E_{\text{opt}}$  is limited by local heat release), from (5) follows:

$$P(E \geq E_g) = \frac{\sqrt{\pi}}{2} \exp\left(-\frac{\varphi}{2\Theta_{\text{char}}}\right) \exp\left(-\frac{E_g}{\Theta_{\text{char}}}\right). \quad (6)$$

We should note that condition  $2E_{FC}k_B T \equiv \varphi\Theta_{\text{char}}$  does not impair the criterion of local vibrations. Indeed, at high temperatures ( $k_B T \gg \hbar\omega_0$ )  $E_{FC} \approx \hbar\omega N_{ph} \approx (\omega/\omega_0)k_B T$ ,  $2(\omega/\omega_0)(k_B T)^2 \approx \varphi\Theta_{\text{char}}$ . Here  $\omega$  is the frequency of quasi-local vibrations,  $N_{ph}$  is the average number of acoustic phonons. For instance, the calculation for germanium at room temperature and  $\Theta_{\text{char}} \leq E_g$  [1] results in  $\omega/\omega_0 \leq \varphi E_g / 2(k_B T)^2 \approx 100$ . It shows that some of the heat is used for the excitation of local phonons. Therefore, it is necessary to take into account the phonon accommodation channel, along with the electron channel, to accurately calculate the efficiency coefficient of an electrochemical generator. The condition  $2E_{FC}k_B T \equiv \varphi\Theta_{\text{char}}$  is satisfied, for instance, by the following values:  $E_{FC} \approx 1.1$  eV,  $k_B T \approx 0.027$  eV,  $\Theta_{\text{char}} = 0.2$  eV,  $\varphi = 0.3$  eV for GaAlAs [1,18]. Other optimal values can also be found. If  $E_g = 0$  (similar to narrow band semiconductors and metals), then:

$$P(0) = \frac{\sqrt{\pi}}{2} \exp\left(-\frac{\varphi}{2\Theta_{\text{char}}}\right), \quad (7)$$

which specifies the corresponding formula for the excitation of high-energy electrons, whose energy is equal to or higher than the Schottky barrier  $\varphi$  in Pd/n-Si, Pt/GaAs, Pd/GaP diodes (Fig. 1) [17]. Taking into account formula (6) and the results presented in [1] the efficiency coefficient of an electrochemical generator can be calculated using the formula ( $\Theta_{\text{char}} \leq Q$ ):

$$\eta = \frac{\sqrt{\pi}}{2} \exp\left(-\frac{\varphi}{2\Theta_{\text{char}}}\right) \frac{mE_g}{Q} \exp\left(-\frac{E_g}{\Theta_{\text{char}}}\right), \quad (8)$$

$m$  is the average number of possible transitions along the electron channel of accommodation [1]. The efficiency coefficient of an electrochemical generator based on the Schottky diodes is calculated using the following formula [19, 20]:

$$\eta = \frac{\sqrt{\pi}}{2} \frac{\varphi}{Q} \exp\left(-\frac{\varphi}{2\Theta_{\text{char}}}\right). \quad (9)$$

According to formula (8) the efficiency coefficient is about 40% of the efficiency coefficient obtained when only the electron channel is considered [1], and according to formula (9) the efficiency coefficient is practically 90%. Thus, the effect of thermally stimulated excitation of electrons on the rate of chemcurrent generation is more prominent in non-degenerate semiconductors than in metals. Thus, for  $n$ -type wide-band semiconductors ( $\varphi = 0$ ) using formula (5) we obtain the following:

$$P(E \geq E_g) = \frac{\sqrt{\pi}}{2} \exp\left(\frac{E_{FC}k_B T}{\Theta_{\text{char}}^2}\right) \times \left[1 - \Phi\left(\frac{\sqrt{E_{FC}k_B T}}{\Theta_{\text{char}}}\right)\right] \exp\left(-\frac{E_g}{\Theta_{\text{char}}}\right). \quad (10)$$

We can assume that  $\sqrt{E_{FC}k_B T} \equiv \Theta_{\text{char}}$ . Then the efficiency coefficient calculated using formula (10) is about 40% of the efficiency coefficient obtained, when only the electron channel is considered [1]. At high temperatures

$$P(E \geq E_g) \approx \frac{\Theta_{\text{char}}}{2\sqrt{E_{FC}k_B T}} \exp\left(-\frac{E_g}{\Theta_{\text{char}}}\right), \quad (\sqrt{E_{FC}k_B T} > \Theta_{\text{char}}). \quad (11)$$

The efficiency coefficient is respectively

$$\eta \approx \frac{\Theta_{\text{char}}}{2\sqrt{E_{FC}k_B T}} \frac{mE_g}{Q} \exp\left(-\frac{E_g}{\Theta_{\text{char}}}\right), \quad (T > 400 \text{ K}). \quad (12)$$

At temperatures of about 500 K, the efficiency coefficient calculated using formula (12) is about 45% of the efficiency coefficient obtained, when only the electron channel is considered [1]. We can see that in all the cases, when thermally stimulated excitation of electron was considered, the efficiency coefficient reduced on average by 60% and by 10%, when the barrier ( $\varphi = 0$ ) was not considered (using formula (8)). This case is the closest to the results presented in [1].

### 3. Conclusions

As a result of the study, we derived formulas (8), (9), and (12). We also analyzed the effect of local thermal vibrations on the generation of hot electrons in semiconductors and metals. The study demonstrated a significant

contribution of the phonon channel of chemical energy accommodation at room and higher temperatures in non-degenerate semiconductors. The derived formulas can be used for the modelling of electrochemical generators and their optimization, when considering the problem of conversion of chemical energy into electrical energy.

### Conflict of interests

The author declares that they have no known competing financial interests or personal relationships that could have appeared to influence the work reported in this paper.

### References

1. Grankin V. P., Grankin D. V. Electronic excitation and current generation in a heterostructure under the action of hydrogen atoms. *Russian Journal of Physical Chemistry A*. 2020;94(10): 2047–2050. <https://doi.org/10.1134/S0036024420100118>
2. Grankin V. P., Grankin D. V. Electronic excitation of the surface of UV-irradiated solids in heterogeneous recombination of hydrogen atoms. *Russian Journal of Physical Chemistry A*. 2016;90(6): 1280–1285. <https://doi.org/10.1134/S003602441606008X>
3. Boreskov G. K. *Heterogeneous catalysis*\*. Moscow: Nauka Publ.; 1986. 304 p. (In Russ.)
4. Fischer R., Neumann H. *Field emission from semiconductors*\*. Moscow: Nauka Publ.; 1971. 216 p. (In Russ.)
5. Semenov I. N., Bogdanov R. V. *Energy and chemical process*\*. Leningrad: Khimiya Publ.; 1973. 112 p. (In Russ.)
6. Dmitriev I. S. *Symmetry in the world of molecules*\*. Leningrad branch: Khimiya Publ.; 1976. 128 p. (In Russ.)
7. Golikov G. A. *Handbook of physical chemistry*\*. Moscow: Vysshaya shkola Publ.; 1988. 383 p. (In Russ.)
8. Poltorak O. M. *Thermodynamics in physical chemistry*\*. Moscow: Vysshaya shkola Publ.; 1991. 319 p. (In Russ.)
9. Mitrofanov V. V., Fogel' V. A. *Physics and chemistry of semiconductors*\*. Leningrad: Sudostroenie Publ.; 1965. 219 p. (In Russ.)
10. Muratov T. T. Compensation effect of growth of the lifetime of charged carriers in semiconductors at a magnetic field. *Semiconductors*. 2022;56(11): 831–835. <https://doi.org/10.21883/SC.2022.11.54958.4350>
11. Muratov T. T. Statistical approach to the process of tunnel ionization of impurity centers near the heterointerface. *Condensed Matter and Interphases*. 2021;23(4): 529–534. <https://doi.org/10.17308/kcmf.2021.23/3671>
12. Muratov T. T. Influence of the Zeeman effect on the three-body recombination process in the ultracold plasma. *Izvestiya Vuzov. Fizika*. 2023;66(8): 74–79. (In Russ.). <https://doi.org/10.17223/00213411/66/8/9>
13. Reissland J. A. *The physics of phonons*. London: New York: Wiley; 1973. 319 p.
14. Grankin V. P., Grankin D. V. Non-adiabatic chemo-electronic energy conversion in a Schottky diode\*. In: *Proceedings of the international scientific and technical conference "INTERMATIC-2015". Part 4. MIREA. 1-5 December 2015*. Moscow: 2015. p. 101–104. (In Russ.)
15. Mashkina E. S.  $1/f^2$  noise as a precursor of structural reconstructions near the melting point of crystalline materials with different types of chemical bonds. *Condensed Matter and Interphases*. 2024;26(2): 362–366. <https://doi.org/10.17308/kcmf.2024.26/12071>
16. Abakumov V. N., Perel V. I., Yassievich I. N. *Nonradiative recombination in semiconductors*. New York: Elsevier Publishing Company; 1991, 336 p.
17. Grankin D. V. Energy efficiency of chemical energy conversion into electrical energy by a Schottky diode with a nano-sized metal film\*. In: *Proceedings of the international scientific and technical conference "INTERMATIC-2016". Part 1. MIREA 21–25 November 2016*. Moscow: 2016. p. 108–112. (In Russ.)
18. Mooney P. M. Deep donor levels (DX centers) in III–V semiconductors. *Journal of Applied Physics*. 1990;67(3): R1–R26. <https://doi.org/10.1063/1.345628>
19. Styrov V. V. Nonequilibrium generation of hot electrons in a metal during chemical reaction at the liquid-metal interface. *Technical Physics Letters*. 2015;41(2): 195–199. <https://doi.org/10.1134/S1063785015020261>
20. Styrov V. V., Simchenko S. V. SiC-based nanosized structures with *p-n* junctions for transforming chemical energy into electricity and sensors. *Technical Physics Letters*. 2013;39(7): 621–625. <https://doi.org/10.1134/S1063785013070122>

\*Translated by author of the article

### Information about the author

Temur T. Muratov, PhD in Physical and Mathematical Sciences, Senior Teacher at the Department of Physics, National pedagogical university of Uzbekistan named after Nizami (Tashkent, Uzbekistan).

<https://orcid.org/0000-0002-0905-6620>

[temurmuratov1977@gmail.com](mailto:temurmuratov1977@gmail.com)

Received January 21, 2025; approved after reviewing February 20, 2025; accepted for publication March 17, 2025; published online September 25, 2025.



## Original articles

Research article

<https://doi.org/10.17308/kcmf.2025.27/13181>

## Photoluminescent properties of porous silicon nanoparticles: synthesis, characterization, and cellular imaging

D. A. Nazarovskaia<sup>1</sup>, S. Yu. Turishchev<sup>2</sup>, S. S. Titova<sup>2</sup>, A. A. Shatov<sup>1</sup>, P. A. Tyurin-Kuzmin<sup>1,3</sup>,  
L. A. Osminkina<sup>1,3</sup>✉

<sup>1</sup>Lomonosov Moscow State University,  
1 Leninskie Gory, Moscow 119991, Russian Federation

<sup>2</sup>Voronezh State University,  
1 Universitetskaya pl, Voronezh, 394018, Russian Federation

<sup>3</sup>Institute for Biological Instrumentation of the Russian Academy of Sciences,  
7 Institutskaya st., Pushchino 142290, Russian Federation

### Abstract

**Objective:** This study investigates the stability of photoluminescent (PL) properties of microporous silicon nanoparticles ( $\mu\text{pSi-NPs}$ ) synthesized by electrochemical etching of monocrystalline silicon followed by lyophilization.

**Experimental:** Structural analysis revealed a highly porous architecture with  $< 2$ -nm pores and silicon nanocrystals (nc-Si) with an average size of 3–5 nm. Fourier-transform infrared spectroscopy confirmed the presence of Si–O–Si bonds, indicating surface oxidation of nc-Si. PL studies demonstrated a broad emission band peaking at 685 nm, attributed to exciton recombination in nc-Si. After 5 months of storage, the PL peak shifted to 655 nm, reflecting oxidation-induced size reduction of nc-Si. Raman spectra showed a  $1.5\text{ cm}^{-1}$  shift of the Si phonon peak along with spectral broadening, evidencing phonon confinement and partial amorphization. XANES analysis further confirmed increased suboxide content and structural disorder.

**Conclusions:** Biological experiments demonstrated the biocompatibility of  $\mu\text{pSi-NPs}$  and retention of their PL activity, highlighting their potential for biomedical applications such as bioimaging and biosensing.

**Keywords:** Porous silicon, Lyophilization, Photoluminescence, XANES, Raman scattering, Bioimaging

**Funding:** This work was supported by Russian Science Foundation grant No. 24-15-00137 (<https://rscf.ru/project/24-15-00137/>) for nanoparticle synthesis and structural characterization Lomonosov Moscow State University grant No. 23-SCH06-19 for cellular imaging studies, BASIS Foundation grant No. 23-2-2-18-1 for optical properties investigation.

**Acknowledgments:** The research utilized equipment from the Lomonosov Moscow State University Shared Facilities Center «Technologies for Obtaining New Nanostructured Materials and Their Comprehensive Study».

**For citation:** Nazarovskaia D. A., Turishchev S. Yu., Titova S. S., Shatov A. A., Tyurin-Kuzmin P. A., Osminkina L. A. Photoluminescent properties of porous silicon nanoparticles: synthesis, characterization, and cellular imaging. *Condensed Matter and Interphases*. 2025;27(3): 422–432. <https://doi.org/10.17308/kcmf.2025.27/13181>

**Для цитирования:** Назаровская Д. А., Турищев С. Ю., Титова С. С., Шатов А. А., Тюрин-Кузьмин П. А., Осминкина Л. А. Фотолуминесцентные свойства наночастиц пористого кремния: синтез, характеристика и визуализация в клетках. *Конденсированные среды и межфазные границы*. 2025;27(3): 422–432. <https://doi.org/10.17308/kcmf.2025.27/13181>

✉ Liubov A. Osminkina, e-mail: [osminkina@physics.msu.ru](mailto:osminkina@physics.msu.ru)

© Nazarovskaia D. A., Turishchev S. Yu., Titova S. S., Shatov A. A., Tyurin-Kuzmin P. A., Osminkina L. A., 2025



The content is available under Creative Commons Attribution 4.0 License.

## 1. Introduction

The photoluminescence (PL) of porous silicon (pSi) was first discovered in the early 1990s, generating significant scientific interest due to its potential applications in optoelectronics and biomedicine [1]. However, the practical applications of pSi have been limited by the temporal instability of its PL properties, primarily caused by surface oxidation under ambient conditions. This oxidation leads to a gradual reduction in PL intensity and spectral shifts. Various surface passivation techniques have been developed to address this issue, including chemical modification, thermal oxidation, and polymer coating, all aimed at protecting the silicon surface and preserving its optical properties. The choice of an appropriate stabilization method depends on specific operational requirements and desired material characteristics.

Porous silicon nanoparticles (pSi-NPs) exhibit considerable potential for diverse biological applications, particularly in biosensing [7, 8], targeted drug delivery [9], and novel therapeutic approaches involving controlled interactions with cells and tissues [10, 11]. Their biomedical utility derives from several advantageous properties: excellent biocompatibility, low cytotoxicity, tunable biodegradation rates, and a highly porous structure with large surface area that facilitates efficient drug loading and surface functionalization [12].

The PL phenomenon in pSi-NPs originates from quantum confinement effects in silicon nanocrystals typically ranging from 2 to 7 nm in size. This spatial restriction of charge carriers leads to bandgap widening and a shift of the emission spectrum into the visible range, predominantly the red-orange region. Surface characteristics, including defects and chemical termination (hydride or oxide groups), significantly influence both the intensity and the spectral profile of PL emission [13–15].

These unique optical properties enable various biomedical applications, particularly in diagnostic imaging where pSi-NPs serve as effective contrast agents. Their strong luminescence and broad excitation spectrum allow tracking of cells

and tissues using conventional fluorescence microscopy techniques, both *in vitro* and *in vivo* [16–18].

The pore size critically determines the physicochemical and functional properties of pSi-NPs. Microporous structures (pores < 2 nm) exhibit rapid biodegradation under physiological conditions, which limits their applicability for long-term delivery but makes them useful for short-term therapeutic applications. Mesoporous materials (pores 2–50 nm) provide an optimal balance between degradation rate and loading capacity for therapeutic molecules such as drugs, proteins, and DNA. Macroporous variants (pores > 50 nm) are mainly used in photonics, filtration, and other engineering applications due to their large pore size and limited capacity to effectively retain bioactive molecules [15].

During fabrication, nanoscale pores can generate substantial capillary forces during solvent evaporation, potentially reaching pressures exceeding 100 MPa in 2 nm pores according to the Laplace equation ( $\Delta P = \frac{2\alpha}{r}$ ),

where  $\Delta P$  is the pressure difference between the liquid and vapor phases,  $\alpha$  is the surface tension coefficient of the liquid, and  $r$  is the pore radius. These forces often produce structurally heterogeneous and mechanically fragile materials. Lyophilization has emerged as an effective processing technique that maintains structural integrity while enabling production of highly porous (> 90 %) materials with enhanced PL characteristics. XANES studies have confirmed that lyophilization effectively limits surface oxidation to superficial layers (2–3 nm), preserving the optical properties over extended storage periods [20, 21].

The current study focuses on a comprehensive characterization of microporous silicon nanoparticles produced by electrochemical etching and lyophilization, with particular emphasis on analyzing surface composition and evaluating optical properties. Special attention is given to assessing the stability of these properties during air exposure, as this critically determines their suitability for biological imaging applications. The investigation combines

advanced spectroscopic techniques with morphological analysis to establish structure–property relationships essential for optimizing biomedical performance.

## 2. Experimental

### 2.1. Synthesis of microporous silicon films

Microporous silicon films ( $\mu\text{PSi}$ ) were synthesized by electrochemical etching of monocrystalline silicon wafers (c-Si) with (100) orientation and resistivity of  $10\ \Omega\cdot\text{cm}$ . To ensure uniform and reproducible etching, a thin aluminum layer was deposited on the backside of the wafers to serve as an ohmic contact. The silicon etching was performed in a 1:1 mixture of concentrated HF (48 %) and ethanol at  $50\ \text{mA}/\text{cm}^2$  for 30 minutes. The resulting films were delaminated in a 1:20 HF:ethanol solution at  $4\ \text{mA}/\text{cm}^2$  for 250 seconds [22].

### 2.2. Lyophilic drying

The  $\mu\text{PSi}$  films were rinsed with deionized water (three washing cycles) to remove residual acid and then lyophilized for 12 h using a benchtop freeze-dryer (Advantage 2.0 ES-53). The dried  $\mu\text{PSi}$  powder were stored in sealed glass containers at room temperature in the dark.

### 2.3. Characterization of optical properties

The surface chemical composition of  $\mu\text{PSi}$  powder was studied using an IR-8000 Fourier-transform infrared spectrometer equipped with a diamond ATR accessory in the range of  $400\text{--}4000\ \text{cm}^{-1}$ . Raman scattering and PL spectra of the samples were measured with a Confotec™ MR350 confocal Raman microscope. Raman spectra were recorded using 785 nm laser excitation at a low power of 1 mW to avoid sample overheating, with an acquisition time of 60 s per spectrum. PL spectra were acquired under 488 nm laser excitation with an exposure time of 10 s.

### 2.4. Structural analysis by XANES spectroscopy

X-ray absorption near-edge structure (XANES) spectroscopy was employed to study the local atomic environment and electronic structure of nanoparticles. Si  $L_{2,3}$ -edge and O K-edge XANES spectra were collected using high-

intensity radiation from a “megascience”-class synchrotron source (KISI-Kurchatov synchrotron, NanoPES beamline, NRC “Kurchatov Institute”, Moscow, Russia) [29], enabling tunable X-ray energies without intensity loss. XANES provides information about the local partial density of unoccupied electronic states in the conduction band [23, 24], exhibiting exceptional sensitivity to atomic coordination environments [25–28]. The analysis depth was  $\sim 5\ \text{nm}$  for Si  $L_{2,3}$  spectra [30] and  $\sim 10\ \text{nm}$  for O K spectra [31], with instrumental broadening of 0.1 eV. Experiments were conducted at  $\sim 10^{-10}$  Torr vacuum, detecting total electron yield (TEY) via sample drain current. The synchrotron beam incidence angle was  $90^\circ$  to the surface plane, with samples mounted on Omicron flag-type holders for charge dissipation. Reference spectra were acquired from: crystalline silicon (c-Si), amorphous silicon on Si (a-Si) with native  $\text{SiO}_2$  ( $< 2\ \text{nm}$ ), thermal  $\text{SiO}_2$  film on Si (20 nm).

### 2.5. Nanoparticle preparation and morphology studies

For luminescent labeling applications, lyophilized  $\mu\text{PSi}$  films were fragmented into nanoparticles ( $\mu\text{PSi}$ -NPs) using a FRITSCH Pulverisette 7 premium line planetary mill (30 min in ethanol). The resulting suspensions were sedimented for 24 hours to remove large particles, with the supernatant used for experiments.

Morphology and size distribution of  $\mu\text{PSi}$ -NPs were characterized by transmission electron microscopy (TEM, LEO 912 AB, 100 kV accelerating voltage). For TEM imaging, ethanol suspensions of  $\mu\text{PSi}$ -NPs were drop-cast onto 3 mm copper grids with carbon support films and vacuum-dried for 10 minutes.

### 2.6. Confocal luminescence microscopy

Mesenchymal stem cells (MSCs) were isolated from human abdominal subcutaneous adipose tissue obtained during bariatric surgeries performed at the Medical Research and Education Center of Lomonosov Moscow State University. All donors were female with a mean age of  $39 \pm 7$  years and a body mass index of  $22 \pm 1$ . Written informed consent was obtained from

each participant, and the study protocol was approved by the Local Ethics Committee of the Medical Research and Education Center (IRB00010587, Moscow, Russia; Protocol No. 4, June 4, 2018). Adipose tissue samples (0.5–5 mL) were homogenized and digested in a solution containing Collagenase I (200 U/mL, Worthington Biochemical, USA) and Dispase (40 U/mL, Sigma-Aldrich, USA) with continuous agitation for 30–40 minutes at 37 °C. The digested tissue was centrifuged at 200×g for 10 minutes, after which the supernatant was discarded. The pellet containing MSCs was subjected to hypotonic lysis to remove erythrocytes, filtered through a 100-µm cell strainer (BD Falcon, USA), and centrifuged again at 200×g for 10 minutes. The final pellet was resuspended in culture medium for further expansion.

MSCs were cultured in low-glucose DMEM (1 g/L, PanEco, Russia) supplemented with 10 % fetal bovine serum (HyClone, Cytiva, USA) and 1 % antibiotic-antimycotic solution (HyClone, Cytiva, USA). Cells were maintained at 37 °C in a 5 % CO<sub>2</sub> incubator (Binder, Tuttlingen, Germany) and passaged at 80–90 % confluency using Versene (PanEco, Russia) and trypsin (PanEco, Russia). MSCs at passages 5–6 were used for experiments. To confirm their multipotency, the cells were stained for surface markers CD73, CD90, CD105, and CD34 and induced to differentiate into osteogenic, adipogenic, and chondrogenic lineages as previously described [34].

For microscopy, cells were seeded in confocal dishes and allowed to adhere overnight. µPSi-NPs were then added and incubated with the MSCs for 10 hours prior to imaging. The intracellular localization of the nanoparticles was visualized using a Zeiss LSM780 confocal microscope equipped with a Plan-Apochromat 63×/1.40 Oil DIC objective. Luminescence was excited using a 405 nm diode laser, and the intrinsic luminescence of the nanoparticles was detected in the 409–700 nm range with a pinhole setting of 1 au.

### 3. Results and discussion

Fig. 1 presents a TEM micrograph showing the morphology of the synthesized µPSi-NPs

The image confirms the presence of a well-developed porous structure in the material. The size of individual nanoparticles is estimated to be in the range of 100–200 nm. The micrograph also reveals non-uniform pore structure, which may be attributed to the synthesis conditions and lyophilic drying process.

Fig. 2 displays the FTIR transmission spectrum of µPSi, showing characteristic absorption bands associated with Si-O-Si groups. The band at approximately 460 cm<sup>-1</sup> corresponds to rocking vibrations of Si-O-Si bonds, while the band near 840 cm<sup>-1</sup> indicates symmetric stretching vibrations. Asymmetric stretching vibrations of Si-O-Si are observed at 1050 cm<sup>-1</sup>, confirming the presence of an oxide surface formed during lyophilic drying and subsequent air storage of the samples.

Fig. 3 shows the Si L<sub>2,3</sub>-edge XANES spectra of reference samples (crystalline silicon c-Si, amorphous silicon a-Si, and thermal L<sub>2,3</sub> film) and the studied µPSi powder.

The crystalline silicon (c-Si) spectrum exhibits distinct fine structure (region A) associated with the 0.6 eV spin-orbit splitting of silicon's L<sub>2,3</sub> core level. This characteristic feature reflects the high degree of atomic ordering in the c-Si lattice.

Region A of the amorphous silicon reference exhibits simpler fine structure due to the blurring of electron density states. In the energy

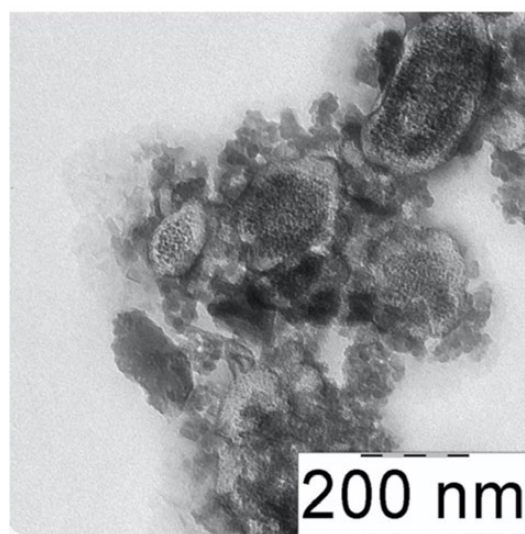
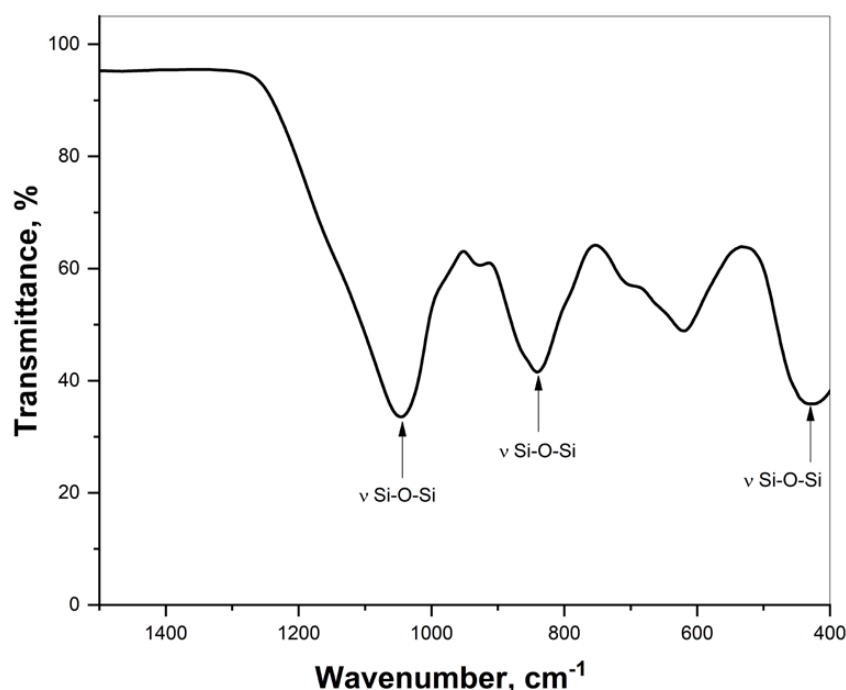


Fig. 1. TEM micrograph of µPSi-NPs



**Fig. 2.** FTIR transmission spectrum of  $\mu$ PSi powder. The absorption bands correspond to the stretching vibrations of Si-O-Si bonds

range of synchrotron radiation up to 104 eV, the absorption edge is absent for the reference thermal  $\text{SiO}_2$  film. However, for the studied  $\mu$ PSi powder, the absorption edge is clearly detected ( $h\nu < 104$  eV) though lacking distinct fine structure features A characteristic of crystalline c-Si, while showing higher intensity than the a-Si reference (Fig. 3b). This indicates certain disordering in the silicon atomic network, whose signal nevertheless remains present in the recorded spectra. Comparative analysis of fine structures in reference spectra of c-Si and a-Si (with native oxide) along with thermal  $\text{SiO}_2$  film reveals that for synchrotron radiation energies above 104 eV (characteristic features B and C), the powder spectrum generally corresponds to silicon atoms bonded to oxygen atoms. Notably, the  $\mu$ PSi powder spectrum (Fig. 3a) shows relative intensity enhancement in the 104–105 eV range compared to references. Such spectral intensity elevation typically indicates contributions from silicon suboxides in the surface layer of  $\mu$ PSi [25, 28]. Deviation from  $\text{SiO}_2$  stoichiometry is further evidenced by altered intensity ratios of features B and C in  $\mu$ PSi compared to references. Additionally, the broadened feature C (Fig. 3b) suggests

possible silicon suboxide contributions. An extra spectral feature around 108 eV (near feature C) results from partial surface charging during leakage current (sample current) measurements. Previous studies [36, 37] have reported various «intensity inversion» effects in  $\text{Si L}_{2,3}$  XANES fine structures, attributed to interaction phenomena between synchrotron radiation and silicon-based structures.

The O K-edge XANES spectra (Fig. 3b) for thermal  $\text{SiO}_2$  film and  $\mu$ PSi powder demonstrate that while the positions and relative intensity distributions of main features A, B, and C indicate predominant  $\text{SiO}_2$  coating on powder particles, the enhanced intensity of feature A reveals deviations from stoichiometric  $\text{SiO}_2$  [38, 39], consistent with  $\text{Si L}_{2,3}$  edge spectroscopy data.

Thus, the  $\text{Si L}_{2,3}$  and O K-edge XANES spectra (Fig. 3) demonstrate that  $\mu$ PSi is characterized by: disordering of the silicon atomic lattice, the presence of suboxides, deviation from stoichiometric  $\text{SiO}_2$  composition. These features indicate a complex and heterogeneous surface structure of the samples.

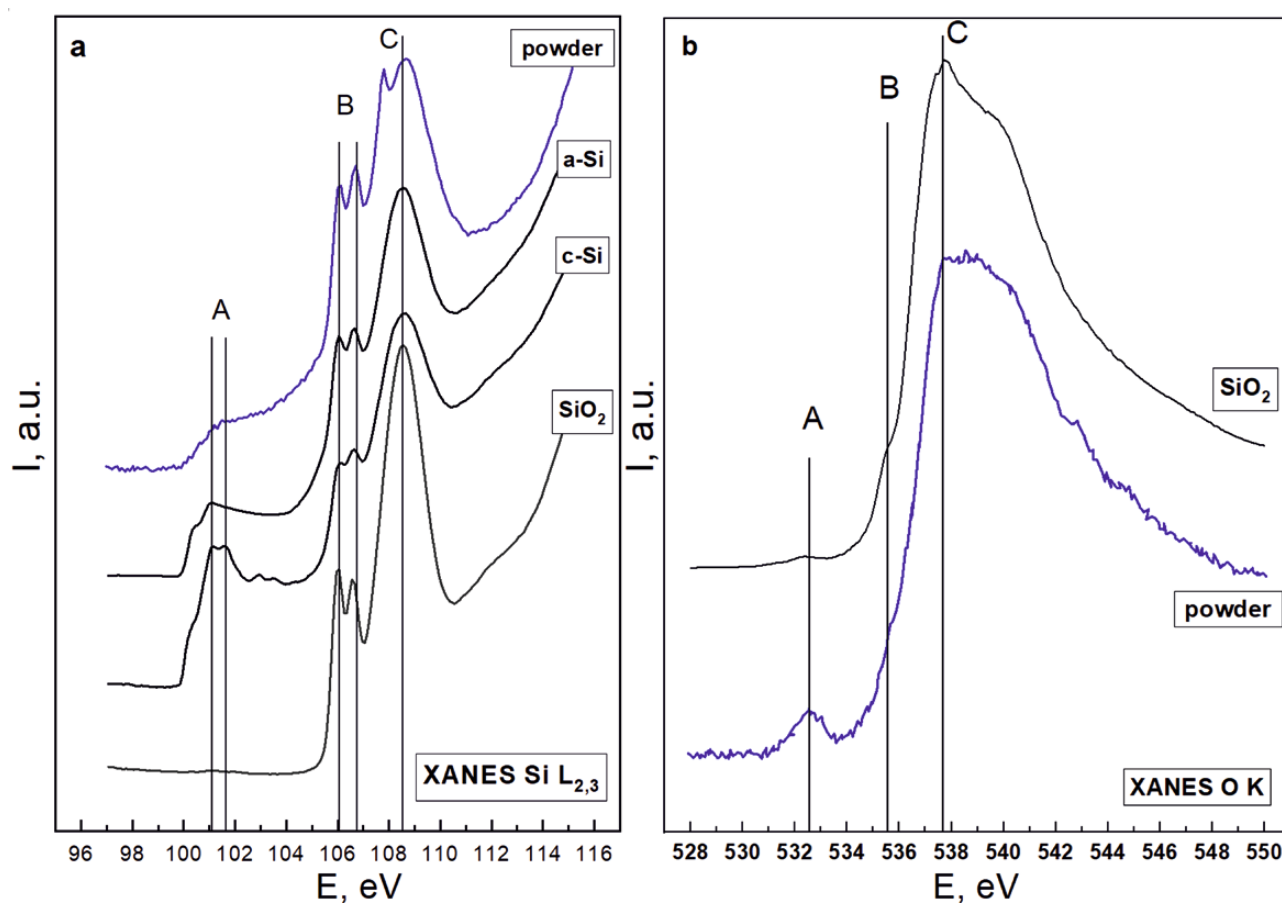


**Fig. 3.** (a) Si  $L_{2,3}$ -edge XANES spectra of  $\mu$ PSi powder and reference samples: crystalline silicon (c-Si), amorphous silicon (a-Si), and thermal  $\text{SiO}_2$  film. Regions A, B, and C correspond to features associated with silicon atoms and their bonding with oxygen. (b) O K-edge XANES spectra of  $\mu$ PSi powder and thermal  $\text{SiO}_2$  film. The relative intensity increase of feature A in the powder indicates deviations from stoichiometric  $\text{SiO}_2$  composition

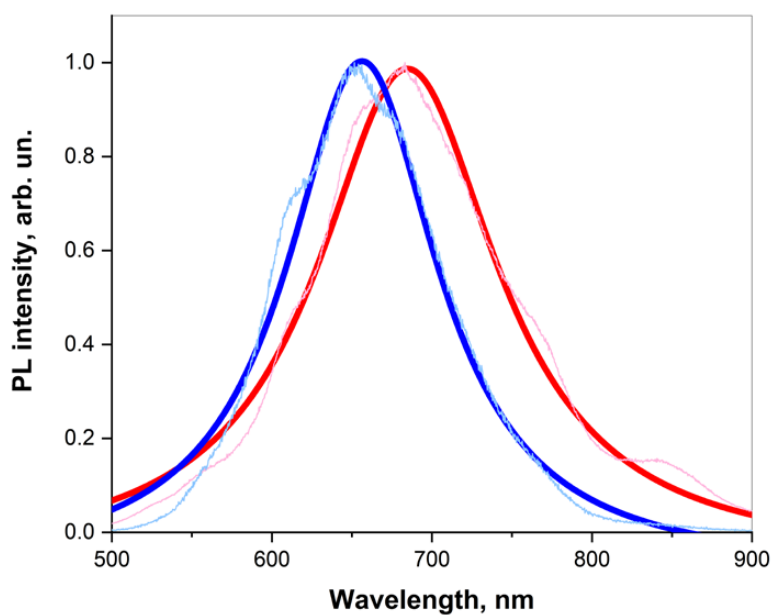


**Fig. 4.** PL spectra of  $\mu$ PSi powder: freshly prepared samples (red) and after 5 months of air storage (blue). Thick lines represent Lorentzian fitting of experimental spectra (thin lines)

Fig. 4 shows the PL spectrum of  $\mu$ PSi powder for freshly prepared samples (red curve) and after 5 months of air storage (blue curve).

The spectrum of freshly prepared samples exhibits a broad band with a maximum at 685 nm, which is attributed to radiative exciton annihilation in silicon nanocrystals (nc-Si). The spectral broadening is explained by the size distribution of nanocrystals, which is typical for such materials.

The position of the PL maximum correlates with the average nanocrystal size  $d$  according to the empirical formula [3]:

$$E(d) = E_0 + \frac{3.73}{d^{1.39}}, \quad (1)$$

where  $E_0$  is the band gap of c-Si (1.12 eV). The average nanocrystal diameter in freshly prepared samples, calculated from PL spectra using formula (1), was determined to be 3.8 nm.

After 5 months of storage, the spectrum shows a blue shift (maximum at 655 nm), indicating a reduction in the average nanocrystal size to 3.3 nm. This effect can be explained by gradual oxidation of silicon nanocrystals in air, leading to

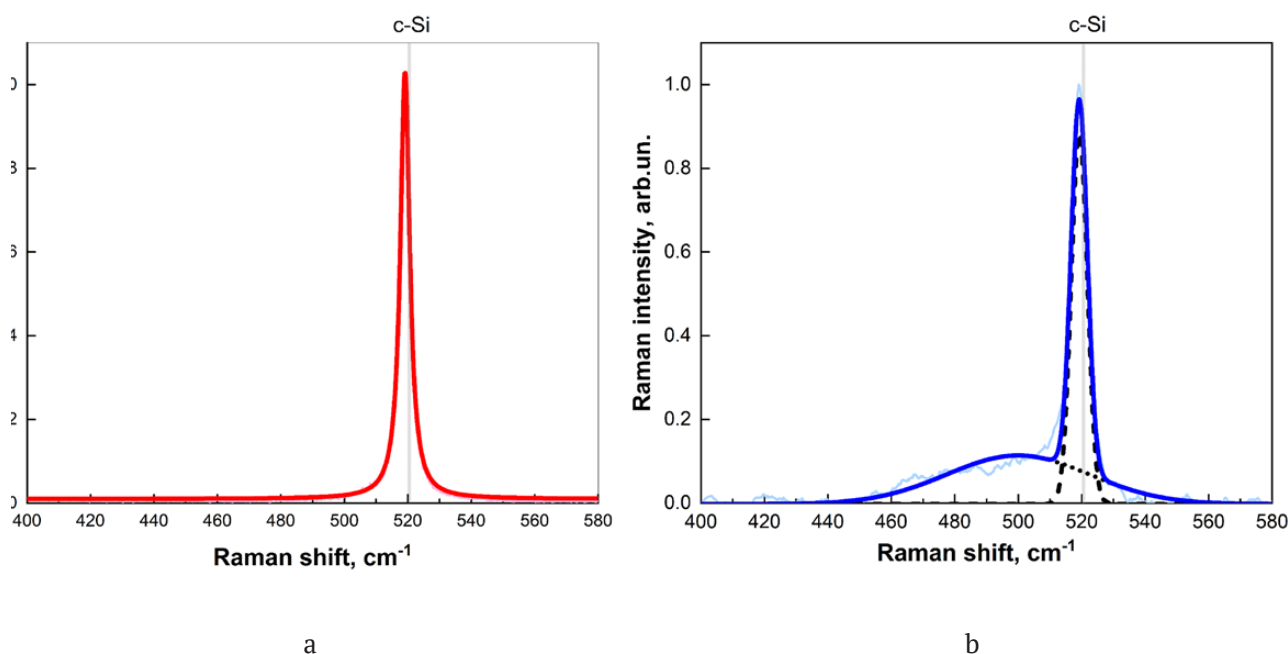
an increased oxide phase fraction and reduction of their effective size.

Fig. 5 presents Raman spectra for freshly prepared  $\mu$ PSi powder (a) and after 5 months of air storage (b). The intense peak in both spectra corresponds to phonon scattering from the silicon lattice. Due to quantum confinement of phonons in small-sized nc-Si, the observed peak is shifted to lower frequencies relative to the value for c-Si ( $520.5 \text{ cm}^{-1}$ ) by  $\Delta\omega = 1.5 \text{ cm}^{-1}$ . This confirms the presence of silicon nanocrystals in the sample structure.

For precise peak position determination, the spectra were fitted with Lorentzian functions, enabling calculation of the average nanocrystal size using the empirical formula [40]:

$$d = 0.543 \left( \frac{52.3}{\Delta\omega} \right)^{0.63}. \quad (2)$$

The calculated average diameter of nanocrystals in freshly prepared samples was 5.3 nm. After air storage, the Raman peak position remains virtually unchanged, indicating preservation of the overall nanocrystal size. However, spectral broadening with formation of



**Fig. 5.** Raman spectra of  $\mu$ PSi powder: (a) freshly prepared and (b) after 5 months of air storage. In (a), the thick line represents Lorentzian fitting of the experimental spectrum (thin line). In (b), the thick line shows the fitting and sticks represent the deconvolution of the experimental spectrum (thin line)

a low-frequency shoulder is observed, associated with partial amorphization of nanocrystals due to surface oxidation [41].

Spectral deconvolution allowed estimation of phase composition: the crystalline and amorphous fractions of the powder after storage were 46.3% and 53.7%, respectively. These changes confirm that surface oxidation leads to structural heterogeneity accompanied by partial loss of crystalline ordering.

It should be noted that the discrepancy between nc-Si sizes calculated from PL and Raman data arises from the different sensitivities of these techniques to surface processes, oxidation state, and phase composition of nanocrystals. PL reflects an average «effective» size including oxidation effects, while Raman characterizes the dimensions of the ordered part of the material crystal lattice.

The photoluminescent properties of  $\mu$ PSi-NPs enable their use as fluorescent labels for cell visualization. Figure 6 shows microscopy images of MSCs (mesenchymal stem cells) after 10 hours of incubation with  $\mu$ PSi-NPs.

Fig. 6b clearly demonstrates the efficient luminescence of  $\mu$ PSi-NPs localized in the cell cytoplasm, indicating that the particles retain their PL properties upon incubation with cells.

#### 4. Conclusions

In this work, the morphological, structural, and optical properties of  $\mu$ PSi-NPs synthesized

by electrochemical etching followed by lyophilization were investigated. Transmission electron microscopy, infrared spectroscopy, and Raman spectroscopy revealed that  $\mu$ PSi powders possess a well-developed porous architecture with silicon nanocrystals of about 4–5 nm in size. The surface of the samples was found to contain oxide groups, as confirmed by IR and XANES spectroscopy.

PL analysis showed that the nanocrystals retain their luminescent properties after 5 months of storage in air. Nevertheless, a blue shift of the PL peak was observed, associated with a reduction in the effective nanocrystal size, most likely due to surface oxidation. Raman spectra further indicated partial surface amorphization of the nanocrystals during storage, manifested by spectral broadening and the appearance of a low-frequency shoulder, which is consistent with oxidation processes. The PL properties of  $\mu$ PSi-NPs, which remain stable during interaction with mesenchymal stem cells, confirm their promise for bioimaging and biosensing applications.

Importantly, the findings demonstrate that lyophilization is an effective method for preserving the structural and optical characteristics of  $\mu$ PSi-NPs during storage, thereby supporting their suitability for future biomedical and optical applications.

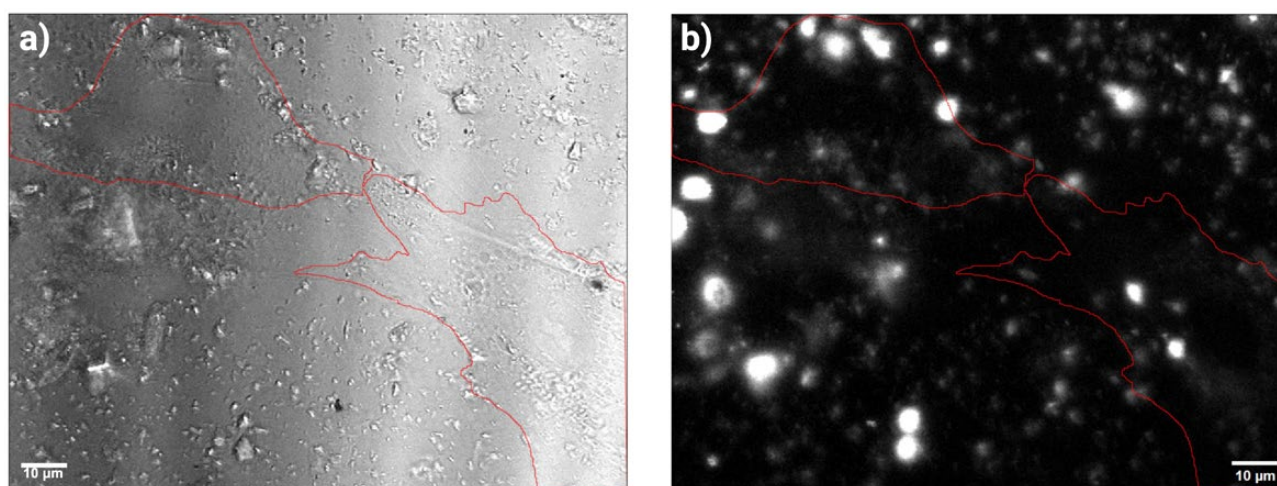


**Fig. 6.** Microscopy images of live MSCs after 10 h of incubation with  $\mu$ PSi-NPs: (a) bright-field image; (b) photoluminescence image. Red lines outline the cell borders. Scale bar: 10  $\mu$ m

## Contribution of authors

The authors contributed equally to this article.

## Conflict of interests

The authors declare that they have no known competing financial interests or personal relationships that could have influenced the work reported in this paper.

## References

- Cullis A. G., Canham L. T. Visible light emission due to quantum size effects in highly porous crystalline silicon. *Nature*. 1991;353(6342): 335–338. <https://doi.org/10.1038/353335a0>
- Lauerhaas J. M., Sailor M. J. Chemical modification of the photoluminescence quenching of porous silicon. *Science*. 1993;261(5128): 1567–1568. <https://doi.org/10.1126/science.261.5128.1567>
- Gongalsky M. B., Kargina J. V., Cruz J. F., ... Sailor M. J. Formation of Si/SiO<sub>2</sub> luminescent quantum dots from mesoporous silicon by sodium tetraborate/citric acid oxidation treatment. *Frontiers in Chemistry*. 2019;7: 165. <https://doi.org/10.3389/fchem.2019.00165>
- Salonen J., Mäkilä E. Thermally carbonized porous silicon and its recent applications. *Advanced Materials*. 2018;30(24): 1703819. <https://doi.org/10.1002/adma.201703819>
- Erogbogbo F., Yong K. T., Roy I., Xu G., Prasad P. N., Swihart M. T. Biocompatible luminescent silicon quantum dots for imaging of cancer cells. *ACS Nano*. 2008;2(5): 873–878. <https://doi.org/10.1021/nn700319z>
- Morozova S., Alikina M., Vinogradov A., Pagliaro M. Silicon quantum dots: synthesis, encapsulation, and application in light-emitting diodes. *Frontiers in Chemistry*. 2020;8: 191. <https://doi.org/10.3389/fchem.2020.00191>
- Sobina I. O., Tyurin-Kuzmin P. A., Pervushin N. V., ... Osminkina L. A. Gold-modified silicon microneedles for real-time SERS analysis and drug delivery at single-cell resolution. *Microchemical Journal*. 2025;2015: 114178. <https://doi.org/10.1016/j.microc.2025.114178>
- Nazarovskaia D. A., Domnin P. A., Gyuppenen O. D., ... Osminkina L. A. Advanced bacterial detection with SERS-active gold-and silver-coated porous silicon nanowires. *Bulletin of the Russian Academy of Sciences: Physics*. 2023;87(Suppl 1): S41–S46. <https://doi.org/10.1134/S1062873823704385>
- Waggoner L. E., Kang J., Zuidema J. M., ... Kwon E. J. Porous silicon nanoparticles targeted to the extracellular matrix for therapeutic protein delivery in traumatic brain injury. *Bioconjugate Chemistry*. 2022;33(9): 1685–1697. <https://doi.org/10.1021/acs.bioconjchem.2c00305>
- Osminkina L. A., Timoshenko V. Y. Porous silicon as a sensitizer for biomedical applications. *Open Material Sciences*. 2016;3(1). <https://doi.org/10.1515/mesbi-2016-0005>
- Zeng Q., Han K., Zheng C., ... Lu T. Degradable and self-luminescence porous silicon particles as tissue adhesive for wound closure, monitoring and accelerating wound healing. *Journal of Colloid and Interface Science*. 2022;607: 1239–1252. <https://doi.org/10.1016/j.jcis.2021.09.092>
- Santos H. A. (ed.). *Porous silicon for biomedical applications (second edition)*. The United Kingdom: Woodhead Publishing; 2021. <https://doi.org/10.1016/b978-0-12-821677-4.00007-0>
- Cullis A. G., Canham L. T., Calcott P. D. J. The structural and luminescence properties of porous silicon. *Journal of Applied Physics*. 1997;82(3): 909–965. <https://doi.org/10.1063/1.366536>
- Skorb E. V., Andreeva D. V., Möhwald H. Generation of a porous luminescent structure through ultrasonically induced pathways of silicon modification. *Angewandte Chemie International Edition*. 2012;21(51): 5138–5142. <https://doi.org/10.1002/anie.201105084>
- Sailor M. J. (ed.). *Porous silicon in practice: preparation, characterization and applications*. Weinheim, Germany: Wiley-VCH Verlag & Co.; 2011. <https://doi.org/10.1002/9783527641901>
- Park J. H., Gu L., von Maltzahn G., Ruoslahti E., Bhatia S. N., Sailor M. J. Biodegradable luminescent porous silicon nanoparticles for in vivo applications. *Nature Materials*. 2009;8: 331–336. <https://doi.org/10.1038/nmat2398>
- Gu L., Hall D. J., Qin Z., ... Sailor M. J. In vivo time-gated fluorescence imaging with biodegradable luminescent porous silicon nanoparticles. *Nature communications*. 2013;4(1): 2326. <https://doi.org/10.1038/ncomms3326>
- Shatskaia M. G., Nazarovskaia D. A., Gonchar K. A., ... Osminkina L. A. Photoluminescent porous silicon nanowires as contrast agents for bioimaging. *Condensed Matter and Interphases*. 2024;26(1): 161–167. <https://doi.org/10.17308/kcmf.2024.26/11819>
- Kelly T. L., Gao T., Sailor M. J. Carbon and carbon/silicon composites templated in rugate filters for the adsorption and detection of organic vapors. *Advanced Materials*. 2011;15(23): 1776–1781. <https://doi.org/10.1002/adma.201004142>
- Amato G., Brunetto N., Parisini A. Characterisation of freeze-dried porous silicon. *Thin Solid Films*. 1997;297(1-2): 73–78. [https://doi.org/10.1016/S0040-6090\(96\)09412-6](https://doi.org/10.1016/S0040-6090(96)09412-6)
- Koyuda D. A., Titova S. S., Tsurikova U. A., ... Turishchev S. Yu. Composition and electronic structure of porous silicon nanoparticles after oxidation under air-or freeze-drying conditions. *Materials Letters*. 2022;312: 131608. <https://doi.org/10.1016/j.matlet.2021.131608>
- Kim D., Kang J., Wang T., ... Sailor M. J. Two-photon in vivo imaging with porous silicon nanoparticles. *Advanced Materials*. 2017;29(39): 1703309. <https://doi.org/10.1002/adma.201703309>

23. Stohr J. (ed.). *NEXAFS Spectroscopy*. Berlin, Germany: Springer International Publishing; 1996.
24. Bunker G. (ed.). *Introduction to XAFS*. Cambridge, the United Kingdom: Cambridge University Press; 2010.
25. Barranco A., Yubero F., Espinos J. P., Groening P., Gonzalez-Elipe A. R. Electronic state characterization of SiOx thin films prepared by evaporation. *Journal of Applied Physics*. 2005;97: 113714. <https://doi.org/10.1063/1.1927278>
26. Liu L., Sham T. K. The effect of thermal oxidation on the luminescence properties of nanostructured silicon. *Small*. 2012;8: 2371–2380. <https://doi.org/10.1002/smll.201200175>
27. Turishchev S. Yu., Parinova E. V., Pisliaruk A. K., ... Sivakov V. Surface deep profile synchrotron studies of mechanically modified top-down silicon nanowires array using ultrasoft X-ray absorption near edge structure spectroscopy. *Scientific Reports*. 2019;9: 8066. <https://doi.org/10.1038/s41598-019-44555-y>
28. Parinova E. V., Fedotov A. K., Koyuda D. A., ... Turishchev S. Y. The composite structures based on nickel rods in the matrix of silicon dioxide formation peculiarities study using synchrotron XANES in electrons and photons yield registration modes. *Condensed Matter and Interphases*. 2019;21(1): 116–125. <https://doi.org/10.17308/kcmf.2019.21/726>
29. Lebedev A. M., Menshikov K. A., Nazin V. G., Stankevich V. G., Tsetlin M. B., Chumakov R. G. Nano PES photoelectron beamline of the Kurchatov Synchrotron Radiation Source. *Journal of Surface Investigation: X-ray, Synchrotron and Neutron Techniques*. 2021;15: 1039–1044. <https://doi.org/10.1134/S1027451021050335>
30. Kasrai M., Lennard W. N., Brunner R. W., Bancroft G. M., Bardwell J. A., Tan K. H. Sampling depth of total electron and fluorescence measurements in Si L- and K-edge absorption spectroscopy. *Applied Surface Science*. 1996;99(4): 303–312. [https://doi.org/10.1016/0169-4332\(96\)00454-0](https://doi.org/10.1016/0169-4332(96)00454-0)
31. Erbil A., Cargill III G. S., Frahm R., Boehme R. F. Total-electron-yield current measurements for near-surface extended X-ray-absorption fine structure. *Physical Review B*. 1988;37: 2450–2464. <https://doi.org/10.1103/PhysRevB.37.2450>
32. Mushahary D., Spittler A., Kasper C., Weber V., Charwat V. Isolation, cultivation, and characterization of human mesenchymal stem cells. *Cytometry Part A*. 2018;93(1): 19–31. <https://doi.org/10.1002/cyto.a.23242>
33. Kulebyakin K., Tyurin-Kuzmin P., Sozaeva L., ... Vorontsova M. Dynamic balance between pth1r-dependent signal cascades determines its pro-or anti-osteogenic effects on MSC. *Cells*. 2022;11(21): 3519. <https://doi.org/10.3390/cells11213519>
34. Kulebyakin K., Tyurin-Kuzmin P., Efimenko A., ... Tkachuk V. Decreased insulin sensitivity in telomerase-immortalized mesenchymal stem cells affects efficacy and outcome of adipogenic differentiation in vitro. *Frontiers in Cell and Developmental Biology*. 2021;9: 662078. <https://doi.org/10.3389/fcell.2021.662078>
35. Turishchev S. Yu., Koyuda D. A., Terekhov V. A., ... Domashevskaya E. P. Electronic structure and composition of the surface layers of the multilayer nanoperiodical structures a-Si/ZrO<sub>2</sub> and a-SiOx/ZrO<sub>2</sub> according to synchrotron studies. *Condensed Matter and Interphases*. 2016;18(4): 558–567. (In Russ., abstract in Eng.). Available at: <https://www.elibrary.ru/item.asp?id=27474862>
36. Watanabe M., Ejima T., Miyata N., Imazono T., Yanagihara M. Studies of multilayer structure in depth direction by soft X-ray spectroscopy. *Nuclear Science and Techniques*. 2006;17(5): 257–267. [https://doi.org/10.1016/S1001-8042\(06\)60048-1](https://doi.org/10.1016/S1001-8042(06)60048-1)
37. Turishchev S. Y., Terekhov V. A., Koyuda D. A., ... Mashin A. I. Synchrotron investigation of the multilayer nanoperiodical Al<sub>2</sub>O<sub>3</sub>/SiO/Al<sub>2</sub>O<sub>3</sub>/SiO:Si structure formation. *Surface and Interface Analysis*. 2012;44(8): 1182–1186. <https://doi.org/10.1002/sia.4868>
38. Turishchev S. Y., Parinova E. V., Pisliaruk A. K., ... Sivakov V. Surface deep profile synchrotron studies of mechanically modified top-down silicon nanowires array using ultrasoft X-ray absorption near edge structure spectroscopy. *Scientific Reports*. 2019;9(1): 8066. <https://doi.org/10.1038/s41598-019-44555-y>
39. Engelhorn K., Recoules V., Cho B. I., ... Heimann P. A. Electronic structure of warm dense silicon dioxide. *Physical Review B*. 2015;91(21): 214305. <https://doi.org/10.1103/PhysRevB.91.214305>
40. Zi J., Zhang K., Xie X. Comparison of models for Raman spectra of Si nanocrystals. *Physical Review B*. 1997;55(15): 9263. <https://doi.org/10.1103/PhysRevB.55.9263>
41. Canham L. T. (ed.). *Handbook of porous silicon*. Berlin, Germany: Springer International Publishing; 2018. <https://doi.org/10.1007/978-3-319-71381-6>

## Information about the authors

*Darya A. Nazarovskaya*, postgraduate Student, Faculty of Physics, Lomonosov Moscow State University (Moscow, Russian Federation).

<https://orcid.org/0000-0001-8151-9602>

[nazarovskaia.da22@physics.msu.ru](mailto:nazarovskaia.da22@physics.msu.ru)

*Sergey Yu. Turischev*, Dr. Sci. (Phys.–Math.), Head of the Department of General Physics and Physical Materials Science, Physics Department, Voronezh State University (Voronezh, Russian Federation).

<https://orcid.org/0000-0003-3320-1979>

[tsu@phys.vsu.ru](mailto:tsu@phys.vsu.ru)

*Sofia S. Titova*, Lecturer, Department of General Physics and Physical Materials Science, Physics Department, Voronezh State University (Voronezh, Russian Federation).

<https://orcid.org/0000-0001-6860-401X>

[titova@phys.vsu.ru](mailto:titova@phys.vsu.ru)

*Artur A. Shatov*, student, Faculty of Physics, Lomonosov Moscow State University (Moscow, Russian Federation).

mr.ArturSh@mail.ru

*Pyotr A. Tyurin-Kuzmin*, Dr. Sci. (Biology), Associate Professor, Faculty of Medicine, Lomonosov Moscow State University (Moscow, Russian Federation); Institute for Biological Instrumentation of the Russian Academy of Sciences (Pushchino, Russian Federation).

<https://orcid.org/0000-0002-1901-1637>

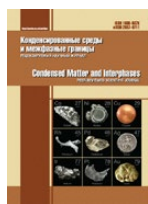
tyurinkuzminpa@my.msu.ru

*Liubov A. Osminkina*, Cand. Sci. (Phys.–Math.), Leading Researcher, Faculty of Physics, Lomonosov Moscow State University (Moscow, Russian Federation); Institute for Biological Instrumentation of the Russian Academy of Sciences (Pushchino, Russian Federation).

<https://orcid.org/0000-0001-7485-0495>

osminkina@physics.msu.ru

Received October 17, 2024; approved after reviewing October 30, 2024; accepted for publication November 15, 2024; published online September 25, 2025.



## Original articles

Research article

<https://doi.org/10.17308/kcmf.2025.27/13019>

## Study of photoluminescence kinetics in bulk GaPN and GaPNAs layers on silicon substrates grown by molecular beam epitaxy

E. V. Nikitina<sup>1,2</sup>, A. K. Kaveev<sup>1</sup>, V. V. Fedorov<sup>2</sup>, E. V. Pirogov<sup>2</sup>, A. M. Nadtochiy<sup>3</sup>, E. I. Vasilkova<sup>2✉</sup>, N. V. Kryzhanovskaya<sup>3</sup>, M. S. Sobolev<sup>2</sup>

<sup>1</sup>Ioffe Institute,  
26 Polytechnicheskaya st., St. Petersburg 194021, Russian Federation

<sup>2</sup>Alferov University,  
8/3 Khlopina st., St. Petersburg 194021, Russian Federation

<sup>3</sup>HSE University Saint Petersburg,  
16 Soyuz Pechatnikov st., St. Petersburg 194100, Russian Federation

### Abstract

**Objective:** The aim of this work is to study bulk GaPN and GaPNAs layers grown by molecular beam epitaxy on silicon substrates. The optical properties of the heterostructures were investigated using photoluminescence. The technique of time-resolved photoluminescence (or photoluminescence kinetics) was employed to evaluate the carrier lifetime in bulk GaPN and GaPNAs layers.

**Experimental:** An investigation of the influence of the buffer layer on the heterostructure characteristics was conducted. The photoluminescence intensity in the bulk GaPN layer was found to be virtually identical for heterostructures employing either a buffer layer grown by Migration-Enhanced Epitaxy (MEE-GaP buffer) or a GaP buffer layer grown with a gradual temperature ramp from 450 to 600 °C.

**Conclusion:** It was shown that the lifetime of minority carriers in the bulk GaPN layer grown on a silicon substrate is determined to a greater extent by defects introduced during the nitrogen incorporation into the GaP lattice, rather than by defects caused by growth on silicon substrate.

**Keywords:** Dilute nitrides, GaPN(As), Photoluminescence, Silicon substrate

**Funding:** The study was supported by the Russian Science Foundation No. 23-79-00032 (<https://rscf.ru/project/23-79-00032/>). The optical investigation of time-resolved photoluminescence was conducted on a unique setup “Complex optoelectronic unit of the National Research University Higher School of Economics - St. Petersburg”.

**For citation:** Nikitina E. V., Kaveev A. K., Fedorov V. V., Pirogov E. V., Nadtochiy A. M., Vasilkova E. I., Kryzhanovskaya N. V., Sobolev M. S. Study of photoluminescence kinetics in bulk GaPN and GaPNAs layers on silicon substrates grown by molecular beam epitaxy. *Condensed Matter and Interphases*. 2025;27(3): 433–440. <https://doi.org/10.17308/kcmf.2025.27/13019>

**Для цитирования:** Никитина Е. В., Кавеев А. К., Федоров В. В., Пирогов Е. В., Надточий А. М., Василькова Е. И., Крыжановская Н. В., Соболев М. С. Исследование кинетики фотолюминесценции объемных слоев GaPN и GaPNAs на подложках кремния, выращенных методом молекулярно-пучковой эпитаксии. *Конденсированные среды и межфазные границы*. 2025;27(3): 433–440. <https://doi.org/10.17308/kcmf.2025.27/13019>

✉ Elena I. Vasilkova, e-mail: [elenvasilkov@gmail.com](mailto:elenvasilkov@gmail.com)

© Nikitina E. V., Kaveev A. K., Fedorov V. V., Pirogov E. V., Nadtochiy A. M., Vasilkova E. I., Kryzhanovskaya N. V., Sobolev M. S., 2025



The content is available under Creative Commons Attribution 4.0 License.

## 1. Introduction

Solid solutions of ternary and quaternary  $A^{III}B^V N$  compounds with a nitrogen mole fraction of a few percent form a new class of promising materials for optoelectronic devices, known as “dilute nitrides”. These solid solutions are promising for fabricating silicon-based optoelectronic devices, such as LEDs, photodetectors, lasers, and high-efficiency multijunction solar cells [1]. The addition of less than one percent of nitrogen to gallium phosphide (GaP) lattice results in the formation of direct-bandgap GaPN material. Increasing the nitrogen mole fraction in ternary and quaternary  $A^{III}B^V N$  compounds leads to a significant reduction in the bandgap energy accompanied by a decrease in the lattice constant [2, 3]. This unusual property of dilute nitrides arises from the substitution of a small fraction of group V elements (P and/or As) with nitrogen atoms, which substantially modifies the conduction band, splitting it into two non-parabolic subbands ( $E^-$  and  $E^+$ ). The Band Anticrossing Model (BACm), describing the formation of this new band structure, was proposed and developed in [4]. Adding arsenic atoms to GaPN to create a quaternary solid solution allows tuning the bandgap energy over a wide range (1.5–2.0 eV) while maintaining lattice matching with silicon substrates through variation of group V elements ratios in GaPNAs [5]. However, experimental studies reveal low minority carrier lifetimes in GaPNAs active layers grown on gallium phosphide and silicon substrates by MOCVD [6] and MBE [7], attributed to the high density of defects. Reducing the defect densities in GaPN(As) solid solutions grown on silicon substrates can be achieved through the optimization of the buffer layer design and epitaxial growth parameters for the dilute nitride layers. The challenge in forming gallium phosphide buffer layers on the silicon surface stems from potential chemical reactions at the interface, where gallium atoms can etch the silicon surface, leading to pit formation [8]. Currently, a commonly used approach to creating a transition layer between the silicon substrate and the active layer based on dilute nitrides is the Migration-Enhanced Epitaxy (MEE) GaP buffer [9]. The MEE technique involves alternating the phosphorus and gallium

flux supply to the substrate at lower growth temperatures. However, the implementation of this technique inevitably reduces the service life of the shutters in a molecular beam epitaxy system [10]. An alternative approach for epitaxial growth of GaP buffer layers on silicon substrate, as demonstrated in [11], involves growing a buffer layer composed of low-temperature (440 °C) and high-temperature (580 °C) bulk GaP sublayers.

In this work, we studied the characteristics of heterostructures with active layers based on bulk ternary GaPN or quaternary GaPN(As) solid solutions, grown by molecular beam epitaxy (MBE) on silicon substrates. The characterization methods employed photoluminescence, X-Ray diffractometry, as well as time-resolved photoluminescence (photoluminescence kinetics).

## 2. Experimental

The studied epitaxial structures were obtained using the MBE method using a Veeco Gen III setup with a radio frequency (RF) inductively coupled nitrogen plasma source on Si (001) substrates with a 4° off-cut toward the [100] direction. The use of [100]-misoriented silicon substrates was necessary to prevent the appearance of antiphase domains at the silicon–gallium phosphide heterointerface. For the same purpose, a phosphorus monolayer was deposited on the silicon surface after substrate annealing in the growth chamber.

The samples studied consisted of a bulk layer of ternary or quaternary GaPN(As) solid solution grown on a buffer layer. Sample #1 featured a MEE-GaP buffer layer based on 45 periods of alternating sublayers of gallium and phosphorus [9], followed by 50 nm GaP layer grown at 450 °C. The buffer layer of other samples (#2, #3, #4) incorporated a thin (1 nm) ALP sublayer deposited at 450 °C, followed by GaP layer grown with a gradual temperature ramp to 600 °C. The ALP sublayer in these samples prevents etching of the silicon surface by gallium atoms. The GaPN bulk layers for samples #1 and #2 were formed under identical growth conditions with a nitrogen flow rate of 0.3 ml/min. For Sample #3, the power of the RF nitrogen plasma source was increased from 225 W (used for #1 and #2) to 250 W with a nitrogen flow of 0.35 ml/min to achieve higher

nitrogen mole fraction in GaPN layer. Sample #4 contained GaPNAs layer, grown with the same nitrogen flow and RF nitrogen plasma source power of 250 W and an arsenic flux to total group V flux ratio (As+P) of 0.1.

Diffraction rocking curves were obtained using a DRON-8 X-Ray diffractometer equipped with a BSV 29 fine-focus X-ray tube. The anode material was copper, utilizing  $K\alpha_1$  radiation ( $\lambda = 1.5405 \text{ \AA}$ ). Photoluminescence spectra were measured using an Accent Optical Technologies setup. The structures were studied by photoluminescence (PL) spectroscopy in the spectral range of 500–800 nm at room temperature. Optical excitation was provided by a continuous-wave solid-state laser operating at 266 nm, with an excitation power density of  $12 \text{ W/cm}^2$ .

The study of the time resolved photoluminescence was carried out by the up-conversion method using a FOG-100-DX-IR device for differential fluorescence kinetics measurements in the visible range. Laser pulses with a duration of 120 fs, a frequency of 80 MHz, and a wavelength of 780 nm, generated by a tunable titanium-sapphire laser CoherentMira 900D with a maximum average power of 1.5 W were used for gating and exciting the samples. To implement the optical excitation of the samples, the excitation

pulse was passed through a frequency-doubling system based on a nonlinear BBO ( $\beta\text{-BaB}_2\text{O}_4$ ) crystal. Thus, the sample excitation during time-resolved photoluminescence investigation was performed at a wavelength of 395 nm, while signal gating was produced by the primary pulse with a wavelength of 780 nm.

### 3. Results and discussion

Fig. 1 presents the room temperature photoluminescence spectra of the studied samples. Samples #1 and #2 featured different buffer layers, but the GaPN layer growth parameters were identical. The PL data revealed that the PL intensity of Sample #2 was 20 % higher, while its PL peak was redshifted. This suggests that Sample #2 achieved improved nitrogen incorporation into the GaP lattice, and the gradient buffer layer contributed to the formation of GaPN layers with enhanced photoluminescence relative to the conventional MEE-GaP buffer layer. As will be shown further by X-ray diffraction analysis, this difference was attributed to distinct strain relaxation mechanisms.

The nitrogen flux during the growth of sample #3 was increased compared to samples #1 and #2. The photoluminescence peak energy of the samples decreased with rising nitrogen

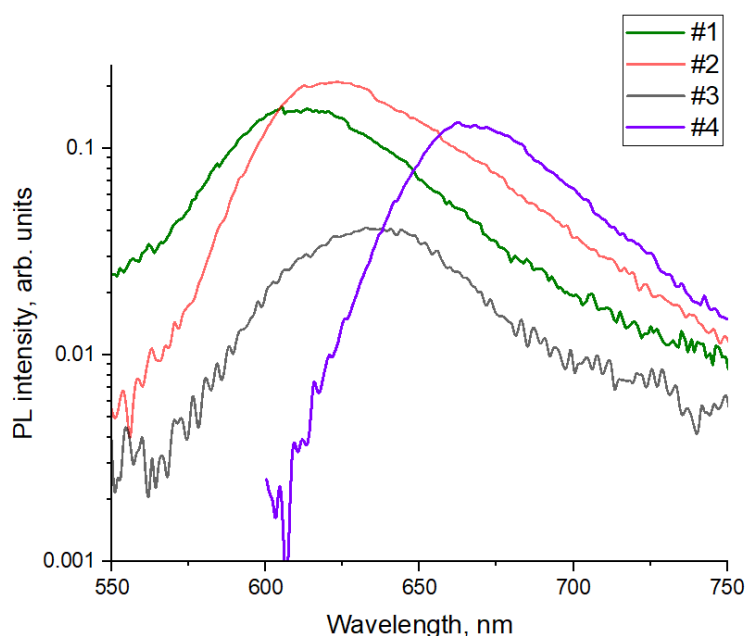


**Fig. 1.** Room-temperature photoluminescence spectra of bulk ternary GaPN (Samples #1, #2, #3) and quaternary GaPNAs (Sample #4) solid solutions

concentration in the epitaxial layer, corresponding to bandgap reduction (emission wavelength redshift). With an increase in nitrogen content in a solid solution there was typically a drastic fall in the photoluminescence peak intensity, as shown in [12]. This may be attributed to the formation of deep levels due to nitrogen incorporation, which act as nonradiative recombination centers. In our case, the peak PL intensity of Sample #3 was over 5 times lower relative to Sample #2. Additionally, PL intensity reduction in Sample #3 can be attributed to the fact that the bulk GaPN layer was no longer lattice-matched to silicon, as confirmed by X-Ray diffraction and will be discussed further, see Fig. 2.

Incorporating arsenic atoms into the GaPN solid solution enables lattice matching to silicon through tuning of group V element ratios, since

nitrogen reduces the lattice constant, while arsenic increases it. In Sample #4, grown with the nitrogen source parameters similar to that of Sample #3 and an As to P flux ratio of 0.1, arsenic incorporation resulted in a threefold increase in PL intensity of Sample #4 compared to Sample #3, accompanied by a PL peak wavelength shift towards 665 nm.

Fig. 2 shows the X-Ray rocking curves of the examined samples measured near the symmetrical Si reflection. The black vertical line indicates the theoretical position of the fully relaxed GaP diffraction peak. The calculated X-Ray rocking curves for GaP layers with different degrees of strain relaxation on silicon substrates are also presented.

The calculated position of the GaP diffraction peak in Sample #1 corresponded to a fully strained layer, while an analysis of the GaPN peak position reveals a nitrogen content of 1.5 %. The GaP diffraction peaks in Samples #2, #3 and #4 let us evaluate an approximate strain relaxation degree of ~ 55 %, as determined by comparing experimental data with the theoretical simulation. This can be attributed to dislocation formation during the initial stages of growth, which induced partial strain relaxation in the epitaxial layers of these samples. Consequently, the lattice parameter of GaP epitaxial layer approaches that of a fully relaxed GaP layer. Despite the significant difference in diffraction peak positions, the nitrogen mole fraction in the GaPN layer of Sample #1 approached that of Sample #2, where the nitrogen content reached approximately 1.8 %. This difference arose from the rightward shift of diffraction peaks due to strain relaxation in epitaxial layers, which is most prominent in Sample #3. The calculated nitrogen mole fraction in the GaPN layer of this sample was approximately 2.24 %, however, the GaPN diffraction peak maximum was significantly shifted towards higher angles, whereas the nitrogen content of approximately 2.1 % should have resulted in a peak alignment between the GaPN layer and silicon substrate. In Sample #4, a phenomenon of lattice parameter expansion was observed upon incorporation of 10 % arsenic into the GaPN(As) layer, while maintaining the same nitrogen mole fraction as in Structure #3.

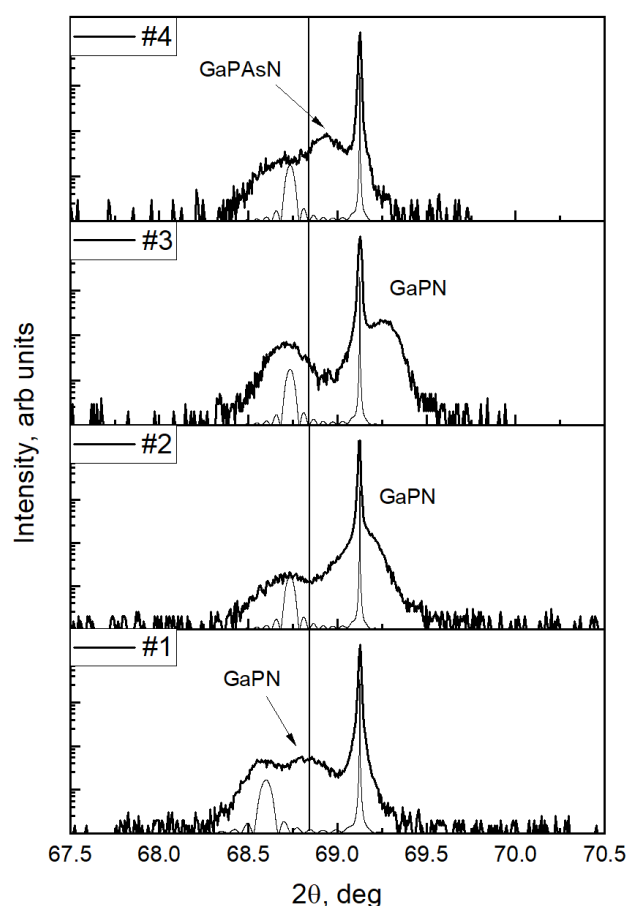


**Fig. 2.** X-Ray diffraction rocking curves around the symmetrical Si reflection for bulk ternary GaPN (Samples #1, #2, #3) and quaternary GaPNAs (Sample #4) solid solutions

Table 1 presents the values of the nitrogen molar fraction, as determined from X-Ray diffraction rocking curves analysis and the Band Anticrossing Model calculations.

A previous study [13] demonstrated that the efficiency of multijunction solar cells based on GaPNAs solid solutions as top junctions and silicon substrates as bottom junctions is also heavily influenced by such a parameter of the material as the minority carrier lifetime. Therefore, we performed studies of the photoluminescence kinetics of heterostructures with bulk GaPN layers at both room temperature (300 K) and cryogenic temperature (5 K).

Figure 3 shows the room-temperature PL intensity decay measured for the light wavelength corresponding to the PL intensity peak.

All samples studied exhibited a PL with a relatively short decay time, though the decays do not show a monoexponential behavior. The PL decline times, evaluated as the  $1/e$  maximum intensity level, estimated approximately 40 ps for the samples containing GaPN layer and 11 ps for the sample with a GaPNAs layer. Bulk GaPN layers, grown on gallium phosphide substrates, demonstrated a comparable minority carrier lifetime of 70–100 ps [14]. Therefore, short minority carrier lifetimes in GaPN layers grown on silicon is determined primarily by defects introduced during the nitrogen incorporation into the GaP lattice, rather than by defects associated with growth on silicon substrate.

Time-resolved photoluminescence studies were performed at a temperature of 5 K. The PL

**Table 1.** Key characteristics of GaPN(As) heterostructures grown on silicon substrates

Sample	PL wavelength, nm	GaPNAs solid solution composition			$\tau_{1/e}$ , ps	
		N molar fraction		As molar fractionAs	5 K	300 K
		PL	XRD			
1	612	0.0145	0.0149	–	2867	42
2	620	0.0175	0.018	–	3678	44
3	636	0.022	0.0224	–	488	35
4	663	0.022	0.0224	0.1	–	11

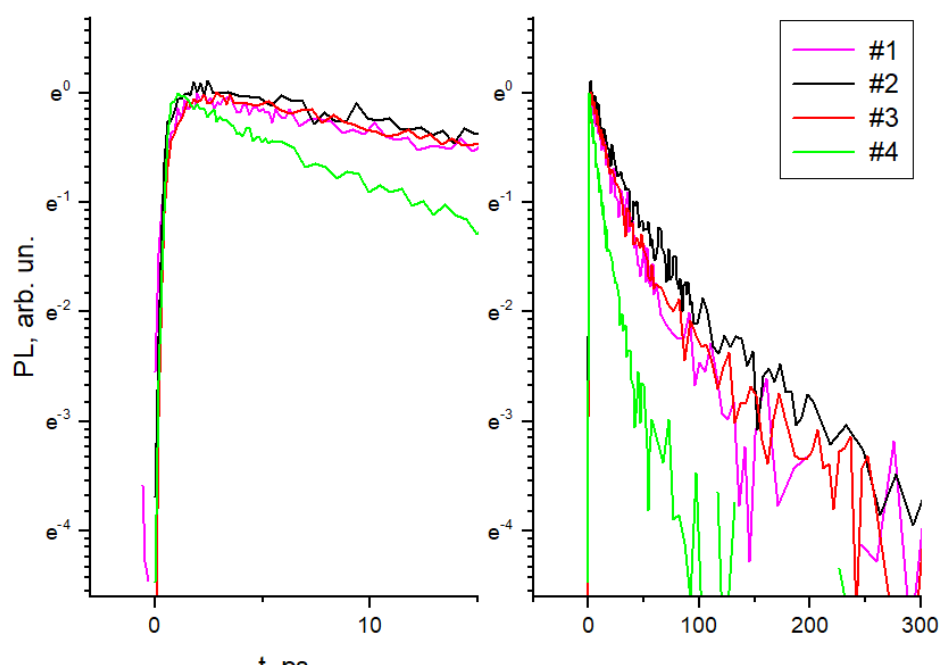


**Fig. 3.** Normalized time-resolved PL intensity decays for GaPN-based active regions, obtained at 300 K for the excitation wavelength of 620 (Samples #1, #2, #3) and 650 nm (Samples #4), displayed in two time windows (left panel – 0–15 ps, right panel – 0–300 ps)

decay kinetics for the samples with a bulk GaPN layer (Samples #1, #2 and #3) are shown in Fig. 4. The left panel shows the initial part of the PL decay, while the right panel presents the complete investigated time range. It should be noted that all decay curves exhibit a persistent background signal - detectable PL intensity preceding the arrival of each excitation pulse. This indicates the presence of slow mechanisms of PL decline with characteristic times exceeding the interval between the excitation pulses.

A comparative analysis of PL decay kinetics at room temperature (Fig. 3) and cryogenic temperature 5 K (Fig. 4) reveals a pronounced increase in PL decline time for all samples at lower temperatures. For instance, Sample #3 exhibits a  $1/e$  decay time value increase to 488 ps when measurement conditions were changed from room temperature to 5 K. Moreover, the low temperature PL decays follow monoexponential kinetics. Thus, one can conclude that temperature decrease drastically extends minority carrier lifetimes in GaPN structures grown on silicon substrates.

Table 1 presents the key properties of the studied heterostructures containing bulk GaPN(As) layers grown on silicon substrates.

#### 4. Conclusion

In this study, we investigated heterostructures containing bulk layers based on ternary GaPN and quaternary GaPNAs solid solutions grown by MBE on silicon substrates. Two buffer layer configurations were considered: a MEE-GaP buffer and a low-temperature GaP buffer with a gradient temperature ramp. It was shown the low-temperature gradient buffer layer exhibited partial elastic strain relaxation with a relaxation degree of about 55%. This strain relaxation led to an increase in the mole fraction of nitrogen incorporated in the GaP matrix, resulting in a redshift of the photoluminescence peak. An increase in the nitrogen flux led to a higher nitrogen mole fraction in the GaPN solid solution, a shift of the photoluminescence peak position to longer wavelengths, and a sharp drop of PL intensity. The addition of arsenic to a GaPN solid solution to create a quaternary solid solution,

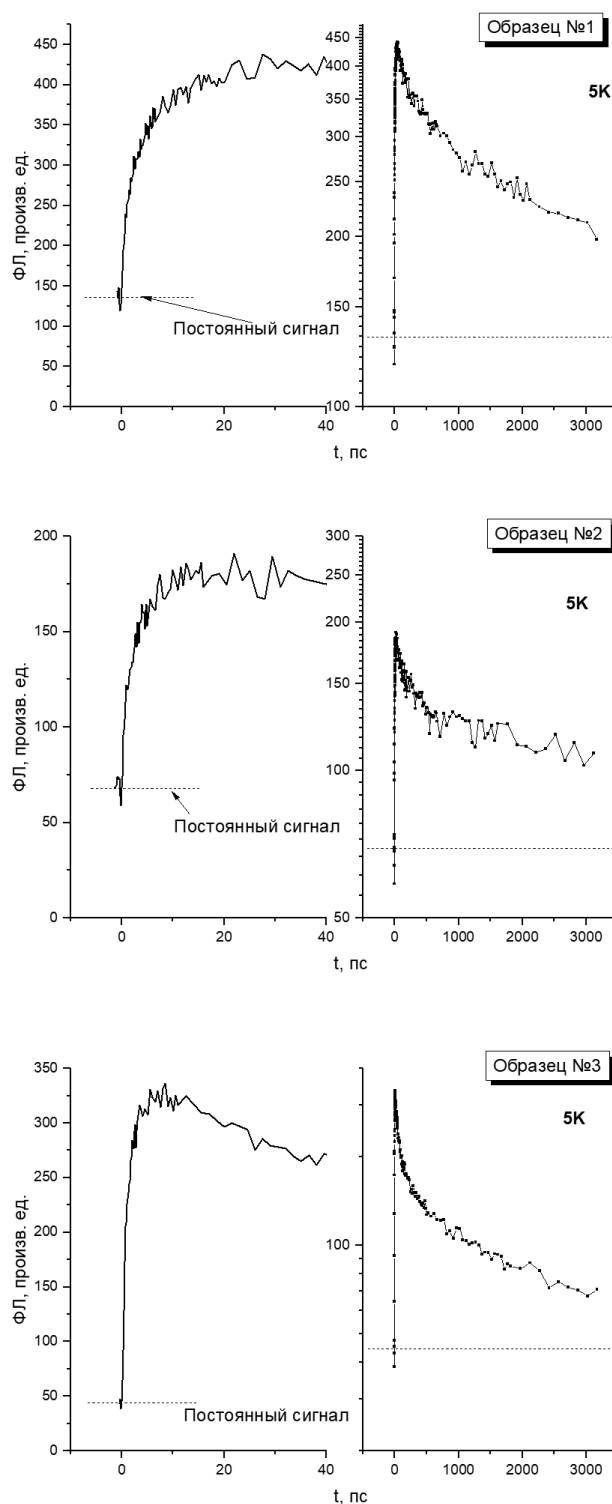


**Fig. 4.** Time-resolved PL intensity decays for GaPN-based active regions, obtained at 5 K for the excitation wavelength of 620 nm, displayed in two time windows (left panel – 0–40 ps, right panel – 0–3000 ps)

$\text{GaP}_{0.88}\text{N}_{0.02}\text{As}_{0.1}$ , allowed a PL maximum at a wavelength of 663 nm at room temperature to be achieved, while the PL intensity increases threefold compared to  $\text{GaP}_{0.98}\text{N}_{0.02}$ .

This study investigated the dependence of photoluminescence kinetics in studied heterostructures on the composition of bulk GaPN and GaPNAs layers. At room temperature, the PL intensity decay time, determined at the 1/e maximum intensity level, measured approximately 40 ps for samples with GaPN layers and 11 ps for a sample with a GaPNAs layer. Reducing the PL kinetics measurement temperature drastically increased minority carrier lifetimes in GaPN structures grown on silicon substrates.

### Contribution of the authors

The authors contributed equally to this article.

### Conflict of interests

The authors declare that they have no known competing financial interests or personal relationships that could have influenced the work reported in this paper.

### References

- Henini M. *Dilute nitride semiconductors*. Elsevier; 2005. <https://doi.org/10.1016/B978-0-08-044502-1.X5000-8>
- Shan W., Walukiewicz W., Yu K. M., ... Tu C. W. Nature of the fundamental band gap in  $\text{GaN}_{1-x}\text{P}_x$  alloys. *Applied Physics Letters*. 2000;76: 3251. <https://doi.org/10.1063/1.126597>
- Buyanova I. A., Pozina G., Bergman J. P., Chen W. M., Xin H. P., Tu C. W. Time-resolved studies of photoluminescence in  $\text{GaN}_{1-x}\text{P}_x$  alloys: evidence for indirect-direct band gap crossover. *Applied Physics Letters*. 2002;81(1): 52–54. <https://doi.org/10.1063/1.1491286>
- Kent P. R. C., Zunger A. Theory of electronic structure evolution in GaAsN and GaPN alloys. *Physical Review B*. 2001;64(11): 115208. <https://doi.org/10.1103/PhysRevB.64.115208>
- Geisz J. F., Friedman D. J. III–N–V semiconductors for solar photovoltaic applications. *Semiconductor Science and Technology*. 2002;17(8): 769–777. <https://doi.org/10.1088/0268-1242/17/8/305>
- Geisz J. F., Olson J. M., Friedman D. J., Jones K. M., Reedy R. C., Romero M. J. Lattice-matched GaNPAs-on-silicon tandem solar cells. In: *Conference Record of the Thirty-first IEEE Photovoltaic Specialists Conference*. 2005. (pp. 695–698). IEEE. <https://doi.org/10.1109/PVSC.2005.1488226>
- Baranov A. I., Gudovskikh A. S., Nikitina E. V., Egorov A. Y. Photoelectric properties of solar cells based on GaPNAs/GaP heterostructures. *Technical Physics Letters*. 2013;39: 1117–1120. <https://doi.org/10.1134/S1063785013120171>
- Khoury M., Tottereau O., Feuillet G., Vennégués P., Zúñiga-Pérez J. Evolution and prevention of meltback etching: Case study of semipolar GaN growth on patterned silicon substrates. *Journal of Applied Physics*. 2017;122(10): 105108. <https://doi.org/10.1063/1.5001914>
- Takagi Y., Yonezu H., Samonji K., Tsuji T., Ohshima N. Generation and suppression process of crystalline defects in GaP layers grown on misoriented Si(100) substrates. *Journal of Crystal Growth*. 1998;187(1): 42–50. [https://doi.org/10.1016/S0022-0248\(97\)00862-2](https://doi.org/10.1016/S0022-0248(97)00862-2)
- Volz K., Beyer A., Witte W., Ohlmann J., Németh I., Kunert B., Stolz W. GaP-nucleation on exact Si (001) substrates for III/V device integration. *Journal of Crystal Growth*. 2011;315(1): 37–47. <https://doi.org/10.1016/j.jcrysgro.2010.10.036>
- Fedorov V. V., Fedina S. V., Kaveev A. K., Kirilenko D. A., Faleev N. N., Mukhin I. S. The formation of single-domain gallium phosphide buffer layers on a silicon substrate without the use of migration enhanced epitaxy technique. *St. Petersburg Polytechnical University Journal: Physics and Mathematics*. 2024;17(2): 120–133. <https://doi.org/10.18721/JPM.17209>
- Rumyantsev O. I., Brunkov P. N., Pirogov E. V., Egorov A. Yu. Study of defects in heterostructures with GaPNAs and GaPN quantum wells in the GaP matrix. *Semiconductors*. 2010;44(7): 893–897. <https://doi.org/10.1134/s1063782610070110>
- Kudryashov D. A., Gudovskikh A. S., Nikitina E. V., Egorov A. Yu. Design of multijunction GaPNAs/Si heterostructure solar cells by computer simulation. *Semiconductors*. 2014;48(3): 381–386. <https://doi.org/10.1134/s1063782614030154>
- Nikitina E. V., Sobolev M. S., Pirogov E. V., ... Kryzhanovskaya N. V. Photoluminescence of GaPNAs/GaP(N) superlattices and bulk GaPN layers on GaP substrates. *Condensed Matter and Interphases*. 2024;26(3): 490–495. <https://doi.org/10.17308/kcmf.2024.26/12224>

### Information about the authors

*Ekaterina V. Nikitina*, Cand. Sci. (Phys.–Math.), Lead Researcher, Alferov University (Saint Petersburg, Russian Federation).

<https://orcid.org/0000-0002-6800-9218>  
mail.nikitina@mail.ru

*Andrey K. Kaveev*, Dr. Sci. (Phys.–Math.), Leading Researcher, Ioffe Institute (Saint-Petersburg, Russian Federation).

<https://orcid.org/0000-0002-3640-677X>  
kaveev@mail.ioffe.ru

*Maxim S. Sobolev*, Cand. Sci. (Phys.–Math.), Head of the Laboratory, Alferov University (Saint Petersburg, Russian Federation).

<https://orcid.org/0000-0001-8629-2064>  
sobolevsm@gmail.com

*Evgeny V. Pirogov*, Researcher, Alferov University (Saint Petersburg, Russian Federation).

<https://orcid.org/0000-0001-7186-3768>  
zzzavr@gmail.com

*Alexey M. Nadtochiy*, Cand. Sci. (Phys.–Math.), Leading Researcher, HSE University (Saint Petersburg, Russian Federation).

<https://orcid.org/0000-0003-0982-907X>  
anadtochiy@hse.ru

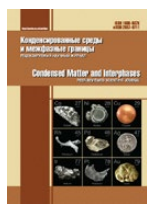
*Elena I. Vasilkova*, postgraduate student, Engineer, Alferov University (Saint Petersburg, Russian Federation).

<https://orcid.org/0000-0002-0349-7134>  
elenvasilkov@gmail.com

*Natalia V. Kryzhanovskaya*, Dr. Sci. (Phys.–Math.), Head of the laboratory, HSE University (Saint Petersburg, Russian Federation).

<https://orcid.org/0000-0002-4945-9803>  
nkryzhanovskaya@hse.ru

*Received October 28, 2024; accepted after reviewing November 11, 2024; accepted for publication November 15, 2024; published online September 25, 2025.*



# Condensed Matter and Interphases

Kondensirovannye Sredy i Mezhfaznye Granitsy  
<https://journals.vsu.ru/kcmf/>

## Original articles

Research article

<https://doi.org/10.17308/kcmf.2025.27/13020>

## Research on the influence of the powder stoichiometry of $(\text{Ag}_x\text{Cu}_{1-x})_{0.7}\text{GaSe}_2$ on the phase composition, structure, and lifetime of photogenerated charge carriers

V. V. Rakitin<sup>1✉</sup>, M. V. Gapanovich<sup>1,2,3</sup>, E. V. Rabenok<sup>1</sup>, D. R. Kalimullina<sup>2</sup>, D. S. Lutsenko<sup>1,2</sup>, I. D. Kulemetev<sup>2</sup>, E. N. Koltsov<sup>1,3</sup>, A. V. Stanchik<sup>4</sup>, V. F. Gremenok<sup>4</sup>

<sup>1</sup>Federal Research Center for Problems of Chemical Physics and Medicinal Chemistry, Russian Academy of Sciences, Academician Semenov av., 1, Chernogolovka, Moscow Region 142432, Russian Federation

<sup>2</sup>Lomonosov Moscow State University, Leninskiye Gory, 1, Moscow 119991, Russian Federation

<sup>3</sup>Moscow Center for Advanced Studies, 20, Kulakova st., Moscow, Russian Federation

<sup>4</sup>Scientific-Practical Materials Research Centre, National Academy of Sciences of Belarus, 19 Petrusya Brovki st., Minsk 220072, Republic of Belarus

### Abstract

**Objective:** This work presents a series of  $(\text{Ag}_x\text{Cu}_{1-x})_{0.7}\text{GaSe}_2$  ( $0 \leq x \leq 1$ ) powders synthesized via a solid-state reaction using the presynthesized ternary compounds  $\text{Cu}_{0.7}\text{GaSe}_2$ ,  $\text{Ag}_{0.7}\text{GaSe}_2$ , and  $\text{Ag}_{0.7}\text{GaSe}_2$ .

**Experimental:** A combination of X-ray diffraction (XRD) and Raman spectroscopy was used to establish that the solid solution region in this system is narrow and lies within the range of  $0.8 \leq x < 1$ .

**Conclusions:** An investigation of low-temperature luminescence spectra and microwave photoconductivity decay kinetics revealed that single-phase samples exhibit increased lifetimes of photogenerated charge carriers. This is attributed to the replacement of deep charge carrier traps, such as selenium vacancies  $V_{\text{Se}}$ , with shallower cationic copper vacancies associated with  $V_{\text{Cu}}$  and  $V_{\text{Se}}-V_{\text{Cu}}$ .

**Keywords:** Chalcopyrite powders, Copper quaternary compounds, Photoactive cathodes, Hydrogen generation

**Funding:** This work was financially supported by the Russian Science Foundation (RSF) (project number 24-43-10003) and the Belarusian Republican Foundation for Fundamental Research (project number T23PHФМ-029). This research utilized a universal research facility “Unit for determining the lifetime of photogenerated current carriers by measuring microwave photoconductivity in the frequency range of 36 GHz” and equipment from the Analytical Center of the Federal Research Center for Problems of Chemical Physics and Medicinal Chemistry, RAS.

**Acknowledgments:** The authors thank Ph.D. D. V. Korchagin and Ph.D. (Phys.-Math.) G. F. Shilov for providing the XRD patterns; Ph.D. (Phys.-Math.) D. M. Sedlovets for providing the Raman spectra.

**For citation:** Rakitin V. V., Gapanovich M. V., Rabenok E. V., Kalimullina D. R., Lutsenko D. S., Kulemetev I. D., Koltsov E. N., Stanchik A. V., Gremenok V. F. Research on the influence of the powder stoichiometry of  $(\text{Ag}_x\text{Cu}_{1-x})_{0.7}\text{GaSe}_2$  on the phase composition, structure, and lifetime of photogenerated charge carriers. *Condensed Matter and Interphases*. 2025;27(3): 441–453. <https://doi.org/10.17308/kcmf.2025.27/13020>

**Для цитирования:** Ракитин В. В., Гапанович М. В., Рабенок Е. В., Калимуллина Д. Р., Луценко Д. С., Кулеметьев И. Д., Кольцов Е. Н., Станчик А. В., Гременок В. Ф. Исследование влияния стехиометрии порошков  $(\text{Ag}_x\text{Cu}_{1-x})_{0.7}\text{GaSe}_2$  на их фазовый состав, структуру и времена жизни фотогенерированных носителей тока. *Конденсированные среды и межфазные границы*. 2025;27(3): 441–453. <https://doi.org/10.17308/kcmf.2025.27/13020>

✉ Vladimir V. Rakitin, e-mail: domi-tyan@yandex.ru

© Rakitin V. V., Gapanovich M. V., Rabenok E. V., Kalimullina D. R., Lutsenko D. S., Kulemetev I. D., Koltsov E. N., Stanchik A. V., Gremenok V. F., 2025



The content is available under Creative Commons Attribution 4.0 License.

## 1. Introduction

There is growing interest in the use of photoelectrochemical cells (PECs) for fuel production. It is known that light-driven water splitting into hydrogen and oxygen can occur on both photoactive anodes and cathodes [1]. The use of cathodes is considered a better solution because of their significantly lower degree of corrosion in PECs. III-V compound-based photoelectrodes are the most efficient for water splitting, but they are expensive and complex to manufacture [2]. Notably, for III-IV compounds, high efficiency is observed for photocathodes based on monocrystalline samples, whereas the efficiency drastically decreases for polycrystalline materials [3]. For complete light-driven water splitting in a PEC, the photocathode must possess an optimal bandgap ( $E_g$ ) of  $\sim 1.7$  eV but not less than 1.23 eV [1, 4]. Among suitable thin-film (1–2  $\mu\text{m}$ ) I-III-VI chalcopyrite semiconductors,  $\text{CuGaSe}_2$  ( $E_g = 1.68$  eV) and  $\text{AgGaSe}_2$  ( $E_g = 1.8$  eV) stand out [5].

The potential of using  $\text{AgGaSe}_2$  –  $\text{CuGaSe}_2$  solid solutions as photocathode materials was first described in [6]. It was established that photocathodes where a small amount of copper ( $\sim 5\%$ ) is substituted with silver atoms yield higher photocurrents than do  $\text{CuGaSe}_2$ -based photocathodes. Furthermore, such materials do not degrade over extended periods, unlike CIGS-based photocathodes [6]. The viability of these materials for photocathodes has also been supported by studies [7, 8, 9]. The materials exhibit reasonably high photocurrent densities (18–27  $\text{mA}/\text{cm}^2$ ) under AM 1.5 illumination. During PEC testing, no significant degradation was observed in the cathode region. A reduction occurs in the anode region, leading to the destruction of the film. For the p-CIGS/ $\text{H}_2\text{SO}_4$  system, it should be noted that when the potential shifts to the negative region, the volume of released hydrogen increases (0.001  $\text{mL}/\text{cm}^2$  at  $-0.3$  V and 0.009  $\text{mL}/\text{cm}^2$  at  $-0.6$  V without illumination; 0.1  $\text{mL}/\text{cm}^2$  at  $-0.3$  V and 1.5  $\text{mL}/\text{cm}^2$  at  $-0.6$  V under illumination). Partial surface film degradation occurs during operation without significant chemical composition changes [5]. Voltammetric studies of the system yielded an open-circuit voltage  $V_{oc} = 0.663$  V, short-circuit

current density  $J_{sc} = 27.9$   $\text{mA}/\text{cm}^2$ , fill factor  $FF = 0.613$ , and efficiency  $\eta = 11.3\%$  [6].

Several issues remain poorly explored. In particular, to increase the efficiency of CIGS-based solar cells, copper-deficient compounds must be used [10]. Furthermore, doping chalcopyrites with alkali metal ions significantly improves their efficiency [11]. However, this phenomenon has not been thoroughly investigated for photocathodes.

Thus, chalcopyrite-structured  $\text{AgGaSe}_2$  –  $\text{CuGaSe}_2$  solid solutions can be considered promising chemical materials for photocathodes in water splitting reactions for the production of hydrogen.

Specifically, [12] investigated the efficiency of solar light-driven water reduction on  $\text{CuGaSe}_2$ -based photocathodes with different monocrystalline plate orientations (321), (312), and (112). The results showed that after annealing in an Se atmosphere, copper-depleted compositions formed on the surface of plates with (321) and (312) orientations, whereas no copper depletion was observed on (112)-oriented plates. It is suggested that monocrystalline plates with copper-depleted compositions form a heterojunction that suppresses the recombination of photoexcited carriers. Compared with stoichiometric materials, photocathodes based on such plates are more efficient.

Reference [13] investigated the influence of the copper-to-gallium ratio on the crystal structure, morphology, and characteristics of Cu-Ga-Se film-based photocathodes obtained via one-step coevaporation. The authors showed that the surface morphology changes from large grains to fine columnar structures depending on the film composition. Different elemental ratios also affect the photocurrent density ( $j_{ph}$ ) of the finished photocathode materials. To measure key photocathode characteristics, an electrochemical cell with a single  $p$ - $n$  heterojunction, Pt/CdS/ $\text{CuGaSe}_2$ , was assembled from films with varying Cu/Ga ratios. The cell surface was modified with Pt particles atop the CdS layer. A 0.5 M  $\text{H}_2\text{SO}_4$  electrolyte (pH = 0.4) and AM1.5 illumination were used. For films with Cu/Ga = 0.85, the photocurrent in this PEC was  $j_{ph} = 19.0$   $\text{mA}/\text{cm}^2$ , whereas for Cu/Ga = 0.33, the photocurrent decreased to

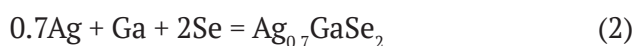
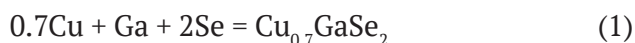
12.1 mA/cm<sup>2</sup> at –0.4 V. Conversely, at 0 V, for Cu/Ga = 0.85, the photocurrent was approximately 0 mA/cm<sup>2</sup>, whereas for Cu/Ga = 0.33, it increased to 8.2 mA/cm<sup>2</sup>. Other compositions, such as Cu/Ga = 1.17, 0.64, 0.44, 0.38, and 0.33, were also obtained in [13], but the near-stoichiometric composition (Cu/Ga = 1.17) was not investigated.

Since water splitting on photocathodes involves photogenerated electrons, one key factor influencing the efficiency of this process is the charge carrier lifetime. We previously established that partial substitution of copper with silver in CuGaSe<sub>2</sub> can increase these lifetimes [14]. Furthermore, in our work [15], for a series of  $\text{Ag}_x\text{Cu}_{1-x}\text{GaSe}_2$  solid solutions with  $x = 0, 0.3, 0.46, 0.63$ , and 1, it was found that the bandgap  $E_g$  changes nonlinearly: first decreasing and then increasing. Using a combination of low-temperature luminescence and time-resolved microwave photoconductivity (TRMC), it was shown that carrier lifetimes increase for samples with  $x$  values ranging from 0 to ~0.4 and again for those with  $x > 0.4$ . This phenomenon is due to the replacement of deep carrier traps, such as selenium vacancies, with shallower cationic vacancies.

Thus, investigating nonstoichiometric chalcopyrites as photoactive cathodes for photoelectrochemical water splitting is highly relevant. This work details the influence of the  $(\text{Ag}_x\text{Cu}_{1-x})_{0.7}\text{GaSe}_2$  powder stoichiometry on the phase composition, structure, and photogenerated charge carrier lifetime.

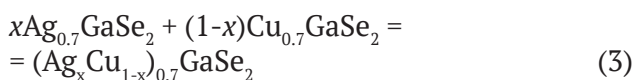
## 2. Experimental

$(\text{Ag}_x\text{Cu}_{1-x})_{0.7}\text{GaSe}_2$  powder synthesis was carried out in two stages. First, the nonstoichiometric ternary chalcopyrite compounds  $\text{Cu}_{0.7}\text{GaSe}_2$  and  $\text{Ag}_{0.7}\text{GaSe}_2$  were prepared. The elemental copper, silver, gallium, and selenium were mixed at the required ratios, sealed in quartz ampoules under vacuum, and placed in a furnace at 1100 °C for 100 hours according to the following schemes:



After high-temperature synthesis, the products were extracted, ground into powder in an agate mortar, remixed in the required proportions, sealed in new quartz ampoules

under vacuum, and annealed again at 650 °C for 100 hours. The proposed solid solution formation scheme is as follows:



This method minimizes component loss during synthesis.

The structure and phase composition of the  $(\text{Ag}_x\text{Cu}_{1-x})_{0.7}\text{GaSe}_2$  powders were studied via X-ray diffraction (XRD, PANalytical Aeris diffractometer, Cu-K<sub>α</sub> radiation) and Raman spectroscopy (Bruker Senterra micro-Raman system, 532 nm excitation). Lattice parameters were determined via the WinXPoW<sup>(R)</sup> software package.

The defect structure was investigated by low-temperature luminescence at 78 K. Photoluminescence (PL) spectra were recorded via an MDR-23U monochromator in a custom optical cryostat. A Hamamatsu R9110 photomultiplier tube (200–850 nm range) was used at the monochromator exit slit. A 532 nm solid-state laser provided excitation.

Reflectance spectra were recorded on a Shimadzu UV-3101 PC spectrophotometer (300–2000 nm range, room temperature). The bandgap ( $E_g$ ) was determined by replotting optical spectra in  $[h\nu - Y(h\nu)]^2$  vs.  $h\nu$  coordinates for direct bandgap semiconductors. The absorption coefficient was estimated via the Kubelka–Munk equation:

$$Y(h\nu) = \frac{(1-R)^2}{2R} \sim \alpha \quad (4)$$

where  $R$  is the reflectance and  $\alpha$  is the absorption coefficient.

The kinetics of photogenerated carrier decay were studied in a contact-free manner via time-resolved microwave photoconductivity at 36 GHz (Universal Research Facility “Unit for determining the lifetime of photogenerated current carriers by measuring microwave photoconductivity in the frequency range of 36 GHz”) [16]. The photoconductivity was excited by an LGI 505 nitrogen laser ( $\lambda = 337$  nm,  $t_{\text{pulse}} = 8$  ns). The detection circuit temporal resolution was ~5 ns. The maximum incident light flux density was 10<sup>16</sup> photons/cm<sup>2</sup> per pulse. The light intensity was varied via filters.

### 3. Results and discussion

#### 3.1. XRD data

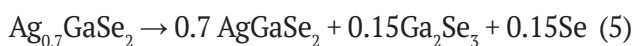
Fig. 1a shows the XRD patterns of the  $(\text{Ag}_x\text{Cu}_{1-x})_{0.7}\text{GaSe}_2$  powders at  $0 \leq x \leq 1$ . A decreasing silver content shifted the main peaks toward higher angles, particularly for the most intense (112), (220)/(204), and (312)/(116) lines.

On the basis of Figs. 1b and 1c, only the end-member  $\text{Cu}_{0.7}\text{GaSe}_2$  and solid solution powder  $(\text{Ag}_x\text{Cu}_{1-x})_{0.7}\text{GaSe}_2$  in the range  $0.8 \leq x < 1$  are single-phase. Powders with compositions in the  $0.7 \leq x \leq 0.1$  range are multiphase.

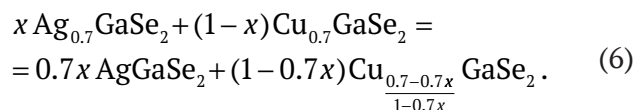
Fig. 2 shows diffractograms of the end-member powders  $\text{Cu}_{0.7}\text{GaSe}_2$  (a) and  $\text{Ag}_{0.7}\text{GaSe}_2$  compared with the stoichiometric  $\text{CuGaSe}_2$  and  $\text{AgGaSe}_2$  obtained previously in [15].

Fig. 2a shows that the peak positions for nonstoichiometric  $\text{Cu}_{0.7}\text{GaSe}_2$  are slightly shifted relative to those of stoichiometric  $\text{CuGaSe}_2$ . No impurity phases were detected; the structure remained tetragonal with space group  $I-42d$  [17, 18, 19, 20]. Fig. 2b shows that the peak positions for nonstoichiometric  $\text{Ag}_{0.7}\text{GaSe}_2$  and stoichiometric  $\text{AgGaSe}_2$  coincide completely. However, the diffractogram of  $\text{Ag}_{0.7}\text{GaSe}_2$  exhibits additional lines (marked \*) corresponding to the cubic  $\text{Ga}_2\text{Se}_3$  phase (space group  $F-43m$ ) [21, 22]. Table 1 lists the lattice parameter  $a$  and unit cell volume  $V$  values for single-phase end-member  $\text{Cu}_{0.7}\text{GaSe}_2$  and solid solution powders  $(\text{Ag}_x\text{Cu}_{1-x})_{0.7}\text{GaSe}_2$  in the range  $0.8 \leq x < 1$ .

This observation can be explained by considering  $\text{Cu}_{0.7}\text{GaSe}_2$  as a solid solution of  $\text{Cu}^{\text{I}}\text{GaSe}_2 - \text{Cu}^{\text{II}}\text{Ga}_2\text{Se}_4$ . Silver, however, does not typically exhibit  $\text{Ag}^{\text{II}}$  valence. Therefore, increasing  $\delta$  in  $\text{Ag}_{1-\delta}\text{GaSe}_2$  leads to decomposition according to Scheme (5):



Annealing  $\text{Cu}_{0.7}\text{GaSe}_2$  with  $\text{Ag}_{0.7}\text{GaSe}_2$  powders may induce a disproportionation reaction (6):



According to this reaction, some copper undergoes a transition from  $\text{Cu}^{\text{I}}$  to  $\text{Cu}^{\text{II}}$ . The single-phase region depends on  $x$ , governed by the mutual solubility of the resulting components, and the maximum possible deviation from the copper stoichiometry in  $\text{Cu}_{1-\delta}\text{GaSe}_2$ :  $1-\delta$  cannot be less than 0.5, as all copper  $\text{Cu}^{\text{I}}$  would transition to  $\text{Cu}^{\text{II}}$ . This explains the initial disappearance of the  $\text{Ga}_2\text{Se}_3$  phase in the XRD patterns of the synthesized  $(\text{Ag}_x\text{Cu}_{1-x})_{0.7}\text{GaSe}_2$  samples within  $0.8 \leq x < 1$  and its reappearance at higher  $x$  values.

Fig. 3 shows the lattice parameters and unit cell volume  $V$  for single-phase  $(\text{Ag}_x\text{Cu}_{1-x})_{0.7}\text{GaSe}_2$  samples as a function of  $x$ .

For samples with  $x$  values ranging from 1 to 0.7, the lattice parameters change linearly, and the unit cell volume increases. This indicates the formation of solid solutions based on  $\text{AgGaSe}_2$  for these  $x$  and  $\delta$  values.

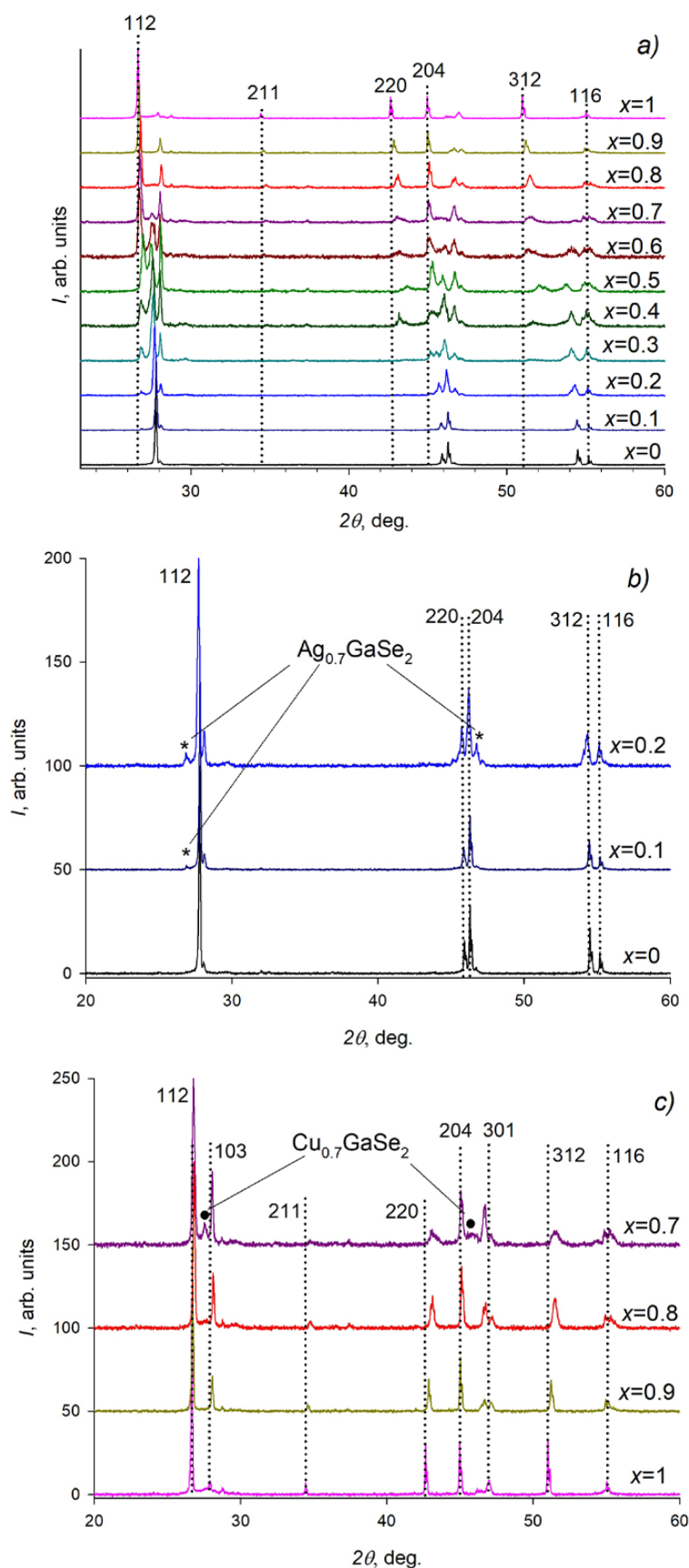
#### 3.2. Raman spectroscopy data

Fig. 4 shows the Raman spectra of nonstoichiometric  $(\text{Ag}_x\text{Cu}_{1-x})_{0.7}\text{GaSe}_2$  powders with varying copper and silver contents. All the spectra confirm the presence of chemical bonds in the  $(\text{Ag}_x\text{Cu}_{1-x})_{0.7}\text{GaSe}_2$  compounds for different values of  $x$ . The main peak shifts toward higher energies when the peak transitions from the  $x = 1$  end-member ( $177 \text{ cm}^{-1}$ ) to the  $x = 0$  end-member ( $184 \text{ cm}^{-1}$ ), which is consistent with our previous findings for stoichiometric  $\text{Ag}_x\text{Cu}_{1-x}\text{GaSe}_2$  powders [15].

Fig. 5 shows the Raman spectra for the end-member powders  $\text{Cu}_{0.7}\text{GaSe}_2$  and  $\text{Ag}_{0.7}\text{GaSe}_2$

**Table 1.** Values of bandgap  $E_g$ , lattice parameter  $a$ , and unit cell volume  $V$  for  $(\text{Ag}_x\text{Cu}_{1-x})_{0.7}\text{GaSe}_2$  powders

Samples	$E_g$ , eV	$E_g$ , theoret. [24]	$a$ , Å	$V$ , Å <sup>3</sup>
$\text{Cu}_{0.7}\text{GaSe}_2$	1.65	1.77	5.5863(28)	343.18(16)
$(\text{Ag}_{0.8}\text{Cu}_{0.2})_{0.7}\text{GaSe}_2$	1.68	1.76	5.9250(22)	379.00(15)
$(\text{Ag}_{0.9}\text{Cu}_{0.1})_{0.7}\text{GaSe}_2$	1.71	1.75	5.9500(23)	378.01(16)
$\text{AgGaSe}_2$ [15]	1.76	1.82	5.9895(30)	390.25(15)



**Fig. 1.** XRD patterns of  $(\text{Ag}_x\text{Cu}_{1-x})_{0.7}\text{GaSe}_2$  powders for  $0 \leq x \leq 1$  (a),  $0 \leq x \leq 0.2$  (b) and  $0.7 \leq x \leq 1$  (c)

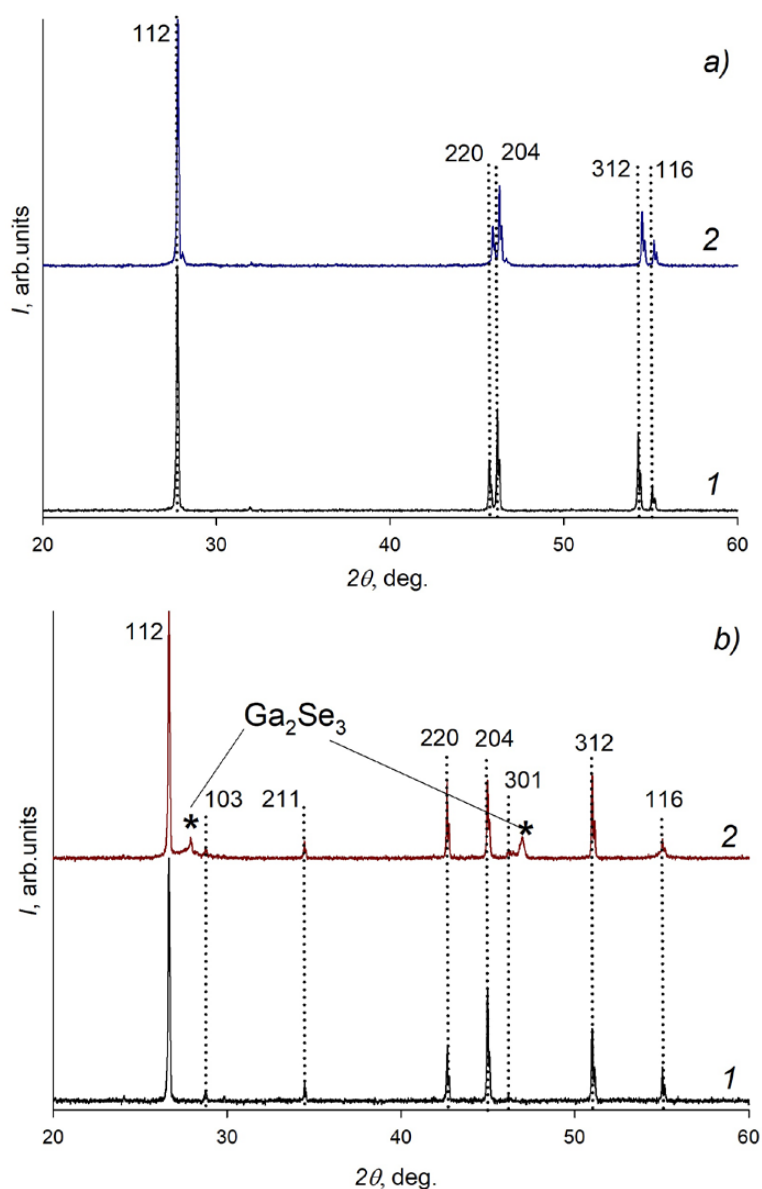


**Fig. 2.** XRD patterns for end-member powders: (a) Powders with copper content:  $\text{CuGaSe}_2$  [15] (1) and  $\text{Cu}_{0.7}\text{GaSe}_2$  (2); (b) Powders with silver content:  $\text{AgGaSe}_2$  [15] (1) and  $\text{Ag}_{0.7}\text{GaSe}_2$  (2)

compared with the stoichiometric  $\text{CuGaSe}_2$  and  $\text{AgGaSe}_2$  obtained in [15]. The peak positions for nonstoichiometric powders at  $x = 0$  and  $x = 1$  agree well with the literature data [23, 24] for stoichiometric  $\text{CuGaSe}_2$  and  $\text{AgGaSe}_2$  chalcopyrites.

The peaks at  $184\text{ cm}^{-1}$  (Fig. 5a) and  $177\text{ cm}^{-1}$  (Fig. 5b), for stoichiometric compositions, belong to the  $A_1$  mode, attributed to vibrations of the Se atom relative to stationary Cu or Ag atoms. As shown in [15], other peaks at approximately 246, 252, and  $273\text{ cm}^{-1}$  belong to various  $B_2$  modes,

primarily involving vibrations of Ga cations relative to the Se atom. Their positions change less noticeably with powder composition: at  $x = 1$ , peaks at  $252\text{ cm}^{-1}$  dominate, whereas at  $x = 0$ , peaks at  $246$  and  $273\text{ cm}^{-1}$  become more intense.

However, in Fig. 5b for  $\text{Ag}_{0.7}\text{GaSe}_2$  (curve 2), an additional peak at  $287\text{ cm}^{-1}$  is observed, along with less intense lines (marked \*). Their appearance can be explained by the formation of the  $\text{Ga}_2\text{Se}_3$  phase and amorphous Se according to Scheme (5), as corroborated by the XRD data.

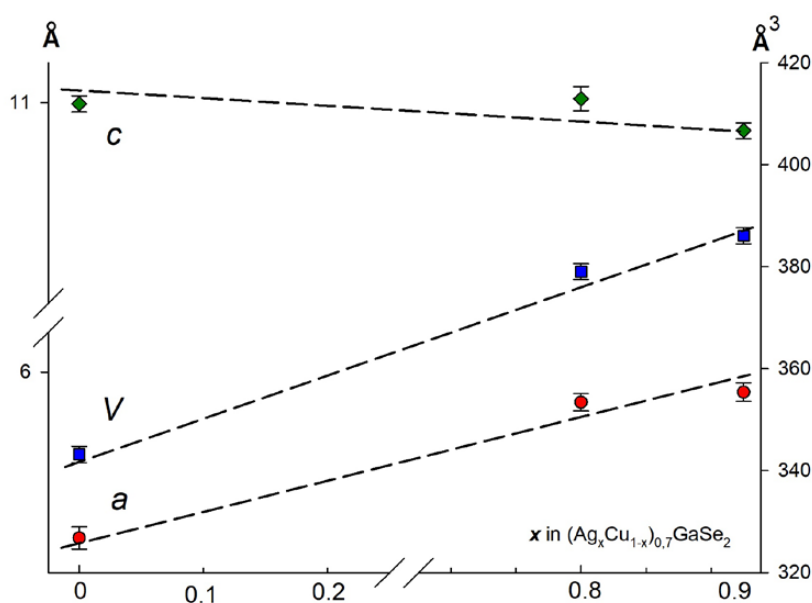


**Fig. 3.** Dependence of the lattice parameters  $a$  and  $c$  and the unit cell volume  $V$  on the composition of the  $(\text{Ag}_x\text{Cu}_{1-x})_{0.7}\text{GaSe}_2$  powders

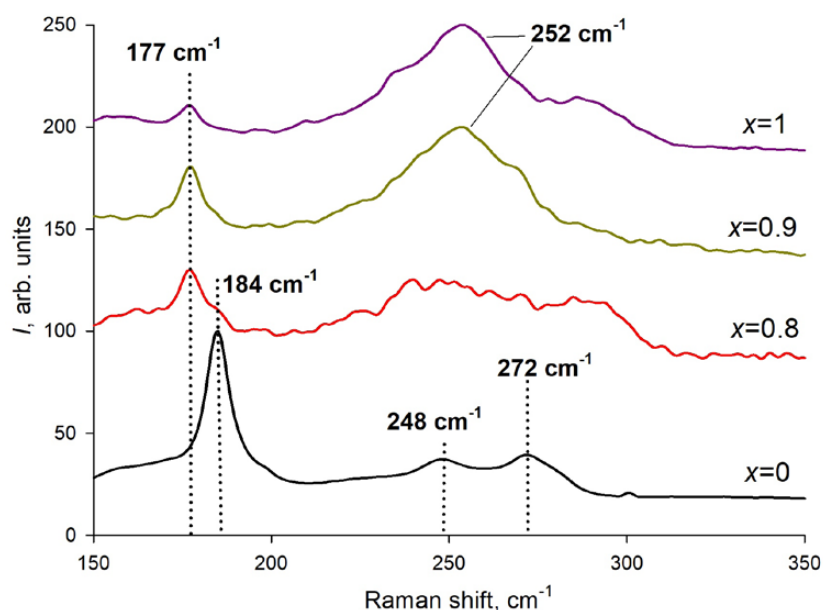


**Fig. 4.** Raman spectra of the  $(\text{Ag}_x\text{Cu}_{1-x})_{0.7}\text{GaSe}_2$  powders

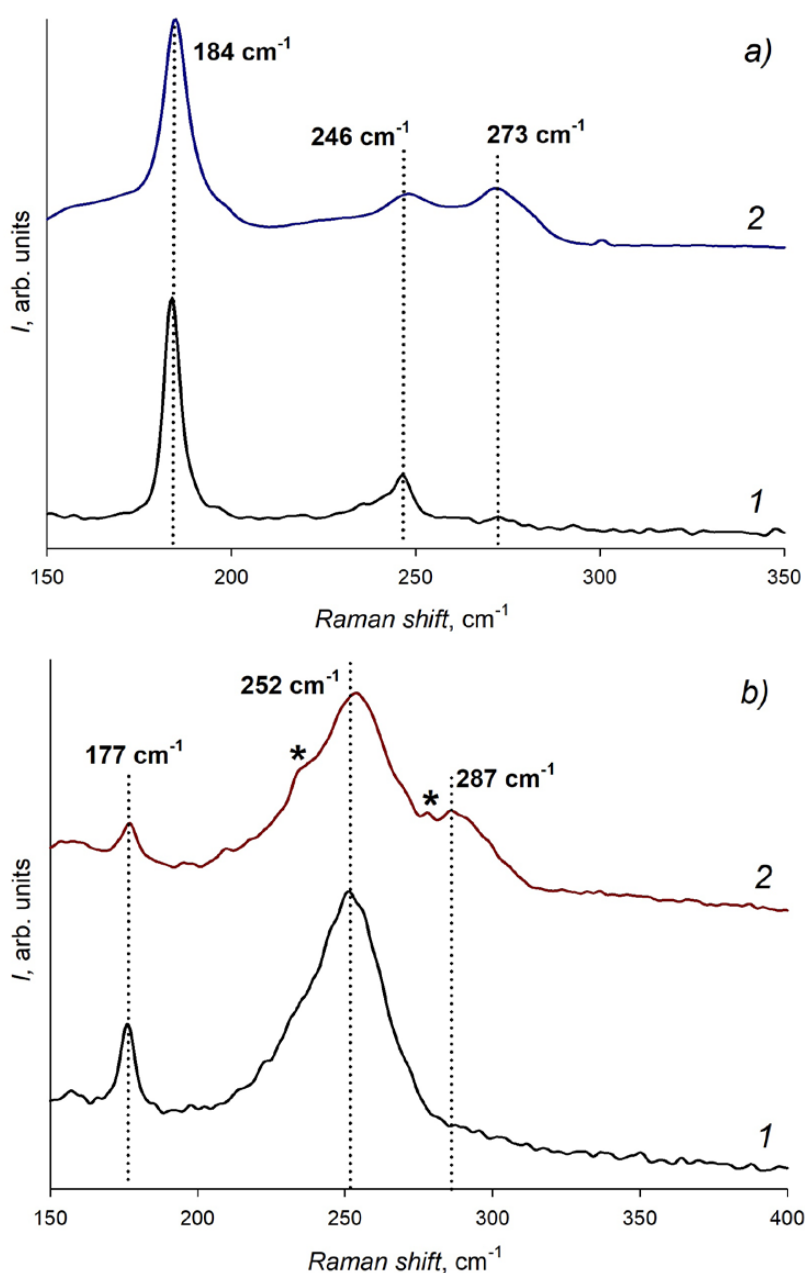
### 3.3. Bandgap determination in powders

Fig. 6 shows absorption spectra plotted as  $[h\nu - Y(h\nu)]^2$  vs.  $h\nu$ , derived via the Kubelka–Munk formula.

As shown in Fig. 6a, the bandgap for the  $\text{Cu}_{0.7}\text{GaSe}_2$  powder is  $\sim 1.69$  eV, which is slightly greater than that for the  $\text{CuGaSe}_2$  powder [15]. This is explained by  $\text{Cu}_{0.7}\text{GaSe}_2$  being a

solid solution of  $\text{Cu}^{\text{I}}\text{GaSe}_2 - \text{Cu}^{\text{II}}\text{Ga}_2\text{Se}_4$ . For single-phase  $(\text{Ag}_x\text{Cu}_{1-x})_{1-\delta}\text{GaSe}_2$  samples, the bandgap decreases smoothly from 1.76 eV to 1.68 eV when  $\text{AgGaSe}_2$  [15] transitions to  $(\text{Ag}_{0.8}\text{Cu}_{0.2})_{0.7}\text{GaSe}_2$ .

Table 1 lists the bandgap  $E_g$ , lattice parameter  $a$ , and unit cell volume  $V$  values for the  $(\text{Ag}_x\text{Cu}_{1-x})_{0.7}\text{GaSe}_2$  powders. Theoretical  $E_g$  values from [25] are included for comparison. The



**Fig. 5.** Raman spectra of end-member powders: (a) Powders with copper content:  $\text{CuGaSe}_2$  [15] (1) and  $\text{Cu}_{0.7}\text{GaSe}_2$  (2); (b) Powders with silver content:  $\text{AgGaSe}_2$  [15] (1) and  $\text{Ag}_{0.7}\text{GaSe}_2$  (2)

theoretical values calculated in [25] are somewhat higher than our experimental values for analogous compositions. However, both the theoretical and experimental  $E_g$  values increase with increasing  $x$  in  $(\text{Ag}_x\text{Cu}_{1-x})_{1-0.7}\text{GaSe}_2$ . The smooth bandgap variation for these compositions can be explained by the increasing unit cell volume. A similar trend, but over a wider  $x$  range, was observed for stoichiometric  $\text{Ag}_x\text{Cu}_{1-x}\text{GaSe}_2$  powders in our previous work [15].

### 3.4. Low temperature luminescence spectra

Fig. 7 shows smoothed, normalized low-temperature luminescence spectra (78 K) for  $\text{AgGaSe}_2$  [15] (Fig. 7a),  $\text{Cu}_{0.7}\text{GaSe}_2$  (Fig. 7d), and solid solutions based on them with various silver contents (Fig. 7b, c). The spectra exhibit a significant full width at half maximum (FWHM) and are probably composite. Deconvolution into multiple Lorentzian curves revealed the peak maxima. The deconvolution results and

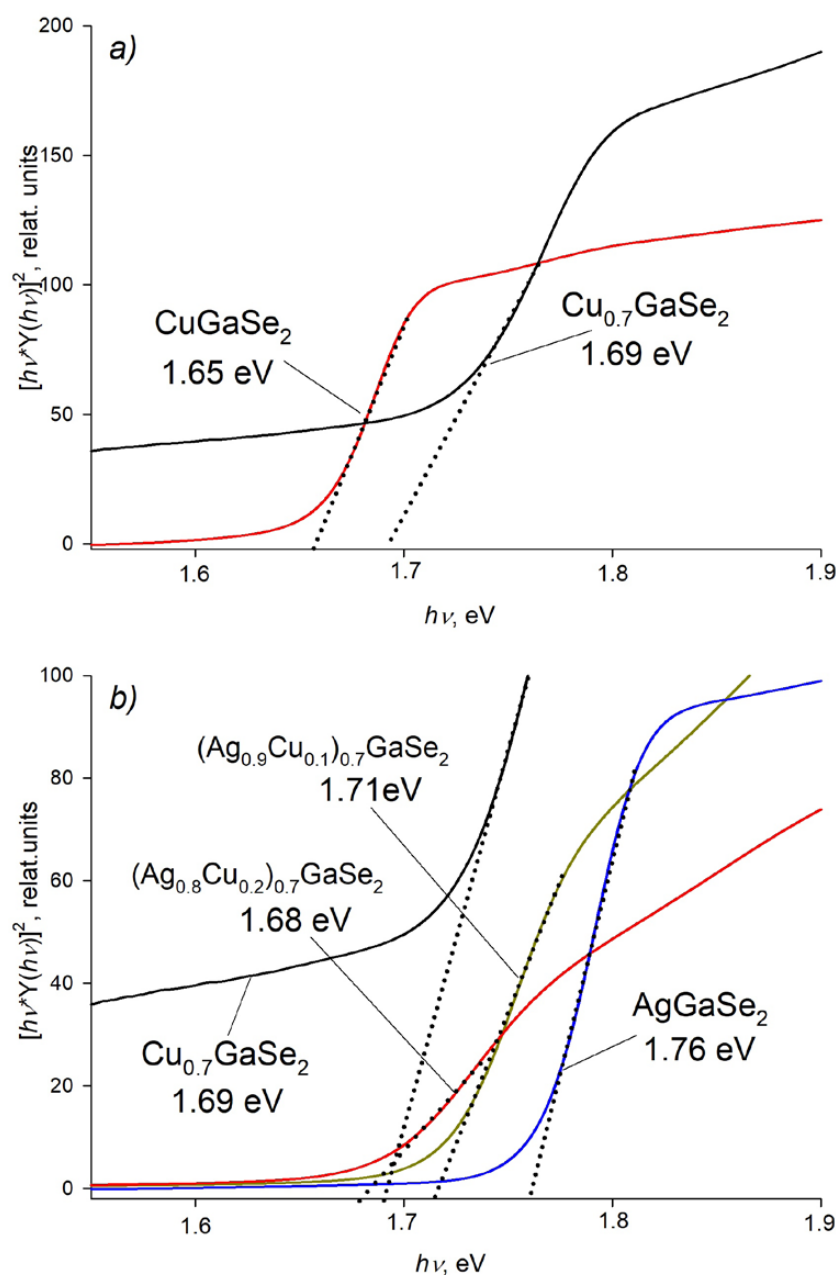


**Fig. 6.** Determination of  $E_g$  in  $[h\nu - Y(h\nu)]^2$  vs.  $h\nu$  coordinates for  $\text{Cu}_{1-x}\text{GaSe}_2$  (a) and  $(\text{Ag}_x\text{Cu}_{1-x})_{0.7}\text{GaSe}_2$  powders (b)

experimental  $E_g$  values are listed in Table 2. All the spectra, except those for  $\text{CuGaSe}_2$  and  $\text{AgGaSe}_2$ , can be decomposed into 3 peaks, denoted  $E_1$ ,  $E_2$ , and  $E_3$  in the table. Minor differences in their maxima are due to the varying  $E_g$  values of the samples. On the basis of the room-temperature bandgap values, the first peak  $E_1$  corresponds to a deep acceptor level,  $E_2$  corresponds to a shallower level (likely a donor), and  $E_3$  corresponds to a shallow donor level or band-to-band transition.

The slightly higher energy of the  $E_3$  peak than that of the  $E_g$  peak at room temperature is due to the temperature-induced increase in the semiconductor  $E_g$  upon cooling. For example, according to [26],  $\text{AgGaSe}_2$  has an  $E_g = 1.824$  eV at 4 K. It can be assumed that the  $E_3$  peak arises from a shallow donor level rather than a band-to-band transition. According to [27], low-temperature (4 K) spectra of  $\text{AgGaSe}_2$  show peaks at  $E = 1.724$  eV (attributed to selenium vacancies  $V_{\text{Se}}$ ) and

$E = 1.764$  eV (attributed to cationic vacancies  $V_{\text{cat}}$ ). The authors studied undoped  $\text{CuGaSe}_2$  powders by low-temperature luminescence at 10 K [28] and reported predominant emission at  $E = 1.67$  eV, which is consistent with [29] and explained by copper vacancy formation. Thus, for the  $\text{Cu}_{0.7}\text{GaSe}_2$ ,  $(\text{Ag}_{0.8}\text{Cu}_{0.2})_{0.7}\text{GaSe}_2$  and  $(\text{Ag}_{0.9}\text{Cu}_{0.1})_{0.7}\text{GaSe}_2$  samples, the  $E_3$  peak may be attributed to this specific defect. Furthermore, for the  $(\text{Ag}_x\text{Cu}_{1-x})_{0.7}\text{GaSe}_2$  samples with  $0.8 \leq x < 1$ , a slight increase in the  $E_3$  peak intensity is observed, which is explained by a decrease in the copper content and a consequent increase in the  $V_{\text{Cu}}$  concentration according to Scheme (6).

The  $E_2$  peak for  $\text{AgGaSe}_2$  may originate from  $V_{\text{Se}}-V_{\text{Cu}}$  defect associations, which form shallower levels than isolated selenium vacancies ( $V_{\text{Se}}$ ). Thus, for the  $(\text{Ag}_{0.8}\text{Cu}_{0.2})_{0.7}\text{GaSe}_2$  and  $(\text{Ag}_{0.9}\text{Cu}_{0.1})_{0.7}\text{GaSe}_2$  samples, the deep acceptor

levels ( $V_{\text{Se}}$ ) are partially replaced by shallower donor levels, where  $V_{\text{Cu}}$  and  $V_{\text{Se}}-V_{\text{Cu}}$  are associated.

### 3.5. Photogenerated charge carrier lifetime data

An investigation of the photogenerated carrier decay kinetics in  $(\text{Ag}_x\text{Cu}_{1-x})_{0.7}\text{GaSe}_2$  powders revealed that the measured microwave photoconductivity decays are well approximated by either a single exponential or the sum of two exponential functions: “fast” and “slow” (Fig. 8). Table 3 lists the characteristic decay times of the fast  $\tau_f$  and slow  $\tau_s$  components of the microwave photoresponse. Biphasic kinetics are characteristic of only the  $(\text{Ag}_{0.9}\text{Cu}_{0.1})_{0.7}\text{GaSe}_2$  sample. The presence of a slow component indicates processes related to the thermal release of carriers from traps and depends on trap depth. As shown by the low-temperature luminescence

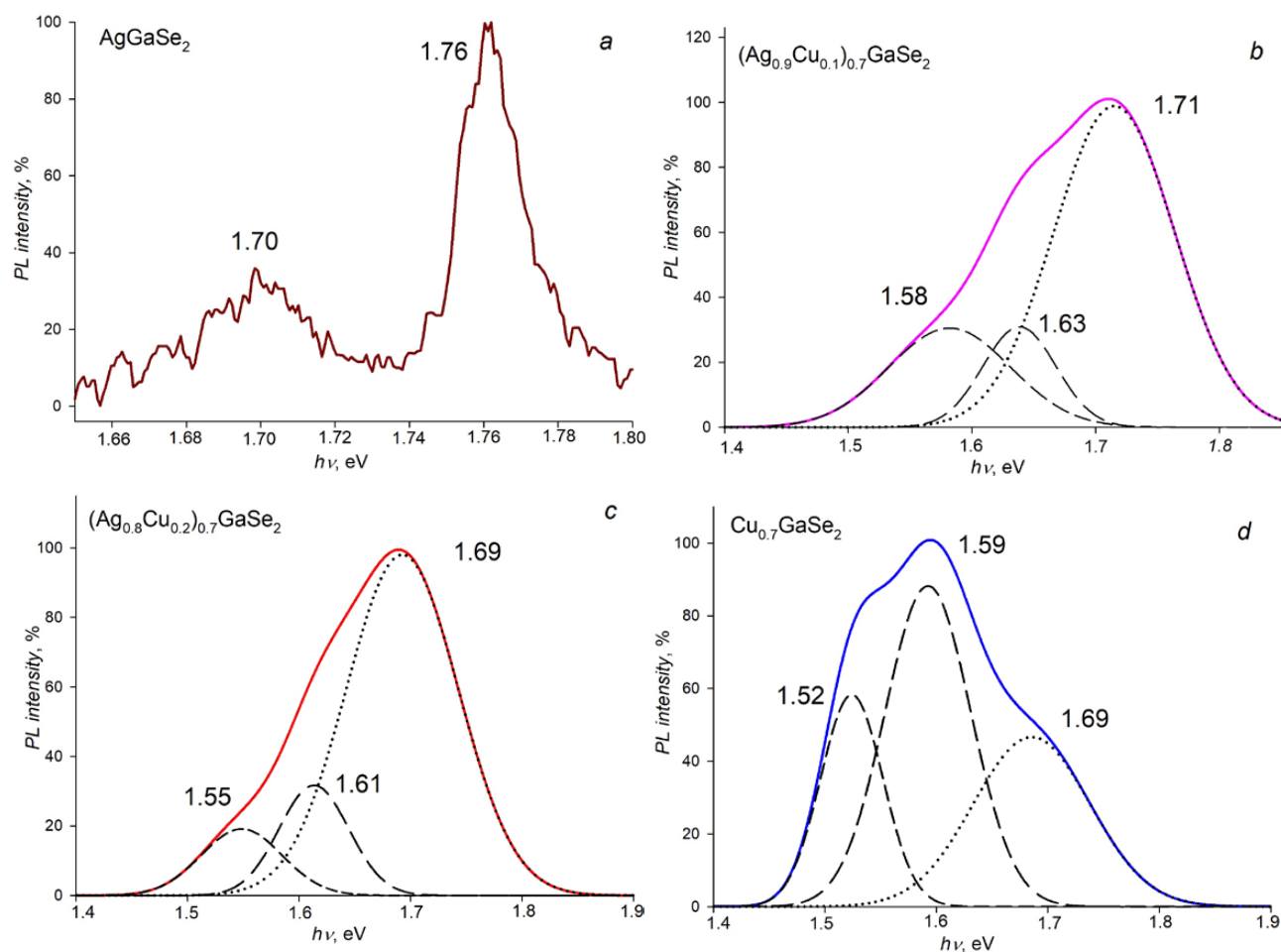


**Fig. 7.** Low-temperature luminescence spectra ( $T = 78$  K) for  $\text{AgGaSe}_2$  [15] (a),  $(\text{Ag}_{0.9}\text{Cu}_{0.1})_{0.7}\text{GaSe}_2$  (b),  $(\text{Ag}_{0.8}\text{Cu}_{0.2})_{0.7}\text{GaSe}_2$  (c), and  $\text{Cu}_{0.7}\text{GaSe}_2$  (d) powders

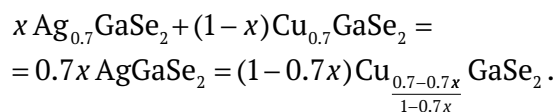
**Table 2.** Maximum  $E_1$ ,  $E_2$ , and  $E_3$  values in low-temperature luminescence spectra (78 K) and experimental  $E_g$  values for  $(\text{Ag}_x\text{Cu}_{1-x})_{0.7}\text{GaSe}_2$  powders

Samples	$E_1$ , eV	$I$ , %	$E_2$ , eV	$I$ , %	$E_3$ , eV	$I$ , %	$E_g$ , eV
$\text{CuGaSe}_2$ [15]	–	–	–	–	<b>1.63</b>	100	<b>1.65</b>
$\text{Cu}_{0.7}\text{GaSe}_2$	<b>1.52</b>	67	<b>1.59</b>	100	<b>1.69</b>	67	<b>1.65</b>
$(\text{Ag}_{0.8}\text{Cu}_{0.2})_{0.7}\text{GaSe}_2$	<b>1.55</b>	19	<b>1.61</b>	31	<b>1.69</b>	100	<b>1.68</b>
$(\text{Ag}_{0.9}\text{Cu}_{0.1})_{0.7}\text{GaSe}_2$	<b>1.58</b>	31	<b>1.63</b>	31	<b>1.71</b>	100	<b>1.71</b>
$\text{AgGaSe}_2$ [15]	<b>1.70</b>	32	–	–	<b>1.76</b>	100	<b>1.76</b>

spectra, the compositions  $(\text{Ag}_{0.8}\text{Cu}_{0.2})_{0.7}\text{GaSe}_2$  and  $(\text{Ag}_{0.9}\text{Cu}_{0.1})_{0.7}\text{GaSe}_2$  exhibit partial replacement of deep acceptor levels ( $V_{\text{Se}}$ ) with shallower donor levels, which are associated with  $V_{\text{Cu}}$  and  $V_{\text{Se}}-V_{\text{Cu}}$ . Thus, it can be assumed that for  $(\text{Ag}_{0.7}\text{Cu}_{0.1})_{0.7}\text{GaSe}_2$ , selenium vacancies ( $V_{\text{Se}}$ ), which act as deep acceptor traps, are the predominant defects. Upon transitioning to the  $(\text{Ag}_{0.9}\text{Cu}_{0.1})_{0.7}\text{GaSe}_2$  composition, shallower traps, i.e., copper vacancies ( $V_{\text{Cu}}$ ) and vacancies associated with  $V_{\text{Se}}-V_{\text{Cu}}$ , which act as shallow acceptor traps, become dominant.

#### 4. Conclusion

A series of samples with the general formula  $(\text{Ag}_x\text{Cu}_{1-x})_{0.7}\text{GaSe}_2$  ( $0 \leq x \leq 1$ ) were synthesized via a solid-state reaction. The solid solution region in this system is narrower than that in previously studied  $\text{Ag}_x\text{Cu}_{1-x}\text{GaSe}_2$  and lies within  $0.8 \leq x < 1$ . The structure of the samples is tetragonal (space group  $I-42d$ ). The narrower  $x$  range is likely caused by a disproportionation reaction:



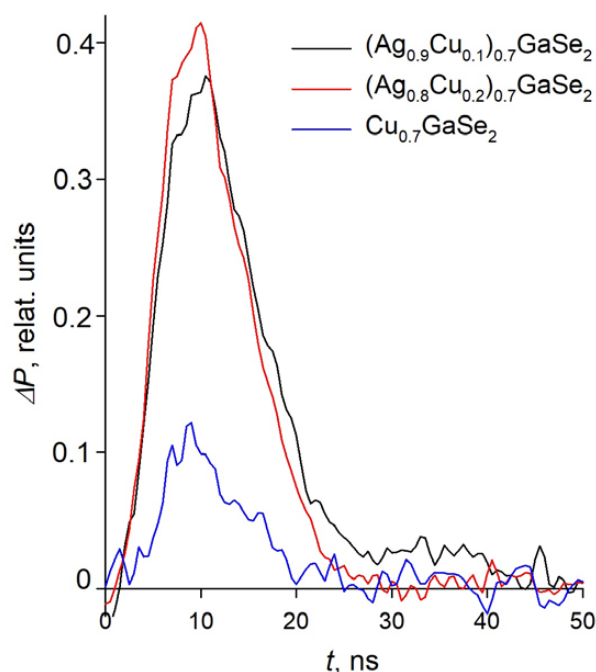
Using a combination of low-temperature luminescence and time-resolved microwave photoconductivity, it was shown that carrier lifetimes increase for sample series with  $x = 0$  and  $0.8 \leq x < 1$ . This phenomenon appears to be caused by the replacement of deep charge carrier traps, such as selenium vacancies ( $V_{\text{Se}}$ ), with shallower cationic copper vacancies associated with  $V_{\text{Cu}}$  and  $V_{\text{Se}}-V_{\text{Cu}}$ .

#### Contribution of the authors

The authors contributed equally to this article.

#### Conflict of interests

The authors declare that they have no known competing financial interests or personal relationships that could have influenced the work reported in this paper.

**Fig. 8.** The microwave photoconductivity decays for the  $(\text{Ag}_{0.9}\text{Cu}_{0.1})_{0.7}\text{GaSe}_2$ ,  $(\text{Ag}_{0.8}\text{Cu}_{0.2})_{0.7}\text{GaSe}_2$  and  $\text{Cu}_{0.7}\text{GaSe}_2$  powders.  $I = 10^{16}$  photons/cm<sup>2</sup> per pulse**Table 3.** Characteristic decay times of the fast,  $\tau_f$ , and slow,  $\tau_s$ , components of the microwave photoresponse

Samples	$\tau_f$ , ns	$\tau_s$ , ns
$\text{Cu}_{0.7}\text{GaSe}_2$	5	–
$(\text{Ag}_{0.8}\text{Cu}_{0.2})_{0.7}\text{GaSe}_2$	5	–
$(\text{Ag}_{0.9}\text{Cu}_{0.1})_{0.7}\text{GaSe}_2$	5	100
$\text{AgGaSe}_2$ [15]	12	910

## References

1. Turner J. A. Sustainable hydrogen production. *Science*. 2004;305(5686): 972–4. <https://doi.org/10.1126/science.1103197>
2. Chiu Y. H., Lai T. H., Kuo M. Y., Hsieh P. Y., Hsu Y. J. Photoelectrochemical cells for solar hydrogen production: Challenges and opportunities. *APL Materials*. 2019;7(8). <https://doi.org/10.1063/1.5109785>
3. Yokoyama D., Minegishi T., Maeda K., ... Domen K. Photoelectrochemical water splitting using a  $\text{Cu}(\text{In}, \text{Ga})\text{Se}_2$  thin film. *Electrochemistry Communications*. 2010;12(6): 851–853. <https://doi.org/10.1016/j.elecom.2010.04.004>
4. Barreto L., Makihiro A., Riahi K. The hydrogen economy in the 21st century: a sustainable development scenario. *International Journal of Hydrogen Energy*. 2003;28(3): 267–284. [https://doi.org/10.1016/S0360-3199\(02\)00074-5](https://doi.org/10.1016/S0360-3199(02)00074-5)
5. Chen Y., Feng X., Liu M., Su J., Shen S. Towards efficient solar-to-hydrogen conversion: fundamentals and recent progress in copper-based chalcogenide photocathodes. *Nanophotonics*. 2016;5(4): 524–547. <https://doi.org/10.1515/nanoph-2016-0027>
6. Zhang L., Minegishi T., Kubota J., Domen K. Hydrogen evolution from water using  $\text{Ag}_x\text{Cu}_{1-x}\text{GaSe}_2$  photocathodes under visible light. *Physical Chemistry Chemical Physics*. 2014;16(13): 6167–6174. <https://doi.org/10.1039/c3cp54590c>
7. Valderrama R. C., Sebastian P. J., Enriquez J. P., Gamboa S. A. Photoelectrochemical characterization of CIGS thin films for hydrogen production. *Solar Energy Materials and Solar Cells*. 2005;88(2): 145–155. <https://doi.org/10.1016/j.solmat.2004.10.011>
8. Marsen B., Dorn S., Cole B., Rocheleau R. E., Miller E. L. Copper chalcopyrite film photocathodes for direct solar-powered water splitting. *MRS Online Proceedings Library (OPL)*. 2006;974: 0974-CC09. <https://doi.org/10.1557/PROC-0974-CC09-05>
9. Jacobsson T. J., Platzer-Björkman C., Edoff M., Edvinsson T.  $\text{CuIn}_x\text{Ga}_{1-x}\text{Se}_2$  as an efficient photocathode for solar hydrogen generation. *International Journal of Hydrogen Energy*. 2013;38(35): 15027–15035. <https://doi.org/10.1016/j.ijhydene.2013.09.094>
10. Conibeer G., Willoughby A. (eds.). *Solar cell materials: developing technologies*. John Wiley & Sons; 2014. 344 p. <https://doi.org/10.1002/9781118695784>
11. Rudmann D., Brémaud D., Zogg H., Tiwari A. N. Na incorporation into  $\text{Cu}(\text{In}, \text{Ga})\text{Se}_2$  for high-efficiency flexible solar cells on polymer foils. *Journal of Applied Physics*. 2005;97(8). <https://doi.org/10.1063/1.1857059>
12. Ikeda S., Fujita W., Katsube R., ... Yoshino K. Crystalline-face-dependent photoelectrochemical properties of single crystalline  $\text{CuGaSe}_2$  photocathodes for hydrogen evolution under sunlight radiation. *Electrochimica Acta*. 2023;454: 142384. <https://doi.org/10.1016/j.electacta.2023.142384>
13. Mahmoudi B., Caddeo F., Lindenberg T., ... Maijenburg A. W. Photoelectrochemical properties of  $\text{Cu-Ga-Fe}$  photocathodes with compositions ranging from  $\text{CuGaSe}_2$  to  $\text{CuGa}_3\text{Se}_5$ . *Electrochimica Acta*. 2021;367: 137183. <https://doi.org/10.1016/j.electacta.2020.137183>
14. Rabenok E. V., Gapanovich M. V. Study of the decay kinetics of photogenerated current carriers in  $\text{Ag}_{1-x}\text{Cu}_x\text{GaSe}_2$  solid solutions. *High Energy Chemistry*. 2023;57(2): 174–175. <https://doi.org/10.1134/S0018143923020108>
15. Rakitin V. V., Gapanovich M. V., Lutsenko D. S., ... Kabyliatski A. V. Studying the effect of composition on the crystal structure, optical properties, and photogenerated current carriers lifetimes in  $\text{Ag}_x\text{Cu}_{1-x}\text{GaSe}_2$  ( $0 \leq x \leq 1$ ) solid solutions. *High Energy Chemistry*. 2024;58(5): 492–498. <https://doi.org/10.1134/S0018143924700474>
16. Novikov G. F., Marinin A. A., Rabenok E. V. Microwave measurements of the pulsed photoconductivity and photoelectric effect. *Instruments and Experimental Techniques*. 2010;53(2): 233–239. <https://doi.org/10.1134/S0020441210020144>
17. Barman B., Handique K. C., Kalita P. K. Observation of negative differential resistance (NDR) in chemically synthesized  $\text{CuGaSe}_2$  nanorods. *Materials Letters*. 2024;357: 135638. <https://doi.org/10.1016/j.matlet.2023.135638>
18. Swamy H. G., Naidu B. S., Reddy P. J. Structure and optical properties of  $\text{CuGaSe}_2$  thin films. *Vacuum*. 1990;41(4–6): 1445–1447. [https://doi.org/10.1016/0042-207X\(90\)93985-R](https://doi.org/10.1016/0042-207X(90)93985-R)
19. Karaagac H., Parlak M. Effects of annealing on structural and morphological properties of e-beam evaporated  $\text{AgGaSe}_2$  thin films. *Applied Surface Science*. 2009;255(11): 5999–6006. <https://doi.org/10.1016/j.apsusc.2009.01.054>
20. Karaagac H., Parlak M. Deposition and characterization of layer-by-layer sputtered  $\text{AgGaSe}_2$  thin films. *Applied Surface Science*. 2011;257(13): 5731–5738. <https://doi.org/10.1016/j.apsusc.2011.01.087>
21. Isik M., Gasanly N. M. Investigation of structural and optical characteristics of thermally evaporated  $\text{Ga}_2\text{Se}_3$  thin films. *Vacuum*. 2020;179: 109501. <https://doi.org/10.1016/j.vacuum.2020.109501>
22. Isik M., Sarigul N., Gasanly N. M. Thermoluminescence characteristics of  $\text{GaSe}$  and  $\text{Ga}_2\text{Se}_3$  single crystals. *Journal of Luminescence*. 2022;246: 118846. <https://doi.org/10.1016/j.jlumin.2022.118846>
23. Theodoropoulou S., Papadimitriou D., Doka S., Schedel-Niedrig T., Lux-Steiner M. C. Structural properties of Ge doped  $\text{CuGaSe}_2$  films studied by Raman and photoluminescence spectroscopy. *Thin Solid Films*. 2007;515(15): 5904–5908. <https://doi.org/10.1016/j.tsf.2006.12.163>
24. Cui Y., Roy U. N., Bhattacharya P., Parker A., Burger A., Goldstein J. T. Raman spectroscopy study of  $\text{AgGaSe}_2$ ,  $\text{AgGa}_{0.9}\text{In}_{0.1}\text{Se}_2$ , and  $\text{AgGa}_{0.8}\text{In}_{0.2}\text{Se}_2$  crystals. *Solid State Communications*. 2010;150(35–36): 1686–1689. <https://doi.org/10.1016/j.ssc.2010.06.022>
25. Boyle J. H., McCandless B. E., Shafarman W. N., Birkmire R. W. Structural and optical properties of  $(\text{Ag}, \text{Cu})(\text{In}, \text{Ga})\text{Se}_2$  polycrystalline thin film alloys. *Journal of Applied Physics*. 201;115(22). <https://doi.org/10.1063/1.4880243>
26. Nigge K. M., Baumgartner F. P., Bucher E. CVT-growth of  $\text{AgGaSe}_2$  single crystals: electrical and photoluminescence properties. *Solar Energy Materials and Solar Cells*. 1996;43(4): 335–343. [https://doi.org/10.1016/0927-0248\(96\)00007-4](https://doi.org/10.1016/0927-0248(96)00007-4)
27. Artus L., Bertrand Y. Anomalous temperature dependence of fundamental gap of  $\text{AgGaS}_2$  and  $\text{AgGaSe}_2$  chalcopyrite compounds. *Solid State Communications*. 1987;61(11): 733–736. [https://doi.org/10.1016/0038-1098\(87\)90727-7](https://doi.org/10.1016/0038-1098(87)90727-7)

28. Weiss T., Birkholz M., Saad M., ... Lux-Steiner M. C. Ag-doped  $\text{CuGaSe}_2$  as a precursor for thin film solar cells. *Journal of Crystal Growth*. 1999;198: 1190–1195. [https://doi.org/10.1016/S0022-0248\(98\)01152-X](https://doi.org/10.1016/S0022-0248(98)01152-X)

29. Schön J. H., Riazzi-Nejad H., Kloc C., Baumgartner F. P., Bucher E. Photoluminescence properties of doped-and undoped- $\text{CuGaSe}_2$  single crystals. *Journal of Luminescence*. 1997;72: 118–120. [https://doi.org/10.1016/S0022-2313\(96\)00385-7](https://doi.org/10.1016/S0022-2313(96)00385-7)

### Information about the authors

*Vladimir V. Rakitin*, Cand. Sci. (Chem.), Senior Researcher, Group of Semiconductor and Composite Materials, Federal Research Center for Problems of Chemical Physics and Medicinal Chemistry, RAS (Chernogolovka, Moscow Region, Russian Federation).

<https://orcid.org/0000-0001-6582-5212>

[domi-tyan@yandex.ru](mailto:domi-tyan@yandex.ru)

*Mikhail V. Gapanovich*, Cand. Sci. (Chem.), Head of Group, Group of Semiconductor and Composite Materials, Federal Research Center for Problems of Chemical Physics and Medicinal Chemistry, RAS (Chernogolovka, Moscow Region, Russian Federation).

<https://orcid.org/0000-0002-9109-6532>

[gmw1@mail.ru](mailto:gmw1@mail.ru)

*Evgenia V. Rabenok*, Cand. Sci. (Phys.-Math.), Senior Researcher, Group of Semiconductor and Composite Materials, Federal Research Center for Problems of Chemical Physics and Medicinal Chemistry, RAS (Chernogolovka, Moscow Region, Russian Federation).

<https://orcid.org/0000-0002-3500-6918>

[jane.rabenok@yandex.ru](mailto:jane.rabenok@yandex.ru)

*Dana R. Kalimullina*, 6th year student, Faculty of Physics, Lomonosov Moscow State University (Moscow, Russian Federation).

[kalimullinadana@mail.ru](mailto:kalimullinadana@mail.ru)

*Denis S. Lutsenko*, Junior Researcher, Group of Semiconductor and Composite Materials, Federal Research Center for Problems of Chemical Physics and Medicinal Chemistry, RAS (Moscow, Russian Federation).

[lutsenkods@my.msu.ru](mailto:lutsenkods@my.msu.ru)

*Ivan D. Kulemetev*, 5th year student, Faculty of Physics, Lomonosov Moscow State University (Moscow, Russian Federation).

[ivan-2002@bk.ru](mailto:ivan-2002@bk.ru)

*Elizar N. Koltsov*, 3rd year postgraduate student, MIPT, Engineer, Group of Semiconductor and Composite Materials, Federal Research Center for Problems of Chemical Physics and Medicinal Chemistry, RAS (Dolgoprudny, Chernogolovka, Moscow Region, Russian Federation).

[elizar.kem@mail.ru](mailto:elizar.kem@mail.ru)

*Alena V. Stanchik*, Cand. Sci. (Phys.-Math.), Associate Professor, Senior Researcher, Laboratory of Semiconductor Physics, Scientific-Practical Materials Research Centre, National Academy of Sciences of Belarus (Minsk, Republic of Belarus).

<https://orcid.org/0000-0001-8222-8030>

[alena.stanchik@bk.ru](mailto:alena.stanchik@bk.ru)

*Valery F. Gremenok*, D.Sci. (Phys.-Math.), Professor, Head of Laboratory of Semiconductor Physics, Scientific-Practical Materials Research Centre, National Academy of Sciences of Belarus (Minsk, Republic of Belarus).

<https://orcid.org/0000-0002-3442-5299>

[gremenok@physics.by](mailto:gremenok@physics.by)

*Received November 8, 2024; accepted after reviewing December 2, 2024; accepted for publication December 4, 2024; published online September 25, 2025.*



# Condensed Matter and Interphases

Kondensirovannye Sredy i Mezhfaznye Granitsy  
<https://journals.vsu.ru/kcmf/>

## Original articles

Research article

<https://doi.org/10.17308/kcmf.2025.27/13022>

## Double borate $\text{NaScB}_2\text{O}_5$ : synthesis, thermal stability, ionic conductivity, IR spectroscopy, and electronic structure

A. N. Sobolev<sup>1,2</sup>, E. V. Kovtunets<sup>1,2</sup>, T. S. Spiridonova<sup>1,2</sup>, A. B. Bogdanov<sup>3</sup>, A. K. Subanakov<sup>1,2</sup>✉

<sup>1</sup>Baikal Institute of Nature Management, Siberian branch of the Russian Academy of Sciences  
6 Sakhyanovoy st., Ulan-Ude 670047, Russian Federation

<sup>2</sup>Banzarov Buryat State University,  
24a Smolina st., Ulan-Ude 670000, Russian Federation

<sup>3</sup>Vinogradov Institute of Geochemistry, Siberian branch of the Russian Academy of Sciences  
1a building, Favorskogo st., Irkutsk 664033, Russian Federation

### Abstract

**Objective:** Sodium scandium double borate ( $\text{NaScB}_2\text{O}_5$ ), whose crystal structure was solved by Backer and Held in 2001, remains a poorly explored compound. The crystal structure has wide channels that may suggest the ionic conduction of sodium ions. Based on this, the aim of the study was to investigate the ionic conductivity of this compound, as well as to study its thermal behavior, measure the IR spectrum, and calculate the electronic structure by quantum chemical method.

**Experimental:** The synthesis of sodium scandium double borate ( $\text{NaScB}_2\text{O}_5$ ), was achieved using a solid-state reaction method.  $\text{NaScB}_2\text{O}_5$  was explored by using thermal analysis, IR spectroscopy, ionic conductivity, theoretical estimates of activation energy, ion transport pathways, and ab initio calculations of the electronic structure.

**Conclusions:** Rietveld method was engaged: monoclinic symmetry (sp. gr.  $P2_1/c$ ),  $a = 7.2460(2) \text{ \AA}$ ,  $b = 9.7887(3) \text{ \AA}$ ,  $c = 5.9289(2) \text{ \AA}$ ,  $\beta = 71.318(1)^\circ$ ,  $Z = 4$ ,  $V = 398.37(2) \text{ \AA}^3$ ,  $R_{\text{wp}} = 2.81$ ,  $\text{GOF} = 1.64$ .  $\text{NaScB}_2\text{O}_5$  borate is characterized by incongruent melting at  $1090^\circ\text{C}$ . The calculated ab initio IR spectrum of  $\text{NaScB}_2\text{O}_5$  exhibited a high degree of consistency with the experimentally obtained IR spectrum. The calculated energy barrier for oxygen ion migration, determined to be  $0.998 \text{ eV}$ , exhibits a reasonable degree of agreement with the experimentally determined activation energy of  $0.9 \text{ eV}$ . The title compound exhibits an ionic conductivity of  $0.6 \cdot 10^{-3} \text{ S/cm}$  at  $1023 \text{ K}$ . The band gap was about  $6.83 \text{ eV}$ .

**Keywords:** Sodium scandium borate; Solid-phase synthesis; Thermal analysis; IR spectroscopy; Electrical conductivity

**Funding:** The work was supported by a grant from the Russian Science Foundation (No. 23-23-00451) and partially with the financial support of the Ministry of Science and Higher Education of the Russian Federation (State assignment of the BIP SB RAS No. 0273-2021-0008)."

**Acknowledgments:** The authors express their gratitude to Dr. R. Yu. Shendrik for help with the ArDI web application. The studies by XRD, thermal analysis, FT-IR spectroscopy and conductivity were carried out using the resources of the Center for Collective Use of BIP SB RAS. Ab initio calculations were performed on the «Academician V. M. Matrosov» complex of the Irkutsk Supercomputer Center of the Siberian Branch of the Russian Academy of Sciences [<https://hpc.icc.ru/>].

**For citation:** Sobolev A. N., Kovtunets E. V., Spiridonova T. S., Bogdanov A. I., Subanakov A. K. Double borate  $\text{NaScB}_2\text{O}_5$ : synthesis, thermal stability, ionic conductivity, IR spectroscopy, and electronic structure. *Condensed Matter and Interphases*. 2025;27(3): 454–463. <https://doi.org/10.17308/kcmf.2025.27/13022>

**Для цитирования:** Соболев А. Н., Ковтунец Е. В., Спиридонова Т. С., Богданов А. И., Субанакوف А. К. Двойной борат  $\text{NaScB}_2\text{O}_5$ : синтез, термическое поведение, электропроводность и электронная структура. *Конденсированные среды и межфазные границы*. 2025;27(3): 454–463. <https://doi.org/10.17308/kcmf.2025.27/13022>

✉ Alexey K. Subanakov, [subanakov@binm.bscnet.ru](mailto:subanakov@binm.bscnet.ru)

© Sobolev A. N., Kovtunets E. V., Spiridonova T. S., Bogdanov A. I., Subanakov A. K., 2025



The content is available under Creative Commons Attribution 4.0 License.

## 1. Introduction

Borates have a unique set of physicochemical properties, which determines their significant potential for research in various fields. They are excellent starting materials for optical applications. Due to their crystallographic diversity, wide range of optical transparency, and unique properties, borates have been widely recognized as nonlinear optical materials in the ultraviolet (UV) and deep UV region [1–7]. The following nonlinear optical crystals are currently used commercially:  $\beta$ -BaB<sub>2</sub>O<sub>4</sub> [8] and LiB<sub>3</sub>O<sub>5</sub> [9]. In addition to the above, the following nonlinear optical crystals are of particular interest to materials scientists: CsLiB<sub>6</sub>O<sub>12</sub> [10], KBe<sub>2</sub>B<sub>2</sub>O<sub>3</sub>F<sub>2</sub> [11], Sr<sub>2</sub>Be<sub>2</sub>B<sub>2</sub>F<sub>7</sub> [12], and BiB<sub>3</sub>O<sub>6</sub> [13]. Centrosymmetric borates such as  $\alpha$ -BaB<sub>2</sub>O<sub>4</sub> [14], Ca<sub>3</sub>(BO<sub>3</sub>)<sub>2</sub> [15], Ba<sub>3</sub>YB<sub>9</sub>O<sub>18</sub> [16], Ca(BO<sub>2</sub>)<sub>2</sub> [17] having high birefringence are promising materials for light polarization in the deep-UV range of the spectrum.

Pyroborates containing the [B<sub>2</sub>O<sub>5</sub>]<sup>4-</sup> anionic group were first structurally characterized in 1950. [18]. Pyroborates can be divided into two classes: alkaline-earth pyroborates A<sub>2</sub>B<sub>2</sub>O<sub>5</sub> (A = Mg, Ca, Sr (alkaline-earth metals)) [19], Li<sub>3.366</sub>Mg<sub>0.317</sub>B<sub>2</sub>O<sub>5</sub> [20], BaMnB<sub>2</sub>O<sub>5</sub> [21], and transition metal pyroborates MM'B<sub>2</sub>O<sub>5</sub>: Co<sub>2-x</sub>Ni<sub>x</sub>B<sub>2</sub>O<sub>5</sub> [22], Ni<sub>1.5</sub>Zn<sub>0.5</sub>B<sub>2</sub>O<sub>5</sub> [23], Co<sub>1.5</sub>Zn<sub>0.5</sub>B<sub>2</sub>O<sub>5</sub> [23]. In addition, there are pyroborates of alkali Li<sub>2</sub>PbB<sub>2</sub>O<sub>5</sub> [24] and rare earth metals Pr<sub>2</sub>(B<sub>2</sub>O<sub>5</sub>)(MoO<sub>4</sub>) [25]. Borates containing pyroborate group – [B<sub>2</sub>O<sub>5</sub>]<sup>4-</sup> can be considered as one of the most promising for light birefringence in the deep UV range [26]. For high birefringence it is necessary that borate triangles in the [B<sub>2</sub>O<sub>5</sub>]<sup>4-</sup> group are coplanar, i.e. lie in the same plane.

Our scientific interest was attracted by sodium scandium double pyroborate (NaScB<sub>2</sub>O<sub>5</sub>) [27], the crystal structure of which is solved on single crystals, but the other properties and characteristics have not been investigated. For light polarization (birefringence) problems, this double borate is not suitable because the torsional angle between the planes of borate triangles is about 30°, which is unacceptable for significant birefringence. The presence of channels in the crystal structure of this borate implies high ionic conductivity. Therefore, the aim of the present work was to study the ionic conductivity of this compound, as well as to study its thermal behavior, characterize it by IR

spectroscopy and calculate its electronic structure by a quantum chemical method.

## 2. Experimental

For solid-phase synthesis of double borate, the following reagents were used: Na<sub>2</sub>CO<sub>3</sub> (h.p.), Sc<sub>2</sub>O<sub>3</sub> (h.p.), H<sub>3</sub>BO<sub>3</sub> (h.p.). Prior to synthesis, the carbonate and oxide were annealed at 500 °C for 8 h to remove extracted moisture. The reaction mixture of the starting components Na<sub>2</sub>CO<sub>3</sub>, Sc<sub>2</sub>O<sub>3</sub>, and H<sub>3</sub>BO<sub>3</sub> in the ratio of 1:1:4, respectively, was homogenized in an agate mortar and annealed at 300 °C (heating rate 1 °C/min) for 24 h in a muffle furnace to remove volatile reaction products: CO<sub>2</sub> and H<sub>2</sub>O. After annealing, the reaction mixture was homogenized and annealed at 500 °C for 24 h, followed by X-ray diffraction analysis (XRD) of the mixture. Further, stepwise annealing was carried out at 500–600 °C for 5 h and finally at 750–800 °C for 20 h with intermediate grindings until equilibrium was reached. The single-phase nature of the reaction product and the achievement of equilibrium were monitored by XRD.

D8 ADVANCE (Bruker AXS) and DM-20 (TONGDA) diffractometers with CuK $\alpha$ -radiation were used for XRD. The following imaging conditions were used: Bragg–Brentano geometry, scanning range from 8 to 80° by 2 $\theta$  with a step of 0.02°, room temperature.

Rietveld refinement [28] was performed using the TOPAS 4.2 [29, 30] software suite.

An STA 449 F1 Jupiter thermal analyser (NETZSCH) was used for thermogravimetric (TG) and differential scanning calorimetric (DSC) characterization of the title compound. The thermal analysis was carried out in the temperature range of 200–1200 °C in an argon flow at a rate of 10 °C/min, using platinum crucibles. The use of Pt–PtRh thermocouple increased the accuracy of temperature measurement to  $\pm 1^\circ$ .

The theoretical evaluation of activation energy and ion transport pathways was carried out by the SoftBV program [31] computational tools are sought to accelerate materials discovery by computational predictions. Here are introduced a set of computationally inexpensive software tools that exploit the bond-valence-based empirical force field previously developed by the authors to enable high-throughput computational screening of experimental or simulated crystal-structure models of battery materials predicting a variety of

properties of technological relevance, including a structure plausibility check, surface energies, an inventory of equilibrium and interstitial sites, the topology of ion-migration paths in between those sites, the respective migration barriers and the site-specific attempt frequencies. All of these can be predicted from CIF files of structure models at a minute fraction of the computational cost of density functional theory (DFT using bond valence sum maps (BVS)).

For studying the electrical conductivity, the ceramic disks of  $\text{NaScB}_2\text{O}_5$  ( $\varnothing = 10$  mm,  $h = 1.6$  mm) were prepared by pressing the powder at 1 kbar and sintering at 1073 K for 4 h. For preparing the electrode, the disk surface was coated with colloidal platinum, followed by annealing for 1 h. The electrical conductivity was measured by the two-contact method (impedance meter Z-1500J, frequency range 1 Hz – 1 MHz, temperature range of 473–1023 K, heating and cooling rates of 2 K/min). The activation energy values were calculated from the slope of the straight lines corresponding to the Arrhenius dependence in  $\lg(\sigma T) - (10^3/T)$  coordinates.

Ab initio calculations were performed using the VASP software package [32] based on density functional theory (DFT). A pseudopotential approach with basis functions in the form of plane waves was used in the calculations. The kinetic energy limit is 400 eV. A  $2 \times 1 \times 2$  grid of wave vectors centered at the  $\Gamma$  point was used for integration over the Brillouin zone. The positions of the atoms were displaced by the relaxation of the cell with a force of no more than 0.001 eV/Å. The Perdew–Burke–Ernzerhof exchange-correlation functional (PBESol) [33] was used to calculate the electronic structure of  $\text{NaScB}_2\text{O}_5$ . The IR spectrum was calculated in VASP

using the procedures included in the Phonopy code [34]. The HSE06 hybrid functional [35] was used to calculate the electronic density states. The graph of electronic density states was generated in [https://github.com/QijingZheng/pyband].

### 3. Results and discussion

#### 3.1. Crystal structure

The Rietveld method was applied to identify the target phase and its purity. The crystal structure of  $\text{ScB}_2\text{O}_5$  is known and described in [27], the positions of atoms and their displacements were not specified. All reflexes in the diffractogram were assigned to the monoclinic sodium scandium double borate  $\text{NaScB}_2\text{O}_5$  (pr. gr.  $P2_1/c$ ) [27] with low unreliability factors:  $R_{\text{wp}} = 2.81\%$ ,  $R_p = 2.12\%$ ,  $R_{\text{exp}} = 1.71\%$ ,  $\chi^2 = 1.64$ ,  $R_B = 1.59\%$ . Figure 1 shows the experimental, calculated, and difference diffractograms of  $\text{NaScB}_2\text{O}_5$ . The parameters of the  $\text{NaScB}_2\text{O}_5$  unit cell were refined in this work in comparison with the data of [27] are presented in Table 1.

The crystal structure of  $\text{NaScB}_2\text{O}_5$  (Fig. 2a) consists of slightly distorted octahedrons  $[\text{ScO}_6]$ , which form zigzag chains along the “c” axis, connecting through common edges. These chains are joined together through pyroborate groups  $[\text{B}_2\text{O}_5]$  and distorted tetrahedra  $[\text{NaO}_4]$ . Each pyroborate group is connected to five  $[\text{ScO}_6]$  octahedra and three  $[\text{NaO}_4]$  tetrahedra. The pyroborate group consists of two planar triangles  $[\text{BO}_3]$  joined through a common oxygen vertex with a rotation angle of about  $40^\circ$ . Figure 2b illustrates a projection onto the (20) plane showing the “wide

**Table 1.**  $\text{NaScB}_2\text{O}_5$  unit cell parameters in comparison with [27]

Sp. Gr.	monoclinic $P2_1/c$ [in this work]	monoclinic $P2_1/c$ [27]
$a$ , Å	7.2460(2)	7.2339(6)
$b$ , Å	9.7887(3)	9.7966(6)
$c$ , Å	5.9289(2)	5.9233(5)
$\alpha$ , °	90	90
$\beta$ , °	71.318(1)	71.483(8)
$\gamma$ , °	90	90
$V$ , Å <sup>3</sup>	398.37(2)	398.0

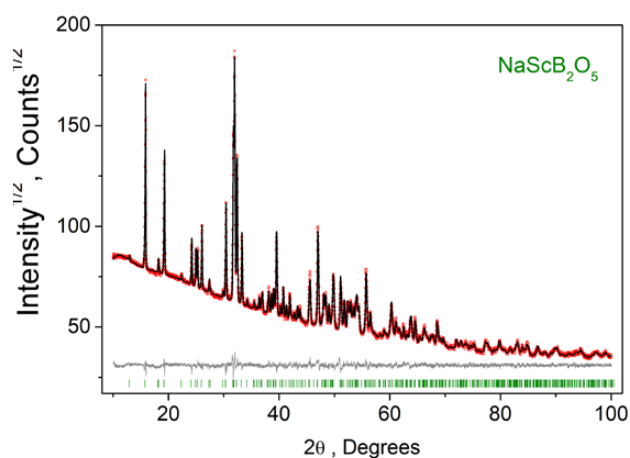


**Fig. 1.** Rietveld plot of  $\text{NaScB}_2\text{O}_5$  – experimental (red), calculated (black), difference (grey), reflections (green)

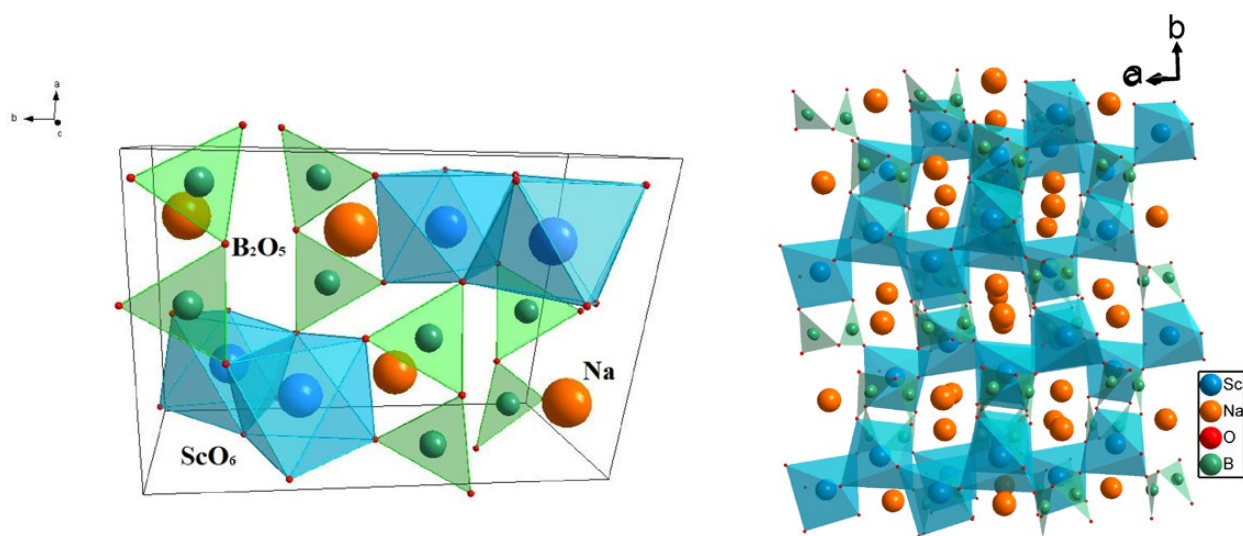


**Fig. 2.** Crystal structure of  $\text{NaScB}_2\text{O}_5$  (a); b – crystal structure projection of  $\text{NaScB}_2\text{O}_5$  onto the  $(20\bar{1})$  plane (b)

channels” filled with sodium cations. The crystal structure of  $\text{NaScB}_2\text{O}_5$  was constructed according to the data [27] in the Diamond 3.2 program.

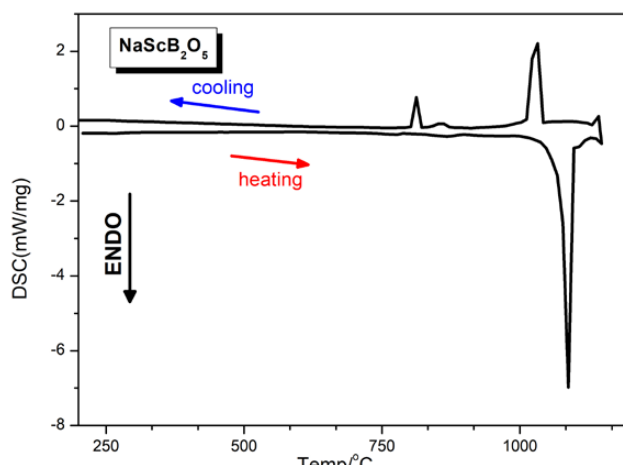
### 3.2. Thermal properties

Fig. 3 shows the heating and cooling curves of  $\text{NaScB}_2\text{O}_5$  in the temperature range from 200 to 1200 °C. The endothermic effect at 1090 °C corresponds to the melting temperature of the double borate. Three endotherms corresponding to the crystallization of  $\text{NaScB}_2\text{O}_5$  decomposition products are observed on the DSC cooling curve, which can be considered as an indirect confirmation of the incongruent melting of this borate. The diffractogram of  $\text{NaScB}_2\text{O}_5$  after melting is presented in the supplementary materials (S1), which shows the reflexes of the following compounds:  $\text{ScBO}_3$  [01-079-0097],  $\text{Sc}_2\text{O}_3$  [00-005-0629], and  $\text{Na}_2\text{Al}_2\text{B}_2\text{O}_7$  [00-053-1124]. The melting of  $\text{NaScB}_2\text{O}_5$  for XRD was carried out in a corundum ( $\text{Al}_2\text{O}_3$ ) crucible, which caused the interaction of the borate melt with the crucible material, so the diffractogram showed reflections of double aluminum and sodium borate ( $\text{Na}_2\text{Al}_2\text{B}_2\text{O}_7$ ). XRD results of samples annealed at temperatures (700, 750, 800, 850, 900, 950 °C) showed the presence of the  $\text{NaScB}_2\text{O}_5$  phase only, which indicates the thermal stability of  $\text{NaScB}_2\text{O}_5$  at these temperatures.

### 3.3. Conductivity measurements

#### 3.3.1. The theoretical evaluation of activation energy and ion transport pathways

Potential barriers and ionic transport pathways of sodium and oxygen were evaluated



**Fig. 3.** DSC curve recorded for  $\text{NaScB}_2\text{O}_5$

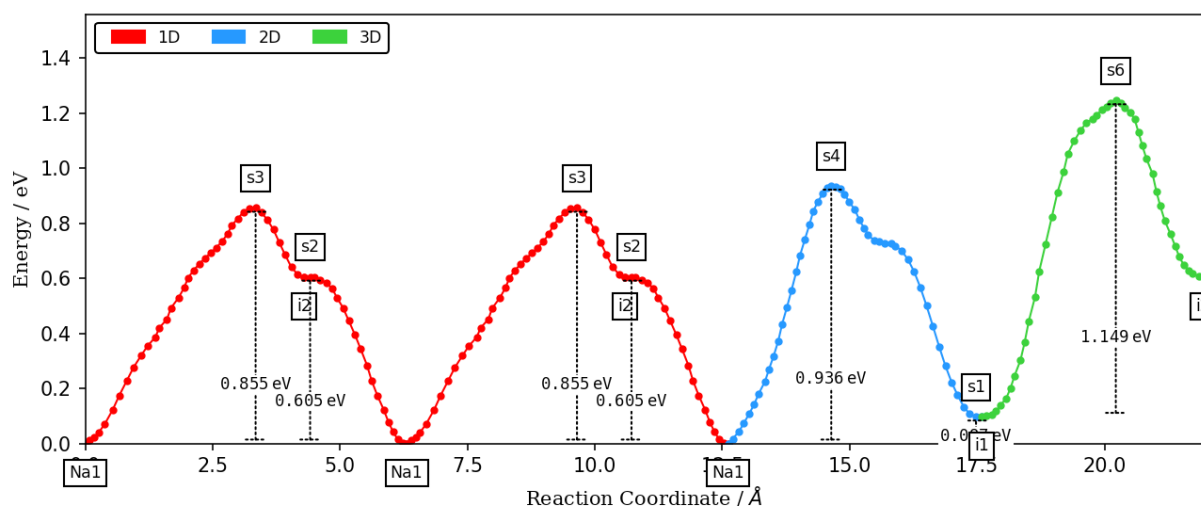
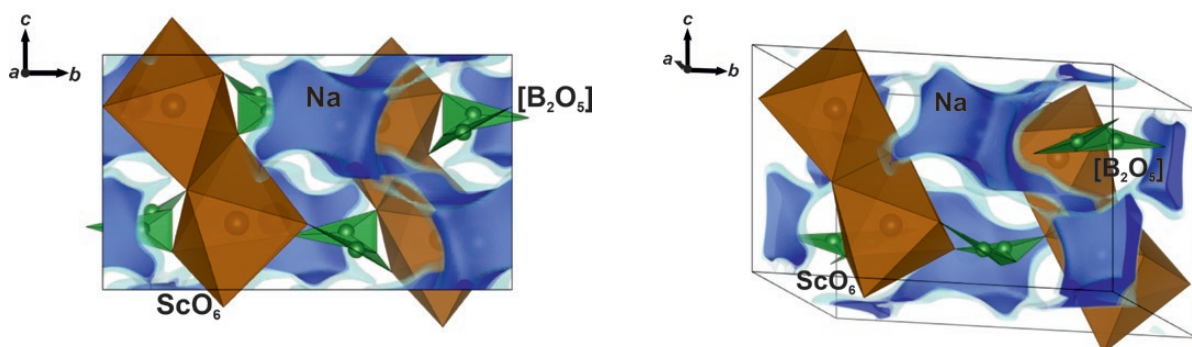
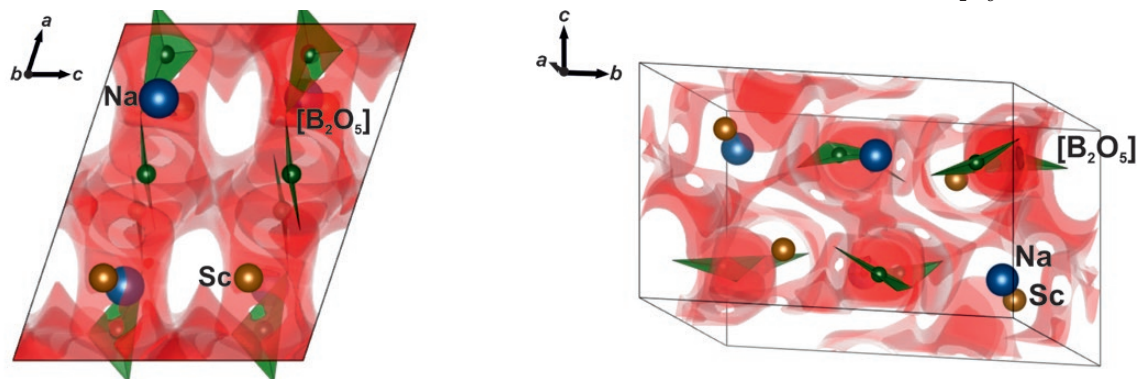
using valence force sum maps. According to calculations, the total electrical conductivity of  $\text{NaScB}_2\text{O}_5$  may include contributions of both sodium and oxygen ions (Table 2), indicating the three-dimensional conductivity of these ions in the crystal structure of the studied borate. However, the barrier of two-dimensional conductivity of sodium (0.936 eV) is comparable to the energy barrier of three-dimensional conductivity of oxygen (0.998 eV), while the analogous one for sodium ions is much lower (1.246 eV). The energy profile along the sodium ion pathway is shown in Fig. 4, and the calculated isosurfaces of the energy barriers of sodium and oxygen ions are shown in Figs. 5 and 6.

**Table 2.** Calculated energy barrier values of testing ions in  $\text{NaScB}_2\text{O}_5$ 

Testing ions	Energy barrier, eV	Dimension of conductivity
Na <sup>+</sup>	0.856	1D [0,0,1]
	0.936	2D (1,0,0)
	1.246	3D
O <sup>2-</sup>	0.629	1D [1,0,-1]
	0.998	3D

### 3.3.2. Experimental measurements of the electrical conductivity

The temperature dependence of the electrical conductivity is presented in Fig. 7 in Arrhenius coordinates. The dependence obtained is close to linear. The conductivity varies from  $0.6 \cdot 10^{-7}$  S/cm (300 °C,  $E_a = 0.7$  eV) to  $0.6 \cdot 10^{-3}$  S/cm (750 °C,  $E_a = 0.9$  eV). Figure 8 shows the impedance spectra of the double borate. The obtained  $Z'(Z'')$

**Fig. 4.** Energy profile along the route of sodium transport in the  $\text{NaScB}_2\text{O}_5$  structure**Fig. 5.** Calculated isosurfaces of activation energies of sodium ion transport in the  $\text{NaScB}_2\text{O}_5$  structure**Fig. 6.** Calculated isosurfaces of activation energies of oxygen ion transport in the  $\text{NaScB}_2\text{O}_5$  structure

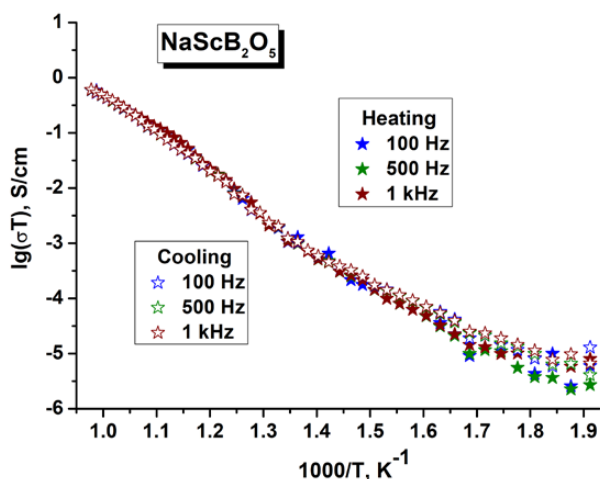


Fig. 7. Temperature dependences of electrical conductivity for  $\text{NaScB}_2\text{O}_5$

interdependence is typical for ionic conductors with blocking electrodes; the line in the low-frequency region corresponding to the ion transport blocking electrodes also indicates the ionic character of the conductivity.

### 3.4. Infrared spectra

The IR spectrum of sodium scandium borate was measured to compare with the spectra of

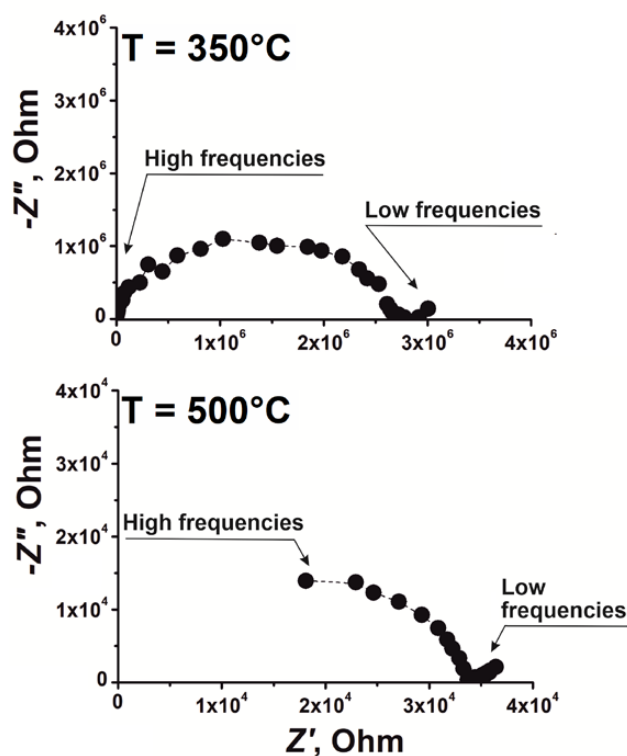


Fig. 8. The impedance profiles for  $\text{NaScB}_2\text{O}_5$  borate measured at different temperatures

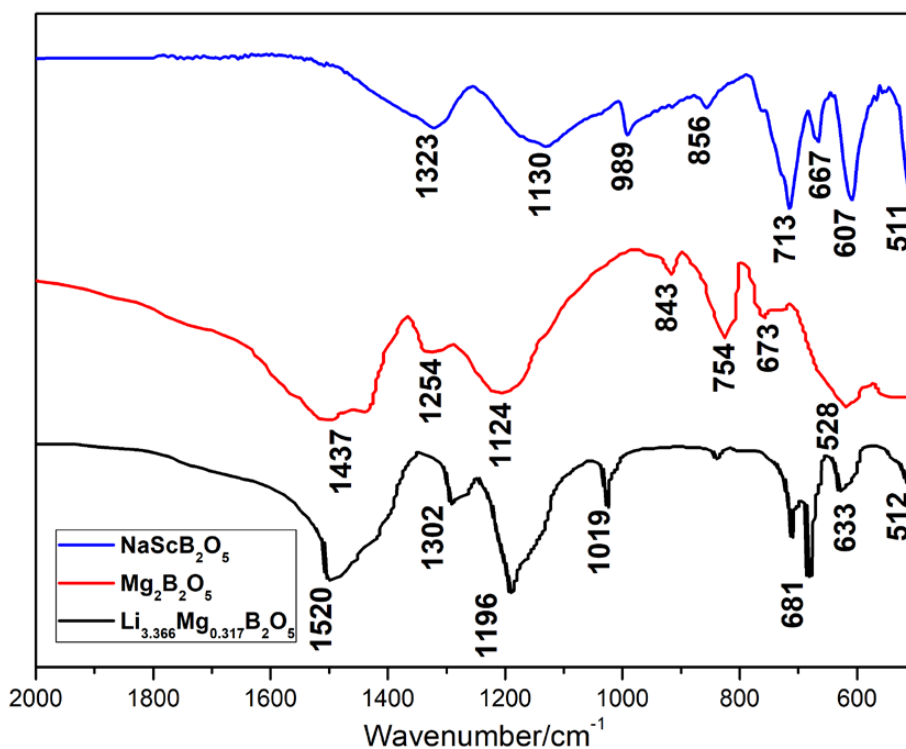


Fig. 9. The infrared spectra of  $\text{NaScB}_2\text{O}_5$ ,  $\text{Mg}_2\text{B}_2\text{O}_5$  and  $\text{Li}_{0.366}\text{Mg}_{0.317}\text{B}_2\text{O}_5$  [20]

known pyroborates and the IR spectrum of  $\text{NaScB}_2\text{O}_5$  calculated by the ab initio method. The band at  $1323\text{ cm}^{-1}$  refers to the antisymmetric valence vibrations of the  $\text{BO}_3$  group, whereas the bands at  $1130$ ,  $989$  and  $856\text{ cm}^{-1}$  refer to the symmetric valence vibrations of the B – O bonds in the  $\text{BO}_3$  group. The bands at about  $713$ ,  $667$ ,  $607\text{ cm}^{-1}$  belong to out-of-plane strain vibrations of the  $\text{BO}_3$  group, and the band at  $511\text{ cm}^{-1}$  to in-plane strain vibrations. Thus, the IR spectra further confirmed the triangular coordination of boron found from the crystal structure solution of  $\text{NaScB}_2\text{O}_5$ . In addition, the obtained IR spectrum of  $\text{NaScB}_2\text{O}_5$  was compared with the IR spectra of minerals using the ArDI Internet application (<https://ardi.fmm.ru/>) [36]. As a result of the search, the following minerals with similar IR spectra were found: Suanite, Shimazakiyite\_B117, Clinocurcate\_B3, and Curcate\_B36\_B36 (S2). All the above minerals belong to borates with the  $\text{B}_2\text{O}_5$  pyrogroup. Additionally, the IR spectrum of  $\text{NaScB}_2\text{O}_5$  was calculated by the ab initio method. The comparison showed a relatively good match between the position of the absorption peaks of the calculated spectrum and the experimental spectrum (Fig. 10). As can be seen from Fig. 10, there is a difference in the intensities of the calculated and experimental spectra. The discrepancy in the intensities between the calculated and experimental IR spectra, in our opinion, is caused, firstly, by the use of the harmonic approximation in the calculation, and secondly, by the neglect of temperature

effects, since the calculation technique implies calculation at absolute zero. Nevertheless, the figure shows a good match between the calculated and measured peak positions, which allowed us to interpret the nature of the oscillations.

### 3.5. Electronic structure

The  $\text{NaScB}_2\text{O}_5$  crystal lattice underwent relaxation to the total energy minimum. The crystal structure of  $\text{NaScB}_2\text{O}_5$  was optimized with the PBEsol functional. The lattice vectors were fixed at values determined experimentally, and the atomic positions were relaxed until the maximum component of the forces acting on the atoms was less than  $0.001\text{ eV/\AA}$ . After relaxation of the geometry, the volume of the unit cell did not change, but the atoms were significantly displaced from their original positions. The maximum displacements of Na atoms were  $0.062\text{ \AA}$ , Sc atoms were  $0.016\text{ \AA}$ , B atoms were  $0.032\text{ \AA}$ , and O atoms were  $0.054\text{ \AA}$ . Then, using the optimized crystal lattice, the zone structure of the substance was calculated using density functional theory with the exchange-correlation interaction HSE06. Figure 11 shows the electron density distribution of  $\text{NaScB}_2\text{O}_5$ . The valence band ceiling is occupied mainly by O-2p orbitals. The bottom of the conduction band consists mainly of 4d-orbitals of scandium. The width of the forbidden zone is approximately  $6\text{ eV}$ .

## 4. Conclusions

Sodium scandium double borate ( $\text{NaScB}_2\text{O}_5$ ) was obtained by solid-phase synthesis. The

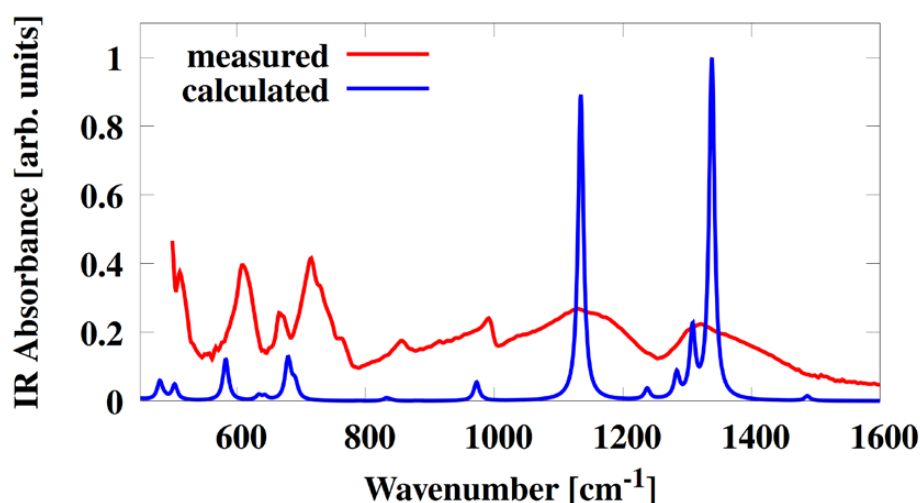
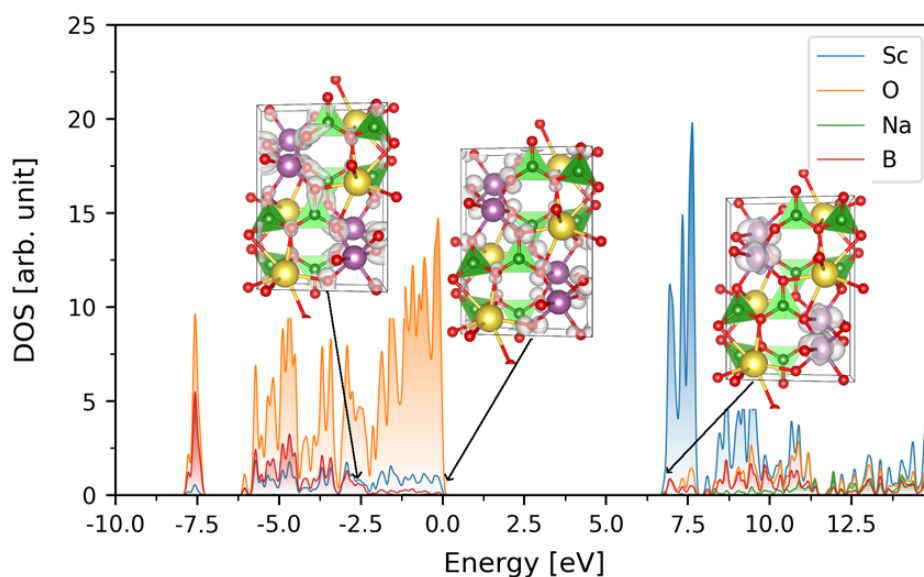


Fig. 10. Measured and calculated infrared spectra of  $\text{NaScB}_2\text{O}_5$



**Fig. 11.** The total and partial density of states in  $\text{NaScB}_2\text{O}_5$

crystallographic parameters of the synthesized sample were refined using the Rietveld method. The incongruent melting temperature was 1090 °C. A comparison of the experimental and calculated IR spectra showed good agreement of the peak positions, which allowed us to interpret the nature of the vibrations. The valence force sum maps, the energy barriers, and ionic transport pathways of sodium and oxygen ions were calculated, according to which the three-dimensional oxygen conductivity (0.998 eV) and the two-dimensional sodium conductivity (0.936 eV) are considered to be the most probable. The experimental conductivity measurements agree with the calculated data ( $E_a = 0.9$  eV). The ionic conductivity value of  $\text{NaScB}_2\text{O}_5$  is  $0.6 \cdot 10^{-3}$  S/cm at 750 °C. The band gap is 6.83 eV.

*Supplementary materials to the article are published in the electronic version on the journal's website.*

### Contribution of the authors

Andrey N. Sobolev A. – Visualization, Investigation, Writing. Evgeniy V. Kovtunets – Conceptualization, Software. Tatyana S. Spiridonova – Visualization, Investigation, Writing. Alexander I. Bogdanov – Visualization, Investigation, Writing. Alexey K. Subanakov – Data curation, Writing- Original draft preparation, Writing- Reviewing and Editing, Supervision.

### Conflict of interests

The authors declare that they have no known competing financial interests or personal relationships that could have influenced the work reported in this paper.

### References

1. Huang C., Mutailipu M., Zhang F., ... Pan S. Expanding the chemistry of borates with functional  $[\text{BO}_2]^-$  anions. *Nature Communications*. 2021;12: 1–8. <https://doi.org/10.1038/s41467-021-22835-4>
2. Li S., Li W., Li X., ... Li C. A bifunctional primitive strategy induces enhancements of large second harmonic generation and wide UV transmittance in rare-earth borates containing  $[\text{B}_5\text{O}_{10}]$  groups. *Chemical Science*. 2024;15: 8959–8965. <https://doi.org/10.1039/d4sc01853b>
3. Wu H., Wei Z., Hu Z., Wang J., Wu Y., Yu H. Assembly of  $\pi$ -conjugated  $[\text{B}_3\text{O}_6]$  units by mer-isomer  $[\text{YO}_3\text{F}_3]$  octahedra to design a UV nonlinear optical material,  $\text{Cs}_2\text{Yb}_3\text{O}_6\text{F}_2$ . *Angewandte Chemie*. 2024;136. <https://doi.org/10.1002/ange.202406318>
4. Zhang W., Hou X., Han S., Pan S. Toward the ultraviolet (UV) or deep-UV nonlinear optical crystals: the combination of  $\pi$ -conjugated planar  $[\text{XY}_3]$  and tetrahedral  $[\text{XY}_4]$ . *Coordination Chemistry Reviews*. 2024;505: 215664. <https://doi.org/10.1016/j.ccr.2024.215664>
5. Li Q.-F., Chen W.-F., Lan Y.-Z., Cheng J.-W. Recent progress in ultraviolet and deep-ultraviolet nonlinear optical aluminoborates. *Chinese Journal of Structural Chemistry*. 2023;42(3): 100036. <https://doi.org/10.1016/j.cjsc.2023.100036>
6. Kang L., Lin Z. Deep-ultraviolet nonlinear optical crystals: concept development and materials discovery. *Light: Science & Applications*. 2022;11: 1–12. <https://doi.org/10.1038/s41377-022-00899-1>
7. Halasyamani P. S. Zhang W. Viewpoint: inorganic materials for UV and deep-UV nonlinear-optical applications.

- Inorganic Chemistry*. 2017;56: 12077–12085. <https://doi.org/10.1021/acs.inorgchem.7b02184>
8. Chen C., Li R. The anionic group theory of the non-linear optical effect and its applications in the development of new high-quality nlo crystals in the borate series. *International Reviews in Physical Chemistry*. 1988;8: 65–91. <https://doi.org/10.1080/01442358909353223>
  9. Chen C., Wu Y., Jiang A., .... Lin S. New nonlinear-optical crystal: LiB<sub>3</sub>O<sub>5</sub>. *Journal of the Optical Society of America B*. 1989;6(4): 616. <https://doi.org/10.1364/josab.6.000616>
  10. Mori Y., Kuroda I., Nakajima S., Sasaki T., Nakai S. New nonlinear optical crystal: cesium lithium borate. *Applied Physics Letters*. 1995;67: 1818–1820. <https://doi.org/10.1063/1.115413>
  11. Chen C. T., Wang G. L., Wang X. Y., Xu Z. Y. Deep-UV nonlinear optical crystal KBe<sub>2</sub>BO<sub>3</sub>F<sub>2</sub>-discovery, growth, optical properties and applications. *Applied Physics B*. 2009;97: 9–25. <https://doi.org/10.1007/s00340-009-3554-4>
  12. Chen C., Wang Y., Wu B., Wu K., Zeng W., Yu L. Design and synthesis of an ultraviolet-transparent nonlinear optical crystal Sr<sub>2</sub>Be<sub>2</sub>B<sub>2</sub>O<sub>7</sub>. *Nature*. 1995;373: 322–324. <https://doi.org/10.1038/373322a0>
  13. Fröhlich R., Bohatý L., Liebertz J. *Acta Crystallographica Section C: Structural Chemistry*. Die Kristallstruktur von Wismutborat, BiB<sub>3</sub>O<sub>6</sub>. 1984;40: 343–344. <https://doi.org/10.1107/S0108270184004078>
  14. Guoqing Z., Jun X., Xingda C., .... Fuxi G. Growth and spectrum of a novel birefringent α-BaB<sub>2</sub>O<sub>4</sub> crystal. *Journal of Crystal Growth*. 1998;191(3): 517–519. [https://doi.org/10.1016/S0022-0248\(98\)00162-6](https://doi.org/10.1016/S0022-0248(98)00162-6)
  15. Zhang S., Wu X., Song Y., Ni D., Hu B., Zhou T. Growth of birefringent Ca<sub>3</sub>(BO<sub>3</sub>)<sub>2</sub> crystals by the Czochralski method. *Journal of Crystal Growth*. 2003;252: 246–250. [https://doi.org/10.1016/S0022-0248\(03\)00867-4](https://doi.org/10.1016/S0022-0248(03)00867-4)
  16. Ming H., Xiaolong C., Yuping S., Jun L., Jingtai Z., Chengjun D. YBa<sub>3</sub>B<sub>9</sub>O<sub>18</sub>: a promising scintillation crystal. *Crystal Growth and Design*. 2007;7(2): 199–201. <https://doi.org/10.1021/cg0606141>
  17. Chen X., Zhang B., Zhang F., .... Pan S. Designing an excellent deep-ultraviolet birefringent material for light polarization. *Journal of the American Chemical Society*. 2018;140: 16311–16319. <https://doi.org/10.1021/JACS.8B10009>
  18. Berger S. V., Hassel O., Webb M., Rottenberg M. The crystal structure of cobaltpyroborate. *Acta Chemica Scandinavica*. 1950;4: 1054–1065. <https://doi.org/10.3891/ACTA.CHEM.SCAND.04-1054>
  19. Cheng W. D., Zhang H., Zheng F. K., Chen J. T., Zhang Q. E., Pandey R. Electronic structures and linear optics of A<sub>2</sub>B<sub>2</sub>O<sub>5</sub> (A = Mg, Ca, Sr) pyroborates. *Chemistry of Materials*. 2000;12: 3591–3594. <https://doi.org/10.1021/cm000188l>
  20. Zhou C., Cheng J., Li H., Beysen S. Li<sub>3.366</sub>Mg<sub>0.317</sub>B<sub>2</sub>O<sub>5</sub>: the first pyroborate in the Li<sub>2</sub>O-MgO-B<sub>2</sub>O<sub>3</sub> system. *Inorganic Chemistry Communications*. 2018;93: 92–96. <https://doi.org/10.1016/j.inoche.2018.05.018>
  21. Maschmeyer E. M., Sanjeeva L. D., Ranmohotti G. S. Crystal structure of BaMnB<sub>2</sub>O<sub>5</sub> containing structurally isolated manganese oxide sheets. *Acta Crystallogr Sect E Crystallogr Commun*. 2016;72: 1315–11320. <https://doi.org/10.1107/S2056989016013074>
  22. Platonov M. S., Ivanova N. B., Kazak N. V., Ovchinnikov S. G. Crystal structure and magnetism of Co<sub>2-x</sub>Ni<sub>x</sub>B<sub>2</sub>O<sub>5</sub> pyroborate. *Journal of Siberian Federal University. Mathematics & Physics*. 2011;4: 298–307. Режим доступа: <https://elib.sfu-kras.ru/bitstream/handle/2311/2425/platonov.pdf?sequence=1>
  23. Busche S., Bluhm K. Synthese und Kristallstruktur der ersten zinkhaltigen Pyroborate Ni<sub>1.5</sub>Zn<sub>0.5</sub>(B<sub>2</sub>O<sub>5</sub>) und Co<sub>1.5</sub>Zn<sub>0.5</sub>(B<sub>2</sub>O<sub>5</sub>). *Zeitschrift für Naturforschung B*. 1995;50(10): 1445–1449. <https://doi.org/10.1515/znbn-1995-1003>
  24. Yan J., Chu D., Chen Z., Han J. Li<sub>2</sub>PbB<sub>2</sub>O<sub>5</sub>: a pyroborate with large birefringence induced by the synergistic effect of stereochemical active lone pair cations and π-conjugated [B<sub>2</sub>O<sub>5</sub>] groups. *Inorganic Chemistry*. 2022;61(46): 18795–801. <https://doi.org/10.1021/acs.inorgchem.2c03469>
  25. Held P., Becker P. Diprasedymium(III) pyroborate molybdate(VI), Pr<sub>2</sub>(B<sub>2</sub>O<sub>5</sub>)(MoO<sub>4</sub>). *Crystallographic Communications*. 2008;64(6). <https://doi.org/10.1107/S1600536808010386>
  26. Zhang M., An D., Hu C., Chen X., Yang Z., Pan S. Rational design via synergistic combination leads to an outstanding deep-ultraviolet birefringent Li<sub>2</sub>Na<sub>2</sub>B<sub>2</sub>O<sub>5</sub> material with an unvalued B<sub>2</sub>O<sub>5</sub> functional gene. *Journal of the American Chemical Society*. 2019;141: 3258–3264. <https://doi.org/10.1021/jacs.8b13402>
  27. Becker P., Held P. Crystal structure of sodium scandium borate, NaScB<sub>2</sub>O<sub>5</sub>. *Zeitschrift für Kristallographie – New Crystal Structures*. 2001;216(1-4): 35. <https://doi.org/10.1524/NCRS.2001.216.14.35>
  28. Rietveld H. M. A profile refinement method for nuclear and magnetic structures. *Journal of Applied Crystallography*. 1969;2: 65–71. <https://doi.org/10.1107/s0021889869006558>
  29. Coelho A. A. Topas: general profile and structure analysis software for powder diffraction data. Bruker AXS, 2005.
  30. Dinnebier R. E., Leineweber A., Evans J. Rietveld refinement practical powder diffraction pattern analysis using TOPAS. 2019. <https://doi.org/10.1515/9783110461381-201>
  31. Chen H., Wong L. L., Adams S. SoftBV – a software tool for screening the materials genome of inorganic fast ion conductors. *Acta Crystallographica Section B Structural Science, Crystal Engineering and Materials*. 2019;75: 18–33. <https://doi.org/10.1107/S2052520618015718>
  32. Kresse G. Ab initio molecular dynamics for liquid metals. *Journal of Non-Crystalline Solids*. 1995;192–193: 222–229. [https://doi.org/10.1016/0022-3093\(95\)00355-X](https://doi.org/10.1016/0022-3093(95)00355-X)
  33. Perdew J. P., Ruzsinszky A., Csonka G. I., ... Burke K. Restoring the density-gradient expansion for exchange in solids and surfaces. *Physical Review Letters*. 2008;100: 1–4. <https://doi.org/10.1103/PhysRevLett.100.136406>
  34. Togo A., Tanaka I. First principles phonon calculations in materials science. *Scripta Materialia*. 2015;108: 1–5. <https://doi.org/10.1016/j.scriptamat.2015.07.021>
  35. Krukau A. V., Vydrov O. A., Izmaylov A. F., Scuseria G. E. Influence of the exchange screening parameter on the performance of screened hybrid functionals. *The Journal of Chemical Physics*. 2006;125(22). <https://doi.org/10.1063/1.2404663>

36. Shendrik R. Yu., Plechov P. Yu., Smirnov S. Z. ArDI – the system of mineral vibrational spectroscopy data processing and analysis. *New Data on Minerals*. 2024;58(2): 26–35. (In Russ.). <https://doi.org/10.25993/fm.2024.58.2024.008>

### Information about the authors

*Andrey N. Sobolev*, Laborant at the Institute of Natural Sciences, Banzarov Buryat State University (Ulan-Ude, Russian Federation).

<https://orcid.org/0009-0006-2286-1380>  
sobolevan02@mail.ru

*Evgeniy V. Kovtunets*, Research Scientist of the Baikal Institute of Nature Management SB RAS, (Ulan-Ude, Russian Federation).

<https://orcid.org/0000-0003-1301-1983>  
kovtunets@gmail.com

*Tatyana S. Spiridonova*, Cand. Sci. (Chem.), Senior Research Scientist of the Baikal Institute of Nature Management SB RAS, (Ulan-Ude, Russian Federation).

<https://orcid.org/0000-0001-7498-5103>  
spiridonova-25@mail.ru

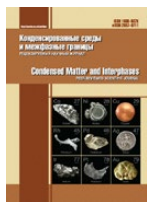
*Alexander I. Bogdanov*, Cand. Sci. (Phys.–Math.), Senior Research Scientist of the Vinogradov Institute of Geochemistry SB RAS, (Irkutsk, Russian Federation).

<https://orcid.org/0000-0001-8639-4730>  
alex.bogdanov2012@gmail.com

*Alexey K. Subanakov*, Cand. Sci. (Chem.), Head of the Oxide Systems Laboratory of the Baikal Institute of Nature Management SB RAS, (Ulan-Ude, Russian Federation).

<https://orcid.org/0000-0002-1674-283X>  
subanakov@binm.bsnet.ru

*Received 24.10.2024; approved after reviewing 02.12.2024; accepted for publication 05.12.2024; published online 25.09.2025.*



## Original articles

Research article

<https://doi.org/10.17308/kcmf.2025.27/13023>

## Coupled effects of concentration polarization in systems with anion-exchange membranes before and after their participation in electrodialysis of tartrate-containing solutions

O. A. Yurchenko✉, K. V. Solonchenko, N. D. Pismenskaya

Kuban State Technological University  
149 Stavropolskaya st., Krasnodar 350040, Russian Federation

### Abstract

**Objective:** Homogeneous anion-exchange membranes ASE and heterogeneous anion-exchange membranes MA-41P were studied in  $20 \pm 1$  mM  $\text{NaXH}_{(2-x)}\text{T}$  solutions with pH 2.5 and 9.0, where T is tartaric acid residue. Optical images and contact angles of membrane surfaces, as well as their current-voltage curves and pH of desalinated solutions, were measured before and after using ASE and MA-41P in electrodialysis.

**Experimental results:** The study determined that in alkaline solutions, the development patterns of concentration polarization do not differ from those of strong electrolytes. In acidic solutions, the ability of tartrates to participate in protonation-deprotonation reactions causes a 4–5 times increase in the empirical limiting current as compared to the theoretical limiting current calculated within the convective-diffusion model. The article discusses the mechanisms of tartrate transfer through anion-exchange membranes in cases when the desalinated solution contains mainly tartaric acid molecules.

**Conclusions:** Long-term operation (about 50 hours) under intensive current regimes results in the appearance of numerous caverns on the ASE surface and leads to an increase in the proportion of ion-exchange material on the MA-41P surface. The surfaces of both membranes become more hydrophobic. An analysis of current-voltage curves suggests that the electrochemical degradation of the ASE surface and specific interactions of tartrates with weakly basic fixed groups of both membranes lead to reduced proton generation and affect the development of electroconvection.

**Keywords:** Electrodialysis, Tartrates, Anion-exchange membranes, Current-voltage curves, Limiting current, Electroconvection, Catalytic water dissociation

**Financing:** The study was funded by the Russian Science Foundation and Kuban Science Foundation, project No. 24-29-20097

**For citation:** Yurchenko O. A., Solonchenko K. V., Pismanskaya N. D. Coupled effects of concentration polarization in systems with anion-exchange membranes before and after their participation in electrodialysis of tartrate-containing solutions. *Condensed Matter and Interphases*. 2025;27(3): 464–477. <https://doi.org/10.17308/kcmf.2025.27/13023>

**Для цитирования:** Юрченко О. А., Солонченко К. В., Письменская Н. Д. Сопряженные явления концентрационной поляризации в системах с анионообменными мембранами до и после их участия в электродиализе тартрат-содержащих растворов. *Конденсированные среды и межфазные границы*. 2025;27(3): 464–477. <https://doi.org/10.17308/kcmf.2025.27/13023>

✉ Olesya A. Yurchenko, [olesia93rus@mail.ru](mailto:olesia93rus@mail.ru)

© Yurchenko O. A., Solonchenko K. V., Pismanskaya N. D., 2025



The content is available under Creative Commons Attribution 4.0 License.

## 1. Introduction

Electrodialysis (ED) has been increasingly used for the extraction of tartaric acid from food industry waste for conversion of tartrate salts into tartaric acid [1], for the correction of pH of wine materials [2], and for the tartrate stabilization in wine [3]. Tartrate stabilization by means of electrodialysis involves removal of tartaric acid anions and potassium cations from the desalination chambers of electrodialyzers in applied electric field through anion-exchange membranes (AEM) and cation-exchange membranes (CEM) respectively. This helps to prevent tartrate precipitation during long-term wine storage [4–7]. Systematic studies of the application of electrodialysis in winemaking began in the 1970s [8, 9, 10] and resulted in the development of an automated technology [11, 12, 13] involving conventional membrane stacks with alternating cation and anion-exchange membranes [14] or a standard ED combined with bipolar membrane electrodialysis [15, 16]. The degree of wine demineralization in the desalination unit is controlled based on the electrical conductivity, which depends on the type of wine. A reduction in the electrical conductivity of wine by 20% corresponds to a 10–15% reduction in the concentration of tartaric acid. Exact parameters of ED for tartrate stabilization are usually determined specifically for each type of wine [17]. It is known that the optimal concentration of tartaric acid anions can be obtained, when the electrical conductivity is reduced by 15–20% for young wines, by 5–15% for aged wines [18], and by 20–30% for dessert wines [18, 19].

There are several factors that limit the widespread introduction of ED for the treatment of solutions with tartrates or various forms of other polybasic acids. One of the main drawbacks is low current efficiency and higher energy consumption as compared to those observed in the electrodialysis of strong electrolytes (for instance, NaCl) [20, 21]. Another drawback is the rapid degradation of the properties of anion-exchange membranes in solutions of polybasic acids and their salts [22, 23] as compared to strong electrolyte solutions. Both factors are associated with the structural features and the participation of polybasic acids in protonation-deprotonation reactions with water.

Tartaric acid (2,3-dihydroxybutanedioic acid, according to IUPAC,  $C_4H_6O_6$ ) is a fairly large molecule containing two hydroxyl and two carboxyl groups (Fig. 1).

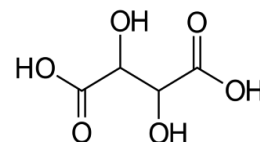
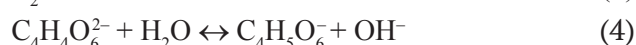
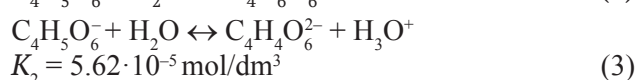
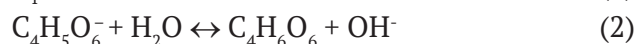
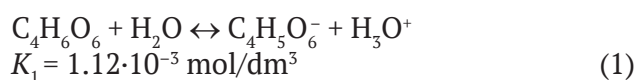


Fig. 1. Structural formula of tartaric acid [24]

The structure of tartaric acid ( $H_2T$ , where T is the acidic residue) results in a high degree of hydration of its anions (their hydration numbers are  $14 \pm 3$  [25]) and the possibility of steric hindrance during the transfer of these anions through an AEM [26]. There is also a possibility of specific interactions between carboxyl groups and primary and secondary amines, which are fixed groups in membranes. Such interactions, namely the formation of bound species, are characteristic for polybasic acids [27]. The binding behavior is caused by electrostatic interactions and the formation of hydrogen bonds, as well as by the donor-acceptor proton sharing between the carboxyl groups of acids and weakly basic amino groups [27]. The formation of bound species explains the sorption of polyvalent acid anions, including tartrates, by anion-exchange membranes described in a large number of studies [22, 23].

The protonation-deprotonation reactions, whose equilibrium constants can easily be found in reference literature [28], are described by the following equations:



Calculations based on these constants result in the distribution of molar fractions of various forms of tartaric acid depending on the pH of the solution (Fig. 2). These dependencies show that the electric charge of tartrates is extremely sensitive to the pH of the medium.

The purpose of our study was to perform a comparative analysis of the development of concentration polarization in anion-exchange

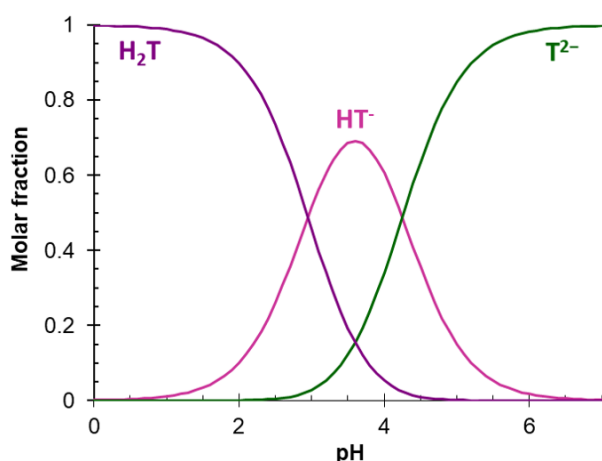


**Fig. 2.** Distribution of molar fractions of various forms of tartaric acid depending on the pH of the solution

membrane/ $\text{Na}_x\text{H}_{(2-x)}\text{T}$  solution systems with a pH of 2.5 or 9.0 depending on the characteristics of the membrane surface, and to assess the impact of long-term membrane operation in these solutions on the process.

For this purpose we used an ASE homogeneous membrane (Astom, Japan) and an MA-41P heterogeneous membrane (LLC Shchekinoazot, Russia). The studies were performed using “fresh” membrane samples and samples that were employed in a laboratory ED unit during the extraction of tartrates from  $\text{Na}_x\text{H}_{(2-x)}\text{T}$  solutions in underlimiting and overlimiting current modes.

## 2. Materials and methods

### 2.1. Solutions

Experiments were conducted in  $20 \pm 1$  mM  $\text{Na}_x\text{H}_{(2-x)}\text{T}$  solutions prepared from tartaric acid powder (Vecton, Russia) and distilled water (resistance  $1 \text{ M}\Omega\cdot\text{cm}$ , pH  $5.6 \pm 0.1$ ). The pH

values were adjusted using a  $100 \pm 1$  mM NaOH solution (Vecton, Russia). The total molar concentration of tartrates in the prepared solutions was determined using a DIONEX ICS-3000 chromatographic system (USA) with a conductometric detector and background signal suppression unit. The electrical conductivity of the solutions was measured at  $25^\circ\text{C}$  using an Expert-002 conductometer (OOO Econix-Expert, Russia). The distribution of various forms of tartaric acid depending on the pH of the solution was calculated taking into account the equilibrium constants of tartaric acid dissociation for the 1st and 2nd stages [28]. The main characteristics of the solutions are presented in Table 1.

### 2.2. Membranes

Some of the properties of anion-exchange membranes manufactured by Astom, Japan (ASE), and OOO Shchekinoazot, Russia (MA-41P) were described in previous articles [28, 29] and are summarized in Table 2. IR-Fourier spectroscopy [30] demonstrated that the ion-exchange material of a “fresh” pseudohomogeneous ASE membrane contains practically no weakly basic fixed groups. The electrochemical behavior of a heterogeneous MA-41P membrane in NaCl solutions also indicates the absence of such groups, at least previous to the operation of the membrane in intensive current modes [30]. The membranes are reinforced with nylon fabric (MA-41P) [31] or a mixture of polyethylene and polypropylene (ASE) [32]. The absence of macropores ensures a low volume fraction of intergel spaces ( $f_2$ ) in the ASE membrane (Table 2). On the contrary, the MA-41P

**Table 1.** Some characteristics of the  $20 \pm 1$  mM  $\text{Na}_x\text{H}_{(2-x)}\text{T}$  solution

pH	Electrical conductivity, $\mu\text{S}\cdot\text{cm}^{-1}$	$\text{H}_2\text{T}$ , %	$\text{HT}^-$ , %	$\text{T}^{2-}$ , %
$2.5 \pm 0.1$	$1525 \pm 5$	$73.5 \pm 0.1$	$26.0 \pm 0.1$	$0.5 \pm 0.1$
$9.0 \pm 0.1$	$3570 \pm 5$	0	$0.1 \pm 0.1$	$99.9 \pm 0.1$

**Table 2.** Some properties of the studied anion-exchange membranes

Membrane	Type	Ion-exchange matrix	Fixed groups	$Q$ , $\text{mM}\cdot\text{g}_{\text{wet}}^{-1}$ *	$f_2^{**}$	$\Theta^{***}$
ASE	homogeneous	PS+DVB	$-\text{N}^+(\text{CH}_3)_3$	1.93	0.06	1.0
MA-41P	heterogeneous			0.92	0.26	0.25

\* Exchange capacity of the swollen membrane; determination error  $\pm 0.05 \text{ mM}\cdot\text{g}_{\text{wet}}^{-1}$

\*\* Volume fraction of intergel spaces in NaCl solutions; determination error  $\pm 0.02$

\*\*\* Proportion of conductive surface; determination error  $\pm 0.02$

PS+DVB – polystyrene cross-linked with divinylbenzene

membrane is characterized by a rather high  $f_2$  due to the presence of macropores between the threads of the reinforcing material and the ion-exchange composite, as well as between the inert binder and resin particles. Additionally, the AB-17-2 resin, which is part of MA-41P, contains only 2% of DVB.

Heterogeneous membranes MK-40 and MA-41 (OOO *Shchekinoazot*, Russia) are auxiliary. They contain sulfonate fixed groups (MK-40) and quaternary amines (MA-41). The characteristics of these membranes are detailed in [33, 34]. Prior to experiments, all the membranes underwent salt pretreatment [35]. They were then divided into 2 samples, each of which was equilibrated with a  $20 \pm 1$  mM  $\text{Na}_x\text{H}_{(2-x)}\text{T}$  solution with pH 2.5 or 9.0.

### 2.3. Methods

The surface of swollen membranes was visualized using a SOPTOP CX40M optical microscope (Yuyao, Zhejiang, P.R., China). The MA-41P membrane was preliminarily soaked in a solution containing anthocyanins for 12 hours to increase the contrast of the anion-exchange resin particles on the surface of the inert binder – polyethylene.

Contact angles of the swollen membrane surfaces were measured using the sessile drop method as detailed in [36].

The current-voltage characteristics of the analyzed membranes were studied in a flow-through four-chamber electrodialysis cell described in [37]. The schematic diagram of the cell is shown in Fig. 1. One of the solutions presented in Table 1 was pumped through all the chambers of the ED cell. The average linear velocity of the solution in the chambers (V) was  $0.40 \pm 0.01$  cm·s<sup>-1</sup>. The intermembrane distance (h), the length of the solution desalination path (L), and the polarized membrane area (S) were  $6.6 \pm 0.1$  mm,  $20 \pm 1$  mm, and  $400 \pm 2$  mm<sup>2</sup>, respectively. Luggin capillaries were connected to the geometric centers of the surfaces of the studied anion-exchange membranes (\*AEM). The distance between their tips and the surface was about 0.8 mm. The capillaries were connected to microchambers containing measurement Ag/AgCl electrodes EVL-1M3.1 (Gomel, Belarus). They in turn were connected to an Autolab PGSTAT-100 electrochemical station (Metrohm Autolab B.V., Kanaalweg, Netherlands). The same station was used to polarize the membrane stack of the ED

cell through polarizing platinum electrodes. The current density scan rate was  $2.3 \cdot 10^{-3}$  mA cm<sup>-2</sup>. Parallel to determining the current-voltage characteristics, the inlet and outlet pH in the desalination chamber was measured at regular intervals. To perform the measurements, combined electrodes were used, which were immersed in flow-through microchambers and connected to Expert-001 pH meters (OOO *Econix-Expert*, Russia).

All measurements were performed before and after electrodialysis desalination of  $20 \pm 2$  mM solutions of  $\text{Na}_x\text{H}_{(2-x)}\text{T}$  with pH 2.5 or 9.0. During electrodialysis, the membranes functioned at current densities from 0 to  $2.0$  mA·cm<sup>-2</sup> for 10 hours.

The reduced current-voltage characteristics (CVCs) were plotted in  $i - \Delta\phi'$  coordinates [38]. The reduced potential drop  $\Delta\phi'$  was determined based on the measured potential drops  $\Delta\phi$ :

$$\Delta\phi' = \Delta\phi - IR_{\text{ef}}. \quad (5)$$

Here  $I$  is the applied current,  $R_{\text{ef}}$  is the effective ohmic resistance of the membrane and the solution located between the Luggin capillaries. It was determined based on the current-voltage characteristics as  $d\phi/dI$  where  $I \rightarrow 0$ .

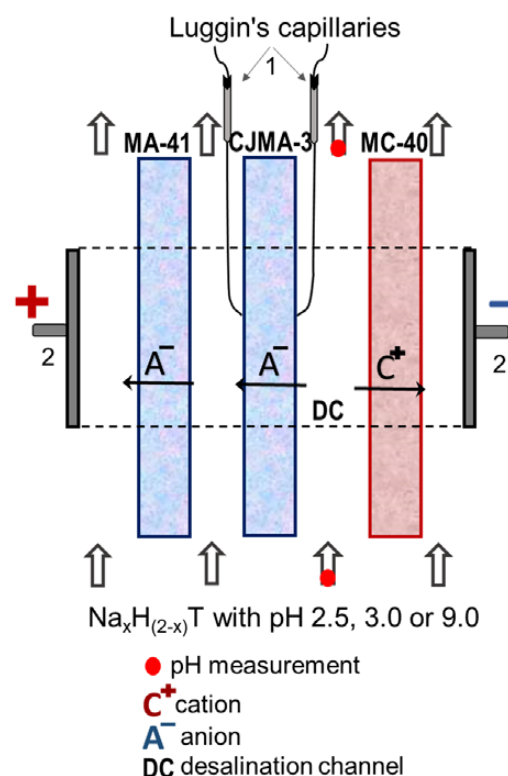


Fig. 3. Schematic diagram of the laboratory electrodialysis cell

The theoretical limiting current  $i_{\text{lim}}^{\text{Lev}}$  was determined using the Levich equation derived within the framework of the convection-diffusion model [39]:

$$i_{\text{lim}}^{\text{Lev}} = \frac{z_1 F D c_1}{h(t_A - T_A)} \left[ 1.47 \left( \frac{h^2 V_0}{L D} \right)^{1/3} \right]. \quad (6)$$

Here  $D$  is the diffusion coefficient of the electrolyte;  $z_1$  and  $c_1$  are the charge number and the concentration of the counterion ( $\text{HT}^-$  for the solution with pH 2.5 and  $\text{T}^{2-}$  for the solution with pH 9.0);  $t_A$  is the transport number of the co-ion

(cation  $\text{Na}^+$ ) during infinite dilution. The transport number  $T_A$  of the co-ion in the AEM was considered to be zero due to low electrolyte concentrations in the desalination and concentration chambers. For  $20 \pm 1$  mM solutions of  $\text{Na}_x\text{H}_{(2-x)}\text{T}$  with pH 2.5 and 9.0 the calculated values of  $i_{\text{lim}}^{\text{Lev}}$  were 0.56 and 4.10  $\text{mA cm}^{-2}$  respectively.

### 3. Results and discussion

#### 3.1. Optical images and contact angles of membrane surfaces

Fig. 4 shows optical images of the surfaces of the swollen membranes before and after ED.

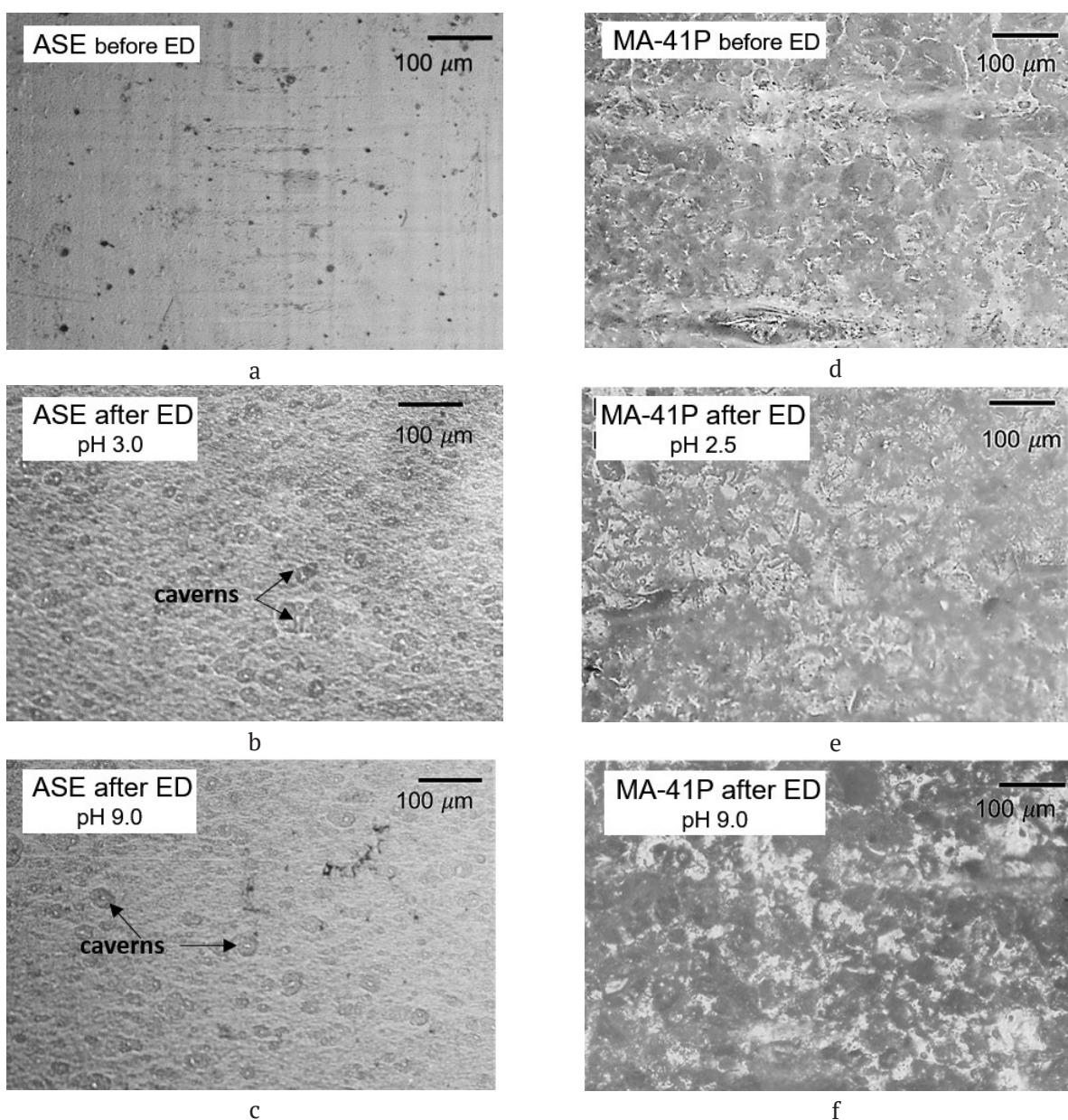


**Fig. 4.** Optical images of the surfaces of ASE (a, b, c) and MA-41P (d, e, f) membranes before and after ED

**Table 3.** Contact angles of membrane surfaces before and after their use for ED extraction of tartrates

Membrane	$\text{Na}_x\text{H}_{(2-x)}\text{T}$ with pH 2.5		$\text{Na}_x\text{H}_{(2-x)}\text{T}$ with pH 9.0	
	Before ED	After ED	Before ED	After ED
ASE	$33 \pm 2^\circ$	$31 \pm 3^\circ$	$35 \pm 2^\circ$	$45 \pm 3^\circ$
MA-41P	$60 \pm 4^\circ$	$69 \pm 2^\circ$	$61 \pm 4^\circ$	$68 \pm 2^\circ$

Table 3 presents the contact angles of the studied membrane surfaces before and after ED. During ED, these surfaces were facing the desalination chamber.

The surface of a “fresh” (not used in ED) ASE membrane was almost homogeneous (Fig. 4a). The ion-exchange material slightly protruded above the fibers of the reinforcing fabric. Other irregularities did not exceed a few micrometers. Apparently, the geometric heterogeneity is caused by the specifics of the pasting method of membrane manufacturing. The geometry of the ASE surface after ED underwent significant changes. Optical images (Fig. 4b, c) clearly demonstrate the appearance of caverns. They are evenly distributed over the membrane surfaces and reach several tens of  $\mu\text{m}$  in diameter. Moreover, when the membrane contacted the acidic solution (pH 2.5), the number of caverns increased compared to the alkaline solution (pH 9.0). The appearance of these caverns is no different from those observed on the surface of AMX and AMX-sb membranes [40] produced by Astom before switching to the production of ASE. This fact, as well as the results of IR spectroscopy [30], suggests that previously produced membranes (AMX) and new membranes (ASE) contain the same ion-exchange materials. It is these materials that undergo electrochemical destruction during membrane operation in intensive current modes. In other words, the use of a different inert binder and reinforcing material apparently did not help to reduce the electrochemical degradation of the ASE surface as compared to AMX during ED processing of tartrate-containing solutions.

The surface of a “fresh” heterogeneous MA-41P membrane consists of an inert binder (low-pressure polyethylene) and anion-exchange resin particles (Fig. 4d) and is rougher than the surface of a “fresh” ASE membrane. Threads of the reinforcing fabric were sometimes observed on the surface of MA-41P. No caverns identifiable

by means of optical microscopy appeared after the use of the membrane in ED processing of tartrate-containing solutions (Fig. 4e, f). At the same time, the linear dimensions of the resin particles on the surface increased. A particularly noticeable increase in the linear dimensions and a 27% increase in the proportion of conductive surface as compared to a “fresh” membrane was observed after ED in  $\text{Na}_x\text{H}_{(2-x)}\text{T}$  with pH 9.0. Apparently, changes in the linear dimensions of the resin particles (and MA-41P membranes) were caused by the factor we previously identified when studying MA-41 membranes kept in tartrate-containing solutions for a long time [41], namely the stretching of the ion-exchange matrix, when highly hydrated anions were introduced into its pores [25]. When an  $\text{Na}_x\text{H}_{(2-x)}\text{T}$  solution with pH 2.5 is replaced with a solution with pH 9.0, the electric charge of tartaric acid anions increases. This should facilitate increased hydration and, respectively, result in an increase in the linear dimensions of the resin particles.

We should note that the use of ASE in a  $\text{Na}_x\text{H}_{(2-x)}\text{T}$  solution with pH 2.5 does not result in any noticeable changes in the contact angle  $\theta$  of the membrane surface as compared to “fresh” membranes (Table 3). When a solution with pH 9.0 was used, the increase in the contact angle of the ASE surface after ED significantly exceeded the measurement error. The surfaces of the MA-41P membrane became more hydrophobic after the ED of both acidic and alkaline solutions. The observed changes in the hydrophilic/hydrophobic balance were most likely caused by the loss of electrical charge by some fixed groups located on the surfaces of the studied membranes. We can assume that under intensive current modes, some of the quaternary amines transformed into weakly basic amino groups. This phenomenon was described in a number of studies, including [42]. In alkaline solutions, these groups were deprotonated and lost their electric charge [43]. In acidic solutions, they formed bound species

with  $\text{HT}^-$  anions, which have zero electric charge [30]. The hydrophilic/hydrophobic balance of the ASE membrane after ED in an acidic tartrate-containing solution is apparently affected by two opposing factors. On one hand, a decrease in the electric charge of the surface should contribute to an increase in the measured contact angle. On the other hand, an increase in the roughness parameters of the surface should result in a decrease in the contact angle [43], if the  $\theta$  of the material does not exceed  $90^\circ$ .

### 3.2. Current-voltage characteristics of membranes and pH of desalinated solutions $\text{Na}_x\text{H}_{(2-x)}\text{T}$ with pH 9.0

Fig. 5 demonstrates the current-voltage characteristics of ASE and MA-41P membranes determined in a 20 mM  $\text{Na}_x\text{H}_{(2-x)}\text{T}$  solution with pH 9.0, and the difference in the inlet and outlet pH in the desalination chamber of the laboratory electrodialyzer, measured in parallel to the measurement of the CVC. The data was

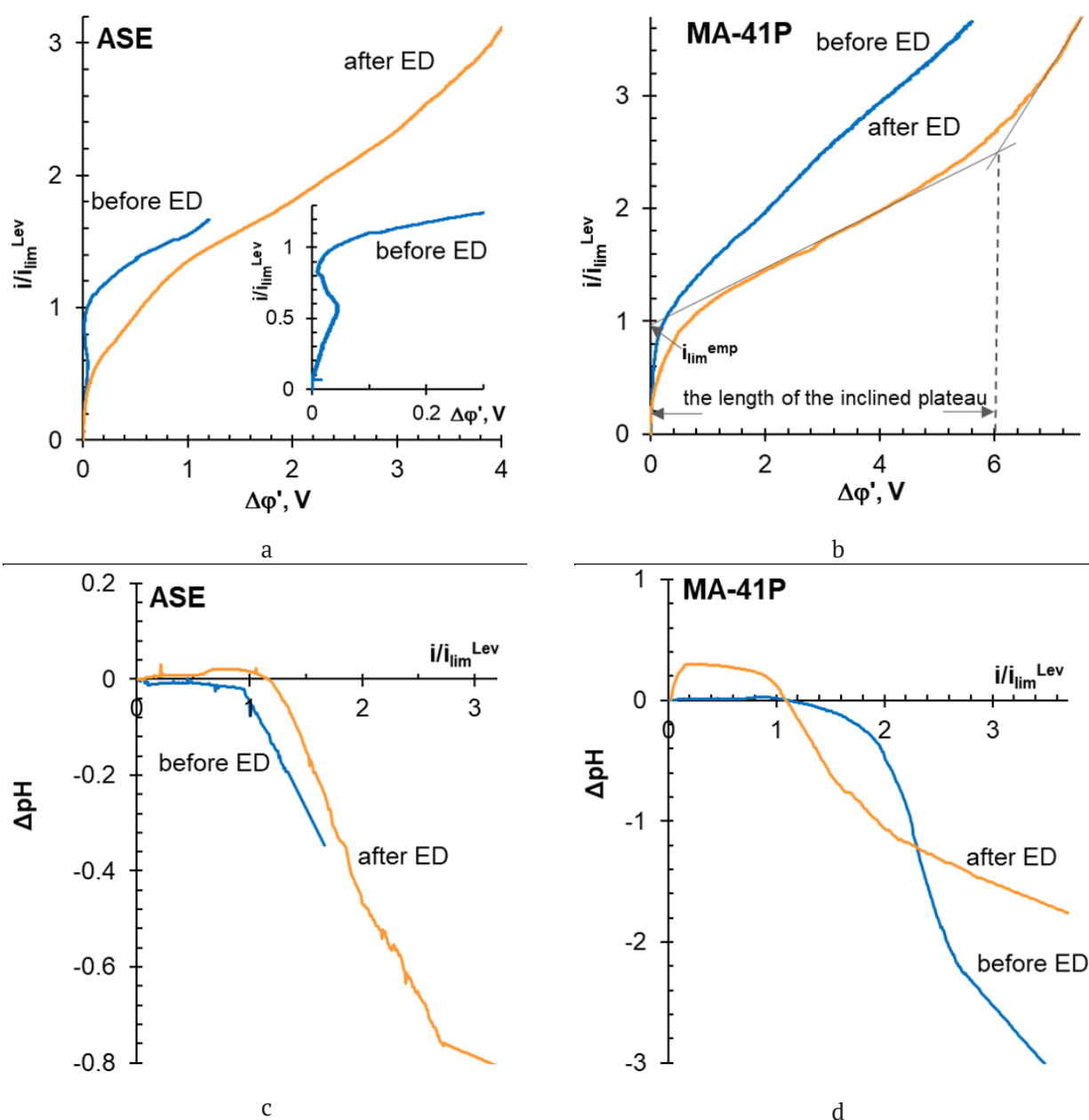


**Fig. 5.** Current-voltage characteristics of ASE (a) and MA-41P (b) membranes obtained in a 20 mM  $\text{Na}_x\text{H}_{(2-x)}\text{T}$  solution with pH 9.0, and the difference between the inlet and outlet pH in the desalination channel of the laboratory electrodialyzer, measured in parallel with obtaining the CVCs of ASE (c) and MA-41P (d) membranes. Explanations are provided in the text

obtained using “fresh” membranes (before ED) and membranes used for the ED processing of the said solutions (after ED). The results of the graphical processing of the CVC are summarized in Table 4. The empirical limiting current  $i_{\text{lim}}^{\text{emp}}$  and the length of the inclined plateau in the CVC were determined as shown in Fig. 5b.

We should note that the  $\text{Na}_x\text{H}_{(2-x)}\text{T}$  solution with pH 9.0 contains only trace amounts of  $\text{HT}^-$  anions and almost 100% of  $\text{T}^{2-}$  anions (Fig. 2, Table 1). Due to the Donnan exclusion of protons formed as a result of autoprotolysis of water, the pH of the internal solution of the AEM was higher than that of the external solution. In this case,  $\text{T}^{2-}$  anions in both the membrane and the depleted solution did not undergo any changes. Therefore, the mechanism of their transfer (Fig. 6a) and development of concentration polarization were the same as observed in strong electrolytes.

Increased current density causes a gradual decrease in the concentration of the electrolyte

( $\text{Na}_2\text{T}$ ) in the depleted solution near the membrane surface. The decrease results from the diffusion limitations for the transport of the electrolyte to the AEM interface. A limiting state is formed, when the concentration of  $\text{Na}_2\text{T}$  in the solution near the interphase region is infinitely low as compared to that in the depth of the solution in the desalination chamber. This state corresponds to  $i_{\text{lim}}^{\text{Lev}}$ , determined within the framework of the convection-diffusion model using equation (4). For fresh ASE membranes,  $i_{\text{lim}}^{\text{emp}}$  exceeds  $i_{\text{lim}}^{\text{Lev}}$  by 18% (Fig. 5a, Table 4), and the initial section of CVC demonstrates a characteristic decrease in conductivity (insertion in Fig. 5a). This indicates the presence of the Dukhin–Mishchuk electroconvection near the ASE surface, which develops in a thresholdless manner [44, 45]. Slight electroconvective vortices transport the more concentrated solution to the surface, thus shifting the formation of the limiting state ( $i_{\text{lim}}^{\text{emp}}$ ) towards the region of higher current densities. At

**Table 4.** Values of empirical limiting currents and lengths of the inclined plateau section found by means of graphical processing of CVCs

pH of $\text{Na}_x\text{H}_{(2-x)}\text{T}$	Parameter	ASE		MA-41P	
		Before ED	After ED	Before ED	After ED
9.0	$i_{\text{lim}}^{\text{emp}}/i_{\text{lim}}^{\text{Lev}*}$	1.18	0.98	1.08	0.95
	length of plateau, V	1.09	3.30	2.09	6.01
2.5	$i_{\text{lim}}^{\text{emp}}/i_{\text{lim}}^{\text{Lev}}$	3.55	4.13	4.95	3.56
	length of plateau, V	0.56	1.24	2.14	2.63

\* The error in determining  $i_{\text{lim}}^{\text{emp}}$  is  $\pm 3\%$

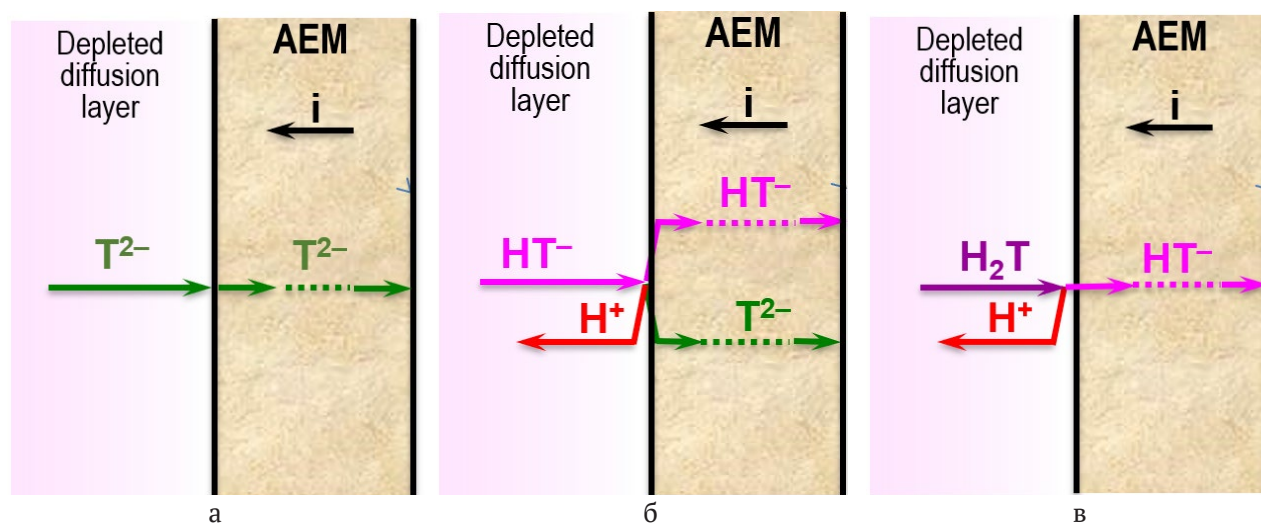


**Fig. 6.** Schematic representation of the transport mechanisms of anions  $\text{T}^{2-}$  (a),  $\text{HT}^-$  (b) and  $\text{H}_2\text{T}$  (c) in anion-exchange membrane and adjacent depleted solution in an applied electric field

higher current densities, the shortage of charge carriers in the near-membrane depleted solution result in a rapid potential drop (the region of the inclined plateau in the CVC). It is known that the slope of the CVC plateau can be accounted for by catalytic water dissociation (CWD) with the participation of fixed membrane groups and Rubinstein–Zaltzman electroconvection [46, 47]. Both processes develop in the threshold mode. According to [38], for the feed solutions with the concentration of electrolyte of 20 mM, the critical reduced potential drop for the onset of CWD is 0.3 V.

Indeed, after reaching this value, acidification of the desalinated solution was observed (Fig. 5c), which increased with an increase in the applied current. Despite the constant influx of protons, formed as a result of CWD, into the near-membrane solution, after reaching the threshold value of  $\Delta\phi'$  equal to the length of the inclined plateau, potential drop did not significantly grow with an increase in the current density. This overlimiting section of the CVC corresponds to the formation of large clusters of EC vortices in accordance with the Rubinstein–Zaltzman mechanism [47, 48].

For the MA-41P membrane (Fig. 5b), the concentration polarization developed in a similar way. The difference in the process, as compared to the ASE membrane, was caused by both electrical and geometric heterogeneity of the MA-41P surface. In our previous studies [31] we demonstrated that the heterogeneity parameters of this membrane are optimal for the development of both types of electroconvection. Therefore, with only 25% of the conductive surface, MA-41P demonstrated  $i_{\text{lim}}^{\text{emp}}$  equal to  $i_{\text{lim}}^{\text{Lev}}$ , within the limits of measurement error. Similar to ASE, catalytic water dissociation begins at critical values of the reduced potential drop (Fig. 5d). However, the intensive delivery of the electrolyte by clusters of EC vortices to the MA-41P surface shifted the intense acidification of the desalinated solution towards the region of higher  $i/i_{\text{lim}}^{\text{Lev}}$ . Provided that all other conditions were equal, local current density values in the area of anion-exchange resin particles on the MA-41P surface were higher than those of the ASE. Therefore, the desalinated solution became more acidic, and the recorded reduced potential drops had higher values for the heterogeneous membrane as compared to

the homogeneous one [31].

After the ED processing of the  $\text{Na}_x\text{H}_{(2-x)}\text{T}$  solution with pH 9.0, the empirical limiting current decreased by 17%, while the length of the inclined plateau increased by 3.0 times for the ASE membrane as compared to the fresh sample. For the MA-41P membrane, these parameters were 12% and 3.0 times, respectively (Fig. 5a, b, Table 4). The difference between the inlet and outlet pH in the desalination channel decreased for both studied membranes (Fig. 5d, e). The causes of these changes have already been discussed in section 3.1. On one hand, specific interactions of tartrates with weakly basic fixed groups on the membrane surface weakened the influence of these catalytically active groups (primary and secondary amines) on the generation of  $\text{H}^+$  and  $\text{OH}^-$  ions. On the other hand, these interactions apparently led to a decrease in the electric charge of the surface. This, in turn, resulted in a weakening of electroconvection developed in accordance with the Dukhin–Mishchuk mode. The weakening of this type of electroconvection is most obvious in the CVC of the ASE membrane used in ED. We should note that the CVC of a fresh membrane contained a section where the value of the reduced potential drop decreased as compared to that reached at  $i \approx 0.5i_{\text{lim}}^{\text{Lev}}$  (Fig. 5a). The CVC of the same membrane after ED demonstrated only a slowdown in the growth of  $\Delta\phi'$  at  $0.6i_{\text{lim}}^{\text{Lev}} < i < 1.1i_{\text{lim}}^{\text{Lev}}$ .

Apparently, changes in the surface charge negatively affect the space charge density, which determined the degree of development of Rubinstein–Zaltzman electroconvection. As a result, the threshold potential drops at which individual EC vortices merge into large clusters are shifted towards the region of higher  $\Delta\phi'$ . Moreover, for both membranes, the “lengthening” of the inclined plateau, which is an indicator of this phenomenon, takes place despite the fact that the hydrophobicity of the ASE and MA-41P surfaces increased after ED. In other words, facilitating the slip of EC vortices along the membrane surface had less influence on the degree of electroconvection development than changes in the structure of the double electric layer and the space charge region, which was caused by specific interactions of tartrates with fixed groups on the membrane surface.

**$\text{NaH}_{x(2-x)}\text{T}$  with pH 2.5**

Current-voltage characteristics of ASE and MA-41P membranes obtained in a 20 mM  $\text{NaH}_{x(2-x)}\text{T}$  solution with pH 2.5 are presented in Fig. 7. The results of their graphical processing are summarized in Table 4. Changes in the pH of desalinated solutions caused by phenomena developing at the AEM/depleted solution interface appear to be insignificant, considering a fairly high concentration of protons in the core of the flow. They cannot be recorded on the  $\Delta\text{pH} - i$  dependencies. Therefore, we are not going to discuss these dependencies.

Note that the feed  $\text{NaH}_{x(2-x)}\text{T}$  solution with pH 2.5 contained only 26.5% of tartrate anions. These were mostly  $\text{HT}^-$  anions. The other tartrates are located in tartaric acid molecules, which should not participate in electric charge transfer. The fact that for fresh membranes, the values of  $i_{\text{lim}}^{\text{emp}}$  exceed the values of  $i_{\text{lim}}^{\text{Lev}}$  by 3.55 (ASE) and 4.95 (MA-41P) times indicates the presence of mass transfer caused by the participation of various forms of tartaric acid in the protonation-deprotonation reactions. Indeed, the effect of these reactions on the transfer of  $\text{HT}^-$  anions has been studied both by means of experimental methods and mathematical modelling. These results are summarized in [38], and the mechanism of transfer, called acid dissociation (AD), is

schematically presented in Fig. 6b.  $\text{HT}^-$  anions participate in protonation-deprotonation reactions in accordance with equations (1) and (2) presented in the introduction. These reactions occurred both in solutions and in AEMs. At the same time, the Donnan exclusion of co-ions took place in the AEM [48]. Therefore, protons, which are one of the products of reactions (1), (3), were excluded from the membrane, and the AEM was enriched with doubly charged  $\text{T}^{2-}$  anions. Doubling the electric charge of counterions in the membrane and the constant influx of protons into the near-membrane depleted solution resulted in an increase in current density without a significant increase in the potential drop.  $\Delta\phi'$  began to grow only when the AEM was saturated with  $\text{T}^{2-}$  anions. In this case, the rate of proton influx into the depleted solution ceased to increase with increased current density. Therefore, the incoming protons could not compensate for the increase in the resistance of the near-membrane solution, which was caused by diffusion limitations of counterion ( $\text{HT}^-$ ) delivery from the depth of the desalinated solution to the membrane surface. Theoretical estimates demonstrate that at the maximum possible concentration of monovalent anions in the feed solution, which corresponds to pH 3.6 (Fig. 1), we can expect an increase in  $i_{\text{lim}}^{\text{emp}}$  by 2.2 times

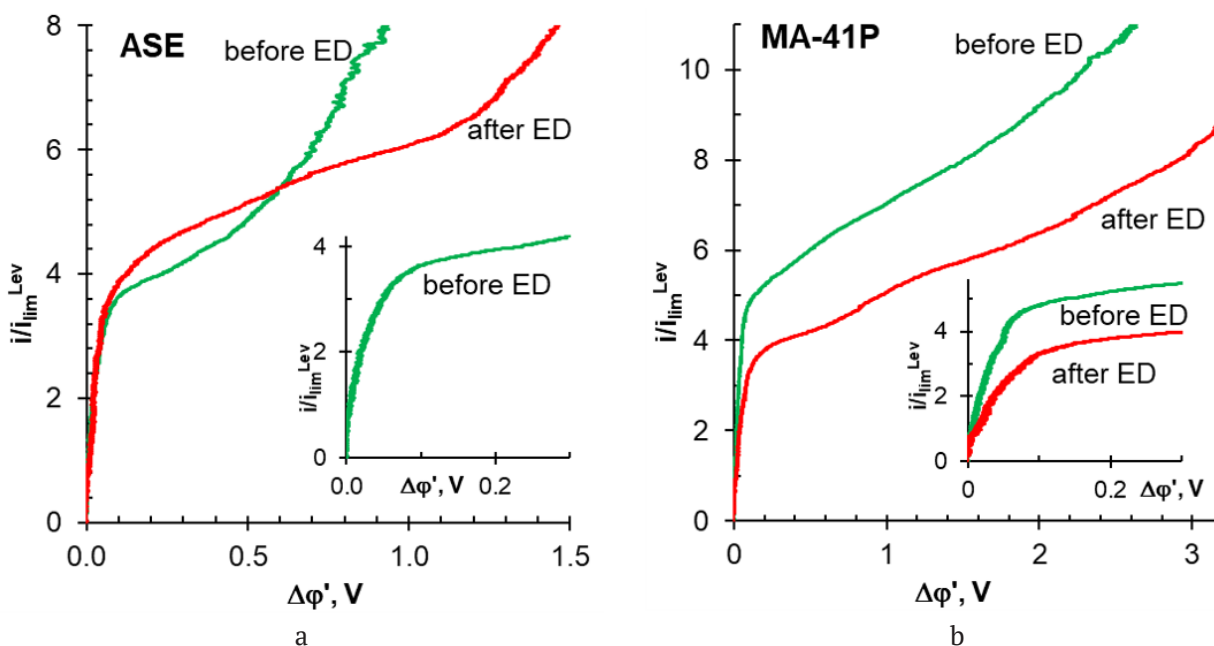


**Fig. 7.** Current-voltage characteristics of ASE (a) and MA-41P (b) membranes obtained in a 20 mM  $\text{NaH}_{x(2-x)}\text{T}$  solution with pH 2.5. Explanations are provided in the text

as compared to the limiting current  $i_{\text{lim}}^{\text{Lev}}$ . Higher values of recorded empirical limiting currents (Fig. 7, Table 4) indicate the anions initially contained in the feed solution were not the only ones being transferred through anion-exchange membranes. The source of additional  $\text{HT}^-$  anions were, apparently, tartaric acid molecules located in the near-membrane depleted solution. By analogy with the results of mathematical modelling [49] and the experimental study [50] of the transfer of weak acetic acid in membrane systems, the following scheme can be suggested (Fig. 6c). The dissociation of  $\text{H}_2\text{T}$  near the AEM surface is stimulated by the constant removal of resulting protons and  $\text{HT}^-$  anions from the reaction zone caused by an external electric field. Based on the results of mathematical modelling [50], we can expect that the degree of  $\text{H}_2\text{T}$  dissociation will be higher, when the tartaric acid molecules are closer to the AEM surface and at higher values of the applied current density. A similar hypothesis was suggested by Martí-Calatayud et al. [51]. They performed ED separation of citric acid and nitrate anions and observed the enhanced transfer of citrates through the AEM as the number of nitrates in the desalinated solution decreased. Apparently,  $\text{HT}^-$  anions are the first to be transferred from the feed depleted solution into the AEM. As charge carriers in the near-membrane solution are depleted, irreversible acid dissociation intensifies near the AEM surface. The observed values of  $i_{\text{lim}}^{\text{emp}}$  can be explained by at least two factors: the values of the kinetic constants of tartaric acid protonation-deprotonation reactions and the rate of  $\text{H}_2\text{T}$  molecule delivery from the depth of the solution to the AEM/depleted solution interface. Kinetic constants depend on the values of the equilibrium constants of acid dissociation for the first and second stages and on the rate of product removal from the reaction zone. The rate of  $\text{H}_2\text{T}$  molecule delivery to the AEM boundary will depend on the solution flow rate in the desalination chamber (thickness of the depleted diffusion layer), as well as on the degree of electroconvection development according to the Dukhin-Mishchuk mode. The characteristics of the MA-41P surface are more favorable for the development of this type of EC [31] than the ASE. The fact that for MA-41P the recorded

values of  $i_{\text{lim}}^{\text{emp}}$  of a fresh membrane were higher than for ASE suggests that under the conditions of the experiment, electroconvective delivery of acid to the AEM surface is crucial. Unfortunately, in acidic solutions, the influence of Dukhin-Mishchuk EC on the CVC shape is masked by the influx of protons into the depleted solution, which are generated by the AD mechanism (insets in Fig. 7). Therefore, this hypothesis needs to be further verified by means of mathematical modelling.

We should note that the length of the inclined plateau on the CVCs obtained for the solution with pH 2.5 for fresh ASE and MA-41P membranes decreased by almost 2 times as compared to the solution with pH 9.0. Intense oscillations of the potential drop in the overlimiting section of the CVC indicate the formation of EC vortex clusters according to the Rubinstein-Zaltzman mechanism. The causes of the intensification of this type of electroconvection in acidic solutions are not yet fully clear.

Long-term operation of membranes during the electrodialytic processing of  $\text{Na}_x\text{H}_{(2-x)}\text{T}$  solution with pH 2.5 had a different effect on the CVCs of the studied membranes. When the ASE membrane was used, the empirical limiting current increased by 16%, and the length of the inclined plateau increased by 2.2 times as compared to the fresh sample. The behavior of the MA-41P membrane after ED was different. The empirical limiting current decreased by 28%, and the length of the inclined plateau increased only by 20%.

The increase in  $i_{\text{lim}}^{\text{emp}}$  in the case of ASE could be facilitated by Dukhin-Mishchuk EC. Its enhancement is most likely caused by the appearance of numerous caverns on the surface of the membrane after ED. A similar effect was observed in the case of long-term operation of AMX and AMX-sb membranes [41], which were taken out of production and replaced with ASE [52]. It is known [46], that excessive development of the Dukhin-Mishchuk EC can shift the Rubinstein-Zaltzman formation of EC vortex clusters towards the region of higher potentials. This is apparently what happened in the case of the ASE membrane. Noticeable hydrophobization of the MA-41P surface (Table 4) is an indicator of partial loss of electric charge by its fixed

groups. Apparently, the change in the structure of the double electric layer caused a weakening of the Dukhin–Mishchuk EC and reduced the number of tartaric acid molecules delivered to the conductive surface of this membrane.

#### 4. Conclusions

Voltammetry combined with optical visualization and measurement of contact angles of swollen membrane surfaces is a highly informative method for studying mass transfer mechanisms of various forms of tartaric acid.

When the feed solution  $\text{Na}_x\text{H}_{(2-x)}\text{T}$  (T is the tartaric acid residue) contains mainly doubly charged  $\text{T}^{2-}$  anions, the mechanisms of transfer of these ions through anion-exchange membranes (AEM) do not differ from the well-known mechanisms of strong electrolyte transfer. The presence of geometric heterogeneity and high electric charge of the homogeneous membrane surface (ASE, Astom, Japan) or optimal parameters of electrical heterogeneity of the heterogeneous membrane (MA-41P, ООО *Shchekinoazot*) stimulate electroconvection and overlimiting mass transfer.

When the feed solution  $\text{Na}_x\text{H}_{(2-x)}\text{T}$  contains 26.5% of anions and 73.5% of acid molecules, the mechanisms of tartrate transfer in membrane systems become more complex. Regardless of the properties of AEM surfaces, the empirical limiting currents  $i_{\text{lim}}^{\text{emp}}$ , which are determined by means of graphical processing of current-voltage characteristics, appear to be several times higher than those that could be caused by the transfer of tartrate anions present in the feed solution. The observed increase in  $i_{\text{lim}}^{\text{emp}}$  can be caused by the irreversible dissociation of tartaric acid in the depleted solution near the AEM surface. It results from the continuous removal of protons and  $\text{HT}^-$  anions from the reaction zone in the applied electric field.

Long-term participation in the electrodialytic processing of  $\text{Na}_x\text{H}_{(2-x)}\text{T}$  solutions with pH 2.5 or 9.0 affects the hydrophilic/hydrophobic balance and morphology of ASE and MA-41P surfaces, as well as the degree of electroconvection development in the depleted solution adjacent to them. The dependence of  $i_{\text{lim}}^{\text{emp}}$  registered in acidic solutions on the conditions affecting the development of electroconvection suggests that

irreversible dissociation of tartaric acid is limited by its delivery to the anion-exchange membrane surface.

#### Author contributions

Yurchenko O. A. – research hypothesis, text writing, final conclusions. Solonchenko K. V. – selection and systematization of material, conducting research, text editing. Pismenskaya N. D. – text writing, research concept, final conclusions.

#### Conflict of interests

The authors declare that they have no known competing financial interests or personal relationships that could have influenced the work reported in this paper.

#### References

1. Andrés L. J., Riera F. A., Alvarez R. Recovery and concentration by electrodialysis of tartaric acid from fruit juice industries waste waters. *Journal of Chemical Technology and Biotechnology*. 1997;70(3): 247–252. [https://doi.org/10.1002/\(sici\)1097-4660\(199711\)70:3<247::aid-jctb763>3.0.co;2-8](https://doi.org/10.1002/(sici)1097-4660(199711)70:3<247::aid-jctb763>3.0.co;2-8)
2. Ioannidou S. M., Filippi K., Kookos I. K., Koutinas A., Ladakis D. Techno-economic evaluation and life cycle assessment of a biorefinery using winery waste streams for the production of succinic acid and value-added co-products. *Bioresource Technology*. 2022;348: 126295. <https://doi.org/10.1016/j.biortech.2021.126295>
3. Ncube A., Fiorentino G., Colella M., Ulgiati S. Upgrading wineries to biorefineries within a Circular Economy perspective: An Italian case study. *Science of the Total Environment*. 2021;775: 145809. <https://doi.org/10.1016/j.scitotenv.2021.145809>
4. Liu G., Wu D., Chen G., Halim R., Liu J., Deng H. Comparative study on tartaric acid production by two-chamber and three-chamber electro-electrodialysis. *Separation and Purification Technology*. 2021;263: 118403. <https://doi.org/10.1016/j.seppur.2021.118403>
5. El Rayess Y., Castro-Muñoz R., Cassano A. Current advances in membrane processing of wines: A comprehensive review. *Trends in Food Science and Technology*. 2024;147: 104453. <https://doi.org/10.1016/j.tifs.2024.104453>
6. Cabrita M. J., Garcia R., Catarino S. *Recent developments in wine tartaric stabilization*. Recent Advances in Wine Stabilization and Conservation Technologies. New York: Nova Publishers; 2016. Режим доступа: <http://hdl.handle.net/10174/19263>
7. Thoukis G. *Chemistry of wine stabilization: a review*. Washington: Chemistry of Wine Making, American Chemical Society; 1974. Режим доступа: <http://jklis.prv.pl/1.pdf>
8. Audinos R., Roson J. P., Jouret C. Application de l'électrodialyse à l'élimination de certains composants du jus de raisin et du vin essais de laboratoire. *OENO One Vin*. 1979;13: 229–239. <https://doi.org/10.20870/oeno-one.1979.13.3.1402>
9. Paronetto L., Braido A. *Some tests on tartrate stabilization of musts and wines by electrodialysis*. Vignevini. 1977;4:

- 9–15. Режим доступа: <https://agris.fao.org/search/en/providers/123819/records/64735a0753aa8c896307d146>
10. Wucherpennig K. Stabilization of grape juice and wine against tartar by means of electrodialysis. In: *Proceedings of the International Symposium on Separation Processes "Membr. Ion-Exch. Freeze-Cone. Food Ind."* A.P.R.I.A., Paris; 1975. 5–9.
11. Escudier J. L. Stabilisation tartrique des vins par membranes: resultats et developpements technologiques. In: *Proceedings of 11 eme Colloque Viticole et Oenologique Montpellier, France*; 1997.
12. Moutounet M., Escudier J.-L., Saint-Pierre B. In: *Les Acquisitions Récents dans les Traitements Physiques du Vin (ed. B. Don`eche)*. Paris: Tec. et Doc., Lavoisier. 1994. Режим доступа: [https://www.researchgate.net/profile/Jean-Louis-Escudier-2/publication/304496184\\_Determination\\_du\\_degre\\_d\\_instabilite\\_tartrique\\_DIT\\_principes\\_et\\_applications/links/6570e65ad21eb37cd4fa251d/Determination-du-degre-dinstabilite-tartrique-DIT-principes-et-applications?\\_cf\\_chl\\_tk=5z9Ff3qrXe\\_gnwCwDxEsImpb5Zas.oJ1GrbxdZc92I8-1733311140-1.0.1.1-XOzdBDi8lnhM m0ht2lVWq1S-shEy93 VpyvVInJYRXZ2c](https://www.researchgate.net/profile/Jean-Louis-Escudier-2/publication/304496184_Determination_du_degre_d_instabilite_tartrique_DIT_principes_et_applications/links/6570e65ad21eb37cd4fa251d/Determination-du-degre-dinstabilite-tartrique-DIT-principes-et-applications?_cf_chl_tk=5z9Ff3qrXe_gnwCwDxEsImpb5Zas.oJ1GrbxdZc92I8-1733311140-1.0.1.1-XOzdBDi8lnhM m0ht2lVWq1S-shEy93 VpyvVInJYRXZ2c)
13. Wollan D. Membrane and other techniques for the management of wine composition. *Managing Wine Quality*: 2021: 183–212. <https://doi.org/10.1016/b978-0-08-102065-4.00032-8>
14. Gonçalves F., Fernandes C., Cameira dos Santos P., De Pinho M. N. Wine tartaric stabilization by electrodialysis and its assessment by the saturation temperature. *Journal of Food Engineering*. 2003;59(2-3): 229–235. [https://doi.org/10.1016/s0260-8774\(02\)00462-4](https://doi.org/10.1016/s0260-8774(02)00462-4)
15. El Rayess Y., Achcouthy S., Ghanem C., Rizk Z., Nehme N. *Clarification and stabilization of wines using membrane processes*. In: Recent advances in wine stabilization and conservation technologies. NY, USA, Hauppauge: Nova Science Publishers; 2016: 111–135.
16. Vecino X., Reig M., Gibert O., Valderrama C., Cortina J. L. Integration of monopolar and bipolar electrodialysis processes for tartaric acid recovery from residues of the winery industry. *ACS Sustainable Chemistry and Engineering*. 2020;8(35): 13387–13399. <https://doi.org/10.1021/acssuschemeng.0c04166>
17. Soares P. A. M. H., Gerales V., Fernandes C., Dos Santos P. C., De Pinho M. N. Wine tartaric stabilization by electrodialysis: prediction of required deionization degree. *American Journal of Enology and Viticulture*. 2020;60(2): 183–188. <https://doi.org/10.5344/ajev.2009.60.2.183>
18. Ribéreau-Gayon P., Glories Y., Maujean A., Dubourdieu D. *Handbook of enology: the chemistry of wine, stabilization and treatments*. 2nd ed. Volume 2: Dunod, Paris. 2006.
19. Gómez Benítez J., Palacios Macías V. M., Szekely Gorostiaga P., Veas López R., Pérez Rodríguez L. Comparison of electrodialysis and cold treatment on an industrial scale for tartrate stabilization of sherry wines. *Journal of Food Engineering*. 2003;58(4): 373–378. [https://doi.org/10.1016/s0260-8774\(02\)00421-1](https://doi.org/10.1016/s0260-8774(02)00421-1)
20. Fidaleo M., Ventriglia G. Application of design of experiments to the analysis of fruit juice deacidification using electrodialysis with monopolar membranes. *Foods*. 2022;11(12): 1770. <https://doi.org/10.3390/foods11121770>
21. Liu G., Wu D., Chen G., Halim R., Liu J., Deng H. Comparative study on tartaric acid production by two-chamber and three-chamber electro-electrodialysis. *Separation and Purification Technology*. 2021;263: 118403. <https://doi.org/10.1016/j.seppur.2021.118403>
22. Zhang Y., Pinoy L., Meesschaert B., Van der Bruggen B. Separation of small organic ions from salts by ion-exchange membrane in electrodialysis. *AIChE Journal*. 2011;57(8): 2070–2078. <https://doi.org/10.1002/aic.12433>
23. Chandra A., Chattopadhyay S. Chain length and acidity of carboxylic acids influencing adsorption/desorption mechanism and kinetics over anion exchange membrane. *Colloids and Surfaces A: Physicochemical and Engineering Aspects*. 2020;589: 124395. <https://doi.org/10.1016/j.colsurfa.2019.124395>
24. Koga Y., Kondo T., Miyazaki Y., Inaba A. The effects of sulphate and tartrate ions on the molecular organization of water: towards understanding the Hofmeister series (VI). *Journal of Solution Chemistry*. 2012;41: 1388–1400. <https://doi.org/10.1007/s10953-012-9880-x>
25. Chandra A., Bhuvanesh E., Chattopadhyay S. A critical analysis on ion transport of organic acid mixture through an anion-exchange membrane during electrodialysis. *Chemical Engineering Research and Design*. 2022;178: 13–24. <https://doi.org/10.1016/j.cherd.2021.11.035>
26. Laucirica G., Pérez-Mitta G., Toimil-Molares M. E., Trautmann C., Marmisollé W. A., Azzaroni O. Amine-phosphate specific interactions within nanochannels: binding behavior and nanoconfinement effects. *The Journal of Physical Chemistry C*. 2019;123(47): 28997–29007. <https://doi.org/10.1021/acs.jpcc.9b07977>
27. Lide D. R. *CRC handbook of chemistry and physics* (Vol. 85). CRC Press; 2004.
28. Sugimoto Y., Ujike R., Higa M., Kakihana Y., Higa M. Power generation performance of reverse electrodialysis (RED) using various ion exchange membranes and power output prediction for a large RED stack. *Membranes*. 2022;12: 1141. <https://doi.org/10.3390/membranes12111141>
29. Pismenskaya N., Rybalkina O., Solonchenko K., Pasechnaya E., ... Nikonenko V. How chemical nature of fixed groups of anion-exchange membranes affects the performance of electrodialysis of phosphate-containing solutions? *Polymers*. 2023;15(10): 2288. <https://doi.org/10.3390/polym15102288>
30. Pismenskaya N.D., Pokhidnia E.V., Pourcelly G., Nikonenko V.V. Can the electrochemical performance of heterogeneous ion-exchange membranes be better than that of homogeneous membranes? *Journal of Membrane Science*. 2018;566: 54–68. <https://doi.org/10.1016/j.memsci.2018.08.055>
31. *Monopolar membranes*. Available at: <http://azotom.ru/monopolyarnye-membrany/>
32. Chen G. Q., Wei K., Hassanvand A., Freeman B. D., Kentish S. E. Single and binary ion sorption equilibria of monovalent and divalent ions in commercial ion exchange membranes. *Water Research*. 2020;175: 115681. <https://doi.org/10.1016/j.watres.2020.115681>
33. Kozaderova O. A., Kim K. B., Gadzhiev C. S., Niftaliev S. I. Electrochemical characteristics of thin heterogeneous ion exchange membranes. *Journal of Membrane Science*. 2020;604: 118081. <https://doi.org/10.1016/j.memsci.2020.118081>
34. Vasilyeva V. I., Meshcheryakova E. E., Falina I. V., Kononenko N. A., Brovkina M. A., Akberova E. M. Effect of

- Heterogeneous Ion-Exchange Membranes Composition on Their Structure and Transport Properties. *Membranes and Membrane Technologies*. 2023;13(3): 163–171. <https://doi.org/10.31857/S2218117223030082>
35. Berezina N. P., Timofeev S. V., Kononenko N. A. Effect of conditioning techniques of perfluorinated sulphocationic membranes on their hydrophylic and electrotransport properties. *Journal of Membrane Science*. 2002;209(2): 509–518. [https://doi.org/10.1016/S0376-7388\(02\)00368-X](https://doi.org/10.1016/S0376-7388(02)00368-X)
36. Ponomar M., Krasnyuk E., Butylskii D., ... Pismenskaya N. Sessile drop method: critical analysis and optimization for measuring the contact angle of an ion-exchange membrane surface. *Membranes*. 2022;12: 765. <https://doi.org/10.3390/membranes12080765>
37. Rybalkina O. A., Sharafan M. V., Nikonenko V. V., Pismenskaya N. D. Two mechanisms of H<sup>+</sup>/OH<sup>−</sup> ion generation in anion-exchange membrane systems with polybasic acid salt solutions. *Journal of Membrane Science*. 2022;651: 120449. <https://doi.org/10.1016/j.memsci.2022.120449>
38. Maletzki F., Rösler H. W., Staude E. Ion transfer across electrodialysis membranes in the overlimiting current range: stationary voltage current characteristics and current noise power spectra under different conditions of free convection. *Journal of Membrane Science*. 1992;71(1-2): 105–116. [https://doi.org/10.1016/0376-7388\(92\)85010-G](https://doi.org/10.1016/0376-7388(92)85010-G)
39. Lévêque M. A. *The laws of heat transmission by convection*. Les Annales des Mines: Memoires. 1928;12(13). 201–299.
40. Rybalkina O. A., Tsygurina K. A., Sarapulova V.V., Mareev S.A., Nikonenko V.V., Pismenskaya N. D. Evolution of current-voltage characteristics and surface morphology of homogeneous anion-exchange membranes during the electrodialysis desalination of alkali metal salt solutions. *Membranes and Membrane Technologies*. 2019;9(2): 131–145. <https://doi.org/10.1134/S2218117219020093>
41. Pismenskaya N., Sarapulova V., Nevakshenova E., Kononenko N., Fomenko M., Nikonenko V. Concentration dependencies of diffusion permeability of anion-exchange membranes in sodium hydrogen carbonate, monosodium phosphate, and potassium hydrogen tartrate solutions. *Membranes*. 2019;9(12): 170. <https://doi.org/10.3390/membranes9120170>
42. Zabolotskii V. I., Chermit R. K., Sharafan M. V. Mass transfer mechanism and chemical stability of strongly basic anion-exchange membranes under overlimiting current conditions. *Russian Journal of Electrochemistry*. 2014;50(1): 45. <https://doi.org/10.7868/S0424857014010113>
43. Quéré D. Rough ideas on wetting. *Physica A: Statistical Mechanics and its Applications*. 20022;313(1-2): 32–46. [https://doi.org/10.1016/s0378-4371\(02\)01033-6](https://doi.org/10.1016/s0378-4371(02)01033-6)
44. Dukhin S. S. Electrokinetic phenomena of the second kind and their applications. *Advances in Colloid and Interface Science*. 1991;35: 173–196. [https://doi.org/10.1016/0001-8686\(91\)80022-C](https://doi.org/10.1016/0001-8686(91)80022-C)
45. Mishchuk N. A. Concentration polarization of interface and non-linear electrokinetic phenomena. *Advances in Colloid and Interface Science*. 2010;160(1-2): 16–39. <https://doi.org/10.1016/j.cis.2010.07.001>
46. Rubinstein I., Zaltzman B. Electro-osmotically induced convection at a permselective membrane. *Physical Review E*. 2000;62(2): 2238. <https://doi.org/10.1103/PhysRevE.62.22381>
47. Zaltzman B., Rubinstein I. Electro-osmotic slip and electroconvective instability. *Journal of Fluid Mechanics*. 2007;579: 173–226. <https://doi.org/10.1017/S0022112007004880>
48. Helfferich F. G. *Ion exchange*. Courier Corporation; 1995.
49. Zabolotskii V.I., Lebedev K.A., Sheldeshov N.V. Ion-transfer across a membrane in the presence of a preceding slow homogeneous chemical reaction in the diffusion layer. *Russian Journal of Electrochemistry*. 2017;53(9): 1083–1097. <https://doi.org/10.7868/S0424857017090079>
50. Sharafan M. V., Gorobchenko A.D., Nikonenko V.V. Effect of acetic acid dissociation reaction on the limiting current density in a system with a rotating membrane disk. *Membranes and Membrane Technologies*, 2024;6(4): 290–297. In press.
51. Martí-Calatayud M. C., Ruiz-García M., Pérez-Herranz V. On the selective transport of mixtures of organic and inorganic anions through anion-exchange membranes: A case study about the separation of nitrates and citric acid by electrodialysis. *Separation and Purification Technology*. 2025;354: 128951. <https://doi.org/10.1016/j.seppur.2024.128951>
52. Anion exchange membranes. Available at: <https://www.astom-corp.jp/en/product/10.html>
- ## Information about the authors
- Olesya A. Yurchenko, Cand. Sci. (Chem.), Junior Research Fellow, Department of Physical Chemistry, Kuban State University (Krasnodar, Russian Federation). <https://orcid.org/0000-0001-5623-8657>  
olesia93rus@mail.ru
- Ksenia V. Solonchenko, postgraduate student, Engineer, Department of Physical Chemistry, Kuban State University (Krasnodar, Russian Federation). <https://orcid.org/0009-0005-8152-7879>  
sol.ksenia17@yandex.ru
- Natalia D. Pismenskaya, Dr. Sci. (Chem.), Professor at the Department of Physical Chemistry, Kuban State University (Krasnodar, Russian Federation). <https://orcid.org/0000-0001-5736-0136>  
n\_pismen@mail.ru
- Received October 28, 2024; accepted after reviewing November 8, 2024; accepted for publication November 15, 2024; published online September 25, 2025.

## Information about the authors

*Olesya A. Yurchenko*, Cand. Sci. (Chem.), Junior Research Fellow, Department of Physical Chemistry, Kuban State University (Krasnodar, Russian Federation).  
<https://orcid.org/0000-0001-5623-8657>  
[olesia93rus@mail.ru](mailto:olesia93rus@mail.ru)

*Ksenia V. Solonchenko*, postgraduate student, Engineer,  
Department of Physical Chemistry, Kuban State University  
(Krasnodar, Russian Federation).  
<https://orcid.org/0009-0005-8152-7879>  
[sol.ksenia17@vandex.ru](mailto:sol.ksenia17@vandex.ru)

*Natalia D. Pismenskaya*, Dr. Sci. (Chem.), Professor at the Department of Physical Chemistry, Kuban State University (Krasnodar, Russian Federation).  
<https://orcid.org/0000-0001-5736-0136>  
[n\\_pismen@mail.ru](mailto:n_pismen@mail.ru)

*Received October 28, 2024; accepted after reviewing November 8, 2024; accepted for publication November 15, 2024; published online September 25, 2025.*



# Condensed Matter and Interphases

Kondensirovannye Sredy i Mezhfaznye Granitsy  
<https://journals.vsu.ru/kcmf/>

## Short communication

Short communication

<https://doi.org/10.17308/kcmf.2025.27/13177>

## The influence of fullerene C<sub>60</sub> on the thermal stability of polyvinyl chloride

T. T. Sadykov✉, A. G. Mustafin, E. I. Kulish, R. M. Akhmetkhanov

Ufa University of Science and Technology,  
32 ul. Zaki Validi, Ufa 450076, Russian Federation

### Abstract

**Objective:** Polyvinyl chloride (PVC) is one of the most widely used industrial polymers, yet its practical application is limited by its low thermal and thermo-oxidative stability. The degradation of PVC is accompanied by the elimination of HCl and the formation of isolated and conjugated double bonds, which leads to polymer aging and deterioration of material properties. Despite the availability of numerous fundamental studies devoted to the degradation and stabilization of PVC, the mechanism of its decomposition remains under discussion, with radical, ionic, and combined pathways being considered. Therefore, the search for efficient stabilizers is still largely empirical. The aim of this work was to reveal the features of thermal and thermo-oxidative degradation of rigid and plasticized PVC in the presence of fullerene C<sub>60</sub>.

**Experimental:** The objects of study included industrial PVC grade S-7059M, fullerene C<sub>60</sub>, phenolic antioxidants (diphenylolpropane, ionol), and ester plasticizers (dioctyl phthalate, dioctyl sebacate). Thermal and thermo-oxidative dehydrochlorination was carried out at 175 °C in a bubbling-type reactor under nitrogen or oxygen flow. Stabilizing effects were evaluated by the rate of HCl release, thermal stability time (according to GOST 14041-91), and melt flow index measurements. It was shown that fullerene C<sub>60</sub> significantly inhibits PVC dehydrochlorination, reducing the rate of HCl release by more than twofold. The maximum effect is achieved at a content of 0.1 mmol per mol of PVC. In plasticized PVC systems, fullerene demonstrated high antioxidative activity, comparable to or exceeding that of industrial phenolic antioxidants. An «echo-stabilization» effect was observed, attributed to the inhibition of ester plasticizer oxidation.

**Conclusions:** Thus, fullerene C<sub>60</sub> can be considered a promising stabilizer for PVC, effectively retarding its thermal and thermo-oxidative degradation. The revealed regularities confirm the predominant role of the radical mechanism in PVC dehydrochlorination and highlight the potential of fullerene for extending the service life of PVC materials.

**Keywords:** Polyvinyl chloride, Fullerene C<sub>60</sub>, Polymer dehydrochlorination, Ester plasticizers, Phenolic antioxidants

**For citation:** Sadykov T. T., Mustafin A. G., Kulish E. I., Akhmetkhanov R. M. The influence of fullerene C<sub>60</sub> on the thermal stability of polyvinyl chloride. *Condensed Matter and Interphases*. 2025;27(3): 478–482. <https://doi.org/10.17308/kcmf.2025.27/13177>

**Для цитирования:** Садыков Т. Т., Мустафин А. Г., Кулиш Е. И., Ахметханов Р. М. Влияние фуллерена C<sub>60</sub> на термоустойчивость поливинилхлорида. *Конденсированные среды и межфазные границы*. 2025;27(3): 478–482. <https://doi.org/10.17308/kcmf.2025.27/13177>

✉ Timur T. Sadykov, e-mail: [gttima@mail.ru](mailto:gttima@mail.ru)

© Sadykov T. T., Mustafin A. G., Kulish E. I., Akhmetkhanov R. M., 2025



The content is available under Creative Commons Attribution 4.0 License.

## 1. Introduction

It is well known that polyvinyl chloride (PVC), characterized by relatively low thermal and thermo-oxidative stability, tends to undergo chemical transformations, mainly through the elimination of HCl and the formation of isolated and conjugated C=C bonds in the macromolecules. The insufficient stability of PVC leads to its aging, accompanied by changes in the overall set of properties of materials based on this polymer. Therefore, PVC requires effective stabilization – a set of measures aimed at reducing or preventing polymer aging. However, the stabilization of PVC is associated with certain difficulties. This is largely due to the fact that insufficient attention has been paid to the mechanism of PVC degradation itself. In many monographs and reviews devoted to the stabilization and processing of polyvinyl chloride, the degradation mechanism is not discussed at all [1–8].

Although a number of monographs, long since recognized as classical works, have been published [9–13], the question of the mechanism of PVC degradation remains the subject of active debate between the proponents of radical, ionic, and combined mechanisms. As a result, the development of new stabilizing additives for PVC, as well as the creation of compositions based on them, is still carried out largely intuitively and empirically.

Accordingly, for a better understanding of the degradation mechanism of PVC, special interest lies in the study of fullerene C<sub>60</sub> as a stabilizer, since it belongs to the class of inhibitors of chain radical reactions. It has been shown [14–17] that C<sub>60</sub> inhibits the thermal and thermo-oxidative decomposition of several homo- and copolymers of methyl methacrylate, polyvinylpyrrolidone, and polyethylene glycol, including under high-temperature conditions.

However, no information has been found on the effect of fullerenes on the decomposition of PVC. In this regard, it appears highly relevant to study the regularities of thermal and thermo-oxidative degradation of rigid and plasticized PVC in the presence of fullerene C<sub>60</sub>.

## 2. Experimental

Thermal and thermo-oxidative dehydrochlorination of plasticized PVC was carried out at

175 °C in a bubbling-type reactor under a nitrogen or oxygen flow (3.5 L/h). The dehydrochlorination rate was determined according to the procedure described in [18]. The thermal stability time of PVC ( $\tau$ ) was determined from the induction period corresponding to the color change of the Congo red indicator during HCl evolution in the course of polymer degradation (175 °C) in accordance with GOST 14041-91. The melt flow index was evaluated using an extrusion plastograph mi 2.2 (“Gutter”, FRG).

Polyvinyl chloride S-7059M was purified by Soxhlet extraction with ethanol. Fullerene C<sub>60</sub> (ZAO “Fullerene Center,” Nizhny Novgorod, Russia; 99.0%) was used without additional purification.

Antioxidants diphenylolpropane (DPP, 99.7%) and 2,6-di-tert-butyl-4-methylphenol (ionol, 99.8%) were also used without additional purification. Ester plasticizers dioctyl phthalate (DOP) and dioctyl sebacate (DOS) were purified by filtration through a column packed with aluminum oxide.

## 3. Results and discussion

The study showed that under conditions of thermal and thermo-oxidative degradation of neat PVC, fullerene C<sub>60</sub> significantly (by a factor of two) reduces the rate of polymer dehydrochlorination (Fig. 1). The maximum decrease in the dehydrochlorination rate is observed at a fullerene concentration of 0.1 mmol per mol of PVC.

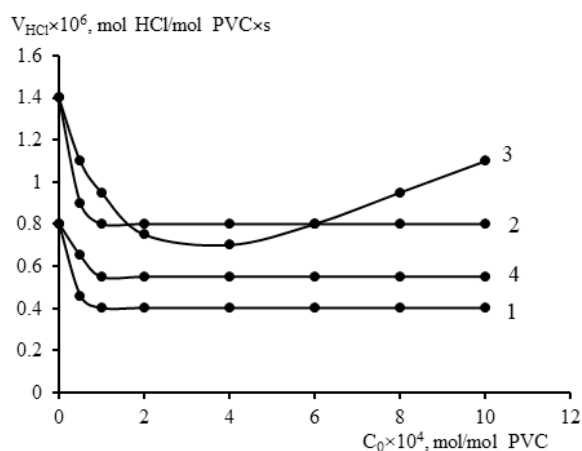
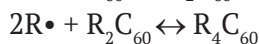
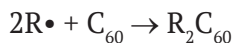
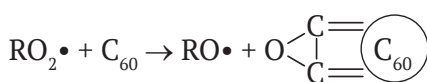
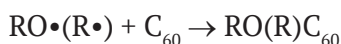


**Fig. 1.** Dependence of the rate of thermal (1, 4) and thermo-oxidative (2, 3) dehydrochlorination of PVC on the concentration of fullerene C<sub>60</sub> (1, 2) and diphenylolpropane (3, 4)

The inhibiting effect of fullerene in the radical-chain process of purely thermal degradation is associated with its interaction with free radicals to form thermally stable diamagnetic compounds [16]:



In thermo-oxidative degradation, reactions with active radicals  $R\cdot$  and  $RO_2\cdot$ , as described in the literature [14, 16], are also possible:



It should also be noted that when PVC is combined with fullerene, the latter exhibits a slight acceptor effect toward HCl released during degradation, as evidenced by the thermal stability time. This may be related to the sorption of hydrogen chloride by the fullerene structure (Table 1).

Even greater stabilizing efficiency of C<sub>60</sub> is observed when it is introduced into PVC plasticized with ester plasticizers (Figs. 2, 3). In terms of antioxidative activity, fullerene is practically not inferior to DPP and significantly surpasses ionol.

Obviously, under these conditions the well-known “echo-stabilization” effect occurs: fullerene C<sub>60</sub> inhibits the thermal oxidation of ester plasticizers, which in turn reduces the destabilizing influence of oxidized plasticizers on PVC degradation [19].

The high stabilizing efficiency of fullerene C<sub>60</sub> in relation to plasticized PVC is also confirmed by the thermal stability time. As shown by the data in Table 2, the introduction of fullerene leads to a significant increase in thermal stability in model plasticized compositions additionally containing metal-containing HCl acceptors.

The evaluation of rheological properties of model PVC plasticates with fullerene C<sub>60</sub>, based on the melt flow index (MFI), demonstrated that the incorporation of fullerene C<sub>60</sub> into the

**Table 1.** Thermal stability time of PVC in the presence of fullerene C<sub>60</sub>

Component	Composition, phr (parts by mass per 100 parts by mass of PVC)					
	1	2	3	4	5	6
PVC	100	100	100	100	100	100
Fullerene C <sub>60</sub>	-	0.05	0.1	0.3	0.5	1.0
$\tau$ , min (175 °C)	4	6	9	10	13	18

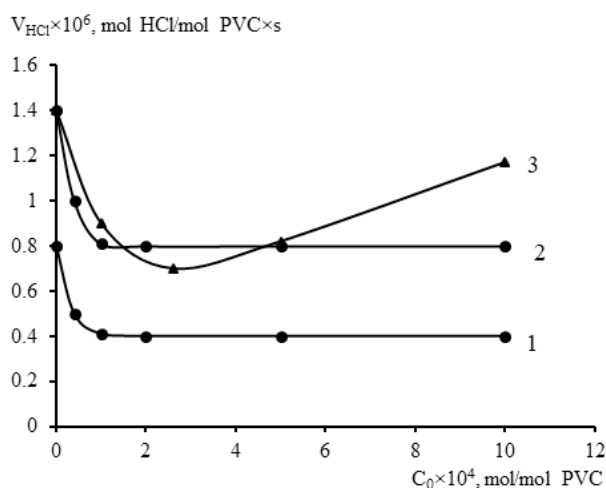


**Fig. 2.** Dependence of the rate of thermo-oxidative dehydrochlorination of PVC plasticized with dioctyl phthalate (40 phr) on the concentration of fullerene C<sub>60</sub> (1), diphenylolpropane (2), and ionol (3)

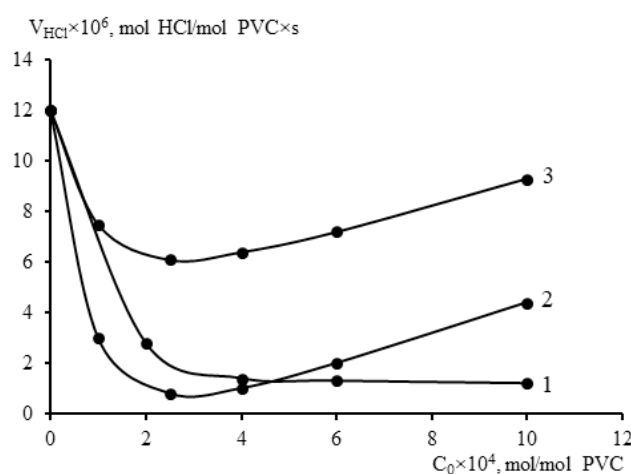


**Fig. 3.** Dependence of the rate of thermo-oxidative dehydrochlorination of PVC plasticized with dioctyl sebacate (40 phr) on the concentration of fullerene C<sub>60</sub> (1), diphenylolpropane (2), and ionol (3)

**Table 2.** Thermal stability time of PVC compositions

Component	Composition, phr (parts per 100 parts of PVC)							
	1	2	3	4	5	6	7	8
PVC	100	100	100	100	100	100	100	100
DOP	40	40	40	40	40	40	40	40
Calcium stearate	-	-	2	2	2			
Lead sulfate (tribasic)	-	-	-	-	-	1	1	1
Fullerene C <sub>60</sub>	0.5	1	-	0.5	1	-	0.5	1
τ, min (175 °C)	7	12	17	36	45	66	98	132

**Table 3.** Melt flow index of model PVC compositions

Component	Composition, phr (parts per 100 parts of PVC)			
	1	2	3	4
PVC	100	100	100	100
DOP	40	40	40	40
Lead sulfate (tribasic)	2	2	2	2
Fullerene C <sub>60</sub>	–	0.05	0.2	1.0
MFI, g/10 min (T = 180 °C, P = 15 kg)	19.8	14.9	11.2	5.3

composition results in a regular decrease in the MFI values (Table 3).

#### 4. Conclusions

Thus, under conditions of thermal and thermo-oxidative degradation of neat PVC, fullerene C<sub>60</sub> effectively inhibits the dehydrochlorination process. The high antioxidative efficiency of C<sub>60</sub>, comparable to or exceeding that of industrial phenolic antioxidants, leads to a significant reduction in the dehydrochlorination rate of PVC plasticized with esters. The strong stabilizing effect of fullerene C<sub>60</sub> is also confirmed in PVC compositions by the thermal stability time. The revealed regularities of the influence of C<sub>60</sub> on the thermal and thermo-oxidative degradation of both rigid and plasticized PVC support the radical mechanism of PVC degradation.

#### Contribution of the authors

The authors contributed equally to this article.

#### Conflict of interests

The authors declare that they have no known competing financial interests or personal relationships that could have influenced the work reported in this paper.

#### References

1. Wilkie C., Summers J., Daniels C. *Polyvinyl chloride\**. Transl. from eng., ed. Zaikov G. E. Saint Petersburg: Professiya Publ.; 2007. 728 p. (In Russ.)
2. Ulyanov V. M., Rybkin E. P., Gutkovich A. D., Pishin G. A. *Polyvinyl chloride\**. Moscow: Khimiya Publ.; 1992. 288 p. (In Russ.)
3. Gorshkov S. V., Bannikov V. N. *New effective thermostabilizers of polyvinyl chloride compositions\**. Moscow: VNIYESM Publ.; 1992. 40 p. (In Russ.)
4. Shtarkman B. P. *Plasticization of polyvinyl chloride\**. Moscow: Khimiya Publ.; 1975. 248 p. (In Russ.)
5. Kuzminskiy A. S. (ed.). *Aging and stabilization of polymers\**. Moscow: Khimiya Publ.; 1966. 212 p. (In Russ.)
6. Maslova I. P., Zolotareva K. A., Glazunova N. A. *Chemical additives to polymers\*. Handbook*. Moscow: Khimiya Publ.; 1973. 272 p. (In Russ.)
7. Gorbunov B. N., Gurchik Ya. A., Maslova I. P. *Chemistry and technology of stabilizers of polymeric materials\**. Moscow: Khimiya Publ.; 1981. 368 p. (In Russ.)
8. Kirillova E. I., Shulgina E. S. *Aging and stabilization of thermoplastics\**. Leningrad: Khimiya Publ.; 1988. 240 p. (In Russ.)
9. Minsker K. S., Fedoseeva G. T. *Degradation and stabilization of polyvinyl chloride*. Moscow: Khimiya Publ.; 1972. 420 p. (In Russ.)
10. Minsker K. S., Fedoseeva G. T. *Degradation and stabilization of polyvinyl chloride*. Moscow: Khimiya Publ.; 1979. 272 p. (In Russ.)
11. Minsker K. S., Kolesov S. V., Zaikov G. E. *Aging and stabilization of vinyl chloride-based polymers*. Moscow: Nauka Publ.; 1982. 272 p. (In Russ.)
12. Minsker K. S., Kolesov S. V., Zaikov G. E. *Degradation and stabilization of vinyl chloride-based polymers*. Oxford: Pergamon Press; 1988. 508 p.

13. Zilberman E. N. (ed.). *Production and properties of polyvinyl chloride*. Moscow: Khimiya Publ.; 1968. 432 p. (In Russ.)

14. Ginzburg B. M., Shibaev L. A., Ugolkov V. L. Effect of fullerene C<sub>60</sub> on thermal oxidative degradation of polymethyl methacrylate prepared by radical polymerization. *Russian Journal of Applied Chemistry*. 2001;74(8): 1329–1337. <https://doi.org/10.1023/a:1013714614891>

15. Shibaev L. A., Antonova T. A., Vinogradova L. V., Ginzburg B. M., Zgonnik V. N., Melenevskaya E. Yu. Effect of fullerene C<sub>60</sub> on thermal degradation of fullerene-containing polymers and mechanical mixtures of polymers with fullerene C<sub>60</sub>. *Russian Journal of Applied Chemistry*. 1998;71(5): 862–868. Available at: <https://elibrary.ru/item.asp?id=13729303>

16. Troitsky B. B., Khokhlova L. V., Konev A. N., Denisova V. N., Novikova M. A., Lopatin M. A. Temperature and concentration limits for fullerenes C<sub>60</sub> and C<sub>70</sub> as inhibitors of polymer degradation. *Polymer Science, Series A*. 2004;46(9): 1541–1548. Available at: <https://elibrary.ru/item.asp?id=13449755>

17. Karaulova E. N., Bagriy E. I. Fullerenes: functionalisation and prospects for the use of derivatives. *Russian Chemical Reviews*. 1999;68(11): 889–907. <https://doi.org/10.1070/rc1999v068n11abeh000499>

18. Gabitov I. T., Zakharov V. P., Mustafin A. G., Akhmetkhanov R. M. Low-toxic nitrogen-containing antioxidant for polyvinyl chloride. *Russian Journal of Applied Chemistry*. 2015;88(4): 626–629. <https://doi.org/10.1134/S1070427215040126>

19. Minsker K. S., Abdullin M. I. “Echo-stabilization” effect during thermal degradation of polyvinyl chloride\*. *Doklady Chemistry*. 1982;263(1): 140–143. (In Russ.)

\* Translated by author of the article

## Information about the authors

*Timur T. Sadykov*, Cand. Sci. (Chem.), Associate Professor at the Department of Physical Chemistry and Chemical Ecology, Ufa University of Science and Technology (Ufa, Russian Federation).

<https://orcid.org/0000-0003-2042-1032>

[gtime@mail.ru](mailto:gtime@mail.ru)

*Akhat G. Mustafin*, Dr. Sci. (Chem.), Professor, Head of the Department of Physical Chemistry and Chemical Ecology, Ufa University of Science and Technology (Ufa, Russian Federation).

<https://orcid.org/0000-0002-8342-8787>

[agmustafin@gmail.com](mailto:agmustafin@gmail.com)

*Elena I. Kulish*, Dr. Sci. (Chem.), Professor, Head of the Department of Macromolecular Compounds and General Chemical Technology, Ufa University of Science and Technology (Ufa, Russian Federation).

<https://orcid.org/0000-0002-6240-0718>

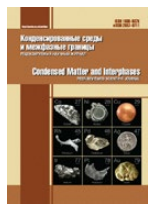
[onlyalena@mail.ru](mailto:onlyalena@mail.ru)

*Rinat M. Akhmetkhanov*, Dr. Sci. (Chem.), Associate Professor, Professor at the Department of Macromolecular Compounds and General Chemical Technology, Ufa University of Science and Technology (Ufa, Russian Federation).

<https://orcid.org/0000-0003-0016-0218>

[rimasufa@rambler.ru](mailto:rimasufa@rambler.ru)

Received January 23, 2025; approved after reviewing February 20, 2025; accepted for publication March 17, 2025; published online September 25, 2025.



## Short communication

Short communication

<https://doi.org/10.17308/kcmf.2025.27/13021>

## Infrared synchrotron nanovisualization of a biomimetic layer composed of trimethyldihydroquinoline and nanocrystalline hydroxyapatite

P. V. Seredin<sup>1</sup>✉, D. L. Goloshchapov<sup>1</sup>, Y. A. Peshkov<sup>1</sup>, N. S. Buylov<sup>1</sup>, A. Y. Potapov<sup>1</sup>,  
K. S. Shikhaliev<sup>1</sup>, Yu. A. Ippolitov<sup>2</sup>, Raul O. Freitas<sup>3</sup>, Francisco C. B. Maia<sup>3</sup>

<sup>1</sup>Voronezh State University,  
1 Universitetskaya pl., Voronezh 394018, Russian Federation

<sup>2</sup>Voronezh State Medical University,  
10 Studentcheskaya st., Voronezh 394036, Russian Federation

<sup>3</sup>Brazilian Synchrotron Light Laboratory (LNLS), Brazilian Center for Research in Energy and Materials (CNPEM),  
Campinas 13083-970, Sao Paulo, Brazil

### Abstract

**Objective of the article:** This study presents the findings of research on a biomimetic organomineral layer composed of trimethyl-dihydroquinoline, polymerized in the presence of nanocrystalline carbonate-substituted non-stoichiometric hydroxyapatite (n-cHAp).

**Experimental part:** The morphological features of the biomimetic layer were visualized using synchrotron infrared near-field spectroscopy.

**Conclusions:** It has been demonstrated that the biomimetic layer formed on the surface of dental enamel exhibits a morphological structure characterized by a uniformly distributed and densely packed composite film of poly(2,2,4-trimethyl-1,2-dihydroquinoline-6,7-diol) and n-cHAp. The resulting dental coating, based on polydihydroquinoline and nanocrystalline hydroxyapatite, possesses a Vickers hardness coefficient comparable to that of healthy enamel.

**Keywords:** trimethyl-dihydroquinoline, biomimetic layer, dental enamel, near-field infrared spectroscopy, synchrotron radiation

**Funding:** The study was funded by the Russian Science Foundation, as part of scientific project No. 23-15-00060.

### Acknowledgments:

Authors thank the Brazilian Synchrotron Light Laboratory for providing beamtime for SINS and s-SNOM experiments at the Imbuia beamline of Sirius (Proposal 20241295).

**For citation:** Seredin P. V., Goloshchapov D. L., Peshkov Y. A., Buylov N. S., Potapov A. Yu., Shikhaliev Kh. S., Ippolitov Yu. A., Raul O. Freitas, Francisco C. B. Maia. Infrared synchrotron nanovisualization of a biomimetic layer composed of trimethyldihydroquinoline and nanocrystalline hydroxyapatite. *Condensed Matter and Interphases*. 2025;27(3): 483–489. <https://doi.org/10.17308/kcmf.2025.27/13021>

**Для цитирования:** Середин П. В., Голощапов Д. Л., Пешков Я. А., Буйлов Н. С., Потапов А. Ю., Шихалиев Х. С., Ипполитов Ю. А., Raul O. Freitas, Francisco C. B. Maia. ИК-синхротронная нановизуализация биомиметического слоя на основе триметилдигидрохинолина и нанокристаллического гидроксиапатита. *Конденсированные среды и межфазные границы*. 2025;27(3): 483–489. <https://doi.org/10.17308/kcmf.2025.27/13021>

✉ Pavel V. Seredin, e-mail: [paul@phys.vsu.ru](mailto:paul@phys.vsu.ru)

© Seredin P.V., Goloshchapov D.L., Peshkov Y.A., Buylov N.S., Potapov A.Yu., Shikhaliev Kh.S., Ippolitov Yu.A., Raul O. Freitas, Francisco C. B. Maia, 2025



The content is available under Creative Commons Attribution 4.0 License.

## 1. Introduction

In the past decade, there has been an exponential increase in interest in dental biomaterials with antimicrobial properties applied to the surfaces of dental tissues in the form of thin films. One promising class of compounds with broad-spectrum antibacterial activity is quinoline and its derivatives [1], which can form homogeneous films [2] with antimicrobial activity [3]. However, there are virtually no reports in the literature on the use of quinolines in dentistry. This lack of research can be attributed to the unsatisfactory adhesion strength of these dental materials to the surfaces of hard dental tissues, as well as their low stability and short functional lifespan.

The first problem can be solved by the incorporation of functional groups into the composition of quinoline derivatives, which allows for the chemical adsorption of the polymer on the surface of the material [4, 5]. As has been repeatedly shown, increasing the stabilization and functioning of such films is possible using nanoparticles of various materials [6]. The strategy of forming dental layers that combine both remineralization functions and antimicrobial properties on the surface of enamel is the optimal solution to this problem [7–9].

At the same time, the formation of biomimetic layers should replicate the biogenic complexity of enamel at the nanoscale, where conjugation within individual crystals occurs via protein chains [10]. Determining the mechanisms of conjugation of organomineral systems at the nanoscale is a complex task requiring the use of a wide range of methods. One possible approach is the use of near-field infrared microscopy coupled with an atomic force microscope [11]. Combining the advantages of these methods allows the determination of the features of molecular conjugation of various compounds while simultaneously recording the topographic arrangement of structural elements of the composite. For enamel apatite, this method allows us to visualize and establish the characteristics of biogenic apatite both during formation and destruction in pathologies at the submicron level [12, 13]. For synthetic nanomaterials based on hydroxyapatite, it becomes possible to identify the features of surface phase formation and the

composite hierarchy at the level of individual nanocrystals [14].

In this study, synchrotron near-field infrared nanospectroscopy, combined with atomic force microscopy, was utilized to investigate the organic-mineral interactions and the hierarchical structure of the biomimetic layer formed from the nanopolymer dihydroxyquinoline and nanocrystalline hydroxyapatite.

## 2. Materials and methods

To create biotemplates, samples of intact human teeth were selected and diagnosed as free of carious lesions in hard tissues based on laser-induced contrast imaging data [15, 16]. Flat, parallel segments of dental tissue were obtained by sectioning the crown of the tooth perpendicularly to the occlusal surface, near the cusp, using the method we proposed earlier [16, 17].

Nanocrystalline carbonate-substituted non-stoichiometric hydroxyapatite, with average nanocrystal sizes of  $25 \times 25 \times 50$  nm (n-chAp) [18], was synthesized using a chemical precipitation method [19, 20].

2,2,4-Trimethyl-1,2-dihydroquinoline-6,7-diol hydrobromide (6,7-DiOH-TMDHQ) was synthesized by demethylation of 6,7-dimethoxy-2,2,4-trimethyl-1,2-dihydroquinoline using hydrobromic acid.

To obtain organomineral biomimetic layers, a solution containing n-chAp in distilled water was prepared [21]. The biotemplate was then introduced into the solution, followed by the immediate addition of 6,7-DiOH-TMDHQ, which initiated an auto-oxidation reaction.

Experiments utilizing infrared scattering scanning near-field optical microscopy (IRs-SNOM) were conducted using equipment of the IMBUIA-nano channel at the Brazilian Synchrotron Light Laboratory (LNLS). A set of quantum cascade lasers (QCL) (MirCat, DRS Daylight Solutions Inc.) was employed, covering a spectral range from  $930$  to  $1730$   $\text{cm}^{-1}$ , with a minimum frequency step of  $1$   $\text{cm}^{-1}$  for single-frequency excitation. To capture the amplitude and phase of the scattered signal, the optical setup was equipped with a pseudo-heterodyne (psHet) system and an asymmetric Michelson interferometer (neaSNOM, Neaspec GmbH) [22, 23].

The surface morphology and topology of the mineralized biomimetic layer were examined using a scanning electron microscope (SEM) (TESCAN VEGA 3, Czech Republic). Samples were affixed to aluminum microscopic substrates with adhesive carbon tape and subsequently coated with gold (Au) for 120 seconds using a sputtering device from Quorum Techniques Ltd (Q150T).

The mechanical properties of natural mineralized hard tissue and the deposited organomineral layers were analyzed using the Vickers hardness test.

### 3. Experimental results and discussion

Scanning electron microscopy images of a segment of healthy enamel (biotemplate) and a sample of 6,7-DiOH-PTMDHQ/ n-cHAp are shown in Figures 1a and 1b. The analysis of the local morphology of the natural mineralized tissue (Figure 1a) reveals the oriented growth of enamel prisms [10, 24, 25], which are formed by dense rows of hydroxyapatite nanocrystals, as illustrated in the inset of Figure 1a [26]. In samples with the biomimetic coating of 6,7-DiOH-PTMDHQ/n-cHAp, the formation of thin polymer films is observed, which contain agglomerates of synthetic hydroxyapatite (Figure 1b). A detailed examination of the morphology of the biomimetic layer (Figure 1b, inset) allows us to conclude that spherical agglomerates, measuring 100-200 nm, were evenly distributed within the 6,7-DiOH-PTMDHQ layer. This size is larger than the characteristic dimensions of the nanocrystals of n-cHAp [19] used in this study to

form the layer. Furthermore, the agglomerates were not merely incorporated into the 6,7-DiOH-PTMDHQ film; they were also partially enveloped by this nanopolymer.

To identify the characteristics of the deposition of individual structural elements in the biomimetic organomineral layer on the biotemplate, while considering the local chemical inhomogeneities of its morphology (Figure 2), infrared synchrotron scanning near-field optical microscopy (IR s-SNOM) with nanometer spatial resolution was used [13, 27, 28]. For signal excitation, we utilized radiation from a powerful quantum cascade infrared laser, which enabled spectral chemical mapping with a resolution of approximately 30 nm. Homogeneous areas of the samples in the enamel prism region were selected for analysis [29].

To simultaneously display the spectral-chemical features of the sample areas alongside the topology of their surfaces (Figures 2 a, b, e, f), near-field images of the optical phase and amplitude obtained from s-SNOM were visualized. These images correspond to infrared absorption and reflection from surface areas of  $500 \times 500 \text{ nm}^2$  (Figures 2 c, d, g, h). For constructing the chemical image, a resonant photon energy of  $1043 \text{ cm}^{-1}$  was utilized, which corresponds to the characteristic vibrations associated with the phosphate band  $\nu_3 \text{ PO}_4^{3-}$  of enamel apatite and synthesized nanocrystalline hydroxyapatite (Figures 2 c, d, g, h).

The analysis of the atomic force microscopy images of the surface topology of the reference

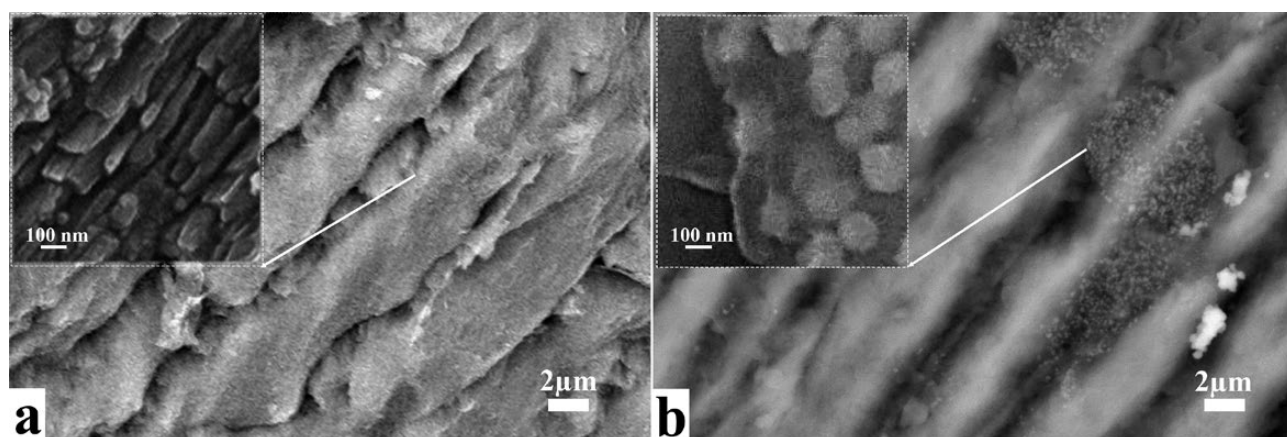


**Fig. 1.** SEM results. (a) natural enamel (biotemplate); (b) PTMDHQ – coating on the enamel surface based on 2,2,4-trimethyl-1,2-dihydroquinoline-6,7-diol polymerized in the presence of n-kHAp

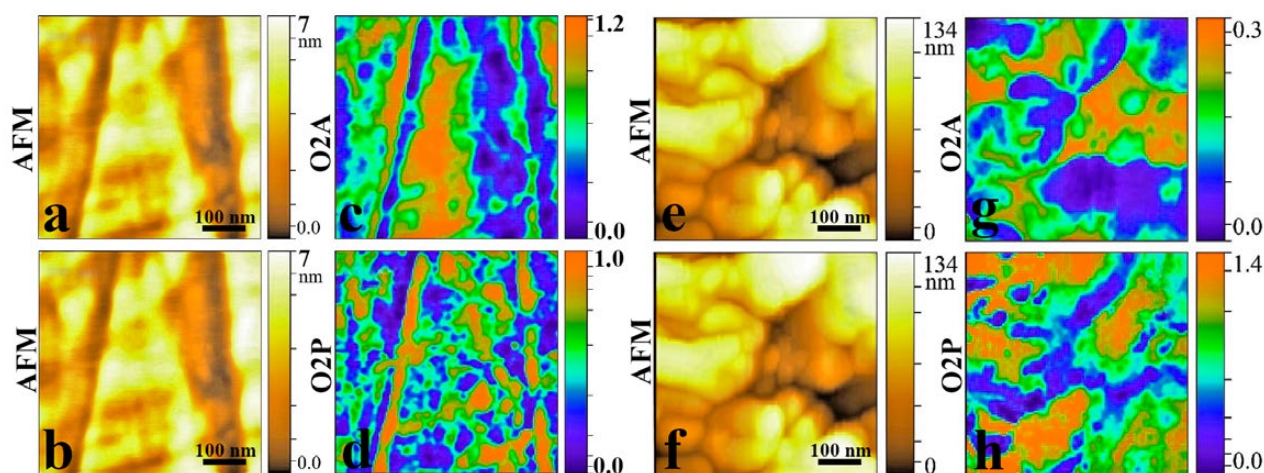


**Fig. 2.** Results of s-SNOM nanoimaging for a sample of natural enamel (top), PTMDHQ (bottom). For each sample, 2D AFM images of the surface topography over a  $500 \times 500 \text{ nm}^2$  area are simultaneously presented, as well as chemical images of these areas - the second harmonic intensity distribution for optical amplitude (O2A) and phase (O2P), corresponding to IR reflection and absorption, respectively, at resonance frequencies of  $1043 \text{ cm}^{-1}$

sample of natural enamel (Figures 2 a, b) revealed that, despite fine polishing, grooves left by the abrasive material were still visible. The contrast obtained using infrared scattering-type near-field optical microscopy (IR s-SNOM), which reflects the distribution of phosphate groups in the dental matrix in this area (Figures 2 c, d), visualized the path of the enamel prism formed by the dense packing of apatite nanocrystals. Additionally, a sufficiently homogeneous distribution of the amino acid network was detected, which correlates with existing literature [7, 12]. From the chemical contrast image, it can be observed that the localization area of the enamel rod on the AFM topology (Figure 2b) coincides with the maximum value of the optical phase, which is proportional to the intensity of optical absorption of the mode  $\nu_3 \text{ PO}_4^{3-}$  at  $1043 \text{ cm}^{-1}$  (Figure 2d). The analysis of the 2D AFM topology of the PTMDHQ sample (Figures 2 d, e) demonstrates that its surface exhibits a characteristic rough morphology, formed because of the pre-treatment procedure of the enamel using orthophosphoric acid and calcium hydroxide [9], as well as the deposition of PTMDHQ. The changes in the nanorelief reached approximately 130 nm and revealed the emergence of enamel prism nanocrystals from the biotemplate surface, which became apparent after etching (Figure 2e).

Analyzing the chemical spectral images of the PTMDHQ sample, which were constructed based on the distribution of optical amplitude and phase (Figures 2g, h), it is important to note that the effective depth for useful signal extraction in the infrared s-SNOM method reached 100 nm [30]. Thus, taking into account technological data on the thickness of the deposited biomimetic layers of PTMDHQ (approximately 40 nm), the chemical contrast in the spectral images simultaneously reflects the characteristics of both the layer and the biotemplate (Figures 2g, h). PTMDHQ was deposited on the surface of biotemplates along with nanocrystals of defective n-HA, which measure approximately  $20 \times 50 \text{ nm}$  and exhibit a morphological organization like that of natural enamel apatite [19, 20]. Previous studies have demonstrated that hydroxyapatite (HA) forms complexes with hydroxyquinoline via the formation of  $\pi$ - $\pi$  bonds [31]. This leads to the formation of globular structures of varying sizes, with diameters dependent on the initial organization of hydroxyapatite. Upon analyzing the chemical images obtained using s-SNOM (Figures 2g, h), which visualize the distribution of absorption and reflection at the resonance frequency of the phosphate mode at  $1043 \text{ cm}^{-1}$ , several observations can be made. On the surface of the PTMDHQ sample, areas of localization of the phosphate mode with a radial shape were

evident (Figure 2g), indicating the presence of agglomerates (particles) of phosphates with diameters of approximately 100 nm. This finding is consistent with the results obtained from scanning electron microscopy (Figure 1b, inset). Furthermore, the maximum intensity of signal localization from the film on the s-SNOM maps coincided with the peak absorption of the phosphate mode at  $1043\text{ cm}^{-1}$ , corresponding to the emergence of enamel prisms of apatite. Thus, the analysis of s-SNOM data suggests that calcium phosphate globules, surrounded by an organic shell and incorporated into the structure of the biomimetic film at varying depths, have formed on the surface of the PTMDHQ sample. A compact structure consisting of PTMDHQ/n-cHAp particles, uniformly distributed across the enamel surface and forming a continuous layer, has been established.

To determine the mechanical properties of the biomimetic layers based on PTMDHQ, which were deposited in the presence of nanocrystalline hydroxyapatite on the enamel surface, microhardness tests were conducted using the Vickers method. A slice of healthy enamel without an organomineral layer (biotemplate) was used as a reference sample. The results of Vickers microhardness measurements (VHN) at a load of 50 g and a loading time of 10 seconds indicated that the VHN for the healthy enamel sample (biotemplate) was  $362 \pm 21$ , while for the biomimetic organomineral layers of PTMDHQ, the VHN was  $322 \pm 26$ . The comparison of these values with known literature data for healthy enamel, which was reported as  $338 \pm 16$  [32], revealed that the VHN for the PTMDHQ sample was only 10% lower than that of healthy natural enamel.

The data obtained suggest the potential for using PTMDHQ/n-cHAp to create new hybrid biocoatings on the enamel surface. Additionally, they underscore the necessity for further research focused on enhancing the mechanical properties of the developed biomimetic layers.

#### 4. Conclusion

The study presents the results of research on a biomimetic organomineral layer composed of trimethyldihydroquinoline polymerized in the presence of nanocrystalline, carbonate-

substituted, non-stoichiometric hydroxyapatite. The morphological features of the biomimetic layer were visualized using near-field synchrotron infrared spectroscopy.

It has been demonstrated that the biomimetic layer formed on the surface of dental enamel exhibits a morphological structure characterized by a uniformly distributed and densely packed composite film of poly(2,2,4-trimethyl-1,2-dihydroquinoline-6,7-diol) and n-cHAp. Furthermore, the dental coating developed from polydihydroxyquinoline and nanocrystalline hydroxyapatite possesses a Vickers hardness coefficient comparable to that of healthy enamel.

#### Contribution of the authors

The authors contributed equally to this article.

#### Conflict of interests

The authors declare that they have no known competing financial interests or personal relationships that could have influenced the work reported in this paper.

#### References

1. Setlur A. S., Karunakaran C., Anusha V., ... Kusanur R. Investigating the molecular interactions of quinoline derivatives for antibacterial activity against *Bacillus subtilis*: computational biology and in vitro study interpretations. *Molecular Biotechnology*. 2024;66: 3252–3273. <https://doi.org/10.1007/s12033-023-00933-6>
2. Wang R., Cao Y., Jia D., Liu L., Li F. New approach to synthesize 8-hydroxyquinoline-based complexes with  $\text{Zn}^{2+}$  and their luminescent properties. *Optical Materials*. 2013;36: 232–237. <https://doi.org/10.1016/j.optmat.2013.08.032>
3. Abeydeera N., Benin B. M., Mudarmah K., ... Huang S. D. Harnessing the dual antimicrobial mechanism of action with Fe(8-Hydroxyquinoline)<sub>3</sub> to develop a topical ointment for mupirocin-resistant MRSA infections. *Antibiotics*. 2023;12: 886. <https://doi.org/10.3390/antibiotics12050886>
4. Nowicki J., Jaroszewska K., Nowakowska-Bogdan E., Szmatoła M., Hłowska J. Synthesis of 2,2,4-trimethyl-1,2-*H*-dihydroquinoline (TMQ) over selected organosulfonic acid silica catalysts: selectivity aspects. *Molecular Catalysis*. 2018;454: 94–103. <https://doi.org/10.1016/j.mcat.2018.05.016>
5. Kumar G., Sathe A., Krishna V. S., Sriram D., Jachak S. M. Synthesis and biological evaluation of dihydroquinoline carboxamide derivatives as anti-tubercular agents. *European Journal of Medicinal Chemistry*. 2018;157: 1–13. <https://doi.org/10.1016/j.ejmech.2018.07.046>
6. Ball V. Composite materials and films based on melamins, polydopamine, and other catecholamine-based materials. *Biomimetics*. 2017;2: 12. <https://doi.org/10.3390/biomimetics2030012>

7. Seredin P., Goloshchapov D., Emelyanova A., ... Mahdy I. A. Rapid deposition of the biomimetic hydroxyapatite-polydopamine-amino acid composite layers onto the natural enamel. *ACS Omega*. 2024. <https://doi.org/10.1021/acsomega.3c08491>
8. Kaushik N., Nhat Nguyen L., Kim J. H., Choi E. H., Kumar Kaushik N. Strategies for using polydopamine to induce biomineralization of hydroxyapatite on implant materials for bone tissue engineering. *International Journal of Molecular Sciences*. 2020;21(18): 6544. <https://doi.org/10.3390/ijms21186544>
9. Seredin P., Goloshchapov D., Kashkarov V., ... Prutskij T. Biomimetic mineralization of tooth enamel using nanocrystalline hydroxyapatite under various dental surface pretreatment conditions. *Biomimetics*. 2022;7(3): 111. <https://doi.org/10.3390/biomimetics7030111>
10. Teaford M. F., Smith M. M., Ferguson M. W. J. *Development, function and evolution of teeth*. Cambridge University Press; 2007.
11. Freitas R. O., Cernescu A., Engdahl A., ... Klementieva O. Nano-infrared imaging of primary neurons. *Cells*. 2021;10: 2559. <https://doi.org/10.3390/cells10102559>
12. Amarie S., Zaslansky P., Kajihara Y., Griesshaber E., Schmahl W. W., Keilmann F. Nano-FTIR chemical mapping of minerals in biological materials. *Beilstein Journal of Nanotechnology*. 2012;3: 312–323. <https://doi.org/10.3762/bjnano.3.35>
13. Seredin P., Goloshchapov D., Peshkov Y., ... Freitas R. O. Identification of chemical transformations in enamel apatite during the development of fissure caries at the nanoscale by means of synchrotron infrared nanospectroscopy: a pilot study. *Nano-Structures; Nano-Objects*. 2024;38: 101205. <https://doi.org/10.1016/j.nanoso.2024.101205>
14. López E. O., Rossi A. L., Bernardo P. L., Freitas R. O., Mello A., Rossi A. M. Multiscale connections between morphology and chemistry in crystalline, zinc-substituted hydroxyapatite nanofilms designed for biomedical applications. *Ceramics International*. 2019;45: 793–804. <https://doi.org/10.1016/j.ceramint.2018.09.246>
15. Seredin P., Goloshchapov D., Kashkarov V., ... Prutskij T. Development of a visualisation approach for analysing incipient and clinically unrecorded enamel fissure caries using laser-induced contrast imaging, micro-Raman spectroscopy and biomimetic composites: a pilot study. *Journal of Imaging*. 2022;8: 137. <https://doi.org/10.3390/jimaging8050137>
16. Goloshchapov D. L., Kashkarov V. M., Ippolitov Y. A.; Prutskij T., Seredin P. V. Early screening of dentin caries using the methods of micro-Raman and laser-induced fluorescence spectroscopy. *Results in Physics*. 2018;10: 346–347. <https://doi.org/10.1016/j.rinp.2018.06.040>
17. Seredin P., Goloshchapov D., Prutskij T., Ippolitov Y. Phase transformations in a human tooth tissue at the initial stage of caries. *PLoS ONE*. 2015;10: e0124008. <https://doi.org/10.1371/journal.pone.0124008>
18. Goloshchapov D., Buylov N., Emelyanova A., ... Seredin P. Raman and XANES spectroscopic study of the influence of coordination atomic and molecular environments in biomimetic composite materials integrated with dental tissue. *Nanomaterials*. 2021;11: 3099. <https://doi.org/10.3390/nano11113099>
19. Goloshchapov D. L., Minakov D. A., Domashevskaya E. P., Seredin P. V. Excitation of luminescence of the nanoporous bioactive nanocrystalline carbonate-substituted hydroxyapatite for early tooth disease detection. *Results in Physics*. 2017;7: 3853–3858. <https://doi.org/10.1016/j.rinp.2017.09.055>
20. Goloshchapov D. L., Lenshin A. S., Savchenko D. V., Seredin P. V. Importance of defect nanocrystalline calcium hydroxyapatite characteristics for developing the dental biomimetic composites. *Results in Physics*. 2019;13: 102158. <https://doi.org/10.1016/j.rinp.2019.102158>
21. Nakayama M., Kajiya S., Kumamoto A., ... Kato T. Stimuli-responsive hydroxyapatite liquid crystal with macroscopically controllable ordering and magneto-optical functions. *Nature Communications*. 2018;9: 568. <https://doi.org/10.1038/s41467-018-02932-7>
22. Ocelic N., Huber A., Hillenbrand R. Pseudoheterodyne detection for background-free near-field spectroscopy. *Applied Physics Letters*. 2006;89: 101124. <https://doi.org/10.1063/1.2348781>
23. Keilmann F., Hillenbrand R. Near-field microscopy by elastic light scattering from a tip. *Philosophical Transactions of the Royal Society of London. Series A: Mathematical, Physical and Engineering Sciences*. 2004;362: 787–805. <https://doi.org/10.1098/rsta.2003.1347>
24. Beniash E., Stiffler C. A., Sun C.-Y., ... Gilbert P. U. P. A. The hidden structure of human enamel. *Nature Communications*. 2019;10: 4383. <https://doi.org/10.1038/s41467-019-12185-7>
25. Free R., DeRocher K., Cooley V., Xu R., Stock S. R., Joester D. Mesoscale structural gradients in human tooth enamel. *Proceedings of the National Academy of Sciences*. 2022;119: e2211285119. <https://doi.org/10.1073/pnas.2211285119>
26. Besnard C., Marie A., Sasidharan S., ... Korsunsky A. M. Synchrotron X-ray studies of the structural and functional hierarchies in mineralised human dental enamel: a state-of-the-art review. *Dentistry Journal*. 2023;11: 98. <https://doi.org/10.3390/dj11040098>
27. Huth F., Govyadinov A., Amarie S., Nuansing W., Keilmann F., Hillenbrand R. Nano-FTIR absorption spectroscopy of molecular fingerprints at 20 nm spatial resolution. *Nano Letters*. 2012;12: 3973–3978. <https://doi.org/10.1021/nl301159v>
28. Mester L., Govyadinov A. A., Chen S., Goikoetxea M., Hillenbrand R. Subsurface chemical nanoidentification by nano-FTIR spectroscopy. *Nature Communications*. 2020;11: 3359. <https://doi.org/10.1038/s41467-020-17034-6>
29. Freitas R. O., Deneke C., Maia F. C. B., ... Westfahl H. Low-aberration beamline optics for synchrotron infrared nanospectroscopy. *Optics Express*. 2018;26: 11238. <https://doi.org/10.1364/OE.26.011238>
30. Muller E. A., Pollard B., Bechtel H. A., Van Blerkom P., Raschke M. B. Infrared vibrational nanocrystallography and nanoimaging. *Science Advances*. 2016;2: e1601006. <https://doi.org/10.1126/sciadv.1601006>
31. Matsuya T., Otsuka Y., Tagaya M., Motozuka S., Ohnuma K., Mutoh Y. Formation of stacked luminescent complex of 8-hydroxyquinoline molecules on hydroxyapatite coating by using cold isostatic pressing. *Materials Science and Engineering: C*. 2016;58: 127–132. <https://doi.org/10.1016/j.msec.2015.08.020>

32. Chuenarrom C., Benjakul P., Daosodsai P. Effect of indentation load and time on knoop and vickers microhardness tests for enamel and dentin. *Materials Research*. 2009;12: 473–476. <https://doi.org/10.1590/S1516-14392009000400016>

### Information about the authors

*Pavel V. Seredin*, Dr. Sci. (Phys.–Math.), Full Professor, Chair of Department of Solid State Physics and Nanostructures, Voronezh State University (Voronezh, Russian Federation).

<https://orcid.org/0000-0002-6724-0063>

[paul@phys.vsu.ru](mailto:paul@phys.vsu.ru)

*Dmitry L. Goloshchapov*, Cand. Sci. (Phys.–Math.), Assistant Professor, Department of Solid State Physics and Nanostructures, Voronezh State University (Voronezh, Russian Federation).

<https://orcid.org/0000-0002-1400-2870>

[goloshchapov@phys.vsu.ru](mailto:goloshchapov@phys.vsu.ru)

*Yaroslav A. Peshkov*, Laboratory Research Assistant, Department of Solid State Physics and Nanostructures, Voronezh State University (Voronezh, Russian Federation).

<https://orcid.org/0000-0003-0939-0466>

[tangar77@mail.ru](mailto:tangar77@mail.ru)

*Nikita S. Buylov*, Cand. Sci. (Phys.–Math.), Assistant Professor, Department of Solid State Physics and Nanostructures, Voronezh State University (Voronezh, Russian Federation).

<https://orcid.org/0000-0003-1793-4400>

[buylov@phys.vsu.ru](mailto:buylov@phys.vsu.ru)

*Andrey Yu. Potapov*, Cand. Sci. (Chem.), Senior Researcher at the Department of the Organic Chemistry, Voronezh State University (Voronezh, Russian Federation).

<https://orcid.org/0000-0001-8084-530X>

[pistones@mail.ru](mailto:pistones@mail.ru)

*Khidmet S. Shikhaliev*, Dr. Sci. (Chem.), Professor, Head of the Department of Organic Chemistry, Voronezh State University (Voronezh, Russian Federation).

<https://orcid.org/0000-0002-6576-0305>

[chocd261@chem.vsu.ru](mailto:chocd261@chem.vsu.ru)

*Yury A. Ippolitov*, Dr. Sci. (Med.), Full Professor, Head of Dentistry Institute of Postgraduate Medical Education Department, Voronezh State Medical University (Voronezh, Russian Federation).

<https://orcid.org/0000-0001-9922-137X>

[dsvgma@mail.ru](mailto:dsvgma@mail.ru)

*Raul O. Freitas*, Channel Manager, Brazilian Synchrotron Light Laboratory (LNLS), Brazilian Center for Research in Energy and Materials (CNPEM), Campinas 13083-970 (Sao Paulo, Brazil).

<https://orcid.org/0000-0002-3285-5447>

[raul.freitas@lnls.br](mailto:raul.freitas@lnls.br)

*Francisco C. B. Maia*, Research Fellow, Brazilian Synchrotron Light Laboratory (LNLS), Brazilian Center for Research in Energy and Materials (CNPEM), Campinas 13083-970 (Sao Paulo, Brazil).

<https://orcid.org/0000-0002-4998-4624>

[francisco.maia@lnls.br](mailto:francisco.maia@lnls.br)

*Received April 7, 2025; accepted after reviewing April 30, 2025; accepted for publication May 15, 2025; published online September 25, 2025.*



## Short communication

Short communication

<https://doi.org/10.17308/kcmf.2025.27/13201>

## Synchrotron XANES studies of epitaxial tin-silicon solid solutions nanolayers

N. I. Boikov<sup>1</sup>, O. A. Chuvenkova<sup>1</sup>, E. V. Parinova<sup>1</sup>, R. G. Chumakov<sup>2</sup>, A. M. Lebedev<sup>2</sup>, A. Makarova<sup>3</sup>, D. Smirnov<sup>4</sup>, S. S. Titova<sup>1</sup>, K. A. Fateev<sup>1</sup>, S. Yu. Turishchev<sup>1</sup>✉

<sup>1</sup>Voronezh State University,  
1 Universitetskaya pl., Voronezh 394018, Russian Federation

<sup>2</sup>National Research Center “Kurchatov Institute”,  
1 Akademika Kurchatova pl., Moscow 123182, Russian Federation

<sup>3</sup>Free University of Berlin,  
Arnimallee 22, 14195 Berlin, Germany

<sup>4</sup>Dresden University of Technology,  
Zellescher Weg 18, 01069 Dresden, Germany

### Abstract

**Objective:** Functional tin and silicon-based materials and thin-film structures based on them are promising objects for microelectronics devices. An important issue for the study and subsequent application of such materials and structures is the properties control under formation technological regimes variations.

**Experimental:** The specificity of the local atomic surrounding and the features of the electronic structure of tin-silicon solid solutions have been studied by X-ray absorption near edge structure spectroscopy using synchrotron radiation. Nanolayer structures of tin-silicon solid solutions on buffer silicon nanolayers were formed using molecular beam epitaxy.

**Conclusions:** The possibility of forming an epitaxial tin-silicon solid solution in the concentration range significantly exceeding the known solubility limits of Sn in Si is shown. The rearrangement of the local density of the electronic states of tin and silicon indicates the formation of solid solutions with tin concentrations of 2, 8, and 15 at. %.

**Keywords:** Tin, Silicon, Tin and silicon oxides, Electronic structure, Density of states, Local atomic surrounding, Composition, Epitaxial solid solutions, X-ray absorption near edge structure, Synchrotron investigations

**Funding:** The study was supported by Russian Science Foundation (Project 23-22-00465).

**Acknowledgments:** The authors would like to thank A. Tonkikh for the samples provided.

**For citation:** Boikov N. I., Chuvenkova O. A., Parinova E. V., Chumakov R. G., Lebedev A. M., Makarova A., Smirnov D., Titova S. S., Fateev K. A., Turishchev S. Yu. Synchrotron XANES studies of epitaxial tin-silicon solid solutions nanolayers. *Condensed Matter and Interphases*. 2025;27(3): 490–496. <https://doi.org/10.17308/kcmf.2025.27/13201>

**Для цитирования:** Бойков Н. И., Чувенкова О. А., Паринава Е. В., Чумаков Р. Г., Лебедев А. М., Макарова А., Смирнов Д., Титова С. С., Фатеев К. А., Турищев С. Ю. Синхротронные XANES исследования нанослоев эпитаксиальных твердых растворов олово-кремний. *Конденсированные среды и межфазные границы*. 2025;27(3): 490–496. <https://doi.org/10.17308/kcmf.2025.27/13201>

✉ Sergey Yu. Turishchev, e-mail: [tsu@phys.vsu.ru](mailto:tsu@phys.vsu.ru)

© Boikov N. I., Chuvenkova O. A., Parinova E. V., Chumakov R. G., Lebedev A. M., Makarova A., Smirnov D., Titova S. S., Fateev K. A., Turishchev S. Yu., 2025



The content is available under Creative Commons Attribution 4.0 License.

## 1. Introduction

The formation of new promising functional materials with new properties and characteristics for the creation of modern devices based on them is an urgent task. The creation of solid solutions based on silicon, the most common and widely used material for microelectronic devices, is a promising way to achieve new properties of the structures being formed. For example, the introduction of tin atoms into a silicon crystal lattice can lead to changes in the optical properties, processes of generation, recombination, and transfer of charge carriers in the obtained objects [1, 2]. Varying the concentration of embedded tin atoms can make it possible to control the properties of the material, which affect the electronic structure, optical, and electrophysical properties of solid solutions. Obtaining uniform tin-silicon solid solutions is possible using nonequilibrium growth methods such as molecular beam epitaxy, due to the noticeable difference in the lattice parameters of structures based on these atoms and their low mutual solubility [1]. The above makes  $\text{Si}_{1-x}\text{Sn}_x$  solid solutions suitable for creating electronic devices, in particular, various thermoelectric devices, optoelectronic devices such as lasers and LEDs. This paper presents the results of the electronic structure specificity studying for nanolayers of  $\text{Si}_{1-x}\text{Sn}_x$  epitaxial solid solutions grown on crystalline silicon buffer layers and substrates with concentrations exceeding the limits of tin solubility in silicon ( $x > 0.1$  at.%) [3]. The studies were carried out using a non-destructive X-ray absorption near edge structure (XANES) method sensitive to the local surrounding of surface atoms using high-intensity synchrotron radiation [4–6].

## 2. Experimental

The studied samples, which we designate as “SiSn”, were obtained by molecular beam epitaxy on a Si (001) substrate with a 20 nm Si buffer layer [7]. During the formation of the samples, the purified and dried substrates were transported to an ultra-high vacuum film growth chamber, where thermal oxide was desorbed at the temperature of 840 °C. Then, silicon atoms (~ 98, 92 and 85 at. %) and tin atoms (~ 2, 8 and 15 at. %) were simultaneously deposited on a

20 nm thick silicon buffer layer from an electron beam evaporator (Si) and an effusion cell (Sn) sources. The thickness of the deposited SiSn layer was about 5 nm. As a result, the following samples were obtained:  $\text{Si}_{0.98}\text{Sn}_{0.02}$ ,  $\text{Si}_{0.92}\text{Sn}_{0.08}$  and  $\text{Si}_{0.85}\text{Sn}_{0.15}$ . Before conducting synchrotron experiments, the samples were stored in laboratory conditions for several weeks.

The electronic structure of the samples was studied using the non-destructive XANES method, which allows obtaining information about the specificity of the local surrounding of absorbing silicon, tin, and oxygen atoms and the effects of ordering in the structural grid of these atoms of the analyzed surface layer [8]. The XANES method makes it possible to obtain direct experimental information on the distribution of the local partial density of free electronic states in the conduction band of the studied surface layer [4–6, 9–11]. The high-intensity radiation of the ultrasoft X-ray range of BESSY-II synchrotrons, the Russian-German beamline (Helmholtz-Zentrum-Berlin, Berlin, Germany) [12] and KISI-Kurchatov, the NANOPES beamline (NRC Kurchatov Institute, Moscow, Russia) [13] were used. The photon flux was  $10^9$ – $10^{11}$  photons/s, and the storage rings beamcurrent was 50–300 mA. The depth of the analyzed surface layer [14, 15] and the energy resolution for the edges of Si  $L_{2,3}$ , Sn  $M_{4,5}$ , and O K were ~5 nm for silicon, ~10 nm for tin and oxygen, and 0.1 eV, respectively. The total electron yield (TEY) was detected by recording the compensation current of the sample. The vacuum in the experimental chambers was ~  $10^{-10}$  Torr. The angle of incidence of synchrotron radiation was 90° to the surface plane.

## 3. Results and discussion

XANES Si  $L_{2,3}$  (2p) absorption spectra represent the distribution of  $s$  states in the conduction band, which reflect transitions from core 2p states to free  $s$  and  $d$  states in the conduction band. Fig. 1 shows the XANES Si  $L_{2,3}$  spectra for the reference materials (single crystalline silicon c-Si, amorphous silicon a-Si, thermally grown silicon oxide  $\text{SiO}_2$  and the epitaxial buffer layer c-Si Buffer on silicon) and the studied samples of epitaxial solid solutions  $\text{Si}_{0.98}\text{Sn}_{0.02}$ ,  $\text{Si}_{0.92}\text{Sn}_{0.08}$  and  $\text{Si}_{0.85}\text{Sn}_{0.15}$ . Analysis of the obtained spectra shows that the epitaxial silicon buffer layer (c-Si

Buffer) has a well-defined fine structure with two pairs of features corresponding to the spin-doublet splitting of the excited  $L_{2,3}$  silicon core level at 0.6 eV, in the energy range of synchrotron radiation quanta of 100–104 eV, characteristic of the reference single crystalline silicon (c-Si). Note that in this region, the spectrum of the a-Si reference has a simpler, thinner structure without the paired maxima noted above, due to the blurring of the density of electronic states of amorphous silicon. The following absorption edge and the fine structure of XANES Si  $L_{2,3}$  for  $\text{SiO}_2$  are located above the energies of 104 eV, similar features can be detected for the spectra of the c-Si and a-Si references, since they are covered by a natural oxide.

XANES Si  $L_{2,3}$  spectra fine structure of the studied epitaxial solid solutions samples has

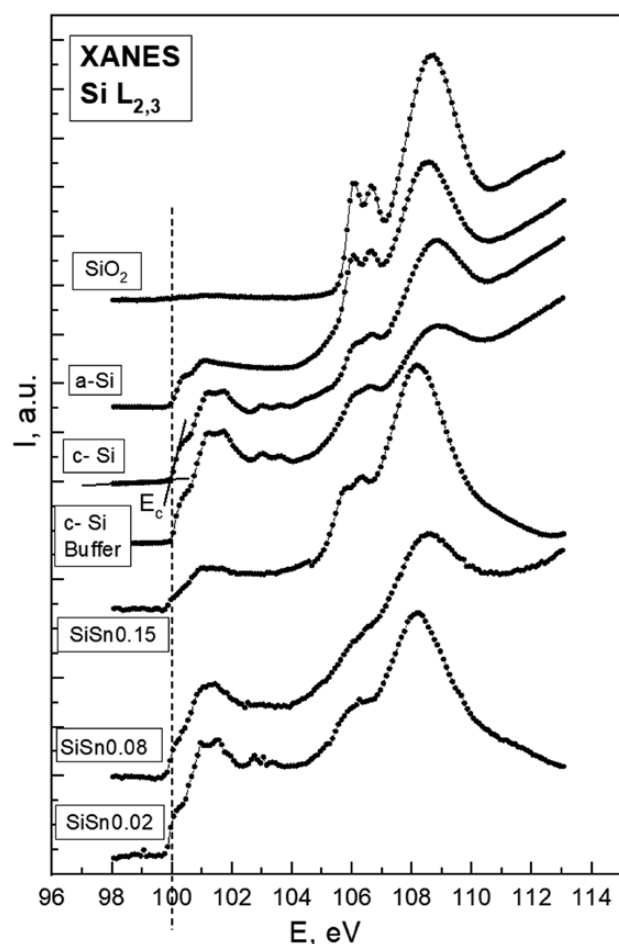


**Fig. 1.** XANES Si  $L_{2,3}$  of references: crystalline silicon (c-Si), amorphous silicon (a-Si), silicon oxide ( $\text{SiO}_2$ ), buffer layer of c-Si (c-Si Buffer) and epitaxial solid solutions  $\text{SiSn}_{0.02}$ ,  $\text{SiSn}_{0.08}$ ,  $\text{SiSn}_{0.15}$

a number of features (Fig. 1). Thus, in a solid solution with 2% tin atoms  $\text{Si}_{0.98}\text{Sn}_{0.02}$ , XANES spectrum fine structure in the absorption region of elementary silicon ( $100 \text{ eV} < h\nu < 104 \text{ eV}$ ) is well expressed and corresponds to crystalline silicon (Fig. 1). And in the region silicon oxide 105–111 eV the characteristic fine structure features are not observed in the spectrum. Here, the fine structure is generally blurred, and the main peak at energies of  $\sim 108 \text{ eV}$  is broadened and shifted to lower values, which may indicate an underoxidized state of silicon atoms from the sample surface [10, 16]. In a solid solution with a higher tin content of 8%  $\text{Si}_{0.92}\text{Sn}_{0.08}$ , the fine structure of the spectrum in the region of elementary silicon is somewhat blurred, which may indicate a slight deviation from the ordering in the lattice of silicon atoms. The fine structure in the area of silicon oxides remains, in general, as unexpressed as in the case of a solid solution with a 2% of the tin content  $\text{Si}_{0.98}\text{Sn}_{0.02}$ . As the tin content increases to 15%  $\text{Si}_{0.85}\text{Sn}_{0.15}$ , the fine structure of the XANES Si  $L_{2,3}$  spectrum in the elementary silicon region becomes even more blurred. However, the width of the characteristic fine structure features in this part of the XANES Si  $L_{2,3}$  spectra for  $\text{Si}_{0.85}\text{Sn}_{0.15}$  and their general appearance differ from the characteristic structureless absorption edge of the amorphous silicon reference. In the silicon oxide region, the fine structure becomes more pronounced and corresponds to that of the natural oxide covering crystalline silicon c-Si reference (Fig. 1). This indicates possible distortions in the lattice of silicon atoms and, at the same time, greater oxidation of silicon atoms from the surface, which are even more noticeable than with a lower tin content in solid solution. Finally, for all nanolayers of solid solutions, there was a slight shift in the position of the absorption edge at 99.9 eV towards lower energies.

Thus, it can be concluded that as the number of tin atoms in solid SiSn solutions increases, the fine structure of the Si  $L_{2,3}$  absorption spectra changes. With an increase in the concentration of tin atoms in the nanolayer of the solid solution, the fine structure of the spectrum is smoothed, that is, the density distribution of free electronic states in the conduction band [8, 10]. In the region of the absorption edge of elementary silicon, corresponding to the position of the bottom of

the conduction band relative to the excited core level ( $\text{Si } L_{2,3}$ ), electronic states are “dragged” into the band gap compared with the data on the fine structure of the crystalline silicon reference spectrum and the  $E_c$  position (Fig. 1). The order in the structural grid of silicon atoms as a whole is undergoing some distortions. That is, the mechanical stresses that probably occur during the formation of nanolayers of solid solutions lead to distortion in the electronic structure of these nanolayers. This includes natural silicon oxide formed during storage in the laboratory. The observed general smoothing of the XANES  $\text{Si } L_{2,3}$  spectra fine structure may occur as a result of the tin atoms incorporation into the lattice of silicon atoms during the formation of a solid solution nanolayer.

Fig. 2 shows the XANES  $\text{Sn } M_{4,5}$  spectra of reference materials (experimentally obtained for tetragonal  $\text{SnO}_2(\text{T})$ , metal foil without natural oxide “Sn foil refresh”, metal foil “tin Sn foil” with natural oxide [4-6] and *ab-initio* calculated for orthorhombic  $\text{SnO}_2(\text{O})$  and tetragonal  $\text{SnO}$  [11]) and the studied samples of epitaxial solid solutions  $\text{Si}_{0.98}\text{Sn}_{0.02}$ ,  $\text{Si}_{0.92}\text{Sn}_{0.08}$  and  $\text{Si}_{0.85}\text{Sn}_{0.15}$ . XANES  $\text{Sn } M_{4,5}$  ( $3d$ ) absorption spectra represent the distribution of  $p$  states in the conduction band, which reflect transitions from core  $3d$  states to free  $p$  and  $f$  states in the conduction band. A detailed discussion of the reference spectra fine structure is given in [4-6, 11]. It is only worth noting that the distribution of the main spectral features and their relative intensities (Fig. 2) of XANES  $\text{Sn } M_{4,5}$  show a significant difference for the references of each compound of the tin-oxygen system. The fine structure of the studied solid solutions is quite similar to each other in terms of the observed spectral features at energies of 487, 493, 497 eV, corresponding to the  $M5$  absorption edge in tin. In general, the fine structure of XANES  $\text{Sn } M_{4,5}$  of the studied solid solutions, based on the presence and location of characteristic peaks and their relative intensity, is a combination of contributions from orthorhombic  $\text{SnO}_2(\text{O})$ , tin monoxide  $\text{SnO}$ , and tetragonal  $\text{SnO}_2(\text{T})$  with a noticeable number of oxygen vacancies. At the same time, there is a redistribution in the intensities of the above-mentioned features. Thus, with an increase in the concentration of tin in solid solutions, the

intensity of the double peak increases at an energy of  $\sim 488$  eV ( $M_5$  edges), associated with a lack of atoms in the oxygen sublattice of tin oxide [4, 5] and its high-energy component at an energy of  $\sim 495$  eV. It is also worth noting that with increasing tin concentration, changes in the pre-edge region of the spectrum become more and more apparent, namely, a small shoulder is formed from the bottom of the conduction band towards lower energies. This may indicate the presence of additional electronic states in the band gap, close to the bottom of the conduction band. Thus, it can be concluded that an increase in the concentration of tin atoms in solid solutions of  $\text{SiSn}$  leads to a change in the fine structure of the tin absorption edge near the bottom of the conduction band with a stable state of the nearest surrounding of tin atoms. The observations made indicate the formation of a stable set of tin compounds in the studied nanolayers of solid

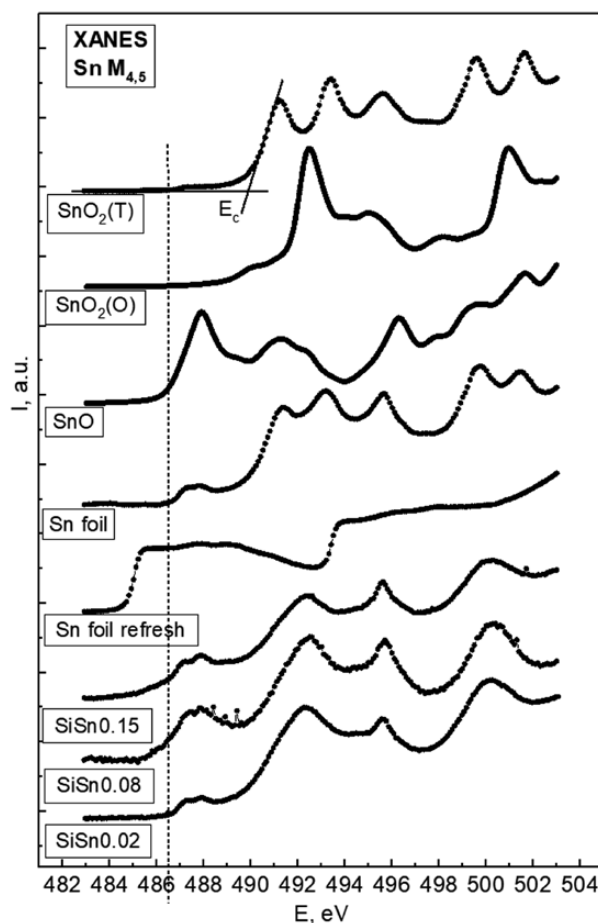
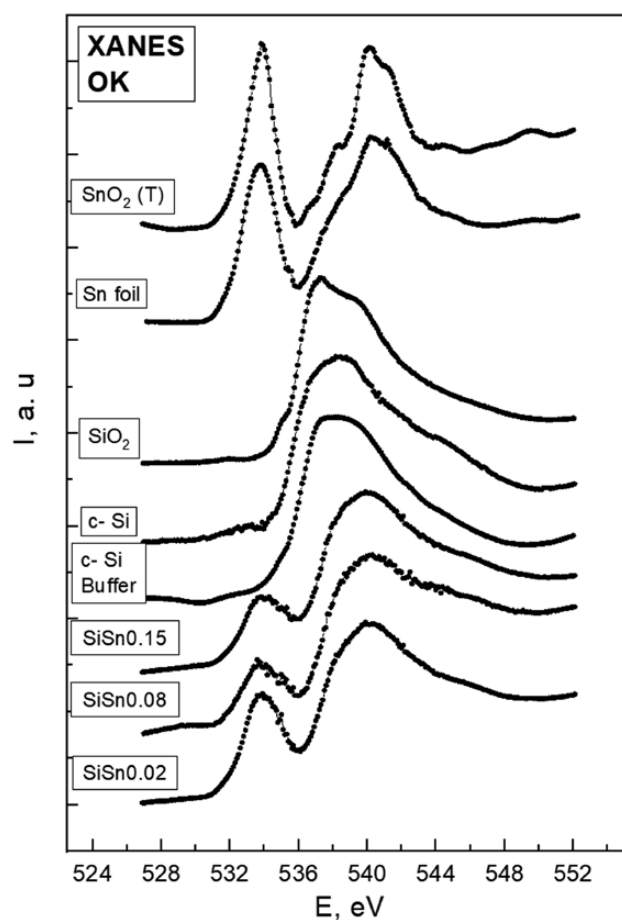


Fig. 2. XANES  $\text{Sn } M_{4,5}$  of references  $\text{SnO}_2(\text{T})$ ,  $\text{SnO}_2(\text{O})$ ,  $\text{SnO}$ ,  $\text{Sn}$  foil,  $\text{Sn}$  foil refresh and epitaxial solid solutions  $\text{SiSn}_{0.02}$ ,  $\text{SiSn}_{0.08}$ ,  $\text{SiSn}_{0.15}$

solutions. There is a good correlation with the data for the absorption edges of silicon, where “dragging” of electronic states near the  $E_c$  was also observed. Thus, the effects of changes in the electronic structure of nanolayers of solid solutions of SiSn are observed as a result of disturbances in the Si atoms local surrounding when Sn atoms are embedded in their lattice and oxygen redistribution during formed solid solutions nanolayers surface natural oxidation with a lack of oxygen for tin atoms.

Fig. 3 shows the O K XANES spectra of references ( $\text{SnO}_2$ (T), Sn foil, c-Si (natural oxide),  $\text{SiO}_2$ , and c-Si Buffer (natural oxide)) and studied samples of  $\text{Si}_{0.98}\text{Sn}_{0.02}$ ,  $\text{Si}_{0.92}\text{Sn}_{0.08}$ , and  $\text{Si}_{0.85}\text{Sn}_{0.15}$  epitaxial solid solutions. XANES O K (1s) absorption spectra are the result of transitions from the core 1s oxygen level to free  $p$  states in the conduction band. It can be seen that the spectra of the presented reference samples



**Fig. 3.** XANES O K of references  $\text{SnO}_2$ (T), Sn foil, c-Si,  $\text{SiO}_2$  and epitaxial solid solutions  $\text{SiSn}_{0.02}$ ,  $\text{SiSn}_{0.08}$ ,  $\text{SiSn}_{0.15}$

differ in their fine structure. Thus, tetragonal tin dioxide has pronounced peaks at energies of 533.9 and 540.2 eV, as well as features at 536–549 eV. In the tin metal foil, the main peaks are most pronounced at the same energies, while the remaining features of the fine structure are smoothed out. The spectra for c-Si (natural oxide),  $\text{SiO}_2$ , and c-Si Buffer (natural oxide) are similar to each other and have a wide peak in the energy range of 537–539 eV. The difference is in a more pronounced step at an energy of 535 eV and a pronounced peak at an energy of 537.3 eV for  $\text{SiO}_2$ . The lack of data on the oxygen edge in orthorhombic tin dioxide and tin single oxide makes the interpretation of the oxygen edge of the studied samples insufficiently complete and is the subject of further research. When considering the edges of oxygen O K absorption (Fig. 3) in the studied solid solutions, it can be seen that the fine structure of the spectra consists of two features at energies of 533.9 eV and in the energy range of 537–539 eV, which corresponds to the features of tin oxides and silicon oxides, respectively. The spectra of solid solutions differ from each other by a slight redistribution of the intensities of these peaks. Thus, the fine structure of the oxygen absorption edge in the studied samples indicates the predominant oxidation of atoms of more electronegative silicon; nevertheless, tin oxides contribute to the electronic spectrum of nanolayers of tin-silicon solid solutions.

#### 4. Conclusions

There is a general agreement of data from the analysis of synchrotron XANES spectra of silicon (Si  $L_{2,3}$ ), tin (Sn  $M_{4,5}$ ), and oxygen (O K) for tin-silicon solid solutions formed by molecular beam epitaxy exceeding the known limits of solubility of Sn in Si (2, 8, and 15%) in the form of thin nanolayers on a crystalline silicon buffer layer. It is shown that even the lowest concentration of tin atoms of 2% during the formation of a solid solution of SiSn makes changes in the specificity of the nearest surrounding of Si and Sn atoms. The appearance of tin atoms surrounded by silicon atoms, during the formation of a solid solution, leads to the effect of electronic states “dragging” into the band gap near the  $E_c$ . When structures are stored in the laboratory conditions, natural and intermediate oxides of silicon and

tin are formed on the surface. An increase in the tin content (up to 15%) leads to a blurring of the density of the electronic states near the bottom of the conduction band.

### Contribution of the authors

All authors made an equivalent contribution to the preparation of the publication.

### Conflict or interests

The authors declare that they have no known competing financial interests or personal relationships that could have appeared to influence the work reported in this paper.

### References

1. Soref R. A., Perry C. H. Predicted band gap of the new semiconductor SiGeSn. *Journal Applied Physics*. 1991;69: 539–548. <https://doi.org/10.1063/1.347704>
2. Moontragoon P., Ikonik Z., Harrison P. Band structure calculations of Si–Ge–Sn alloys: achieving direct band gap materials. *Semiconductor Science and Technology*. 2007;22: 742–748. <https://doi.org/10.1088/0268-1242/22/7/012>
3. Massalski T. B., Okamoto H., Subramanian P. R., Kacprzak L. *Binary Alloy Phase Diagrams*. 2nd ed., 1990, vol. 2, ASM International, Materials Park, Ohio, p. 3362.
4. Chuvenkova O. A., Domashevskaya E. P., Ryabtsev S. V., ... Turishchev S. Yu. XANES and XPS investigations of surface defects in wire like SnO<sub>2</sub> crystals. *Physics of the Solid State*. 2015;57(1): 153–161. <https://doi.org/10.1134/s1063783415010072>
5. Kucheyev S., Baumann T. F., Sterne P. A., ... Willey T. M. Surface electronic states in three-dimensional SnO<sub>2</sub> nanostructures. *Physical Review B*. 2005;72(3): 035404-1-5. <https://doi.org/10.1103/PhysRevB.72.035404>
6. Chuvenkova O. A., Boikov N. I., Ryabtsev S. V., ... Turishchev S. Y. Electronic structure and composition of tin oxide thin epitaxial and magnetron layers according to synchrotron XANES studies. *Condensed Matter and Interphases*. 2024;26(1): 153–160. <https://doi.org/10.17308/kcmf.2024.26/11897>
7. Tonkikh A. A., Zakharov N. D., Eisenschmidt C., Leipner H. S., Werner P. Aperiodic SiSn/Si multilayers for thermoelectric applications. *Journal of Crystal Growth*. 2014;392: 49–51. <http://doi.org/10.1016/j.jcrysgro.2014.01.047>
8. Stohr J. *NEXAFS spectroscopy*. Berlin: Springer: 1996. 403 p.
9. Turishchev S. Yu., Parinova E. V., Pisliaruk A. K., ... Sivakov V. Surface deep profile synchrotron studies of mechanically modified top-down silicon nanowires array using ultrasoft X-ray absorption near edge structure spectroscopy. *Scientific Reports*. 2019;9(8066): 1–7. <https://doi.org/10.1038/s41598-019-44555-y>
10. Ming T., Turishchev S., Schleusener A., ... Sivakov V. Silicon suboxides as driving force for efficient light-enhanced hydrogen generation on silicon nanowires. *Small*. 2021;17(8): 2007650-1-6. <https://doi.org/10.1002/sml.202007650>
11. Manyakin M. D., Kurganskii S. I., Dubrovskii O. I., ... Turishchev S. Yu. Electronic and atomic structure studies of tin oxide layers using X-ray absorption near edge structure spectroscopy data modelling. *Materials Science in Semiconductor Processing*. 2019;99: 28–33. <https://doi.org/10.1016/j.mssp.2019.04.006>
12. Fedoseenko S. I., Iossifov I. E., Gorovikov S. A., ... Kaindl G. Development and present status of the Russian–German soft X-ray beamline at BESSY II. *Nuclear Instruments and Methods in Physics Research Section A: Accelerators, Spectrometers, Detectors and Associated Equipment*. 2001;470: 84–88. [https://doi.org/10.1016/S0168-9002\(01\)01032-4](https://doi.org/10.1016/S0168-9002(01)01032-4)
13. Lebedev A. M., Menshikov K. A., Nazin V. G., Stankevich V. G., Tsetlin M. B., Chumakov R. G. NanoPES photoelectron beamline of the Kurchatov Synchrotron Radiation Source. *Journal of Surface Investigation: X-ray, Synchrotron and Neutron Techniques*. 2021;15: 1039–1044. <https://doi.org/10.1134/S1027451021050335>
14. Kasrai M., Lennard W. N., Brunner R. W., Bancroft G. M., Bardwell J. A., Tan K. H. Sampling depth of total electron and fluorescence measurements in Si L- and K-edge absorption spectroscopy. *Applied Surface Science*. 1996;99: 303–312. [https://doi.org/10.1016/0169-4332\(96\)00454-0](https://doi.org/10.1016/0169-4332(96)00454-0)
15. Erbil A., Cargill III G. S., Frahm R., Boehme R. F. Total-electron-yield current measurements for near-surface extended x-ray-absorption fine structure. *Physical Review B*. 1988;37: 2450–2464. <https://doi.org/10.1103/PhysRevB.37.2450>
16. Barranco A., Yubero F., Espinos J. P., Groening P., Gonzalez-Elipe A. R. Electronic state characterization of SiOx thin films prepared by evaporation. *Journal of Applied Physics*. 2005;97: 113714. <https://doi.org/10.1063/1.1927278>

### Information about the authors

*Nikolai I. Boikov*, engineer-physicist, Joint Scientific and Educational Laboratory “Atomic and Electronic Structure of Functional Materials” of Voronezh State University and the National Research Center “Kurchatov Institute”, Voronezh State University (Voronezh, Russian Federation).

<https://orcid.org/0000-0002-0512-8666>

[boykov-hfmm@bk.ru](mailto:boykov-hfmm@bk.ru)

*Olga A. Chuvenkova*, Cand. Sci. (Phys.-Math.), Senior Researcher, Joint Scientific and Educational Laboratory “Atomic and Electronic Structure of Functional Materials” of Voronezh State University and the National Research Center “Kurchatov Institute”, Voronezh State University (Voronezh, Russian Federation).

<https://orcid.org/0000-0001-5701-6909>

[chuvenkova@phys.vsu.ru](mailto:chuvenkova@phys.vsu.ru)

*Elena V. Parinova*, Cand. Sci. (Phys.-Math.), Assistant Professor, General Physics Department, Voronezh State University (Voronezh, Russian Federation).

<https://orcid.org/0000-0003-2817-3547>

[parinova@phys.vsu.ru](mailto:parinova@phys.vsu.ru)

*Ratibor G. Chumakov*, Cand. Sci. (Phys.-Math.), Senior Researcher of the National Research Center “Kurchatov Institute” (Moscow, Russian Federation).

<https://orcid.org/0000-0002-3737-5012>

[ratibor.chumakov@gmail.com](mailto:ratibor.chumakov@gmail.com)

*Alexei M. Lebedev*, Cand. Sci. (Phys.-Math.), Senior Researcher of the National Research Center “Kurchatov Institute” (Moscow, Russian Federation).

<https://orcid.org/0000-0002-4436-6077>

[lebedev.alex.m@gmail.com](mailto:lebedev.alex.m@gmail.com)

*Dmitry Smirnov*, Cand. Sci. (Phys.-Math.), Researcher, Institut für Festkörper- und Materialphysik, Technische Universität Dresden (Dresden, Germany).

[anna.makarova@fu-berlin.de](mailto:anna.makarova@fu-berlin.de)

*Anna Makarova*, Cand. Sci. (Phys.-Math.), Researcher, Institut für Chemie und Biochemie, Freie Universität Berlin (Berlin, Germany).

[anna.makarova@fu-berlin.de](mailto:anna.makarova@fu-berlin.de)

*Sofia S. Titova*, Teacher of General Physics Department, Voronezh State University, (Voronezh, Russian Federation).

<https://orcid.org/0000-0001-6860-401X>

[titova@phys.vsu.ru](mailto:titova@phys.vsu.ru)

*Kirill A. Fateev*, Laboratory assistant in physics of General Physics Department, Voronezh State University, (Voronezh, Russian Federation).

[fateev@phys.vsu.ru](mailto:fateev@phys.vsu.ru)

*Sergey Yu. Turishchev*, Dr. Sci. (Phys.-Math.), Associate Professor, Head of the General Physics Department, Voronezh State University (Voronezh, Russian Federation).

<https://orcid.org/0000-0003-3320-1979>

[tsu@phys.vsu.ru](mailto:tsu@phys.vsu.ru)

*Received October 16, 2024; approved after reviewing November 18, 2024; accepted for publication November 18, 2024; published online September 25, 2025.*



# Condensed Matter and Interphases

Kondensirovannye Sredy i Mezhfaznye Granitsy  
<https://journals.vsu.ru/kcmf/>

## Chronicle

<https://doi.org/10.17308/kcmf.2025.27/13024>

## 90 years of the scientific school of solid state physics at Voronezh State University: from solid state physics to nanophysics (Scientific and historical essay)

E. P. Domashevskaya

Voronezh State University,  
1 Universitetskaya pl., Voronezh 394018, Russian Federation

### Abstract

**For citation:** Domashevskaya E. P. 90 years of the scientific school of solid state physics at Voronezh State University: from solid state physics to nanophysics (Scientific and historical essay). *Condensed Matter and Interphases*. 2025;27(3): 497–517. <https://doi.org/10.17308/kcmf.2025.27/13024>

**Для цитирования:** Домашевская Э. П. 90 лет научной школе физики твердого тела Воронежского государственного университета: от физики твердого тела до нанофизики (Научно-исторический очерк). *Конденсированные среды и межфазные границы*. 2025;27(3): 497–517. <https://doi.org/10.17308/kcmf.2025.27/13024>

### Foundation of the scientific school in Voronezh

The emergence of solid state physics at Voronezh State University is associated with the outstanding personality of Maria Afanasyevna Levitskaya, one of the first female physicists in Russia and the Soviet Union, a comrade-in-arms and colleague of the famous academician Abram Fedorovich Ioffe. M. A. Levitskaya was invited in 1935 by VSU Rector Norin A.Ya to head first the Department of Theoretical Physics at the Physics and Mathematics Department, and then (1937) the Department of Electromagnetic Oscillations that she created. Thus, in 1935, in connection with the appearance at VSU of the famous professor M. A. Levitskaya, became the beginning of the development of modern fundamental physical trends and scientific schools in Voronezh, and above all, a scientific school in the field of solid state physics.

Maria Afanasyevna received an excellent education, first in St. Petersburg at the Physics and Technology Department of the Higher Women's

Bestuzhev Courses (1901–1904), the last two semesters of which she completed at the University of Berlin (1905–1906), where she specialized under the scientific supervision of the founders of quantum physics Max Planck and Paul Drude. Then in 1911–1914 she completed an internship in Göttingen and Holland [1–4]. After returning from Europe, Maria Afanasyevna worked for about twenty years (1923–1934) at the Leningrad Physico-Technical Institute at the invitation of its first director, Academician Abram Fedorovich Ioffe, carrying out the first research in solid state physics with him, and headed the Ultrashort Wave Department. It is interesting that the Academic Council of this institute, which included academicians I. V. Kurchatov, A. P. Aleksandrov, N. N. Semenov, and Ya. I. Frenkel, who later became famous throughout the world, included only one woman – M. A. Levitskaya. Fig. 1 shows a 1927 photograph of the staff of the Leningrad Physico-Technical Institute of the USSR Academy of Sciences, headed by the director, Academician A. F. Ioffe.

✉ Evelina P. Domashevskaya, e-mail: [fft@phys.vsu.ru](mailto:fft@phys.vsu.ru)  
© Domashevskaya E. P., 2025



The content is available under Creative Commons Attribution 4.0 License.



**Fig. 1.** The collective of the Leningrad Physico-Technical Institute LPTI of the USSR Academy of Sciences headed by the director Academician A. F. Ioffe in 1927

With her main discovery of submillimeter waves, M. A. Levitskaya proved the unity of the electromagnetic nature of radio waves and light in a single scale of electromagnetic oscillations, independently and almost simultaneously with another female physicist, Alexandra Andreevna Glagoleva-Arkadyeva [5]. In 1909, in the *Journal of the Russian Physical Society*, M. A. Levitskaya published her first original study, “Radiation of a Rectilinear Resonator in the Region of Short Electromagnetic Waves.”

In the early thirties, after the publication of the unique monograph “Infrared Rays” [6], M. A. Levitskaya was awarded the academic degree of Doctor of Physical and Mathematical Sciences “for outstanding scientific achievements” without defending her dissertation, following I. V. Kurchatov.

This is the background to the emergence and development of modern scientific physical schools at the Voronezh State University, including the scientific school of solid state physics. Already in the post-war period of restoration of science and education since 1961, the Department of Electromagnetic Oscillations began to be called the Department of Solid State Physics, after several other departments that originated in its depths separated from the large system-forming Department of Electromagnetic Oscillations,

including the Department of Radiophysics and the Department of Optics and Nuclear Physics. Why did the remaining basic department begin to be called the Department of Solid State Physics since 1961? The fact is that M. A. Levitskaya, together with A. F. Ioffe, stood at the origins of the then emerging physics of solid state in the 1920s and 1930s, studying the electromechanical and deformation properties of classical solids, single crystals of rock salt and quartz, using X-ray methods, which they mastered in Germany from the great scientist Wilhelm Conrad Roentgen, who discovered X-rays in November 1895, called X-rays only in Russia and Germany. In English-speaking countries, this radiation is still called X-rays. In 1903–1906, A. F. Ioffe completed an internship at the University of Munich with Nobel Prize Laureate (1901) V. K. Roentgen, carrying out work on the mechanical and electrical properties of crystals.

When Maria Afanasyevna, together with A. F. Ioffe, began studying the mechanical properties of single crystals, Max Born had already published the general theory of crystal lattices (1916). The Born’s electrostatic theory correctly described a number of properties of single crystals, could not, however, explain some of the observed phenomena. For example, a sample of crystalline rock salt NaCl breaks under a stress of 0.4 kg/mm, whereas according to theoretical

estimates it should be  $200 \text{ kg/mm}^2$ . According to this theory, the same crystal should have high elastic properties regardless of the loads applied to it. Meanwhile, in practice, a transition from elastic to plastic deformation is observed, often caused by small external forces. Experimenters could answer all these questions only by looking inside the substance. This opportunity was provided to experimental physicists by the famous X-rays discovered by Roentgen in 1895 and their diffraction on NaCl single crystals, discovered by his students led by Laue in 1912.

It was around these years (1911–1914) that Maria Afanasyevna was doing an internship at the University of Göttingen in Germany. Returning to Russia, she and A. F. Ioffe began to successfully apply X-ray methods in studies of the mechanical properties of crystals. First of all, the young scientists began to clarify the nature and laws of plastic deformation using NaCl as an example. By recording Lauegrams from NaCl single crystals subjected to continuous mechanical action (compression or stretching), scientists discovered and studied in detail the phenomena of asterism in the form of spot multiplication on the Lauegram after passing a certain limit of load on the crystal, i.e. the elastic limit. In this case, plastic deformation occurs in the crystal, as a result of which the single crystal is subjected to destruction into separate blocks sliding along a certain crystallographic plane relative to each other. In her subsequent works, Maria Afanasyevna proved the role of surface microcracks (defects) in reducing the ultimate strength of crystals compared to the theoretical one. A decrease in their number when dissolved in water led to an increase in tensile strength by 10–100 times and brought it closer to the theoretical limit. Based on the results of these works, in 1924 the work of A. F. Ioffe, M. V. Kirpicheva and M. A. Levitskaya “Deformation and Strength of Crystals” [7] was published in the “Journal of the Russian Physical-Chemical Society”, which is still referred to today.

Therefore, at the Department of Solid State Physics of Voronezh State University, from its very foundation, X-ray methods were established and developed as the main methods for studying solids and various materials - X-ray diffraction (XRD) and X-ray spectroscopy (XRS), which make it possible to obtain data on the atomic structure and electron-energy spectrum of matter, respectively. Under the supervision of Professor M. A. Levitskaya,

XRD studies of metals and alloys, and then semiconductors, were carried by N. A. Ignatiev, R. L. Fogelson and aspirants N. A. Vodopyanova, K. B. Aleynikova. XRS research methods were used in their research by V. S. Kavetsky, I. I. Kapshukov and one of the last aspirants of M. A. Levitskaya, E. P. Domashevskaya.

In the post-war years, Maria Afanasyevna and her student E. A. Kuznetsova conducted XRD studies of second-row stresses in thin layers of rock salt (and aluminum) obtained by evaporation in a vacuum. At the same time, together with her aspirants R. L. Fogelson and N. A. Vodopyanova, Maria Afanasyevna created an XRD method for studying diffusion in metals. This method for determining diffusion coefficients found its greatest development in the works of an associate professor R. L. Fogelson. The values of diffusion coefficients for many metals obtained by him were included in international reference books of the US National Bureau of Standards.

X-ray spectroscopy did not go unnoticed by Maria Afanasyevna either. Aspirants V. S. Kavetsky (future dean of the Physics Department), I. I. Kapshukov and E. P. Domashevskaya (future head of the Solid State Physics Department) were involved in research in this area. After the war, M. A. Levitskaya was the only professor of physics in Voronezh. But already on May 15, 1945, at a scientific session of VSU, Maria Afanasyevna made her first post-war report on tellurium radiation.

During the Great Patriotic War and the post-war period, M. A. Levitskaya studied the structure of atomic nuclei,  $\beta$ -decay, diffusion issues in solids, explored X-ray spectra of alloys and intermetallic compounds, optical spectra of thin metal layers (Fig. 2). Together with the German professor Robert Dopel, interned in Voronezh after the war, he organized a laboratory of nuclear spectroscopy at VSU, and then in 1959 he organized the Department of Nuclear Physics and became its first head, simultaneously heading the Department of Electromagnetic Oscillations. The results of M. A. Levitskaya's research were published in more than 50 articles, in the monograph “Infrared Rays” and the last unpublished manuscript “Vortex Model of the Nucleus”.

From the newspaper “Kommuna” for March 9, 1960: “... Decree of the Presidium of the Supreme Soviet of the USSR of March 7, 1960. *“In commemoration of the 50th anniversary of International Women's Day and noting the active*

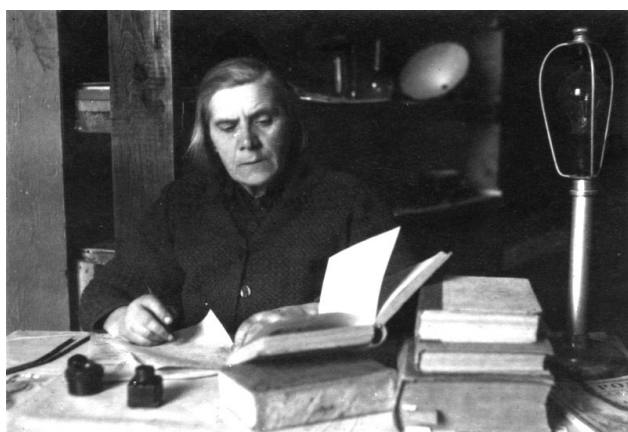


**Fig. 2.** Maria Afanasyevna Levitskaya in the laboratory of the Electromagnetic Oscillations Department in the post-war years (Red Building of VSU on Prospekt Revolyutsii, 24)

*participation of women of the Soviet Union in communist construction and their services to the Soviet state in educating the younger generation, for achieving high labor performance and fruitful social activities, to award ... the Order of the Red Banner of Labor to Professor Maria Afanasyevna Levitskaya, head of the Department of Electromagnetic Oscillations at Voronezh State University... (Fig. 3).*

Thus, M.A. Levitskaya became the founder of the largest scientific school of physics in Voronezh, which currently includes more than 50 doctors of science.

### Achievements of the scientific school in the field of semiconductors

The stimulus for the further development and growth of the Voronezh scientific school of solid state physics at VSU was active research into the electronic structure of semiconductor compounds associated with the rapid development of semiconductor physics. Since the middle of the last century, in connection with Schottky's discoveries of the rectifying properties of a metal-semiconductor heterocontact, a real boom in the field of synthesis of new semiconductor compounds and materials suitable for use in various fields of technology, and above all, in electronics and optoelectronics. Academician A. F. Ioffe, who headed the Physico-Technical Institute of the USSR Academy of Sciences in Leningrad for several decades, did not escape this boom. Single crystals of numerous semiconductor compounds of various types ( $A^{III}B^V$ ,  $A^{II}B^{VI}$ ,  $A^{II}B^{IV}C^V_2$ ) were synthesized and studied at the Physico-Technical Institute. The leadership in these studies in the USSR belonged



**Fig. 3.** The Order of the Red Banner of Labor - an award to M. A. Levitskaya in 1960

to Nina Aleksandrovna Goryunova, the founder of a new scientific direction – the chemistry of complex diamond-like semiconductors [8], laureate of the N. S. Kurnakov Prize of the USSR Academy of Sciences, Cavalier of the Order of Lenin. She infected with her enthusiasm the young associate professor of VSU Ya. A. Ugay, who organized work on the synthesis and research of a new class of semiconductor compounds formed as a result of the chemical interaction of metals of the group (zinc, cadmium) and non-metals of the group (phosphorus, arsenic, antimony) and many other types of compounds. At the same time, co-workers of the Solid State Physics Department used XRD methods to study the state diagrams of zinc-phosphorus, cadmium-phosphorus, zinc-antimony, zinc-arsenic, cadmium-antimony, cadmium-arsenic for the first time, to determine the crystal structures of the numerous compounds formed, and to discover a previously unknown compound  $Cd_6P_7$  [9] (Fig. 4).

But even earlier, aspirant E. P. Domashevskaya used the X-ray spectroscopy method to obtain the world's first experimental evidence of charge transfer from metals of the second and third groups to non-metals of the fifth group during the formation of semiconductor compounds, having measured the shifts of the  $K\alpha$ -lines of the characteristic X-ray spectrum of metals in these compounds [10]. The results obtained were reported at the All-Union Conference on the Physics and Chemistry of Semiconductors in January 1962 in Leningrad under the chairmanship of Professor N. A. Goryunova, and later at the International Conference on Chemical Bonding in



**Fig. 4.** K. B. Aleinikova, V. S. Kavetsky, A. V. Arsenov and A. N. Lukin discuss the results of decoding the crystal structure of  $\text{Cd}_6\text{P}_7$ , the first new semiconductor compound they obtained (the Solid State Physics Department, mid-1970s)

Semiconductors in Minsk under the chairmanship of Academician N.N. Sirota, which was attended by such luminaries of semiconductor science as the Americans Goodenough and Muser, the Frenchman Suchet and others. These results were published in Reports of the USSR Academy of Sciences in co-authorship with Ya. A. Ugai, as well as in the materials of international conferences, subsequently translated to the USA.

The fact is that the obtained data on the positive chemical shifts of the  $K\alpha$ -lines of the metallic elements and the negative chemical shifts on non-metallic elements put an end to the dispute about the mechanisms of formation of chemical bonds in semiconductors and irrefutably substantiated the new donor-acceptor model due to the unshared electron pair of valence electrons in the elements of the Vth group instead of the old speculative  $sp^3$ -hybrid model of Muser and Pearson, in which a negative charge should appear on the metallic element.

With these works, the “semiconductor period” begins at the Solid State Physics Department, but without M.A. Levitskaya, who died on March 7, 1963, 3 weeks before her 80th birthday.

In 1967, junior researcher E. P. Domashevskaya defended her candidate’s dissertation “X-ray spectroscopy studies of the nature of chemical bonding in semiconductor compounds” (Fig. 5) and con-

tinued to study semiconductor compounds with complex atomic composition, combining research with teaching work at the Solid State Physics Department.

After the death of M. A. Levitskaya, her former aspirant, former front-line soldier, Associate Professor Valery Sergeevich Kavetsky, who was also the dean of the Physics Department, which had recently become an independent department, having separated from the mathematicians as part of the Physics and Mathematics Department in 1959, became the head of the Solid State Physics Department.

And then, from the beginning of the 70s, a new method of ultra-soft X-ray spectroscopy was involved in active research of interatomic interaction and electron structure in semiconductors. This was primarily due to the acquisition, on the initiative of E. P. Domashevskaya, of a unique device, an X-ray spectrometer-monochromator, developed at the Leningrad University by A. P. Lukirsky, the son of the famous academician P. A. Lukirsky, a colleague and employee of A. F. Ioffe. This device (the 13th in a row) was built in Leningrad at the

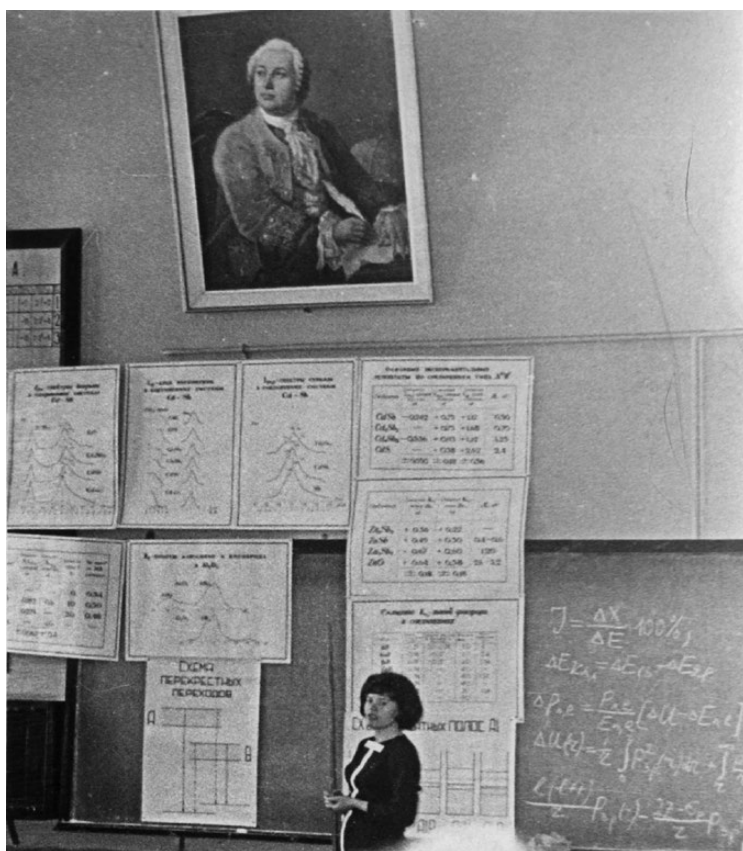


**Fig. 5.** E. P. Domashevskaya defends her PhD thesis at the Academic Council of the Physics Faculty of Voronezh State University in 1967

experimental plant of the NPO “Burevestnik” under the supervision of its general director N. I. Komyak. In Voronezh, the device was constantly improved in the process of work by assistant V. A. Terekhov (Fig. 6), who transferred it to oil-free means of obtaining a high vacuum, modernized the recording means and achieved the best sensitivity of the device in the USSR.

The features of our experimental approach to determining the nature of interatomic interaction in solids consisted of the complex use of two methods: X-ray spectroscopy (XS) and X-ray electron spectroscopy (XES). This combination of methods creates a unique opportunity to obtain information on the distribution of both the integral density of states of valence electrons responsible for the chemical bond and the local partial density of states contributing to the integral density of states of all valence electrons with different symmetry of states  $l$  of atoms of all types  $\alpha$ .

Intensity distribution in XS:

$$I(E_k) \sim \sum p_{l,l+1}(E_k) n_{n,l+1}^\alpha(E_k) + p_{l,l+1}(E_k) n_{n,l+1}^\alpha(E_k), \quad (1)$$

and intensity distribution in XES:

$$I(E_k) \sim \sum \sum c^\alpha \sigma_{\alpha n,l}^\alpha(E_k) n_{n,l}^\alpha(E_k - h\nu - \varphi_0), \quad (2)$$

where  $n_{n,l}^\alpha$  is the local partial density of states of an element of type  $\alpha$  with concentration  $c_\alpha$ ;  $p_{l,l+1}$  – transition probability factor;  $\sigma_{\alpha n,l}$  – weight factor, which has the meaning of photoionization cross-section.

Thus, we performed X-ray spectral studies on a unique laboratory device RSM-500. At the same time, X-ray electron spectra had to be taken in Moscow, mainly in the laboratory of Academician V. I. Nefedov at the Institute of General and Inorganic Chemistry named N. S. Kurnakov of AN USSR or in the laboratory of Professor Yu. A. Teterin at the Kurchatov Institute of Nuclear Physics. The first X-ray electron spectrometers in the USSR from Varian and Hewlett Packard appeared in these centers.

It is precisely thanks to the combination of two methods – X-ray electron spectroscopy and X-ray spectroscopy – on numerous semiconductor binary and ternary compounds of the different types ( $A^{III}B^V$ ,  $A^{II}B^{VI}$ ,  $A^IB^V$ ,  $A^IB^{VII}$ ,  $A^{II}B^V$ ,  $A^{II}B^{IV}C_2^V$ ,  $A^IB^{III}C_2^{VI}$ ) were experimentally discovered and theoretically substantiated previously unknown patterns of interaction of  $d$ -electrons of metals with  $s,p$ -electrons of non-metals elements, which are resonant in nature and are caused by the



**Fig. 6.** Future professor, assistant V. A. Terekhov obtains the first results on the new ultrasoft X-ray spectrometer-monochromator RSM-500 (1970)

mutual arrangement of the interacting elements, metals and non-metals, in the periodic table [11, 12]. This interaction of a fundamental nature manifests itself regardless of the complexity of the composition and nature of the compound or alloy and consists either in the splitting of the  $s, p$ -band and the expulsion of  $s, p$ -states from the  $d$ -band at  $Ed = Es, p$  ( $d-s, p$  resonance) [13], or simply in the repulsion of  $s, p$ -states by  $d$ -electrons at  $Ed \neq Es, p$  with the simultaneous appearance of an admixture of  $s, p$ -states in the  $d$ -band.

For the theoretical description of the phenomenon of  $d-s, p$  resonance, E.P. Domashevskaya and her co-workers, O. V. Farberovich and S. I. Kurgansky (Fig. 7), were the first in Russia to implement a modified method of orthogonalized plane waves OPW, which allows calculating the band spectrum of compounds with  $d$ -metals [14].

Thus, in the 70s, at the Department of Solid State Physics of Voronezh State University, under the supervision of E. P. Domashevskaya formed a unique scientific direction that combines experimental and computational methods for studying the atomic and electronic structure of semiconductor materials and the nature of interatomic interactions in solids and thin films. The result of this most active period of development of experimental and theoretical studies of the atomic and electronic structure of semiconductor compounds of various types was the successful defense of the doctoral dissertation of E. P. Domashevskaya at the Academic Council of the Institute of Metallophysics of the National Academy of Sciences of the Ukrainian SSR in Kyiv in 1979 “The nature of interatomic interaction and

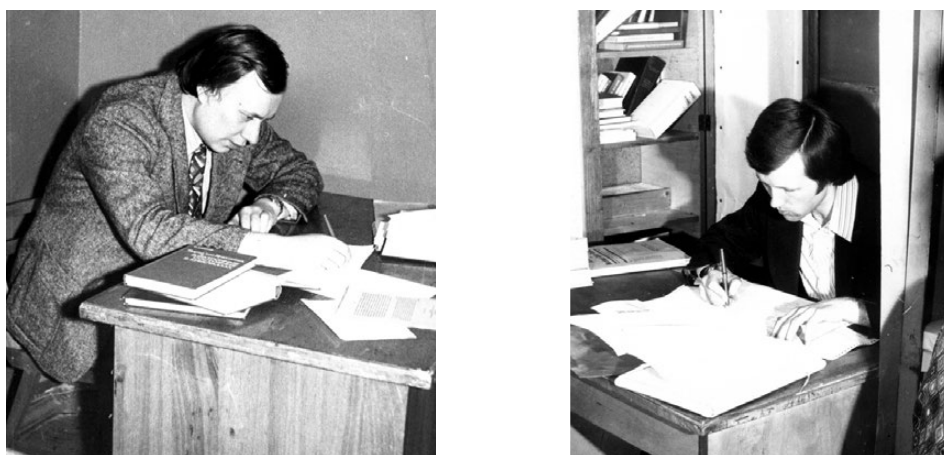


**Fig. 7.** Research Associates O. V. Farberovich and S. I. Kurgansky develop a software package for calculating the electronic structure of semiconductor compounds using the modified method of theorthogonalized plane waves MOPW (the Solid State Physics Department)

patterns of the structure of the energy spectrum of valence electrons in semiconductors” [15] (Fig. 8). Thus, 16 years after the death of M.A. Levitskaya, a doctor of physical and mathematical sciences appeared at the Solid State Physics Department, and soon after the approval of the doctoral dissertation by the Higher Attestation Commission in 1980, E. P. Domashevskaya became the head of the Solid State Physics Department in the position of professor.

In 1978, the VSU Physics Department celebrated the 95th anniversary of M. A. Levitskaya’s birth. The Presidium was represented by all of Maria Afanasyevna’s former aspirants, starting with Professor L. P. Rapoport and ending with E. P. Domashevskaya (Fig. 9).

And five years later, in 1983, the Physics Department celebrated the 100th anniversary of M. A. Levitskaya’s birth not only with a memorial conference, but also with a major cultural event



**Fig. 8.** E. P. Domashevskaya defends her doctoral thesis in Kyiv in 1979

in honor of the outstanding female physicist. Professor E. P. Domashevskaya, already in the role of head of the Solid State Physics Department, developed and approved at the Academic Council of the Physics Department a project for the artistic decoration of the back wall of the Large Physics Auditorium named after Professor M. A. Levitskaya in the form of a wall fresco painting, in the center of which Honored Painter of the Russian Federation Utenkov depicted Maria Afanasyevna Levitskaya surrounded by students (Fig. 10 and Fig. 11).

Following the study and discovery of  $d-s,p$  resonance, Domashevskaya's student O. V. Farberovich, studied in detail and generalized the resonance nature of the  $f-s,p$  interaction of  $f$ -electrons of rare-earth metals with  $s,p$ -electrons of non-metals. In his works, an approach based on the density functional theory was proposed, which allows one to take into account both the band nature of the states of  $f$ -electrons and their strong localization in a single scheme. Within the framework of such a universal approach,

several basic powerful methods for calculating the band structure were implemented, differing in the type of effective potential: the method of orthogonalized plane waves (OPW), the method of augmented plane waves (APW), the Green's function method (GF), the method of linear combination of atomic orbitals (LCAO), the modified OPV method (MOPV), which was interpreted as a combination of the OPV and LCAO methods. As a result of joint work with Professor K. A. Kikoin (I. V. Kurchatov Institute of Atomic Energy), a theory of mixed valence of rare earth compounds was created.

Based on these theoretical studies in the field of multiplet structure, O. V. Farberovich defended his doctoral dissertation in 1985 [16] at the Institute of Steel and Alloys (Moscow) in the department of Nobel Prize laureate A. A. Abrikosov with the support of Nobel Prize laureate V. L. Ginzburg. Thus, in 1985, O. V. Farberovich became the youngest doctor of physical and mathematical sciences at Voronezh State University.



**Fig. 9.** 95th anniversary of M. A. Levitskaya's birthday. In the presidium from left to right: Professor P. V. Cherpakov, Associate Professor E. P. Domashevskaya, Associate Professor A. N. Latyshev, Associate Professor V. S. Kavetsky (Dean of the Physics Faculty), Associate Professor A. M. Meleshina, Professor L. P. Rapoport and Associate Professor N. A. Ignatiev



**Fig. 10.** Honored Artist of the Russian Federation Utenkov presents to the staff of the Solid State Physics Department his original fresco on the wall of the Large Physics Auditorium named after Professor M. A. Levitskaya, painted for the 100th anniversary of her birth in 1983.

Further development of research at the SSP department was associated with the emergence and development of a new interdisciplinary science, technology and engineering – microelectronics. In the first half of the last century in Voronezh the giant of the electronics industry was soon created - the scientific and production association NPO “Elektronika” with the active participation of graduates of the Physics Department of VSU. The Departments of Voronezh State University: Electronics (Head of Department, Associate Professor N. V. Kotosonov), Semiconductor Physics (Head of Department, Professor N. G. Nifontov, and later Professor V. F. Synorov), Solid State Physics (Head of Department, Associate Professor V. S. Kavetsky, Associate Professor N. A. Ignatiev, Professor E. P. Domashevskaya), Inorganic chemistry

(Head of Department, Professor Ya. A. Ugay) began to cooperate with NPO “Elektronika” and train personnel for this rapidly developing industry in new specialties, including specialty 200.200 – microelectronics and semiconductor devices and 200.300 – semiconductor materials.

New requirements of the time and scientific and technological progress shifted the center of gravity of research from bulk semiconductor crystals and materials to the area of planar technologies – thin films and thin-film metal-semiconductor (MS) and metal-insulator-semiconductor (MIS) heterostructures.

By this time (early 70s) an outstanding result was obtained by V. A. Terekhov with her co-workers V. M. Andreeshchev and V. M. Kashkarov on our RSM-500 device: we discovered in the  $L_{2,3}$  spectra



**Fig. 11.** Successor of M. A. Levitskaya, Professor E. P. Domashevskaya, Head of the Solid State Physics and Nanostructures Department of Voronezh State University (1980–2020) gives a lecture in the Large Physics Auditorium named after Professor M. A. Levitskaya against the background of a wall fresco with her image

of heavily doped silicon single crystals  $\delta$ -shaped localized maxima in the forbidden zone, caused by the presence of donor impurities of phosphorus, arsenic, antimony with a concentration of about  $10^{-4}$  at. %.

Only ten years later these results were reproduced in the USA, and then only using synchrotron radiation. Since then, we have been developing the physics of localized states, which play a decisive role in the electrophysical and optical properties of heavily doped and disordered semiconductors. The developed approach was successfully used by us in the study of the total local and partial densities of state of atoms in disordered

condensed media and amorphous semiconductors and dielectrics. Special attention was paid to the study of localized states in the forbidden zone, providing direct information on the nature and number of defects in real materials: heavily doped, ion-implanted semiconductors, hydrogenated amorphous silicon and heterostructures, developed by our colleagues and co-authors at the A. F. Ioffe Physical-Technical Institute of the USSR Academy of Sciences, the P. N. Lebedev Physical Institute of the USSR, the Nizhny Novgorod State University and other institutes. The successful development of this direction was reflected, first of all, in the content of the doctoral dissertation of Vladimir Andreevich Terekhov “Local density of electron states in disordered semiconductors” (1994) [17].

The methods developed within the framework of these studies were successfully used to analyze thin-film systems, coatings and composites within the framework of cooperation with industrial partners JSC “NIET”, VZPP “Mikron”, VZPP “Sborka”, JSC “RIF” (Voronezh) and were reflected in the subsequent doctoral dissertations of Yurakov Yu. A. “Electronic structure and physical properties of thin metal-silicon films” (2000) [18], Turishchev S. Yu. “Electronic and energy structure of nanoscale structures based on silicon and its compounds” (2014) [19] and Lenshina A. S. “Formation and functional properties of nanostructures based on porous silicon” (2021) [20].

### Nanophysics at the Department of SSPNS

Since 2007, the Department of Solid State Physics of Voronezh State University has been called the Department of Solid State Physics and Nanostructures (SSPNS), already having significant scientific achievements in the field of nanostructure and nanomaterial research.

Nanoelectronics emerged as microelectronics developed, and the SSPNS Department of took part in this process. The transition to very large integrated circuits (VLSI) and the gigantic density of active elements packing per unit area of the substrate crystal rapidly dictated new requirements for the ultra-small sizes of these circuit elements. In the course of developing new technologies, there was a gradual transition from micron scaling ( $10^{-6}$  m) to the nanometer range ( $10^{-9}$  m) of manufacturing active elements of microcircuits and the development of new nanotechnologies. In new artificial materials – superlattices, quantum wires and quantum dots – new “quantized” physical properties were

discovered – the quantum Hall effect, quantum electrical conductivity, etc. The SSP Department did not have to radically restructure itself, because we have always used nanophysics methods: diffraction and interference of electrons and quanta on the atomic planes of the crystal, located at subnanometer, angstrom distances ( $1 \text{ \AA} = 0.1 \text{ nm}$ ). But the most important thing is that the depth of the informative layer in our unique method of ultra-soft X-ray spectroscopy, limited by the depth of the X-ray characteristic radiation output of a long wavelength of  $\sim 10 \text{ nm}$ , is also  $\sim 10\text{--}100 \text{ nm}$ .

However, it should be noted that experimentally we obtain averaged information from the entire nanolayer, which has a thickness of several tens of unit cells. But theoretically, it was possible to dismember even one unit cell into separate layers and study the features of the main properties of such a model object in comparison with a real material. This approach was implemented in the works of Sergey Ivanovich Kurgansky, who, in the conceptual approximation of the local density functional within the framework of the computational scheme of the film method of linearized augmented plane waves (LAPW), created a unified method for calculating the electronic band structure, X-ray emission and photoelectron spectra of thin films of subnanometer thickness. He showed that the structure of the valence band in metal oxide films of high-temperature superconductors of the  $\text{YBa}_2\text{Cu}_3\text{O}_{7-x}$  type is determined by the interaction of copper d-electrons with oxygen p-electrons, which is well described by the  $d$ - $s$ , $p$ -resonance model. At the same time, due to the peculiarities of the crystalline structure of the unit cell of these compounds and the isolation of its cuprate layers from each other by Ba–O layers, this model works separately in each cuprate layer with the stoichiometry of  $\text{CuO}$  and  $\text{CuO}_2$ . S. I. Kurgansky defended his doctoral dissertation “Electronic structure of thin films of complex metal oxides” in 1996 [21].

Subsequently, the range of methods and studied nanosystems expanded. The method of augmented cylindrical waves (ACW) was used to study the electronic structure of one-dimensional nanosystems – single-wall carbon and silicon nanotubes. Then, a study was conducted of the atomic and electronic structure of a number of zero-dimensional nanosystems – metal-silicon and metal-germanium clusters containing one atom of a transition metal (Sc, Ti, V, Cr, Y, Zr, Nb, Mo)

and up to twenty atoms of silicon or germanium [22]. Experimentally, the electronic structure of these clusters was much later studied using photoelectron spectroscopy. A comparison of the calculated densities of states with the experimental photoelectron spectra showed that the shape of the density of states of the main isomer with the highest binding energy is close to the experimental spectrum.

Also among the first steps towards theoretical study of zero-dimensional nanosystems was the study of small metal particles (SMP) with sizes of several hundred nanometers. To study the spectral characteristics of SMP, Professor O. V. Farberovich and aspirant Larisa Kurkina developed a time-dependent density functional method at the SSP Department, on the basis of which a series of unique works were carried out to study the nature of optical spectra in SMP. L. I. Kurkina successfully defended first her candidate's and then her doctoral dissertation “Electronic properties of  $s$ , $p$ - and  $3d$ -metal clusters” in 1997 [23], becoming at the age of 31 the youngest doctor of physical-mathematical sciences at the Physics Faculty.

Also, within the framework of the local spin density functional method, but using the “atom in jelly” model, calculations were carried out for Al and Fe clusters of various sizes containing up to 130 atoms, which revealed a non-monotonic change in the electronic structure with an increase in the cluster size and a non-monotonic size dependence of the ionization potential and magnetic moment. It was shown that in aggregates containing up to several tens and even hundreds of atoms, quantum-size effects are clearly manifested, which mainly determine the unique properties of clusters.

In 1999, at an extended meeting of the Academic Council and the Scientific and Technical Council of VSU, the SCIENTIFIC SCHOOL of Evelina Pavlovna Domashevskaya in the field of electronic structure of solids [24] was approved among 11 leading scientific schools of VSU with the presentation of a CERTIFICATE (Fig. 12) and a MEMORIAL MEDAL of VSU.

In the experimental part of the work, the development of nanophysics and nanotechnology continued with the development of manufacturing technology and the study of the electron structure, optical and electrical properties of porous silicon (*por*-Si), which are fundamentally different from the properties of single-crystal silicon, since *por*-Si is a typical nanomaterial. First of all, it luminesces



**Fig. 12.** Certificate of approval by the Academic Council and the Scientific and Technical Council of VSU of the SCIENTIFIC SCHOOL of E. P. Domashevskaya with the presentation of the MEMORIAL MEDAL of VSU

perfectly in the visible region, changing the colors of luminescence from red to green-blue, depending on the size of the pores and, consequently, on the size of the *por*-Si nanocrystals coated with nanolayers of oxide and amorphous phases. To determine the complex phase composition of this nanomaterial using ultra-soft X-ray spectroscopy methods, an algorithm was developed and a special computer program was created to determine the component composition of complex multiphase systems including amorphous phases [25]. A significant part of these developments formed the basis of the candidate's and then doctoral dissertations of A. S. Lenshina. (2021) "Formation and functional properties of nanostructures based on porous silicon" [20].

The transition to the use of low-dimensional systems in microelectronics and condensed matter physics has entailed the intensive development of composite nanomaterial technologies, among which granular metal-dielectric composites with metal particle sizes of about 10-100 nm and possessing unique nonlinear electrical and magnetic properties are of particular interest.

The development of nanocomposite science and technology has led to large-scale studies of

ferromagnetic-diamagnetic materials due to the discovery of tunnel magnetoresistance (TMR) in them, an analogue of giant magnetoresistance (GMR), differing in the mechanisms of charge carrier and spin transport. A large number of studies on GMR were published after the discovery of this effect in 1988 by Albert Fert and Peter Grünberg and the awarding of the Nobel Prize to the authors in 2007. As a result, technologies of magnetically hard and magnetically soft materials for microwave electronics, radio electronics, magnetic sensors, bank cards, etc. were developed.

Around this time, our colleagues from the Voronezh State Technical University developed original magnetron technologies for producing film nanocomposites of metal-dielectric and metal-semiconductor of various variable compositions and studied their electromagnetic properties. The results of these studies were summarized in the collective monograph "Nonlinear Phenomena in Nano and Microheterogeneous Systems" by S. A. Gridnev, Yu. E. Kalinin, A. V. Sitnikov, O. V. Stognei, published in 2012 [26].

At the same time, at the SSPNS Department of Voronezh State University, under the supervision

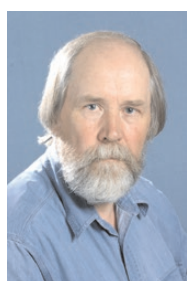
of Head Professor E. P. Domashevskaya, they began to study the influence of the atomic composition, atomic structure and concentration of different components on nonlinear electromagnetic properties using samples synthesized at VSTU. The results of these studies were summarized in the candidate dissertations of aspirants S. A. Storozhilov “Atomic and electronic structure of metal-insulator nanocomposites  $(\text{Co}_{41}\text{Fe}_{39}\text{B}_{20})_x(\text{SiO}_2)_{2/1-x}$  and  $(\text{Co}_{45}\text{Fe}_{45}\text{Zr}_{10})_x(\text{SiO}_2)_{1-x}$ ” (2008), Builov N. S. “Atomic and electronic structure of multilayer nanostructures with metal-composite layers and non-magnetic interlayers” (2020), Ivkov S. A. “Features of structural and transport properties of nanocomposites  $\text{Co}_x(\text{MgF}_2)_{2/100-x}$  and  $(\text{Co}_{45}\text{Fe}_{45}\text{Zr}_{10})_x(\text{MgF}_2)_{100-x}$ ” (2022)

and Peshkov Ya. A. “Phase composition, electronic structure and electric transport properties of multilayer nanostructures based on CoFeB and CoFeZr” (2024). Thus, starting from the late 1970s and up to the present time, 15 doctors of physical and mathematical sciences and more than 60 candidates of sciences have been trained in the scientific school of solid state physics and nanostructures (Fig. 13).

In 2012, Evelina Pavlovna Domashevskaya was awarded the Certificate of the Prime Minister of the Russian Federation Vladimir Vladimirovich Putin “For the support provided in the elections of the President of the Russian Federation in March 2012, a huge contribution to the development of nanotechnology and solid state physics in the territory



O. V. Farberovich  
1985



V. A. Terekhov  
1994



S. I. Kurgansky  
1996



L. I. Kurkina  
1996



V. D. Strygin  
1996



V. I. Kukuev  
1996



Yu. A. Yurakov  
2000



R. V. Kuzmenko  
2002



V. A. Gorbunov  
2003



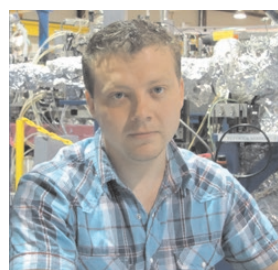
E. S. Rembeza  
2007



E. A. Tutov  
2009



S. V. Ryabtsev  
2011



P. V. Seredin  
2012



S. Yu Turishchev  
2014



A. S. Lenshin  
2021

**Fig. 13.** Doctors of Physical and Mathematical Sciences in the Scientific School of Solid State Physics and Nanostructures of VSTU

*of the Russian Federation and in connection with the celebration of her birthday."*

### Synchrotron studies of nanomaterials

The history of synchrotron studies in VSU is associated with the cooperation of the Solid State Physics Department with German scientists from the University of Leipzig (GDR) in the second half of the 20th century. The first work of junior research fellow E. P. Domashevskaya (co-authored with Ya. A. Ugay) was published in 1965 in the Proceedings of the University of Leipzig based on the results of correspondence participation in the work of the 1st International Conference on X-ray Spectroscopy in 1964, chaired by Professor Armin Meisel.

Twenty years later, in 1984, Professor E. P. Domashevskaya, already the head of the Department of Physics and Solids, took part in the Jubilee International Conference (20 years) on X-ray and Intrashell Processes in Atoms, Molecules and Solids, which was organized by the same Professor of the University of Leipzig Armin Meisel and co-chaired by Nobel laureate Kai Siegbahn, the creator and developer of X-ray electron spectroscopy at the oldest university in Europe, Uppsala (Sweden). Many outstanding scientists from different countries took part in the work of this conference, among which one of the largest delegations was represented by scientists from Sweden. From the

USSR, world-famous scientists in the field of X-ray and electron spectroscopy took part, professors Igor Borisovich Borovsky (Moscow), Mikhail Arnoldovich Blokhin (Rostov-on-Don), academician of the Academy of Sciences of the Ukrainian SSR Vladimir Vladimirovich Nemoshkalenko (Kyiv), professors Vadim Ivanovich Nefedov (Moscow), Tatyana Mikhailovna Zimkina (Leningrad), Miron Yankelevich Amusya (Leningrad), Viktor Aleksandrovich Trapeznikov (Izhevsk), Igor Yakovlevich Nikiforov (Rostov-on-Don), Vladimir Filippovich Demekhin (Rostov-on-Don), Evelina Pavlovna Domashevskaya (Voronezh), Ernst Zagidovich Kumaev (Rostov-on-Don). Sverdlovsk), Lev Nikolaevich Mazalov (Novosibirsk), Mart Elango (Tartu). At this conference E.P. Domashevskaya made the report in English entitled "d-s,p and f-p resonances in compounds" [27]. She then participated in similar conferences in Berkeley (USA) in 1990, in Rome (Italy) in 1996, in Tokyo (Japan) in 1998, in Uppsala (Sweden) in 2003 (Fig. 14), in Berlin (Germany) in 2007.

In 1996, on the initiative of E. P. Domashevskaya, the 1st Russian-German seminar dedicated to the 100th anniversary of Roentgen's discovery of X-ray. The next 2-nd X-ray Seminar was held in Berlin in 1997, and the third one in Yekaterinburg in 1999. And in November 2001, as a result of close cooperation with German colleagues and, in many



**Fig. 14.** E. P. Domashevskaya among the participants of the 9th International Conference on Electron Spectroscopy in the Nobel Hall of the oldest university in Uppsala (Sweden, 2003)

ways, thanks to the scientific and organizational efforts of two world-famous female physicists from St. Petersburg University, professors Tatyana Mikhailovna Zimkina and Vera Konstantinovna Adamchuk, a Russian-German channel and a Joint Use Laboratory were opened in Berlin at the new latest generation synchrotron BESSY II (Fig. 15), the research program of which included

the first project from VSU in 2002, “Study of the features of the electronic structure and the nature of photoluminescence in porous materials and materials containing quantum dots, direct and indirect semiconductors (Si, GaP, InP, GaAs)”.

Since then, several dozen projects have been carried out to study nanomaterials, nanostructures and nanocomposites with various functional



**Fig. 15.** Opening of the Russian-German Channel and the Joint Laboratory at the Berlin Synchrotron BESSY II in November 2001

properties: luminescent, gas-sensitive and magnetic, using the BESSY II synchrotron radiation, the results of which are reported at various international conferences. And Ruslan Ovsyannikov, a former graduate student of Professor E. P. Domashevskaya (Voronezh State University) and a postgraduate student of Professor Eberhardt (Technical University of Berlin) is currently working as a leading researcher at the Berlin synchrotron BESSY II.

Using SR, unusual effects of the interaction of complex silicon-based nanosystems with electromagnetic radiation of nanometer wavelengths (ultrasoft X-ray synchrotron radiation) were discovered for the first time as a result of interference and diffraction of incident and reflected radiation from silicon nanocrystals or interfaces of multilayer structures. We called this new effect the “intensity reversal effect”. Such effects appear at the absorption edges of silicon obtained by synchrotron radiation with a wavelength commensurate with the size of nanocrystals or the thickness of nanolayers. Then, pre-edge interference of synchrotron radiation from nanolayers of “stretched” silicon of a certain thickness was discovered in “silicon on insulator” structures. All these newly discovered effects formed the basis of the doctoral dissertation (2014) of a young scientist, now the head of the Department of General Physics at the Physics Faculty of Voronezh State University, Sergei

Yuryevich Turishchev [19], who leads a group of Voronezh synchrotron scientists, which includes master’s students, postgraduate students and young employees of the Physics Faculty (Fig. 16).

### Nanosized monocrystals of oxide materials

Systems and devices created on the basis of nanomaterials are increasingly used in various fields of modern engineering and technology. The characteristics of such systems are fundamentally different from those of their analogues created using traditional technologies. One example of such materials are oxide nanowires. The unique physical properties of nanowires are determined by several factors: the nanoscale of crystallites; a single-crystal structure with a low degree of defectiveness; and extremely pronounced anisotropy of nanocrystals.

Since the 2000s, a new direction related to the physicochemical studies of filiform nanomaterials has been developing at the SSPNS Department in the group of Senior Researcher S. V. Ryabtsev. Using the gas transport method, filiform nanocrystals of oxide wide-bandgap semiconductors  $\text{SnO}_2$ ,  $\text{ZnO}$ ,  $\text{In}_2\text{O}_3$  and some others were synthesized and studied [28]. By changing the parameters of gas transport synthesis, it is possible to obtain various nanocrystalline forms of oxide materials (Fig. 17). The resulting nanomaterials exhibit the highest sensitivity to the adsorption of a number of gases. High-quality

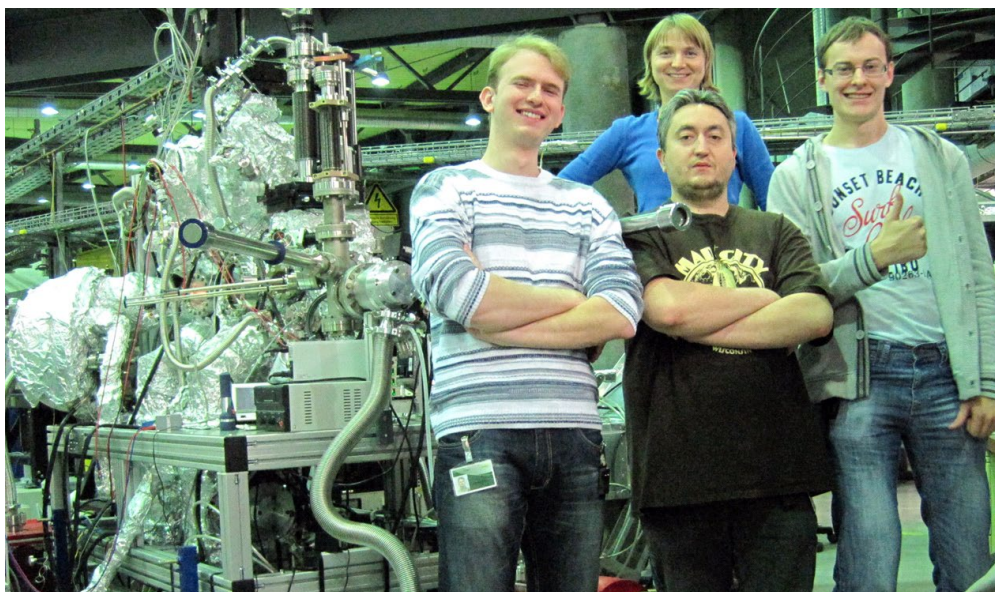


**Fig. 16.** A group of young scientists of the Solid State Physics Department headed by S. Yu. Turishchev at the Russian-German Channel BESSY II synchrotron in Berlin in 2014: (from left to right) Dmitry Nesterov, Sergey Turishchev, Dmitry Spirin and Olga Chuvankova

semiconductor gas sensors were developed on their basis [29]. Combining several sensors (receptors) with different selectivity into a common device with appropriate data processing made it possible to create a laboratory model of the device, the so-called “electronic nose”, which, in a certain sense, is an analogue of the human olfactory organ. The result of the intensive development of nanotechnology was the successful defense of several candidate’s dissertations, and then a doctoral dissertation by S. V. Ryabtsev “Electrical and optical properties of various nanoforms of tin oxide” in 2011 [30].

### Nanoheterostructures based on AIII BV and the Joint Laboratory with the A. F. Ioffe Physico-Technical Institute of the Russian Academy of Sciences

Quantum-size AIIIBV heterostructures invariably attract serious attention from researchers and technologists. All of the AIIIBV-based nanoheterostructures that we study are formed at the Physico-Technical Institute named A. F. Ioffe of RAS by a group of co-workers of Nobel Prize laureate Zhores Ivanovich Alferov, with whom the Solid State Physics Department has

had long-standing close scientific contacts [31]. The formation of self-organizing low-dimensional semiconductor layers on AIII BV single crystals turned out to be especially promising due to the possibility of obtaining spatial (3D) confinement of electrons in stable (dislocation-free) clusters, conductivity and high radiation efficiency due to the low density of defects. Using synchrotron radiation SR, we obtained for the first time the spectra of the near fine structure of X-ray absorption in the region of the main absorption edge of phosphorus  $PL_{2,3}$ , reflecting the local density of states in the conduction band in nanostructures with InP quantum dots grown on GaAs <100> by the method of gas-phase epitaxy from metal-organic compounds, and in porous InP layers obtained by anodic pulsed electrochemical etching of InP <100> single-crystal wafers [32].

In 2008, at the International Conference on Heterostructures dedicated to the 90th anniversary of the A. F. Ioffe Physico-Technical Institute of the Russian Academy of Sciences, chaired by Academician Zh. I. Alferov, professor Domashevskaya E. P. made the plenary report on the results of joint research of VSU and PTI

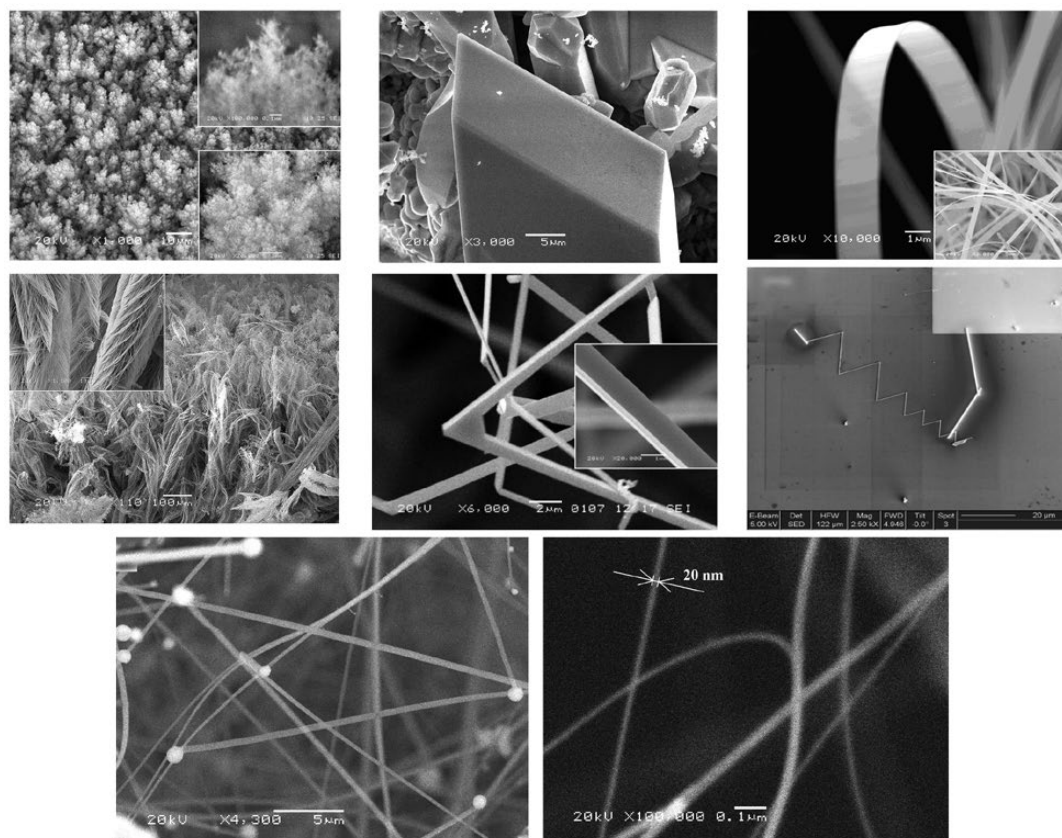


Fig. 17. Various shapes of  $\text{SnO}_2$  nanocrystals obtained by gas transport synthesis

the “Diagnostics of nanoheterostructures using XANES and XRD” (Fig. 18).

Simultaneously with these studies, a group of postgraduate students headed by P. V. Seredin, working on the problem of matching the parameters of crystal lattices in semiconductor heterostructures, showed that as a result of the decomposition of epitaxial solid solutions of three-component ( $\text{Al}_x\text{Ga}_{1-x}\text{As}$ ,  $\text{Ga}_x\text{In}_{1-x}\text{P}$ ,  $\text{In}_x\text{Ga}_{1-x}\text{As}$ ), four-component ( $\text{Ga}_x\text{In}_{1-x}\text{As}_y\text{P}_{1-y}$ ), and even five-component  $\text{Al}_x\text{Ga}_y\text{In}_{1-x-y}\text{As}_z\text{P}_{1-z}$  [33], nanostructures can spontaneously arise, representing superstructural phases of ordering with the formation of a domain structure. In 2012, P. V. Seredin defended his doctoral dissertation “Substructure and optical properties of epitaxial heterostructures based on A3B5” [34]), and at the

age of 32 became the youngest doctor of physical and mathematical sciences in the history of the Physics Department of Voronezh State University. The results of P. V. Seredin’s doctoral dissertation formed the basis of his monograph “New physical phenomena in heterostructures based on A<sup>3</sup>B<sup>5</sup> semiconductors. Promising approaches to creating optoelectronics of the future”, published in Moscow in 2015 [35]. The book describes a new physical phenomenon in semiconductor heterostructures - the spontaneous emergence of periodically ordered structures on the surface and in epitaxial films of A3B5 semiconductors. The regularities of the phenomenon of the emergence of superstructural ordering phases are described, which makes it possible to obtain inclusions of narrow-band semiconductors in a



**Fig. 18.** International Conference on Heterostructures at the A. F. Ioffe Physico-Technical Institute of the Russian Academy of Sciences chaired by Academician Zh. I. Alferov

wide-band matrix, thereby creating the basis for a new technology for obtaining ordered arrays of inhomogeneities - the basis for a new generation of opto- and microelectronics.

In 2014, the Joint Laboratory of Physics of Nanoheterostructures and Semiconductor Materials (VSU-Ioffe Physical-Technical Institute of the Russian Academy of Sciences) was officially established in the form of a Consortium between the Federal State Budgetary Educational Institution of Higher Education “Voronezh State University” and the Federal State Budgetary Institution of Science “Ioffe Physical-Technical Institute of the Russian Academy of Sciences”. The participants of the Consortium are the Solid State Physics and Nanostructures Department of Voronezh State University and the Laboratory of Semiconductor Luminescence and Injection Emitters of the Ioffe Physical-Technical Institute. The heads of the Joint Laboratory on the part of Voronezh State University were young Doctor of Sciences Pavel Vladimirovich Seredin, and on the part of the Ioffe Physical-Technical Institute - former graduate of VSU Solid State Physics Department, now leading researcher, Doctor of Sciences, Laureate of the All-Union Lenin Komsomol Prize Ivan Nikitich Arsenyev.

Research areas developed in the Joint Laboratory of Voronezh State University and the Ioffe Physical-Technical Institute:

- fundamental research into the features of the atomic and electronic structure, optical and

electrophysical properties of semiconductor heterostructures based on A3B5;

- modeling of physical processes in semiconductor technology;

- diagnostics of low-dimensional and quantum-dimensional systems by diffractometric and spectroscopic methods;

- development of fundamental principles for the creation of new bioactive materials that match the composition, morphological and physicochemical properties of human dental and bone tissue;

- studies of metabolic processes in the hard tissues of the human tooth;

Some of the projects implemented in the Joint Laboratory:

1. Project No. 3.130.2014/K, on the topic: “Development of physical and technological approaches to the formation and diagnostics of epitaxial integrated AlInB<sub>5</sub>/Si heterostructures” carried out within the framework of the Project part of the state assignment to universities of the Russian Federation 2014-2016 (Head P.V. Seredin) (2014-2016).

2. Grant of the Russian Foundation for Basic Research 16-32-50003 mol\_nr “Research into the main capabilities of controlled self-organization, self-assembly and superstructuring in epitaxial solid solutions of A3B5 semiconductors and their integration with silicon technology” (Head P.V. Seredin) (2016).



**Fig. 19.** Head of SSPhNS Department, Professor E. P. Domashevskaya and Associate Professor P. V. Seredin at the Joint Laboratory of VSU–PhTI RAS in 2019 (VSU, University Square, 1)

3. Grant of the President of the Russian Federation MD-188.2017.2 for state support of scientific research of young Russian scientists-doctors of science “Epitaxial heterostructures A3B5/por-Si with high functional properties: development of production technology and fundamental research” (Head P.V. Seredin) (2017-2018).

4. RSF Grant 19-72-10007 “Study of the formation features of hybrid semiconductor nanoheterostructures of reduced dimensionality on porous silicon” (Head A.S. Lenshin) (2019-2021).

5. RSF Grant 16-15-00003-P “Development of effective methods of preventive dental care by normalizing metabolic processes in hard tissues of the human tooth in vivo using biomimetic materials with high remineralization potential” - extension (Head P.V. Seredin) (2019-2020).

6. RSF Grant 17-75-10046 “Development of the basics of precision diagnostics of dental caries of different levels of formation based on fundamental research of biogenic samples and biomimetic model environments” (Head D.L. Goloshchapov) (2017-2019).

7. RSF Grant 25-22-00292 “Features of the structure, sorption and luminescent properties of a hybrid core-shell system based on porous silicon for targeted drug delivery” (Head E.P. Domashevskaya) (2025).

In 2020, Honored Scientist, Professor Evelina Pavlovna Domashevskaya handed over the post of head of the Solid State Physics and Nanostructures Department to Doctor of Physical and Mathematical Sciences, Associate Professor Pavel Vladimirovich Seredin, Laureate of several Grants of the President and the Russian Science Foundation.

Thus, numerous directions of the scientific school of SOLID STATE PHYSICS AND NANOSTRUCTURES in Voronezh State University, known far beyond Russia, continue and develop, the foundations of which were laid 90 years ago by an outstanding female physicist, Professor Maria Afanasyevna Levitskaya, who headed the Solid State Physics Department in Voronezh State University for more than 25 years, and were continued by Professor Evelina Pavlovna Domashevskaya, who headed the same Department in Voronezh State University for about 40 years.

## References

1. Khramov Yu. A. *Physicists. Biographical Handbook\**. Moscow: Nauka Publ.; 1983. 398 p. (In Russ.)
2. Kessler I. I. *A tale of lovers\**. Voronezh: Voronezh State University Publ.; 2003. 160 p. (In Russ.)
3. *Scientific schools of X-ray and X-ray electron spectroscopy in Russia\** / E. P. Domashevskaya (ed.). Voronezh: VSU Publishing House. 2015. 330 p. (In Russ.)
4. *Physics department of Voronezh State University\** / O. V. Ovchinnikov, A. N. Bobreshov, E. P. Domashevskaya (eds.). Voronezh: VSU Publishing House. 2021. 275 p. (In Russ.)
5. Ovchinnikov O. V., Latyshev A. N., Smirnov M. S. On the centenary of the discovery of submillimeter electromagnetic waves. *Uspekhi Fizicheskikh Nauk*. 2024;194(09): 1007–1015. <https://doi.org/10.3367/ufnr.2024.07.039724>
6. Levitskaya M. A. *Infrared rays\**. Moscow-Leningrad: USSR Academy of Sciences Publ.; 1935. 136 p. (In Russ.)
7. Ioffe A. F., Kirpicheva M. V., Levitskaya M. A. Deformation and strength of crystals\*. *Uspekhi Fizicheskikh Nauk*. 1967;93(2): 303–314. (In Russ.) <https://doi.org/10.3367/UFNr.0093.196710e.0303>
8. Goryunova N. A. *Complex diamond-like semiconductors\**. Moscow: Sovetskoe Radio Publ.; 1968. 267 p. (In Russ.)
9. Zavalishin E. I., Aleinikova K. B., Rabotkina N. S., Arsenov A. V. The crystal structure of  $\text{Cd}_7\text{P}_{10}$ . *Journal of Structural Chemistry*. 1979;20(1): 146–148. Available at: <https://www.elibrary.ru/item.asp?id=26781433>
10. Domashevskaya E. P., Ugai Y. A. X-ray spectrographic investigations into the nature of the chemical bond in semiconducting aluminum compounds. *Soviet Physics Journal*. 1965;8(6): 51–53. <https://doi.org/10.1007/BF00818404>
11. Nefedov V. I., Salyn Y. V., Domashevskaya E. P., Ugai Y. A., Terekhov V. A. A study by XPS and XRS of the participation in chemical bonding of the 3d electrons of copper, zinc and gallium. *Journal of Electron Spectroscopy and Related Phenomena*. 1975;6(3): 231–238. [https://doi.org/10.1016/0368-2048\(75\)80018-1](https://doi.org/10.1016/0368-2048(75)80018-1)
12. Domashevskaya E. P., Terekhov V. A., Marshakova L. N., Ugai Y. A., Nefedov V. I., Sergushin N. P. Participation of d-electrons of metals of groups I, II, and III in chemical bonding with sulphur. *Journal of Electron Spectroscopy and Related Phenomena*. 1976;9(3): 261–267. [https://doi.org/10.1016/0368-2048\(76\)80045-x](https://doi.org/10.1016/0368-2048(76)80045-x)
13. Domashevskaya E. P., Terekhov V. A. d-s, p resonance and electronic structure of compounds, alloys, and solid solutions. *Physica Status Solidi (B): Basic Solid State Physics*. 1981;105(1): 121–127. <https://doi.org/10.1002/pssb.2221050113>
14. Farberovich O. V., Kurganskii S. I., Domashevskaya E. P. Problems of the opw method. *Physica Status Solidi (B): Basic Solid State Physics*. 1979;94(1): 51–62. <https://doi.org/10.1002/pssb.2220940105>
15. Domashevskaya E. P. *The nature of interatomic interaction and patterns of structure of the energy spectrum of valence electrons in semiconductors\**. Abstract of a dissertation for the degree of Doctor of Physical and Mathematical Sciences. Kyiv: 1979. 40 p. (In Russ.). Available at: [https://rusneb.ru/catalog/000199\\_000009\\_007745826/](https://rusneb.ru/catalog/000199_000009_007745826/)

16. Farberovich O. V. *Electronic structure and physical properties of d- and f-metal compounds\**. Abstract of a dissertation for the degree of Doctor of Physical and Mathematical Sciences. Moscow: 1984. 38 p. (In Russ.). Available at: [https://rusneb.ru/catalog/000199\\_000009\\_004031164/](https://rusneb.ru/catalog/000199_000009_004031164/)
17. Terekhov V. A. *Local density of electron states in disordered semiconductors\**. Abstract of a dissertation for the degree of Doctor of Physical and Mathematical Sciences. Voronezh: 1994. 31 p. (In Russ.). Available at: [https://rusneb.ru/catalog/000199\\_000009\\_000045115/](https://rusneb.ru/catalog/000199_000009_000045115/)
18. Yurakov Yu. A. *Electronic structure and physical properties of thin metal-silicon films\**. Abstract of a dissertation for the degree of Doctor of Physical and Mathematical Sciences. Voronezh: 2000. 33 p. (In Russ.). Available at: [https://rusneb.ru/catalog/000199\\_000009\\_003203397/](https://rusneb.ru/catalog/000199_000009_003203397/)
19. Turishchev S. Yu. *Electronic and energetic structure of nanosized structures based on silicon and its compounds\**. Abstract of a dissertation for the degree of Doctor of Physical and Mathematical Sciences. Voronezh: 2014. 32 p. (In Russ.). Available at: [https://rusneb.ru/catalog/000199\\_000009\\_005547670/](https://rusneb.ru/catalog/000199_000009_005547670/)
20. Lenshin A. S. *Formation and functional properties of nanostructures based on porous silicon\**. Abstract of a dissertation for the degree of Doctor of Physical and Mathematical Sciences. Voronezh: 2020: 32 p. (In Russ.). Available at: [https://rusneb.ru/catalog/000199\\_000009\\_010256759/](https://rusneb.ru/catalog/000199_000009_010256759/)
21. Kurgansky S. I. *Electronic structure of thin films of complex metal oxides\**. Abstract of a dissertation for the degree of Doctor of Physical and Mathematical Sciences. Voronezh: 1996. 32 p. (In Russ.). Available at: [https://rusneb.ru/catalog/000199\\_000009\\_000142682/](https://rusneb.ru/catalog/000199_000009_000142682/)
22. Borsch N. A. *Atomic and electronic structure of silicon-based nanoforms\**. Abstract of a dissertation for the degree of Candidate of Physical and Mathematical Sciences. Voronezh: 2005. 16 p. (In Russ.). Available at: [https://rusneb.ru/catalog/000199\\_000009\\_003040792/](https://rusneb.ru/catalog/000199_000009_003040792/)
23. Kurkina L. I. *Electronic properties of s,p- and 3d-metal clusters\**. Abstract of a dissertation for the degree of Doctor of Physical and Mathematical Sciences. Moscow: 1997. 37 p. (In Russ.). Available at: [https://rusneb.ru/catalog/000199\\_000009\\_000142345/](https://rusneb.ru/catalog/000199_000009_000142345/)
24. *Leading scientific schools: reference and information materials\**. A. S. Sidorkin (ed.). Voronezh: Voronezh State University Publ.; 2001. 172 p. (In Russ.).
25. Manukovsky E. Yu., Kashkarov V. M., Turishchev S. Yu., Terekhov V. A. Using the method of ultrasoft X-ray emission spectroscopy to analyze the composition of the surface layers of porous silicon. *Chemical Physics and Mesoscopy*. 2001;3(1): 104–105. (In Russ.). Available at: <https://www.elibrary.ru/item.asp?id=44459077>
26. Gridnev S. A., Kalinin Yu. E., Sitnikov A. V., Stogney O. V. *Nonlinear phenomena in nano and microheterogeneous systems\**. Moscow: BINOM. Laboratoriya znaniy Publ.; 2012. 352 p. (In Russ.).
27. Domashevskaya E. P. *d-s,p and f-p resonances in compounds. X international conference on X-ray and inner-shell processes in atoms, molecules and solids. Aug. 20–24, 1984.-Leipzig: 1984. Part 1: 115–116.*
28. Domashevskaya E. P., Hadia N. M. A., Ryabtsev S. V., Seredin P. V. Structure and photoluminescence properties of SnO<sub>2</sub> nanowires synthesized from SnO powder *Condensed Matter and Interphases*. 2009;11(1): 5–9. Available at: <https://www.elibrary.ru/item.asp?id=13084940>
29. Shaposhnik A. V., Zvyagin A. A., Yukish V. A., Ryabtsev S. V., Domashevskaya E. P. *Method of selective air analysis for acetone*. Patent RF: No. RU 2377551 C2. Publ. 27.12.2009. Application No. 2007145706/28 dated 10.12.2007. (In Russ.). Available at: <https://patenton.ru/patent/RU2377551C2.pdf>
30. Ryabtsev S. V. *Electrophysical and optical properties of various nanoforms of tin oxide\**. Abstract of a dissertation for the degree of Doctor of Physical and Mathematical Sciences. Voronezh: 2011. 32 p. (In Russ.). Available at: [https://rusneb.ru/catalog/000199\\_000009\\_004857465/](https://rusneb.ru/catalog/000199_000009_004857465/)
31. Domashevskaya E. P. To the 90th anniversary of Zhores Alferov, Nobel Prize laureate and a Full Member of the Academy of Sciences. *Condensed Matter and Interfaces*. 2020;22(1): 135–143. Available at: <https://www.elibrary.ru/item.asp?id=42883105>
32. Domashevskaya E. P., Terekhov V. A., Kashkarov V. M., ... Alferov Zh. I. Synchrotron investigations of an electron energy spectrum in III–V-based nanostructures. *Semiconductor*. 2003;37(8): 992–997. <https://doi.org/10.1134/1.1601670>
33. Ternovaya V. E. *Structural and optical characteristics of epitaxial five-component solid solutions in heterostructures on A3B5\**. Abstract of the dissertation for the degree of candidate of physical and mathematical sciences. Voronezh. 2013. 16 p. (In Russ.). Available at: [https://rusneb.ru/catalog/000199\\_000009\\_005537826/](https://rusneb.ru/catalog/000199_000009_005537826/)
34. Seredin P. V. Substructure and optical properties of epitaxial heterostructures based on A3B5\*. Abstract of a dissertation for the degree of Doctor of Physical and Mathematical Sciences. Voronezh. 2012. 32 p. (In Russ.). Available at: [https://rusneb.ru/catalog/000199\\_000009\\_005056124/](https://rusneb.ru/catalog/000199_000009_005056124/)
35. Seredin P. V. *New physical phenomena in heterostructures based on A3B5 semiconductors. Promising approaches to the creation of optoelectronics of the future\**. Moscow: Novyi indeks Publ.; 2015. 220 p. (In Russ.). Available at: [https://rusneb.ru/catalog/000199\\_000009\\_007890641/](https://rusneb.ru/catalog/000199_000009_007890641/)

\* Translated by author of the article

## Information about the author

Evelina P. Domashevskaya, Dr. Sci. (Phys.–Math.), Full Professor, Department of Solid State Physics and Nanostructures, Voronezh State University (Voronezh, Russian Federation).

<https://orcid.org/0000-0002-6354-4799>  
fft@phys.vsu.ru

Received May 28, 2025; published online September 25, 2025.

Translated by Evelina P. Domashevskaya



# ВЕКТОН-ЦЕНТР

ВСЕ НЕОБХОДИМОЕ ДЛЯ ВАШЕЙ ЛАБОРАТОРИИ

- ✓ лабораторное оборудование
- ✓ лабораторная мебель
- ✓ химические реактивы
- ✓ лабораторная посуда



## Вектон-Центр исполнит любой каприз для вашей лаборатории

Общество с ограниченной ответственностью «Вектон-Центр» было основано в 2007 году как представительство крупнейшей компании ЗАО «ВЕКТОН», г. Санкт-Петербург, которая уже более 20 лет занимается производством химических реактивов.

Первоначально основным направлением работы компании была поставка химических реактивов, посуды и расходных материалов для лабораторий. Сейчас мы занимаемся комплексным оснащением лабораторий практически во всех отраслях Российской промышленности, образования и науки. Мы готовы предоставить широкий ассортимент лабораторной мебели и оборудования различного назначения для применения в пищевой, тяжелой и легкой промышленности, а так же в нефтегазовой отрасли.

Современные потребности лабораторий предъявляют высокие требования к качеству используемого оборудования, химических реактивов и расходных материалов. Компания «Вектон-Центр» готова предложить лучшую продукцию для осуществления поставленных задач. Мы предъявляем высокие требования не только к поставляемой продукции, но и к работающему персоналу.

Сотрудники компании могут оказать профессиональную консультацию при подборе лабораторного оборудования, лабораторной мебели, химреактивов, посуды и расходных материалов для лабораторий.

## 6 причин для сотрудничества с нами



**С нами надежно и спокойно**  
мы не исчезнем завтра с рынка - с 2007 года стабильно растем и развиваемся



**С нами удобно**  
это действительно удобно, когда можно купить все необходимое в одном месте



**Разные варианты оплаты**  
предоплата по договору в размере 100%, 50/50, 30/70 или отсрочка



**С нами выгодно**  
предлагаем оптимальные цены, работаем по прайсам производителей



**Любые варианты доставки**  
самовывоз, транспортная компания или с помощью наших машин



**Система скидок и поощрений** для наших постоянных клиентов

Для вас и за вас решим даже самые сложные задачи по комплексному оснащению лабораторий, созданию лабораторий под ключ, подбору оптимального оборудования под ваши цели с учетом технических требований.

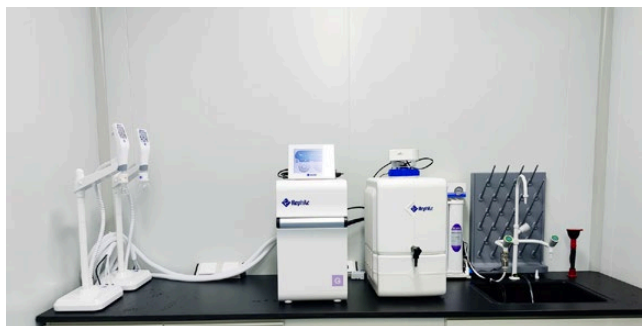
---



**Простые и сложные химические соединения, наборы**



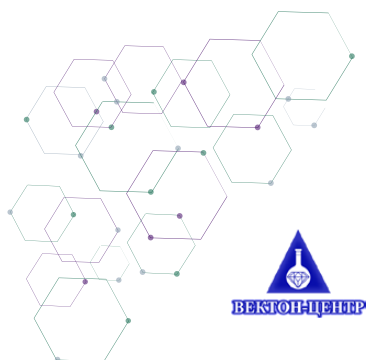
**Лабораторный пластик, стекло, принадлежности**



**Общелабораторное и аналитическое оборудование**



**Лабораторная мебель различных конфигураций и цветов**



**Если вы согласны с тем, что время - деньги, приходите к нам за решением своих задач по оснащению лаборатории!**

**Задать вопросы или оставить заявку вы можете любым удобным способом:**

по телефонам +7 (473) 260-20-54, +7 (473) 232-40-49  
или по электронной почте [vekonvm@list.ru](mailto:vekonvm@list.ru)

Подробную информацию о нас вы найдете на сайте [www.vekonvm.ru](http://www.vekonvm.ru)  
Адрес офиса: г. Воронеж, 394026, проспект Труда, 48/5, 2 этаж



комплексное оснащение и  
снабжение лабораторий

- оборудование
- мебель
- посуда
- расходные материалы

Компания “ПроЛаб-Трейд” с 2013 года помогает решать различные задачи по оснащению химических лабораторий на производствах, в образовательных учреждениях и науке. Найти оптимальное решение, сочетающее в себе приемлемую цену без потери качества, - главная цель нашей работы.



Больше 10 лет мы занимаемся как комплексным оснащением новых лабораторий, так и дооснащением существующих. Огромный опыт и знания, накопленные за все время работы, позволяют нам четко выполнять обязательства и экономить ваш бюджет.

Многолетнее партнерство с ведущими Российскими и зарубежными производителями дает возможность нашим заказчикам получать необходимое лабораторное оборудование, мебель, посуду и расходные материалы по ценам производителей, а также гарантирует качество поставляемых товаров, подтвержденное соответствующей документацией.

## Заказать в одном месте все, что нужно для вашей лаборатории, - это удобно!



грамотный подбор  
оборудования  
от специалистов с  
опытом работы  
10+ лет



доставка в любой  
регион России



собственное производство  
лабораторного  
оборудования и посуды  
OmnisLab



официальные дилеры и  
представители  
производителей (ЛОИП, Simple  
PRO, Смоленское СКТБ СПУ,  
BIOSAN, Mettler Toledo, Unico,  
Минимед и др.)



постоянный  
участник  
Госзакупок



ПроЛаб-Трейд



## ПОДБЕРЕМ ДЛЯ ВАС



### Лабораторное оборудование

- весовое оборудование
- термостаты
- сушильные шкафы
- муфельные печи
- шейкеры
- мешалки магнитные
- оборудование для хроматографии
- анализаторы влажности
- спектрометры и спектрофотометры
- ламинарные боксы
- стерилизаторы и многое другое



### Лабораторная мебель

- вытяжные шкафы
- столы специализированные
- столы-мойки
- столы на опорных тумбах
- стеллажи к столам
- тумбы хранения
- шкафы хранения
- зонты вытяжные
- технологические стойки к лабораторным столам
- вспомогательное оборудование и многое другое



### Лабораторная посуда из стекла и пластика

- колбы конические, круглодонные, мерные и др.
- воронки лабораторные
- воронки делительные
- стаканы высокие и низкие
- банки из светлого и темного стекла с винтовыми и притертыми крышками
- пипетки
- чашки Петри и многое другое

**Поделитесь с нами своей задачей по оснащению лаборатории и мы обязательно поможем вам сэкономить время, деньги и нервы!**

Открыты для общения с Пн по Пт с 9.00 до 18.00 по мск времени.

#### Наш офис в Москве

г. Москва, ул. Кольская, д. 1

+7 (495) 210-34-35

info@plt-lab.ru



**ПроЛаб-Трейд**

www.plt-lab.ru

#### Наш офис в Краснодаре

г.Краснодар, ул. Уральская, д.126Б

+7 (861) 248-88-01

prolabtreid.3@list.ru

